Università degli Studi di Siena

Facoltà di Scienze Matematiche Fisiche e Naturali

Tesi di Dottorato in Fisica Sperimentale
PhD Thesis in Experimental Physics

XIX Ciclo

Measurement of Kinematic Properties and Fractions of Charged Particle Species Produced in Association with B Mesons Using the CDF II Detector

Candidato

Pierluigi Catastini

Relatore

Dott. **Maria Agnese Ciocci**

Tutor

Prof. **Giovanni Punzi**

Contents

Chapter 1

Introduction and Motivations

In this chapter I summarize the motivations and the evolution steps of my work.

1.1 The Same Side Kaon Tagging for B_s oscillations

The search for and the study of flavor oscillation in the neutral $B_s\bar{B}_s$ meson system is one of the most important goals of particle physics and a flagship analysis of the CDF Run II physics program. The phenomenon of neutral $B-\bar{B}$ flavor oscillations, or mixing, refers to the particle-antiparticle transition in the neutral B meson system, where B can be either B^0 or B_s. The rate at which these transformations occur is characterized by the mass difference, denoted Δm, between the two quantum states of the meson. In particular, the knowledge of both the mixing frequencies of $\bar{B}_b^0$ and $\bar{B}_s^0$ meson (Δm_d and Δm_s) allows to improve the knowledge of the weak interactions by measuring the elements of Cabibbo-Kobayashi-Maskawa (CKM) matrix. It would facilitate a test of CKM matrix unitarity and potentially probe for new physics beyond the Standard Model (SM); more details about mixing phenomenology are described in chapter 2.

In a simplified picture, a mixing analysis is a measurement of the asymmetries between the observed number of $\bar{B}$ and B mesons as a function of time. This obviously requires the knowledge of the B flavor when it is produced and when it decays. The B flavor at decay time can be inferred from the charges of the decay products[1], while the B flavor at production time has to be inferred by indirect techniques known as *flavor tagging* algorithms.

One of the B flavor tagging techniques is called *Same Side Tagging* (SST) that in the case of the B_s meson, for a reason that will be clear in a few, is specialized to *Same Side Kaon Tagging* (SSKT).

The idea behind the SST is related to the process of the B meson formation. The b quarks are produced in a $p-\bar{p}$ collision; they then form a B meson by coupling with one of the lighter quark species. This process, called fragmentation, is believed to be dominated by strong interaction, which conserves the quark flavor. Therefore, quark-

[1]For example in the exclusive decay mode $B_s \to D_s^- \pi^+$ and $\bar{B}_s \to D_s^+ \pi^-$ the charge of the pion in the final state is directly related to the B_s flavor.

antiquark pairs are produced during fragmentation. In this process, lighter quarks are preferentially generated because of the lower energy needed to create the corresponding pair. From this qualitative description, we can assume that if, for example, a B_s meson is found in a given event, during the fragmentation a $s\bar{s}$ pair was produced: one of the s quark combines with the b quark to create the B_s meson; the other s quark may form a K meson or any other kind of strange hadron. Similarly, as shown in Fig.1.1, pions are more likely to be produced in B^0 and B^+ events. The key point is that the flavor of the particle carrying the antiquark of the sea quark forming the B is directly correlated to the B flavor at production time: if we are able to observe it we can *tag* the B.

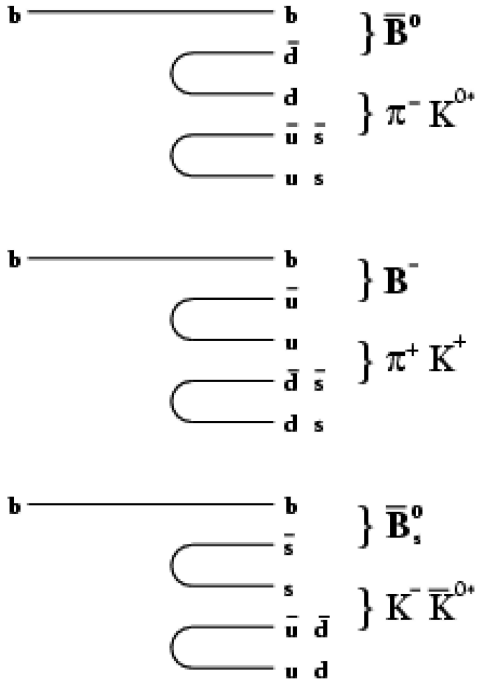

Figure 1.1: Simplified examples of the B-meson formations.

The performances of a flavor tagging algorithm can be resumed by two quantities: the *efficiency* (ϵ), which represents the probability that the tagger gives a response about the B flavor and the *dilution* (D), which is related to the probability that the tagger response is incorrect (P_{wrong}) through the relation:

$$D = 1 - 2P_{wrong} \tag{1.1}$$

An ideal tagger (but it is never the case!) would be characterized by $\epsilon = 1$ and $D = 1$. Of course, the tagger performances are directly related to the resolution δA on the asymmetry (A) measured on a sample of S signal events as:

$$\delta A \propto \frac{1}{\sqrt{\epsilon D^2 S}} \tag{1.2}$$

Equation (1.2) can be also read as: given a sample of S signal events, the performances of our tagging algorithm *will degrade* our effective statistics and the resolution on the asymmetry will be equivalent to the one of a measurement performed in a sample of $\epsilon D^2 S$ signal events using a perfect tagger.

SST for B^0 and B^+ events have already been used at CDF, both during Run I and II, in B^0 mixing analysis and time-dependent CP violation measurements. In those studies it was pointed out how the SST performances are better then the ones of the other tagging strategies, called Opposite Side taggers[2], (OST), even better then the *combination* of the OST in B^+ events [1] [2]. Why was the SSKT not used since the beginning in B_s mixing analysis ? A characteristics of mixing analysis based on the *amplitude method* [3], used at CDF and previous experiments, is that the dilution of the flavor taggers is not a free parameter but is needed as input, i.e. dilutions must be known before looking for mixing. The OST dilution can be extracted for example from B^+ events because the opposite side characteristics do not depended on the reconstructed B meson and are the same for B^+, B_0 and B_s. On the other hand, in the case of the SSKT there is no straightforward way to measure the dilution on data since the fragmentation is related to the B meson and it is different for B^+, B_0 and B_s: SSKT dilution can only be fitted on B_s data once B_s mixing is observed. The remaining possibility is to rely on Monte Carlo simulation of the quark fragmentation process and use the corresponding prediction on the dilution of SSKT algorithms.

1.1.1 My contribution to the Monte Carlo approach

The Monte Carlo approach for SSKT dilution evaluation faces a quite challenging difficulty: it is unknown how well the fragmentation of each particle type is simulated. In particular, even if similar techniques have been used at LEP [4] where Pythia [85] generator was tuned very carefully and found to be in very good agreement with data in several cases, shower Monte Carlos like Pythia have never been tested at the required level of accuracy in hadronic environment. At the time it was known from CDF Run I that Pythia Monte Carlo was reasonably reproducing data SST performances without the use of particle identification information [6]: however there was no knowledge about Pythia behavior when a particular particle type was selected as required by the SSKT.

Attracted by the potentiality of this tagging method, I performed some studies to understand the Pythia Monte Carlo behavior in fully reconstructed B decays [63]. In fact it was evident that due to the complicated background composition, even with higher statistics, a detailed data-Monte Carlo comparison for SSKT could not be performed in semileptonic B decays. On the other hand, the production of a Monte Carlo sample of fully reconstructed B decays, due to the low selection efficiency, was considered quite challenging. As shown in [5] and [63], it was also evident that simplified Pythia generations (only the direct production of $b\bar{b}$ couples are allowed) do not properly reproduce data distributions while a Pythia sample, with all the QCD process allowed, was in better agreement with the data. Applying several ad hoc solutions, I was the first to produce a Pythia Monte Carlo sample of fully reconstructed B decays

[2]Opposite Side Tagging infers the B flavor at production time looking at the properties of the decay products of the other b hadron of the event. A detailed description of OST is out of the scope of this thesis.

(all the QCD processes allowed and the full detector simulation included). My first data-Monte Carlo comparisons in $B^+ \to J/\psi\, K^+$ decays are reported in [63]. In that study, I compare some kinematic distributions of particle seen around B^+ meson in data and Monte Carlo without selecting a particular particle species. A reasonable agreement was found, confirming what observed in Run I [6].

Another important step through the understanding of SSKT was the application of Particle Identification (PID) information both to data and Monte Carlo. Up to that moment, Monte Carlo had been tested without looking at the involved particle types [6]. The detector simulation was found to be unsatisfactory regarding the PID. Using the parametrization of CDF Particle Identification detector resolutions (time-of-flight measurement and energy loss of charged particles in the drift chamber) extracted in data in [83] [84], I developed in [62] a parametric simulation of PID response to different particle types: π, K, p, e and μ.

For the first time in CDF run II I showed a comparison between data and MC, using $B^+ \to \overline{D}^0\, \pi^+$, about tagging performances without the use of PID. Monte Carlo expectations on the dilution of the SST were found in good agreement with data: in [62] I tested three different selection strategies of the tagging particle and the resulting dilutions agreed with Monte Carlo within statistical uncertainties. More relevant, for the first time at hadron colliders I also tested SST in a B^+ samples applying a selection on PID variables to select an enhanced sample of Kaons produced in association with the B meson. Also in that case, the agreement of the dilution expectations were good. In addition, several kinematic variables of particles seen around $B^+ \to \overline{D}^0\, \pi^+$ were compared: see, for example, Fig.1.2 where P_T and P_T^{rel} [3] distributions are shown (left and right respectively). I did the same kinematic comparisons also after applying a cut

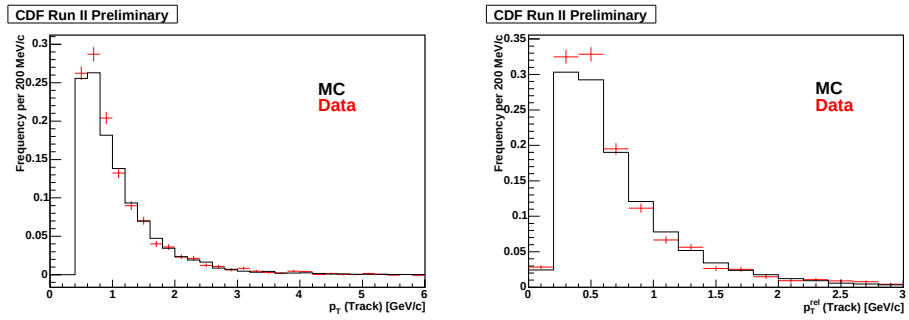

Figure 1.2: Left: P_T spectrum of tracks around the B^+ meson; data (points) and Monte Carlo (histogram). Right: p_T^{rel} spectrum of tracks around the B^+ meson; data (points) and Monte Carlo (histogram).

on PID variables Fig.1.3 to select kaons. In this case the kinematics agreement was found to be poor, even if the tagging performances were consistent. I produced the same distributions for tracks selected around $B_s \to D_s^-\, \pi^+$ decays. This was a novelty (also without using PID selections) because Run I comparisons were performed in

[3] The transverse component with respect to the B meson flight direction of the track.

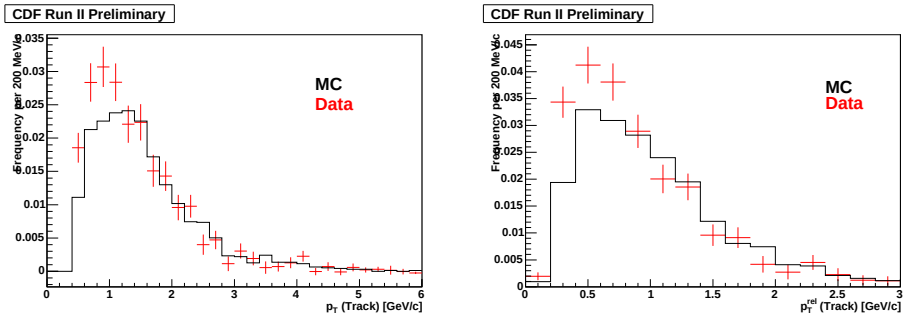

Figure 1.3: After the selection of an enhanced kaon sample.Left: P_T spectrum of tracks around the B^+ meson; data (points) and Monte Carlo (histogram). Right: p_T^{rel} spectrum of tracks around the B^+ meson; data (points) and Monte Carlo (histogram).

semileptonic decays of B^+ only. The agreement between data and Monte Carlo was found to be very good, see Fig.1.4 and Fig.1.5, even when applying a selection on PID information to enhance the kaon content. Anyway, the B_s comparisons suffer the low statistics and the agreement between data and Monte Carlo is within large uncertainties. Moreover, the most important result of [62] was the measurement of

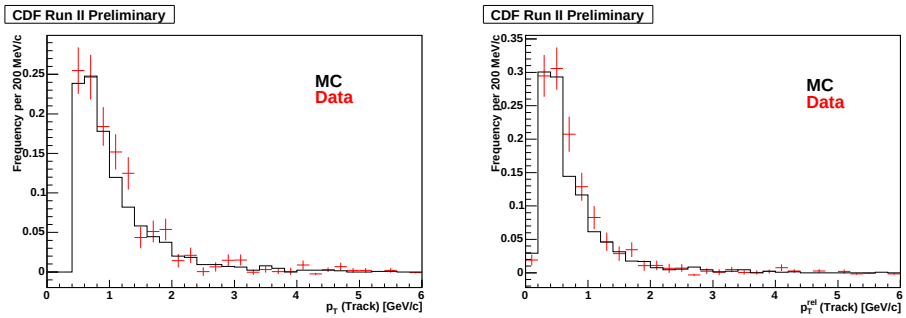

Figure 1.4: Left: P_T spectrum of tracks around the B_s meson; data (points) and Monte Carlo (histogram). Right: p_T^{rel} spectrum of tracks around the B_s meson; data (points) and Monte Carlo (histogram).

the SSKT performances in B_s Monte Carlo. I found:

$$\epsilon D^2 = 2.91 \pm 0.64\% \tag{1.3}$$

It was the first time that such a number was obtained with reliable simulation of the detector and of the PID response. Consider that the combination of all the OST algorithms at the time provided $\epsilon D^2 \sim 1.2\%$ [2]: the SSKT alone was expected to be a factor two more powerful; in addition, the procedure I followed to select the tagging track[4] was obviously not optimized: my aim was to test the Monte Carlo accuracy

[4]The one that is supposed to carry the right charge correlation with the B flavor at production time.

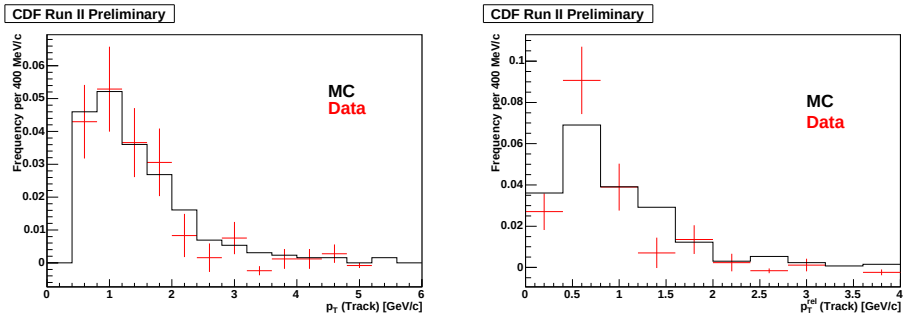

Figure 1.5: After the selection of an enhanced kaon sample.Left: P_T spectrum of tracks around the B_s meson; data (points) and Monte Carlo (histogram). Right: p_T^{rel} spectrum of tracks around the B_s meson; data (points) and Monte Carlo (histogram).

before optimize. Those results were used for new CDF II projections [7] on B_s mixing and shown at conferences and financial committees [8], [9], [10], [11], [12], [13].

The picture that could be taken from what described and from additional improvements I looked for was that the SST and SSKT dilution predicted for B^+ and B^0 mesons by Monte Carlo were in good agreement with data. This was true in several configuration [62], with and without using PID information, even if several tests on kinematics variables showed discrepancies between data and Monte Carlo distributions, in particular when PID was applied. In chapter 4 I resume the most important results of this work.

1.1.2 SSKT on data: B_s mixing observation

It was clear that the application of SSKT would have dramatically improved the B_s mixing analysis. At the time, a lot of interest grow and a strong effort of the CDF collaboration started according a well defined strategy: since Monte Carlo is not far from data, we had to asses systematics on the dilution extracted from Pythia to use the tagger on data. Several techniques I developed in my studies where then used to asset systematic uncertainties. The SSKT has been finally applied to data [57], performances of an optimized algorithm where found to be (systematics included) $\epsilon D^2 = 4.0 + 0.9 - 1.2$ %. B_s mixing was observed and Δm_s measured by CDF [14] few months before this thesis was written. Fig.1.6 shows the amplitude scan on data using OST only (left) and SSKT only (right): notice the higher resolution on the measured asymmetry provided by the SSKT respect to the OST. The amplitude scan resulting from the combination of OST and SSKT is shown in Fig.1.7 where a clear peak to the oscillation is visible.

In conclusion the SSKT has a very important role in the B_s mixing result and my studies pushed the collaboration towards the application of this tagger on data.

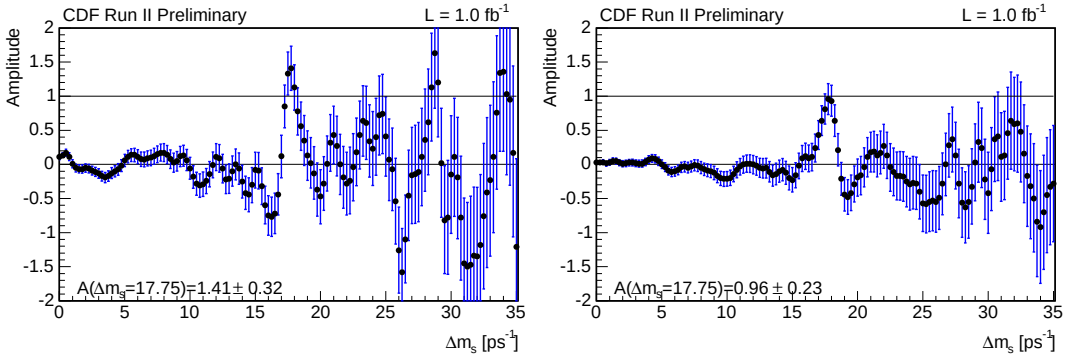

Figure 1.6: Amplitude scan of B_s events using all the OST algorithms only (left) and the SSKT only (right).

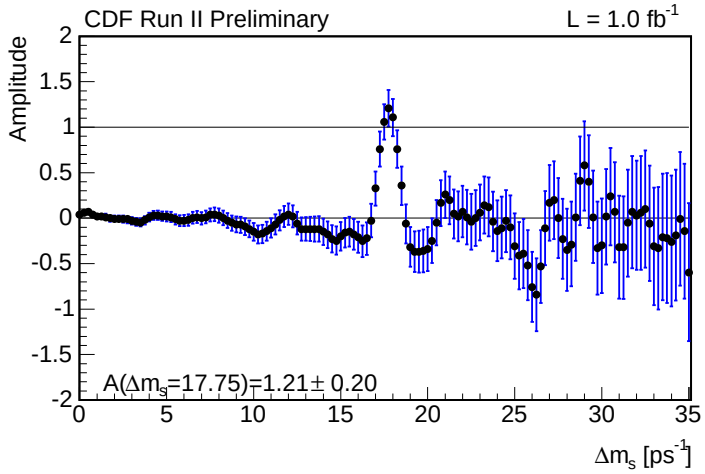

Figure 1.7: Amplitude scan scan of B_s events using of all flavor tagging algorithms.

1.2 Why the particle fractions

In the same period I was totally involved in the SSKT development, a measurement of the particle fractions produced around B mesons was performed using semileptonic decays of B^+, B^0 and B_s [74]. The conclusions of the analysis are that Monte Carlo seems to overestimate the Kaon fraction with respect to data in B_s while the particle content seems to be reproduced for other B mesons.

I was interested in this kind of measurement for two reasons: it is a good test of Monte Carlo behavior for the B non-perturbative fragmentation process; even if the dilution was reasonably reproduced for B^+ and B^0, there was evidence that, when applying PID selections, the agreement of kinematic distributions was not satisfactory. In particular, even if we are now using SSKT and SST in mixing analysis and systematics

are reasonably covering all the discrepancies, the understanding of which particles are actually tagging and how they are kinematically related to the B is not completely understood. This feature can be investigated to improve the tagging performances.

In addition, during the SSKT development, I used for the first time PID information to select enhanced samples in a given particle type to get an idea of how the corresponding kinematics appear. Consider that CDF PID capabilities, as shown in chapter 3 do not allow for a perfect separation between different particle types. An obvious question arises: is there any way to directly see kinematic variable distributions of each particle species produced around the B mesons even if on a statistical base only?

If we had access to such information we could study the properties of the whole B event and understand the kinematics properties of the tagging particles both in the SST and the OST. I spent the last year of my PhD pursuing this goal.

The results from the first part of my work on SSKT boosted the B_s mixing analysis, which is now published and worldwide recognized [14] as one of the best results of CDF Run II up to date. The second part of my work, on the other hand, having to do with a non-standard approach, will require more time before an application to the complex problem of reducing systematics. For this reasons in this thesis I mainly report on this second part.

Chapter 5 describes the B^+, B^0 and B_s decay modes selections. The selected samples will be used in the following chapters for the particle types measurements.

I realized that the particle fraction measurements are not straightforward and they arise several statistical issues, as described in chapter 6. I then found a first solution that allows to extract the particle content and, at the same time, a reasonable description of the P_T distribution of each species. This method is described at the beginning of chapter 6 and is reported in the proceedings [73]. Finally, the core of this thesis, I found a more interesting generalization that allows the extraction of the particle fractions, the corresponding P_T spectra and the distribution of all the kinematic variables related to the considered tracks. This technique is described in chapter 6; its application to fully reconstructed decays of the B mesons (whose selection can be found in 5) is then described in chapter 7. Finally, for the first time at hadron colliders, a *direct* comparison between data and Monte Carlo predictions is shown in chapter 8.

In the conclusions we will review future perspective and applications of this technique.

Chapter 2

Theoretical Overview

The aim of particle physics is the understanding of the behavior of the elementary particles. The Standard Model (SM) is the theory that quantitatively describes the behavior of all known particles and interactions, with the exception of gravity.

In the SM, all matter consists of 12 fundamental fermions (half integer spin particles): six quarks and six leptons subdivided into three generations of quarks and leptons couples. These particles can interact through four different types of forces: *strong*, *weak*, *electromagnetic* and *gravitational*. Leptons participate in the weak interactions, while quarks can also interact via the strong forces governed by a quantum property called *color*. All the particles that have electric charge can interact via electromagnetic force. The interactions between these fundamental particles are described by a set of integer spin particles, or bosons, that are often called the force carriers. The carriers of the strong interaction are called gluons, the carriers of the weak force are W and Z bosons, while photons are the carriers of the electromagnetic force.

While the SM has been incredibly successful in explaining several experimental observation with high level of accuracy, it is by no means complete and many efforts focus on searching for phenomena that cannot be explained by SM. In this chapter we provide an overview of the physics processes underlying the phenomena studied in pour analysis, how they are understood in terms of the SM and how they are relevant for the test of validity of the SM.

2.1 b quark production at the Tevatron

As stated before, this analysis studies the b quark properties associated with their production in high energy $p\bar{p}$ collision. During this collision the constituent particles of the $p\bar{p}$ pair (quarks and gluons) interact, and, as a result, a variety of secondary products may be created.

Quantitatively, the Standard Model describes the strong interaction with a theory called "Quantum Chromodynamics" (QCD). According to this the theory, the force potential between the quarks grows with the distance between them which prevents quarks from existing in a free state. The quarks therefore have to form colorless composite particles, such as mesons and baryons, and can only be observed indirectly.

Mesons are the two-quark states where color neutrality is achieved by coupling a quark-antiquark pair. The baryons are three-quark states where quarks of three different colors (red, blue, green) form a color-neutral (also called white) state.

The strong interactions between quarks conserve quark flavor, which means that when heavy quarks are created during the $p\bar{p}$ collision, they are created in pairs of a quark and the corresponding antiquark. The leading order QCD process resulting in heavy quark creation involve two-to-two QCD transitions as shown in Fig.2.1, via either the annihilation of two lighter quarks or fusion of two gluons. Since the rest frame of the $p\bar{p}$ system is close to being at rest in the detector frame of reference, one can naively expect that in the leading order processes, the heavy quarks will be created with approximately opposite momenta. This leads to the rise of the terms "'same-side" and "opposite-side" b quark when referring to the quark pairs. The 2-2 transition resulting

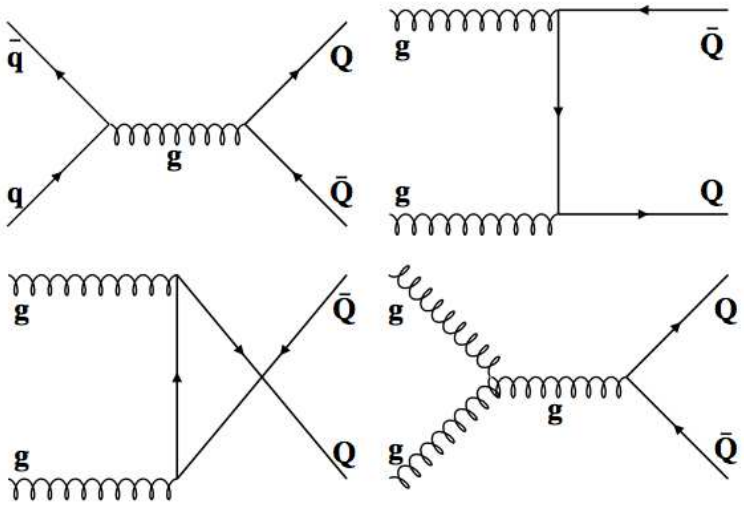

Figure 2.1: The Feynman diagrams showing the flavor creation type transitions leading to heavy quark Q at the Tevatron. These diagrams show the leading order QCD processes.

in $b\bar{b}$ pair production is often referred to as the flavor creation process. The lowest order diagrams in Fig.2.1 contribute to only a part of the total b quark production cross-section. Fig.2.2 shows additional diagrams that when included make a non-trivial contribution to the flavor creation process. These diagrams correspond to the next-to-leading order (NLO) processes called initial and final state gluon emission. Finally, Fig.2.3 shows additional NLO processes that are called flavor excitation and gluon splitting. They contribute significantly to the b quark production at the Tevatron. Note that in these additional NLO processes one cannot make the assumption about the relative momenta of the b quarks and antquarks being roughly opposite. In fact, the study of the momentum correlations of the same side and opposite side b quarks is one of the major sources of information we have for measuring the relative contributions of the flavor creation versus the NLO processes.

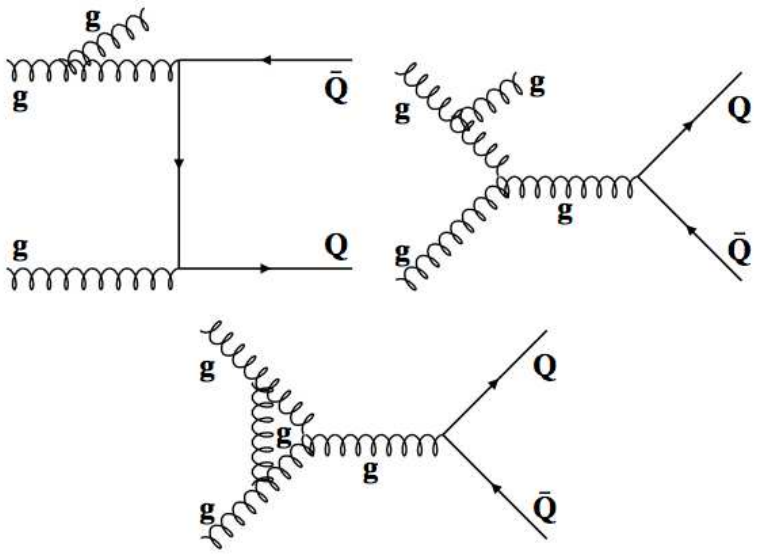

Figure 2.2: The Feynman diagrams showing the flavor creation type transitions leading to heavy quark Q at the Tevatron. These diagrams correspond to the next to leading order QCD processes. The two diagrams on top are called real gluon emission and the bottom is called the virtual gluon emission diagrams.

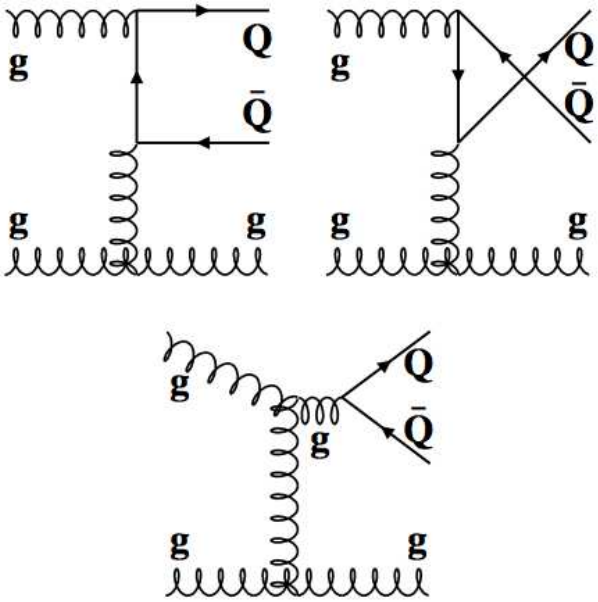

Figure 2.3: The Feynman diagrams showing the flavor excitation (top) and gluon splitting (bottom) leading to heavy quark Q creation. These are the next to leading order QCD processes making significant contribution to the b quark cross-section at the Tevatron.

2.2 Fragmentation models

After a pair of quarks is created in the $p\bar{p}$ collision they undergo a process of forming composite hadron particles. This process is called *fragmentation*. The term *hadronization* is used interchangeably sometimes. Fragmentation is a long distance process with small momentum transfer, so that perturbative QCD techniques cannot be used for an analytical description of this process. instead, a number of models have been proposed to describe quark fragmentation. We will briefly describe two of these models, cluster fragmentation and string fragmentation. The simplified drawings illustrating these models are shown in Fig.2.4 and are explained in the following paragraphs.

In the cluster model the quarks lose part of their momenta through gluon emission and the resulting gluons are split non-perturbatively into pairs of light quarks: $gg \rightarrow q\bar{q}$. These quarks are then broken into colorless clusters which undergo simple decay into pairs of hadrons chosen according to the density of the clusters and their quantum numbers. This model's strong features are the small number of parameters and a simple mechanism for the suppression of heavy particle production and generation of the momentum spectra. However it has encountered significant difficulties in explaining heavy quark fragmentation[1] and the suppression of baryon production. The string

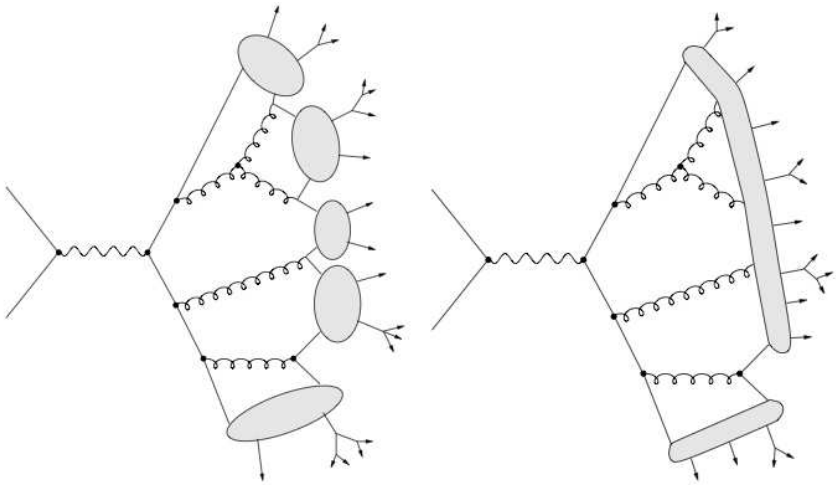

Figure 2.4: Simplified diagrams of the cluster (left) and string (right) fragmentation models.

fragmentation model has been the most successful in quantitatively describing the fragmentation process and is the one most often used in Monte Carlo generators such as Pythia. This model states that a string exists between the quarks produced in a $p\bar{p}$ collision and the energy of this string represents the quark-quark potential and grows with the string size. This leads to the fragmentation of the string *i.e.*, when

[1]It is very difficult to describe both light quark and heavy quark fragmentation within the bounds of the same phenomenological model such as the cluster fragmentation model. The fragmentation of heavy quarks is expected to differ significantly from that of light quarks due to very different kinematics. A heavy quark plays the leading role in determining the kinematics of the fragmentation process and for example will often transfer most of its momentum to the resulting hadron. This is not true for the light quark hadronization.

the distance between the quarks reaches a certain limit, the string breaks into two or more strings by creating quark-antiquark pairs, thus moving into lower energy state. Depending on the initial energy of the $b\bar{b}$ pair this division process may be repeated one or more times. The b quarks then couple with other quarks to form composite particles such as mesons and baryons. A number of other particles may also be created. The string were dubbed so because they are described in QCD as clouds of gluons forming string-like spatial structures, or color fields.

To explain the breaking of the string there are several phenomenological models within the string fragmentation model. The number of these models has grown significantly over the years. Here we will discuss only one such model, the Peterson quark fragmentation model [15]. It has traditionally been the most popular choice for simulations, although it has been found that other fragmentation models describe the experimental results better in some cases. For a recent example and a review of other functions see [16].

The fundamental property of the fragmentation process, which all fragmentation functions aim to describe, is the momentum-energy transfer from the original quark to the resulting hadron. The Peterson fragmentation function is derived from the assumption that the amplitude of the hadronization process is inversely proportional to the energy difference between the initial and the final states of the fragmentation process. If a heavy quark Q with initial momentum P fragments into a hadron H of momentum zP by coupling with a lighter quark $\bar{q}$ (so that a quark q remains in the string), then the energy difference can be written as:

$$\Delta E = E_Q - E_H - E_q = \sqrt{m_Q^2 + P^2} - \sqrt{m_H^2 + (zP)^2} - \sqrt{m_q^2 + (1-z)^2 P^2} \tag{2.1}$$

Making an assumption of a heavy quark fragmentation at high momentum, so that $m_Q \sim m_H$ and $m_Q/P << 1$, and expanding in terms of $(m_Q/P)^2$, one can derive:

$$\Delta E = \frac{m_Q^2}{2P}\left(1 - \frac{1}{z} - \frac{\epsilon_Q}{1-z}\right) \tag{2.2}$$

with the notation $\epsilon_Q = (m_{\bar{q}}/m_Q)^2$. By adding the normalization and the phase space factors, the Peterson fragmentation function relates the transition amplitude to this energy transfer as:

$$|\mathcal{M}(Q \to Q\bar{q})|^2 \propto \frac{1}{\Delta E^2} \tag{2.3}$$

from which we can finally derive a probability $D(z)$ of finding a H hadron of momentum zP among the debris of the original heavy quark Q:

$$D(z) = \frac{N}{z}\frac{1}{(1 - \frac{1}{z} - \frac{\epsilon_Q}{1-z})^2} \tag{2.4}$$

where N is the normalization constant. The parameter ϵ_Q is usually considered a free parameter of the model. It is important to understand that this model is purely phenomenological, and even though it can be tuned to describe many practical situations, it breaks down in many scenarios.

A typical example of the Peterson fragmentation function used in the Monte Carlo generators is shown in Fig.2.5. Note that the momentum fraction transferred to the hadron is larger for a heavier b quark than for a c quark.

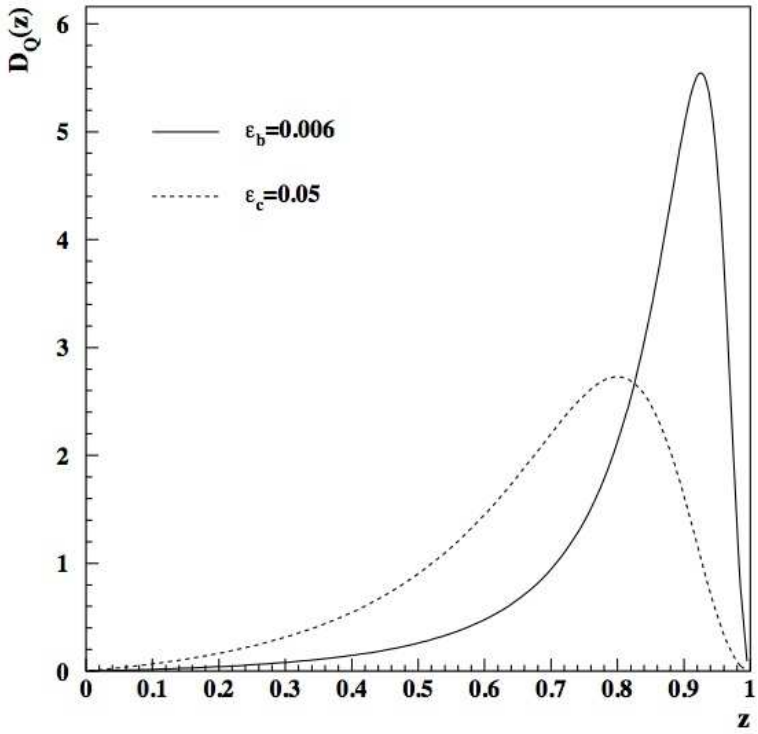

Figure 2.5: An example of the Peterson fragmentation function for b (solid curve) and e (dashed) quarks commonly used in the simulations of the fragmentation process.

2.3 The Standard Model and the CKM

The dynamics of the Standard Model is almost completely determined by the gauge symmetry $SU(3)_{col.} \times SU(2)_L \times SU(2)_Y$ and by the Higgs potential. In fact the spontaneous symmetry breaking of gauge symmetry operated by the Higgs scalar field, breaks the $SU(2)_L \times SU(2)_Y$ symmetry into the residual electromagnetic symmetry $U(1)_{el.}$ generating, in this way, the masses of the weak vector bosons. Therefore, the masses of the quarks and of the leptons rely to the coupling constants between the scalar Higgs and the fermions. So, in this picture, only the electromagnetic and strong interactions are the relic symmetries, turning in the fact that the coupling bosons for those interactions are massless.

In the quark sector, the masses are eigenstates for the electromagnetic and strong interactions but not for the weak interactions. Hence, the experimental evidence is that the weak interaction can changes the flavor of a given quark via a $W^{\pm}$ exchange, *i.e.* via a charged current. The flavor changing is permitted only between different

quark generations[2] and are characterized by the so called CKM (Cabibbo-Kobayashi-Maskawa) matrix elements.

The experimental evidence supports the existence of three generations of lepton and quark doublets. Within the Standard Model, the fermionic fields interact among themselves through the exchange of the gauge bosons: $W^{\pm}$, Z^0, photons and gluons. These interactions are the result of a local invariance of the Lagrangian under gauge symmetry of the group $SU(3)_{col.} \times SU(2)_L \times SU(2)_Y$. In the case of the $SU(2)_L$ symmetry, the interactions are described by coupling terms of the form:

$$\mathcal{L}_{int} = -\frac{g}{\sqrt{2}}(J^{\mu}W^{+}_{\mu} + J^{\mu\dagger}W^{-}_{\mu}) \tag{2.5}$$

where g is the coupling constant of the $SU(2)_L$ group and can be related to the most common Fermi coupling G_F trough the relation $\frac{G_F}{\sqrt{2}} = \frac{g^2}{8M_W^2}$, while the current J^{μ} is defined by

$$J^{\mu} = \frac{1}{\sqrt{2}}\sum_{i=1}^{3}\bar{u}^i_L\gamma_{\mu}d^i_L, \tag{2.6}$$

with the subscript L standing for the chiral projection of the field[3] $d^i_L = \frac{(1-\gamma_5)}{2}d^i$ and the index i runs over the 3 quark generations. This theoretical framework is not able to produce the fermion masses without the introduction of a scalar doublet, the Higgs boson ϕ.
Its introduction generates new terms in the Lagrangian that allow coupling between mass eigenstates. Hence the mass matrix of the 3 generations quark can have off diagonal terms. A general redefinition of the quark fields can be done in order to diagonalize the mass matrix. Such as redefinition have to be a unitary transformation:

$$u^i_L = U^{ij}_u u'^j_L \qquad d^i_L = U^{ij}_d d'^j_L. \tag{2.7}$$

If we apply the field redefinition in Eq. 2.7 into the interaction Lagrangian in Eq. 2.5, we obtain that Eq. 2.6 moves to

$$J^{\mu} = \frac{1}{\sqrt{2}}\sum_{i,j=1}^{3}\bar{u}'^i_L\gamma_{\mu}V_{ij}d'^j_L, \qquad V = U^{\dagger}_u U_d. \tag{2.8}$$

The matrix V is the Cabibbo-Kobayashi-Maskawa (CKM) matrix that determines the strength of the interactions between quarks of different flavor and $W^{\pm}$ bosons. Because the unitarity constraint, the matrix is present only with the charged vector bosons and no flavor changing neutral currents are allowed at tree level. By construction, a $N \times N$ unitary CKM matrix has N^2 real parameters, however $(2 \cdot N - 1)$ parameters can be absorbed by the freedom in the quark field phase selection [17], via a redefinition of

[2] At tree level.

[3] where for each generation we indicate respectively with u^i_l and d^i_l, the up and the down component of the doublet quark field.

the complex phase of the quark fields. Therefore, the number of independent CKM parameters (that has $N = 3$) is 4, and can chosen to be 3 angles and one phase. The last one, arising from the fact that the quark generations are three, is the only source of CP violation in the Standard Model[4].
The CKM Matrix is often written in the form

$$V_{CKM} = \begin{pmatrix} V_{ud} & V_{us} & V_{ub} \\ V_{cd} & V_{cs} & V_{cb} \\ V_{td} & V_{ts} & V_{tb} \end{pmatrix}, \tag{2.9}$$

to emphasize the different physic transitions. The elements are indexed with the quarks flavors that participate in the actual vertex. Hence, each interaction vertex that includes a flavor violation is proportional to the correspondent CKM matrix element. The unitarity of the matrix V implies relations between the V_{CKM} elements such as

$$|V_{ud}|^2 + |V_{us}|^2 + |V_{ub}|^2 = 1, \tag{2.10}$$
$$V_{ud}V_{ub}^* + V_{cd}V_{cb}^* + V_{td}V_{tb}^* = 0. \tag{2.11}$$

These relations hold for any choice of rows or columns. Eq. 2.11 defines a triangle in the complex plane (see Fig 2.6), the *unitary triangle* with angles

$$\alpha = \arg\left[-\frac{V_{td}V_{tb}^*}{V_{ud}V_{ub}^*}\right], \qquad \beta = \arg\left[-\frac{V_{cd}V_{cb}^*}{V_{td}V_{tb}^*}\right], \qquad \gamma = \arg\left[-\frac{V_{ud}V_{ub}^*}{V_{cd}V_{cb}^*}\right]. \tag{2.12}$$

An alternative and convenient parametrization of the CKM matrix is the so called *Wolfenstein parametrization* [18]. In this representation the matrix shows a hierarchy that has the diagonal terms close to unity and the other terms smaller and smaller as they move away from the diagonal. More over, the parametrization shows the matrix dependence by the 4 independent parameters, that are chosen to be λ, A, ρ and η, defined as:

$$\lambda \equiv |V_{us}|, \qquad A \equiv \frac{V_{cb}}{\lambda^2}, \qquad \left|\frac{V_{ub}}{V_{cb}}\right|^2 \equiv \lambda^2(\rho^2 + \eta^2). \tag{2.13}$$

Experimentally, we have that $\lambda \simeq 0.22$, $A \simeq 0.8$, and $\sqrt{\rho^2 + \eta^2} \simeq 0.4$; therefore, expanding V_{CKM} in power series of λ we can write

$$V_{CKM} = \begin{pmatrix} 1 - \frac{1}{2}\lambda^2 & \lambda & A\lambda^3(\rho - \imath\eta) \\ -\lambda & 1 - \frac{1}{2}\lambda^2 & A\lambda^2 \\ A\lambda^3(1 - \rho - \imath\eta) & -A\lambda^2 & 1 \end{pmatrix} + O(\lambda^4). \tag{2.14}$$

where $O(\lambda^4)$ stands for terms of order λ^4 or higher. Indeed the unitarity of the CKM matrix implies that there are six orthogonality conditions between any pair of columns or any pair of rows. These triangles have the same area but different sides. For example, the triangle from the first and second column has two long sides of order λ and one very short of order λ^5, while the sides of the triangle depicted from Eq. 2.11 are all of

[4]In fact, there is another possible source of CP violation arising from the strong sector θ_{QCD}, but no physical evidence has been shown so far.

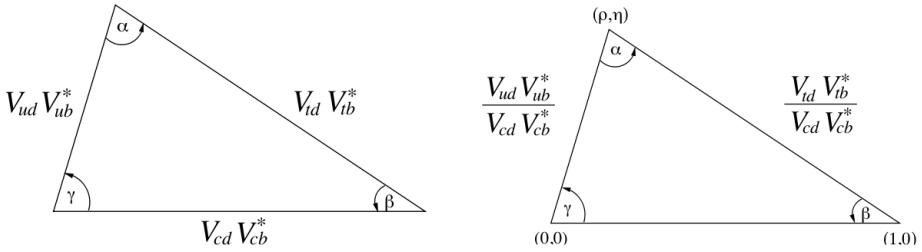

Figure 2.6: The unitarity triangle. The left one is the expression of the Eq. 2.11. On the right the same triangle with all the sides rescaled by the well know quantity $V_{cd}V_{cb}^*$.

the same order $A\lambda^3$. The uniformity between the sides explains why usually physicist refer to this last triangle. It is worth to notice that usually the Eq. 2.11 is rescaled by a factor $A\lambda^3$ and divided by the experimentally precisely measured term $V_{cd}V_{cb}^*$, defining the quantity

$$\bar{\rho} + \imath\bar{\eta} \equiv -\frac{V_{ud}V_{ub}^*}{V_{cd}V_{cb}^*}. \tag{2.15}$$

The rescaled triangle has a vertex in the origin, one on the real axis and one on $(\bar{\rho}, \bar{\eta})$ in the complex plane. The angles of this triangle can be expressed in terms of these new variable:

$$\alpha = \tan^{-1}\left(\frac{\bar{\eta}}{\bar{\eta}^2 + \bar{\rho}(\bar{\rho}-1)}\right), \quad \beta = \tan^{-1}\left(\frac{\bar{\eta}}{1-\bar{\rho}}\right), \quad \gamma = \tan^{-1}\left(\frac{\bar{\eta}}{\bar{\rho}}\right). \tag{2.16}$$

In this triangle, $\bar{\eta}$, $\bar{\rho}$ and $1-\bar{\rho}$ are comparable making easier an estimation of the their values.

2.3.1 Determination of the CKM Elements

In principle all the particle decay phenomena with flavor violation can provide information to determine the CKM matrix elements. However, due to theoretical uncertainties, only few measurements provide results suitable to constrain the Unitary Triangle. The magnitudes of the CKM elements are measured largely, but not exclusively, from semileptonic processes.
A high precision value of $\mid V_{ud} \mid^2$ is obtained comparing the rates for the super-allowed $0^+ \to 0^+ \quad \beta$ decays, like $^{14}O \to^{14} N^*$, to the muon decay rate. From these transitions the world average value is $\mid V_{ud} \mid = 0.974 \pm 0.001$ [19].
The semileptonic decays of strange particles like K^0 and K^+ can be used to study $s \leftrightarrow u$ transitions. In particular, $K^0 \to \pi^- e^+ \nu_e$ gives the best measure of the $\mid V_{us} \mid$. The world average value is found to be $\mid V_{us} \mid = 0.2265 \pm 0.0023$ [19].
The matrix element $\mid V_{cb} \mid$ can be determined studying B meson decays. The b quark decays predominantly into the c quark. The current world average is $\mid V_{cb} \mid = 0.0414 \pm 0.0010(stat.) \pm 0.0018(syst.)$ [19]

Even if B mesons decay predominately in charmed particles, there are some decays involving semileptonic transitions $b \to u\ell^+\nu_\ell$. Because of the large mass difference between the b and u quarks, the lepton momentum is higher than that in the analogous transition $b \to c\ell^+\nu_\ell$. Through a measurement of the lepton spectrum is possible to measure the ratio $\frac{|V_{ub}|}{|V_{cb}|} = 0.090 \pm 0.025$ from which $\mid V_{ub} \mid$ can be inferred from the known $\mid V_{cb} \mid$ value [19].
Because of the unitarity, only four elements are sufficient to determine the entire matrix. In particular following the Wolfenstein parametrization we have

$$\begin{aligned} \lambda &= |V_{us}|, \\ \left|\frac{V_{ub}}{V_{cb}}\right| &= \lambda\sqrt{\rho^2+\eta^2}, \\ |V_{cb}| &= A\lambda^2, \\ |V_{td}^* V_{tb}|^2 &= A^2\lambda^6[(1-\rho)^2+\eta^2]. \end{aligned}$$

It is thus necessary to obtain information also from the CKM elements involving the top quark. B meson mixing measurements can provide such information because within the Standard Model the mixing frequency can be expressed

$$\Delta m_q = M_{12} = -\frac{G_F^2 m_W^2 \eta_B m_{B_q} B_{Bq} f_{B_q}^2}{12\pi^2} S_0(m_t^2/m_W^2)(V_{tq}^* V_{tb})^2. \tag{2.17}$$

where G_F, m_W, m_t are respectively the Fermi coupling constant and the masses of the $W^\pm$ boson and the *top* quark, S_0 is the Inami-Lim function [20], η_B is a parameter that takes account for QCD corrections and m_{B_q}, f_{B_q}, and B_{B_q} are the mass, the decay constant and the bag parameter of the meson B_q^0 respectively. Measurement of Δm in the B_s^0 and B_d^0 systems can provide information on the CKM elements that are difficult to achieve in other ways.
However, lattice QCD calculations introduce an error of roughly 20% on quantities such as f_{B_q} and B_{B_q}. A measurement of both Δm_s and Δm_d values in the same experiment allows a precise measurement of $\mid V_{td} \mid / \mid V_{ts} \mid$ since most of the hadronic uncertainties cancel out:

$$\frac{\Delta m_s}{\Delta m_d} = \frac{m_{B_S}}{m_{B_d}} \xi^2 \left|\frac{V_{ts}}{V_{td}}\right|^2 \tag{2.18}$$

where $\xi = (f_{B_s}\sqrt{B_{B_s}})/(f_{B_d}\sqrt{B_{B_d}})$ is of the order of one and can be estimated by QCD calculation with an uncertainty at the 2% level [19][21]. Fig. 2.7 shows the current determination of the Unitarity Triangle parameters. Five measurements give the strongest constraints [22]: $\sin(2\beta)$, $\mid V_{ub}/V_{cb} \mid$, ϵ_K, Δm_d, and $\Delta m_d/\Delta m_s$.
The world average value for $\sin(2\beta)$ is 0.674 ± 0.026 [23] and it is dominated by the Belle and BaBar experiments measurements of CP violation in $B^0 \to J/\psi K_S^0$ decays [23]. Additionally B-factories will reduce also the uncertainties on the ratio $\mid V_{ub}/V_{cb} \mid$. Both $\sin(2\beta)$ and $\mid V_{ub}/V_{cb} \mid$ have little theoretical uncertainties. On the contrary even though ϵ_K , that is the amount of CP violation in the kaon system, can be measured quite precisely, translation to a limit on ρ and η is spoiled by theoretical uncertainties

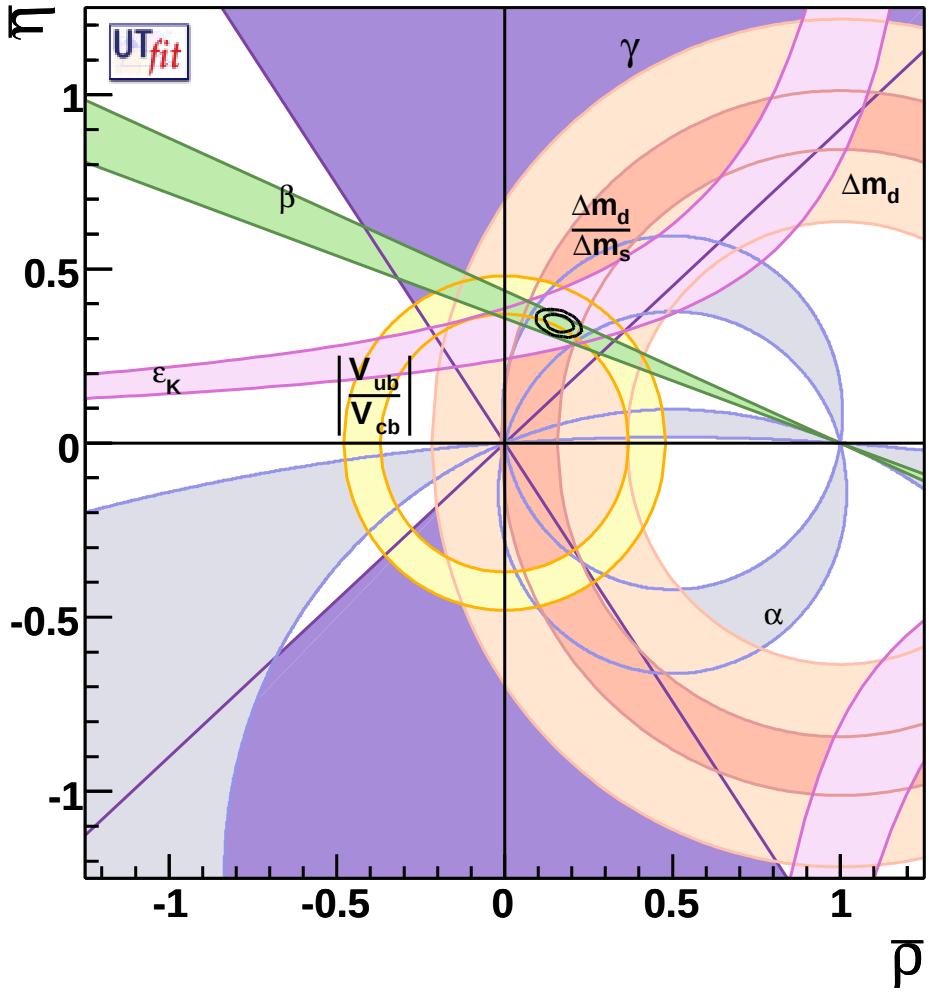

Figure 2.7: Black circles delimits the regions of 68% and 98% probability for the fit results of unitarity Triangle parameters (ρ, η), overlaid in experimental constraints [24].

at 15% level [23].
Therefore the third most precise constraint to the Unitarity Triangle will comes from $\Delta m_d/\Delta m_s$. The recent CDF measurement of $\Delta m_s = 17.77 \pm 0.10 \pm 0.07$ ps^{-1} [14] is included in Fig.2.7.

2.4 The B Meson Mixing

The Standard Model predicts the existence of the mixing phenomenon to take place within the systems of Kaon, charmed and bottom neutral mesons . The Kaon oscillation phenomenon was the first to be observed in the 60's, followed by the more recent mixing in the B^0_d, B^0_s while D^0 oscillations have not been observed so far.

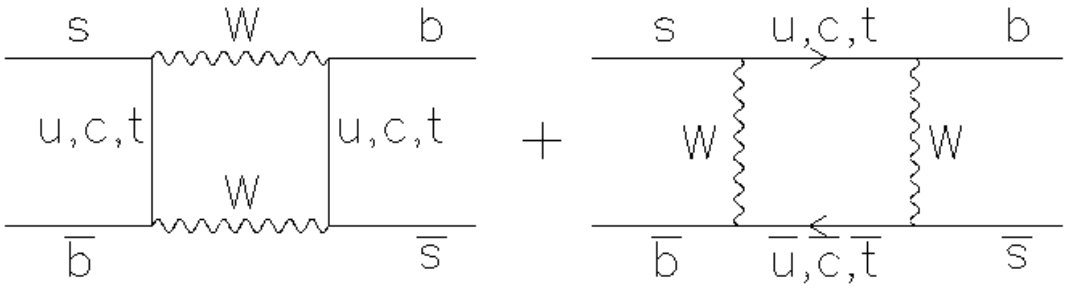

Figure 2.8: Lower level box Diagrams showing the B_s^0 mixing.

Within the b sector, the mixing is predicted to take place in two systems of neutral mesons B_d^0 and B_s^0. The theoretical model is formally identical for both systems, therefore in what follow we will use B in place of B_s or B_d mesons.
In the Standard Model, the mixing arise through the presence of box diagrams like the ones shown in Fig. 2.8. Flavor violation allows the temporal evolution of the initial state $|B^0\rangle(|\bar{B}^0\rangle)$ into the state $|\bar{B}^0\rangle(|B^0\rangle)$. The time evolution of the initial state is described the Schrödinger equation:

$$\imath\frac{\partial}{\partial t}\begin{pmatrix} a(t) \\ b(t) \end{pmatrix} = \left(M - \imath\frac{\Gamma}{2}\right)\begin{pmatrix} a(t) \\ b(t) \end{pmatrix}, \tag{2.19}$$

where M and Γ are 2×2 independent hermitian matrices, the mass and decay matrix respectively, describing the dispersive and adsorbing components of the mixing. In case of CP violation, from CPT invariance of the Hamiltonian, we have that the diagonal elements of the two matrices must be equal ($M_{11} = M_{22} \equiv M$ e $\Gamma_{11} = \Gamma_{22} \equiv \Gamma$), while the presence of flavor changing transitions with $\Delta B = 2$ constraint off diagonal elements to be different from zero. This fact implies that the mass eigenstates are different from the flavor eigenstates $|B^0\rangle$ and $|\bar{B}^0\rangle$. The mass eigenstates are defined as the eigenvectors of the matrix $M - \imath\Gamma/2$ and are expressed in terms of the flavor eigenstates:

$$\begin{aligned} Light\, eigenstate: &\qquad |B_L\rangle = p|B^0\rangle + q|\bar{B}^0\rangle, \\ Heavy\, eigenstate: &\qquad |B_H\rangle = p|B^0\rangle - q|\bar{B}^0\rangle, \end{aligned} \tag{2.20}$$

and the corresponding eigenvalues

$$\lambda_\pm = (M - \frac{\imath}{2}\Gamma) \pm \frac{q}{p}(M_{12} - \frac{\imath}{2}\Gamma_{12}), \tag{2.21}$$

where

$$\left(\frac{q}{p}\right)^2 = \frac{M_{12}^* - \frac{\imath}{2}\Gamma_{12}^*}{M_{12} - \frac{\imath}{2}\Gamma_{12}}. \tag{2.22}$$

Therefore, the temporal evolution of the mass eigenstates is determined by the eigenvalues of the matrix $M - \imath\Gamma/2$

$$|B_{H,L}(t)\rangle = e^{-(\imath M_{H,L} + \Gamma_{H,L}/2)t}|B_{H,L}\rangle. \tag{2.23}$$

so that, given an initial state $|B^0\rangle$ or $|\bar{B}^0\rangle$, using Eqs. 2.23 2.20 we obtain:

$$|B^0(t)\rangle = g_+(t)|B^0\rangle| + \frac{q}{p}g_-(t)|\bar{B}^0\rangle,$$
$$|\bar{B}^0(t)\rangle = \frac{p}{q}g_-(t)|B^0\rangle + |g_+(t)|\bar{B}^0\rangle, \tag{2.24}$$
$$\tag{2.25}$$

where

$$g_\pm(t) = e^{-\imath Mt}e^{-\Gamma t/2}\left[\cosh\frac{\Delta\Gamma t}{4}\cos\frac{\Delta m t}{2} \pm \imath\sinh\frac{\Delta\Gamma t}{4}\sin\frac{\Delta m t}{2}\right], \tag{2.26}$$

with

$$\Delta m = |M_H - M_L|, \quad \Delta\Gamma = |\Gamma_H - \Gamma_L|. \tag{2.27}$$

Therefore the flavor eigenstate oscillates with a time dependent probability proportional to:

$$|g_\pm(t)|^2 = \frac{e^{-\Gamma t/2}}{2}\left[\cosh\frac{\Delta\Gamma t}{2} \pm \cos(\Delta m t)\right]. \tag{2.28}$$

From an experimental point of view, the mixing probabilities are well defined only when we consider decays to final states with well defined flavor, that is, final states f in which a particle can decay but its antiparticle can not. Because of mixing, a B meson can decay into a final state f but also into the final state $\bar{f}$. Therefore the mixing phenomenon can be observed looking at the b flavor when the meson is generated and when it decays. This can be done also without taking into account the time dependence and considering the probability that a B meson mixed at the decay time. Hence, a *time integrated mixing probability* can be defined as:

$$\begin{aligned}\chi_f^{B^0\to\bar{B}^0} &= \frac{\int_0^\infty |\langle\bar{f}|H|B^0(t)\rangle|^2 \mathrm{d}t}{\int_0^\infty |\langle\bar{f}|H|B^0(t)\rangle|^2 \mathrm{d}t + \int_0^\infty |\langle f|H|B^0(t)\rangle|^2 \mathrm{d}t} = \\ &= \frac{|\xi_f|^2(x^2+y^2)}{|\xi_f|^2(x^2+y^2)+2+x^2+y^2},\end{aligned} \tag{2.29}$$

where

$$\xi_f = \frac{q}{p}\frac{\bar{A}_{\bar{f}}}{A_f}, \qquad x = \frac{\Delta m}{\Gamma}, \qquad y = \frac{\Delta\Gamma}{2\Gamma}. \tag{2.30}$$

The mixing probability $\chi_f^{\bar{B}^0\to B^0}$ in the case of $\bar{B}^0$ production can be obtained from Eq. 2.29 substituting ξ_f with $1/\xi_f$. If we neglect the CP violation in the mixing process, we have $|\xi_f|^2 = 1$ and the two probabilities are the same. In this scenario we have

$$\Delta m = 2|M_{12}|, \qquad \Delta\Gamma = 2|\Gamma_{12}|,$$
$$\chi_f = \chi_f^{B^0\to\bar{B}^0} = \chi_f^{\bar{B}^0\to B^0} = \frac{x^2+y^2}{2(x^2++y^2+1)}. \tag{2.31}$$

In the Standard Model the transitions $B^0 \to \bar{B}^0$ and $\bar{B}^0 \to B^0$ are described, at lower order, by the weak interaction mediated by a charged boson W and a quark of type *up* (see Fig. 2.8). As a consequence M_{12} is proportional to the ratio m_q^2/m_W^2, thus the only significant contribution is the one coming from a virtual top exchange, and a similar dependence is expected for the Γ_{12}. More over, the phases of M_{12} and Γ_{12} satisfy the relation

$$\phi_{M_{12}} - \phi_{\Gamma_{12}} = \pi + \mathscr{O}\left(\frac{m_c^2}{m_b^2}\right), \tag{2.32}$$

and this implies that the mass eigenstates must have mass and width difference of opposite sign.

2.4.1 Mixing Phenomenology

Keeping in mind the Eq. 2.28 we can express the 4 mixing probabilities as

$$\begin{aligned}
\mathcal{P}(B \to B) &= \tfrac{e^{-\Gamma t/2}}{2}\left[\cosh\tfrac{\Delta\Gamma t}{2} + \cos(\Delta m t)\right] \\
\mathcal{P}(B \to \bar{B}) &= \tfrac{e^{-\Gamma t/2}}{2}\left[\cosh\tfrac{\Delta\Gamma t}{2} - \cos(\Delta m t)\right]\left|\tfrac{p}{q}\right|^2 \\
\mathcal{P}(\bar{B} \to B) &= \tfrac{e^{-\Gamma t/2}}{2}\left[\cosh\tfrac{\Delta\Gamma t}{2} - \cos(\Delta m t)\right]\left|\tfrac{q}{p}\right|^2 \\
\mathcal{P}(\bar{B} \to \bar{B}) &= \tfrac{e^{-\Gamma t/2}}{2}\left[\cosh\tfrac{\Delta\Gamma t}{2} + \cos(\Delta m t)\right]
\end{aligned} \tag{2.33}$$

therefore, we can conclude that the mixing probabilities depend on the following observables: the mass difference Δm and the decay width difference $\Delta\Gamma$ between the two mass eigenstates, the parameter $\mid q/p \mid^2$ which signals CP violation in the mixing if $\mid q/p \mid^2 \neq 1$. Depending on the B meson system, the importance of the mixing parameters can change deeply, anyway for both B_d and B_s systems the parameter $\mid q/p \mid^2$ is compatible with the unit, so no CP violation is supposed to take place in the B mixing phenomenon. In what follow we will analyze the contribution of Δm and $\Delta\Gamma$ to the two different B meson mixing systems.

B_d^0 mixing

So far, the experimental effort on B mixing phenomena was able to perform high precision measurement of $B_d^0 - \bar{B}_d^0$ oscillations, with different methods as Fig. 2.9 shows. For this system is possible to perform mixing analysis both with time-dependent and time-integrated techniques. However direct time-dependent studies provide better results, therefore combining all the results, and assuming $\frac{\Delta\Gamma_d}{\Gamma_d}$ to be negligible, we got the following estimations [23]:

$$\Delta m_d = 0.507 \pm 0.005\, ps^{-1}, \tag{2.34}$$

or equivalently:

$$x_d = 0.776 \pm 0.008 \qquad \chi_d = 0.188 \pm 0.003\,. \tag{2.35}$$

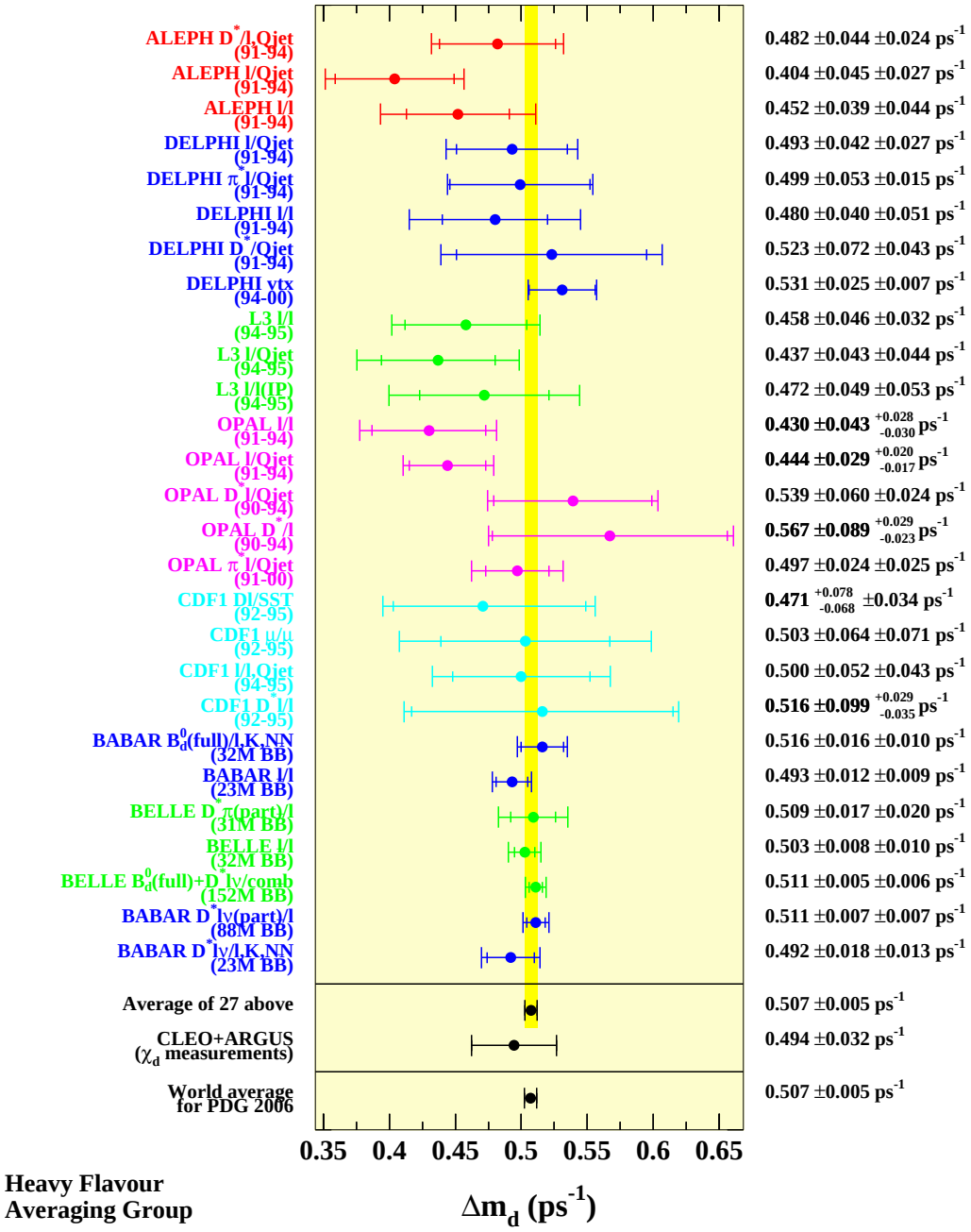

Figure 2.9: Δm_d mixing experimental results [23].

Direct time-dependent studies were also used to constraint the $\frac{\Delta\Gamma_d}{\Gamma_d}$ value. Combining the two better results from `BaBar` [25] and `DELPHI` [26] and taking $1/\Gamma_d = \tau(B_d^0) =$

$1.528 \pm 0.009\, ps$ we got

$$\frac{\Delta\Gamma_d}{\Gamma_d} = -0.009 \pm 0.037. \tag{2.36}$$

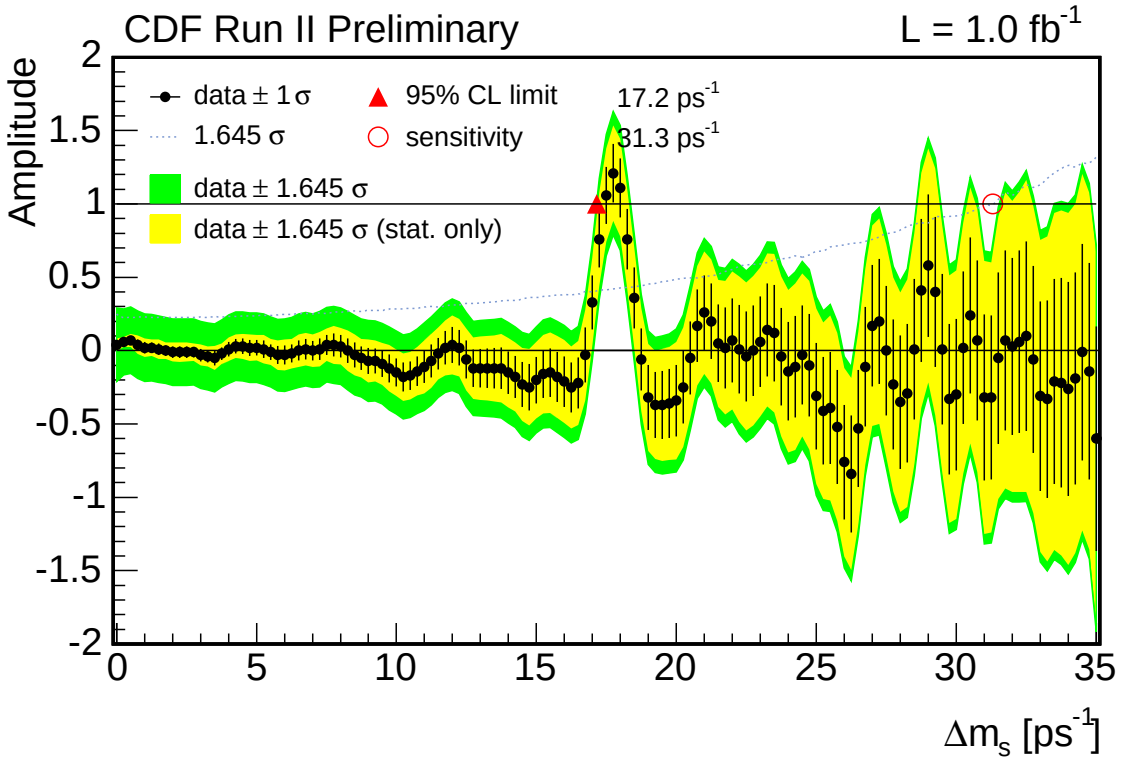

Figure 2.10: CDF $B_s^0 - \bar{B}_s^0$ mixing experimental results [14].

B_s^0 mixing

For the B_s^0 meson,the situation is a little bit different. The time-integrated measurements of $\bar{\chi}$ [23], when compared to our knowledge of χ_d and the b-hadron fractions, indicate that B_s^0 mixing is large, with a value of χ_s close to its maximal possible value of $1/2$. This expectation has been recently confirmed by CDF that reported the observation of B_s^0 mixing [14] measuring $\Delta m_s = 17.77 \pm 0.10 \pm 0.07$ ps^{-1}.

The statistical significance $\mathcal{S}$ of a B_s^0 oscillation signal can be approximated as [3]

$$\mathcal{S} \sim \sqrt{\frac{N}{2}} f_{sig}(1-2w)e^{-\frac{(\Delta m_s \sigma_t)^2}{2}} \tag{2.37}$$

where N is the number of selected and tagged B_s^0 candidates, f_{sig} is the fraction of B_s^0 signal in the selected and tagged sample, w is the total mistag probability[5] and σ_t is

[5]The mistag probability, defined in the next section, can be thought as the probability to mistake the flavor of a quark at generation level.

the resolution on proper time. As can be seen, the quantity $\mathcal{S}$ decreases very quickly as Δm_s increases: the dependence is controlled by σ_t, which is therefore the most critical parameter for Δm_s analyses.
So far, the widely used method for the Δm_s measurements, is the so called *Amplitude Scan* method [3]. If $N(t)_{mix}$ represents the number of B_s^0 that at the time t have mixed, and $N(t)_{nomix}$ represent the number of B_s^0 that at the time t have not mixed, we got, using Eq. 2.33:

$$\frac{N(t)_{nomix} - N(t)_{mix}}{N(t)_{nomix} + N(t)_{mix}} = \mathcal{A}\cos(\Delta m_s \cdot t), \tag{2.38}$$

where the amplitude $\mathcal{A}$ should be equal to 1. The *Amplitude Scan* method consists of measuring the amplitude oscillation $\mathcal{A}$ with different hypotheses of Δm_s value, using maximum likelihood fits on the data sample. The idea is that at the *true value* of Δm_s we must have $\mathcal{A} = 1$, while we get $\mathcal{A} = 0$ at a test value of Δm_s far below the true value. To a good approximation, the statistical uncertainty on $\mathcal{A}$ is Gaussian and equal to $1/\mathcal{S}$ [3].

As we can see in Fig.2.10, a significant deviation from $\mathcal{A} = 0$ is observed in the region around 17.5 ps^{-1}: the significance of the deviation, compatible with $\mathcal{A} = 1$, is more then 5 σ.

Chapter 3

The Experimental Apparatus

The Tevatron accelerator provides, after the latest upgrades, proton-antiproton head-on collisions to energies at center of mass close to 2 TeV. The improved CDF II detector was installed at Tevatron ring to collect information about the interactions taking place during these collisions. This Chapter describes the experimental apparatus: the Tevatron accelerator and CDF II detector, that produced and collected the data used in this analysis, respectively.

3.1 The Accelerator Complex and the Tevatron Collider

The Fermilab National Accelerator Laboratory[1] hosts a large accelerator complex near Chicago where a sophisticated apparatus was build to accelerate and collide protons and antiprotons to exploit high-energy physics processes. Figure 3.1 shows a simplified sketch of the accelerator system, which involves several stages such as: preparing proton and antiproton beams, injecting the beams into the Tevatron where they are accelerated to the energy of 980 GeV and finally colliding them at a center of mass energy $\sqrt{s} = 1.96$ TeV in selected collision areas where the CDF and D0 detectors are installed.

3.1.1 The Proton Source

The process leading to $p\bar{p}$ collisions begins in a Cockroft-Walton chamber, where electrical discharges into hydrogen gas, enveloped within an electrostatic field, produce negative ions, immediately accelerated by a positive voltage applied to a so-called extractor plate. The resulting negative ions are then driven via a magnetic field to the linear accelerator, the Linac. The magnetic transportation system provides also a filtering tool to remove non -H^- ions.
The Linac [28] picks up the H^- ions at energy of 750 KeV, and accelerates them to inject into the Booster. The Linac is divided in two subsystems: a first drift-tube that accelerates the H^- to 116 MeV, and a second side-couple cavity accelerated structure used to bring up the negative ions to the energy of 400 MeV. The Booster [27], is a fast cycling synchrotron about 150 meters in diameter. It provides both acceleration

[1] Also referred to as Fermilab or FNAL

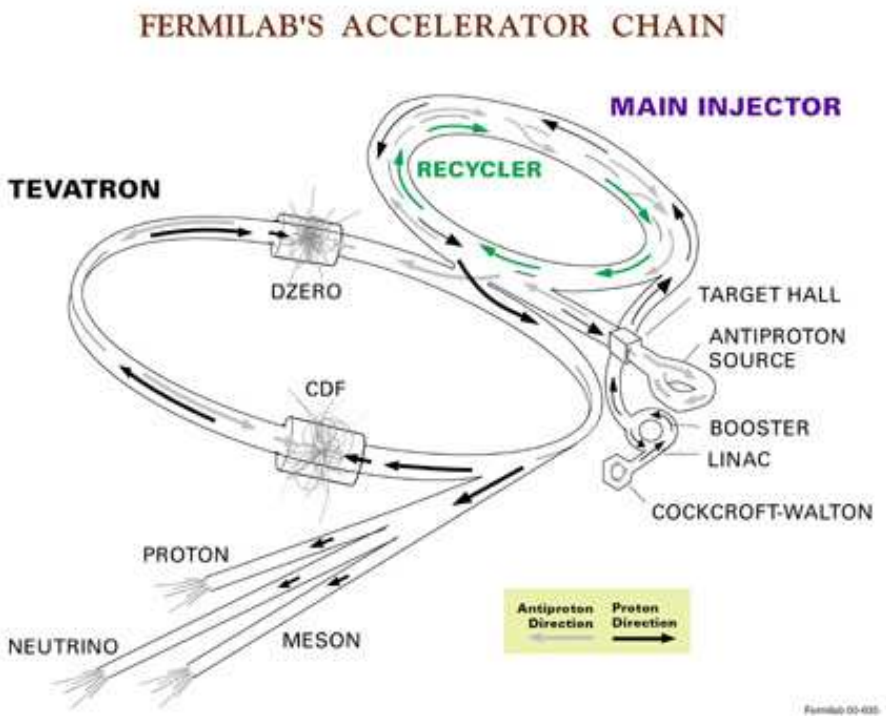

Figure 3.1: The FERMILAB's accelerator chain.

of the ions to the energy to 8 GeV and the conversion of the incoming negative H^- to the final protons (H^+). The Booster loading scheme overlays the injected beam with the one already circulating in the machine. The mixed beams are forced through a carbon foil, which strips off the electrons turning the negative hydrogens into protons. When the bare protons are collected in the Booster, they are accelerated to the energy of 8 GeV varying the phase of RF fields in the accelerator cavities [27] and subsequently injected into the Main Injector. The final "batch" will contain a maximum of 5×10^{12} protons divided among 84 bunches spaced by 18.9 ns of 6×10^{10} protons each.

3.1.2 The Main Injector

During the Run I era the protons and antiprotons were injected into the Tevatron by the Main Ring, an old[2] 400 GeV proton synchrotron. Originally the Main Ring was not designed as a Tevatron injector, it was later adapted to this purpose.

To improve the antiproton production capability, the Run II Upgrade includes the new Main Injector (MI), a new rapid cycling accelerator designed to accomplish several topics such as: accepting 8 GeV protons or antiprotons coming from the Booster, antiproton Accumulator and the Recycler; accelerating the protons to 120 GeV to be delivered to the antiproton target, fixed target experimental area or the neutrino Beamline (NuMI); accelerating protons and antiprotons up to 150 GeV for the Tevatron Injection; accepting 150 GeV antiprotons from the Tevatron ring and decelerating them

[2]The Main Ring was build in the early 1970's.

to 8 GeV to transfer to the Recycler.
The MI is seven times the circumference of the Booster. So it can hold 6 Booster batches with 84 bunches in each of them. In the Collider Mode, the six batches are accelerated to the *flat top* (150 GeV), the maximum energy to which the machine can keep the particles for an extended time. At *flat top* the bunches are coalesced into a single bunch of 27×10^{10} protons that is subsequently injected into the Tevatron. The described procedure constitutes a single MI cycle. To fill the Tevatron with protons thirty-six of such cycles are needed. Due to the fact that the coalescing efficiency is not 100%, the MI is able to prepare at maximum 4 Tevatron bunches per cycle, requiring at minimum 9 cycles to fill the Tevatron ring.
When the Tevatron is filled with the final protons, the MI goes back to its other duties that can summarized as: antiproton production, discussed in Section 3.1.3, and intense beam delivered for the fixed target and/or neutrino experiments.

3.1.3 The Antiproton Source

If the proton production is a relatively easy task, the same is not true for the antiprotons. In fact, the antimatter is harder to come by on Earth, and we have to produce it from scratch [29]. On the other hand, proton-antiproton colliders, compared to proton-proton, have greater advantages, in fact antiprotons can be accelerated in the same ring used for protons, because the opposite charge, reducing the cost of the magnets for a second ring. More over, the production rate for a number of interesting processes is higher in $p\bar{p}$ collisions at $\sqrt{s}$ up to 3 TeV compared with pp collisions at the same energy.
Figure 3.2 shows the general layout of the antiproton source at the Tevatron. As mentioned in the Section 3.1.2 the antiproton production is one of the Main Injector's greater tasks. During antiproton stacking mode, the MI accelerates batch of 5×10^{12} protons at 120 GeV, and sends them to hit a nickel target. The collision with the target produces a shower of secondary particles that are focused by the use of a lithium lens [29]. Then, a pulsed dipole magnet deflects the 8 GeV antiprotons toward the Debuncher [29], while the undesired particles with wrong charge-to-mass ratio are filtered out of the beam and collected by a graphite-core beam-dump. The antiprotons produced in such a way present a high energy spread that must to be reduced to form a narrow antiproton beam. The process of reducing the kinetic energy spread is referred as *cooling* of the beam. New batches of antiprotons are initially collected in the Debuncher synchrotron; they are then cooled using stochastic cooling in the 8 GeV Accumulator synchrotron [27]. The stochastic cooling [29] is a feedback based method: some pick up sensors sample the average motion of particles in the beam and corrects the trajectory for the average using kicker electrodes, which are a pair of electrodes placed around the ring. Integrated over a long period of time, this manifests itself as a damping force applied to the individual particles which evens out their kinetic energies.

The cooled antiprotons are then transferred to the Accumulator where they are prepared for the injection into the MI. The overall production can take from 10 to 20 hours to built up a stack of antiprotons used in the Tevatron collisions. Antiproton

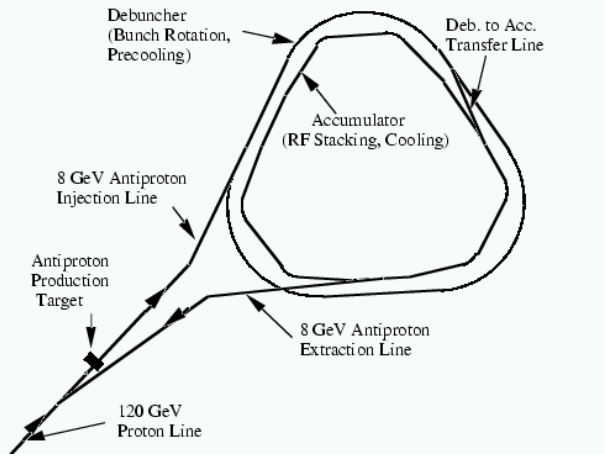

Figure 3.2: Layout of the antiproton source.

availability is the most limiting factor attaining high luminosities, assuming there are no technical problems with the accelerator. this is the main reason of the big effort spent to upgrade the antiproton production at Tevatron for the Run II. In this context is important to mention the Recycler ring [30]. The Recycler is designed to collect the antiprotons left at the end of a Collider *store*[3] and re-use them in a later store. The Recycler also take up the role of the Accumulator as the final storage for 8 GeV antiprotons allowing the existing Antiproton Source to perform more efficiently and produce antiprotons with higher rate.
The Recycler was included in the Fermilab Program in 1997 as an addition to the Main Injector project. Most of the lattice elements (dipoles and quadrupoles) are made out of permanent magnets and the ring shares the tunnel with the MI keeping low constructional and operational costs, but substantial benefits have been achieved after the first colliding stores in the fall of 2005, when, thanks to Recycler and the introduction of the electro cooling of antiprotons, high instantaneous luminosities were reached.

3.1.4 The Tevatron Ring

The Tevatron is the last stage of the Fermilab accelerator chain. The Tevatron is a 1 km radius synchrotron able to accelerate the incoming 150 GeV beams from MI up to 980 GeV, providing a center of mass energy of 1.96 TeV. The accelerator employs superconducting magnets throughout, requiring cryogenic cooling and consequently a large scale production and distribution of liquid helium. During The Run II the Tevatron operated at the 36×36 mode, which refers to the number of bunches in each beam.
The antiprotons are injected after the protons have already been loaded. Just before the antiproton injection a set of electrostatic separators are used to create a pair of non-intersecting helical closed orbits. When the Tevatron loading is complete, the

[3] a roughly 20 hour period of time when the colliding beams are retained within the Tevatron

beams are accelerated to the maximum energy and the collisions begin. In the 36×36 mode, there are 72 regions along the ring where the bunch crossing occurs. While 70 of these are parasitic, in the vicinity of CDF and $D\emptyset$ detectors, additional focusing and beam steering is performed, to maximize the chance the proton strikes an antiproton. The Focusing, driven by quadrupole magnets, reduces the beam spot size increasing the *luminosity*. The instantaneous luminosity, a quantity proportional to number of collision per unit time, is given approximately by:

$$\mathcal{L} = \frac{N_B N_{\bar{p}} N_p f}{2\pi(\sigma_{\bar{p}}^2 + \sigma_{\bar{p}}^2)} \tag{3.1}$$

Where N_B is the number of bunches, $N_{(\bar{p}),p}$ is the number of the (anti)protons per bunch, f is the revolution frequency, and $\sigma^2_{(\bar{p})p}$ is the effective width of the (anti)proton beam. Clearly, smaller values $\sigma^2_{(\bar{p})p}$ result in a larger rate of collisions. During collisions the instantaneous luminosity decreases in time as particles are lost or beam begin to heat up. In the meanwhile new antiprotons are stored in the Accumulator. When the luminosity becomes too much low (approximately after 15-20 hours) it becomes beneficial dumping the current store and start a new cycle. Table 3.1 summarizes the accelerator parameters for the Run II and Run I configurations.

Parameter	Run I	Run II
number of bunches (N_B)	6	36
bunch length [m]	0.6	0.18
bunch spacing [ns]	3500	396
protons/bunch (N_p)	2.3×10^{11}	3.3×10^{11}
antiprotons/bunch ($N_{\bar{p}}$)	5.5×10^{10}	3.6×10^{10}
interactions/crossing	1	1.5
typical luminosity $[cm^{-2}s^{-1}]$	0.16×10^{32}	0.9×10^{32}

Table 3.1: Accelerator parameters for Run I and Run II configurations.

3.2 The CDF II Detector

CDF II is a general purpose detector installed around one of two interaction points along the Tevatron ring, as shown in Fig.3.1. An overview of the detector is shown in Fig. 3.3, the proton and antiproton beams travel toward each other along the horizontal axis called *beam axis* or *beam line*. Any plane perpendicular to the beam line is called a transverse plane and the intersection point of the beam line and the transverse plane is referred to as the *beam spot*.

Close to the beam line there are the tracking systems[4]. A super-conducting magnet located outside the tracking systems forms the CDF solenoid. The magnet creates a uniform horizontal magnetic field of 1.4 T along the z axis inside the tracking volume.

[4]Tracking is the reconstruction of the trajectories of charged particles in the detector.

Outside the tracking volume there are the , electromagnetic (EM) calorimetry, hadronic calorimetry and finally the muon detectors. CDF II is also equipped with dedicated sub-detectors, such as a Time-of-Flight system (TOF) and a Cherenkov Luminosity Counter.
In this Chapter we shall present a general description of the different subsystems of CDF detector, with a main focus on Tracking systems heavily used in this analysis.

3.2.1 Standard Definitions in CDF II

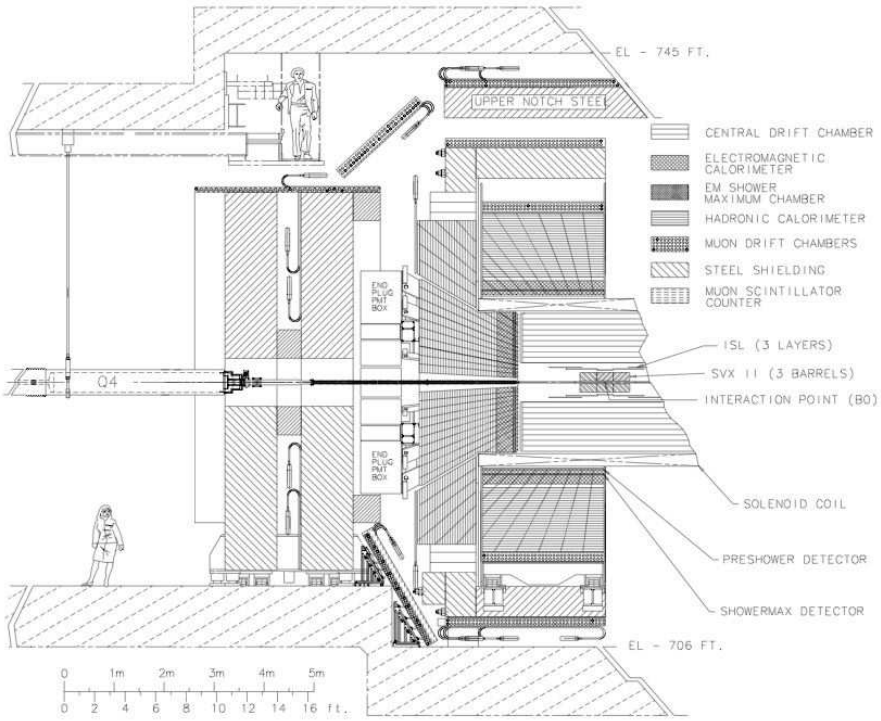

Figure 3.3: CDF II Detector Layout.

The Cartesian coordinate system associated with CDF II has the detector's geometric center in its origin. The x axis is in the (horizontal) plane of the accelerator ring, pointing radially outward, while the y axis points vertically up. The z axis is chosen to complete the right-handed coordinate system. Beams travel approximately parallel to z axis with protons moving in the positive z direction. The center of the detector roughly coincides with the center of the beam crossing region.
The detector is essentially a cylindrically and forward-backward symmetric device, making convenient to work with cylindrical (z, r, ϕ), or polar (r, θ, ϕ) coordinates. Following these conventions, one found that the azimuthal angle ϕ runs in the transverse (x-y) plane, with $\phi = 0$ being the positive direction of the x axis. The Polar angle θ is counted from the positive direction of z axis. The z axis is the same as in carting coordinates.
Another important coordinate is often used instead the polar angle θ, it is called

pseudo-rapidity η and it's defined as:

$$\eta \equiv -\log \tan(\frac{\theta}{2}). \tag{3.2}$$

The choice of a coordinate system such as (r, η, ϕ) is convenient because it is based on the experiment symmetries. The collisions processes are invariant under rotation around the (unpolarized) beam, making ϕ a natural choice. Moreover, the physics processes that take place in an hadronic colliders involve essentially the *partons* (valence/sea quarks or gluons) more than the protons or antiprotons. The partons carry only a fraction of the initial proton or antiproton momentum and as a consequence of possible unbalance in the longitudinal components of the two momenta, the observed physics interactions often show large boosts along the z axis. It can be easily shown that η is the relativistic/massless limit of the more common used quantity, the rapidity ξ, defined as:

$$\xi = -\frac{1}{2}\log\frac{E+p_z}{E-p_z}. \tag{3.3}$$

Where E is the energy of the particle and p_z is the longitudinal component of its momentum. The use of η is then convenient because it is a purely geometrical quantity related to the polar angle θ and, at the same time, the invariance under Lorentz boost is preserved. The detector components (whenever appropriate) were chosen to be uniformly segmented along η and ϕ coordinates, thus simplifying the analysis.

3.2.2 Tracking System

Tracking is a process of reconstructing the trajectories of the particles in the detectors. The reconstructed trajectories are called *tracks*. When charged particles travel in the detector they interact with the detector material which results in the energy loss during material ionization. The tracking systems work by detecting the ionization from tracks and, based on this information, mapping out the particle trajectory. Tracking is of course central to our analysis, at first because we try to measure the yields of the charged particles around B mesons, then because, as we will see, the process of B mesons reconstruction is essentially based on the analysis of track combinations and the corresponding geometrical and kinematical properties.

The inner part of the CDF II is devoted to tracking system: reconstructing the trajectories of charged particles near the collision point turns into the reconstruction of decay vertexes for long lived particles. To collect the information of particle charge and momentum, the CDF II tracking volume is permeated by a uniform magnetic field directed along the z axis. As a consequence of this, within the tracking volume the charged particles move along helicoidal trajectories described by the five parameters:

- z_0 The z coordinate of the closest point to the z axis
- d_0 The Impact Parameter: the distance from the point of the closest approach to z axis

- ϕ_0 The ϕ direction of the transverse momentum of the particle (tangential to the helix) at the point of the closest approach to the z axis
- $\cot\theta$ The helix pitch
- C The helix curvature

The impact parameter and the curvature are signed quantities defined by :

$$C = \frac{q}{2R}, \tag{3.4}$$

$$d_0 = q(\sqrt{x_c^2 + y_c^2} - R), \tag{3.5}$$

where q is the charge of the particle, $(x_c^2 + y_c^2)$ is the center of the helix as projected onto the x-y plane and R is its radius. A graphical view of these variables together with the ϕ_0 is shown in Figure 3.4.

From helix parameters one can easily derive particle's transverse and longitudinal

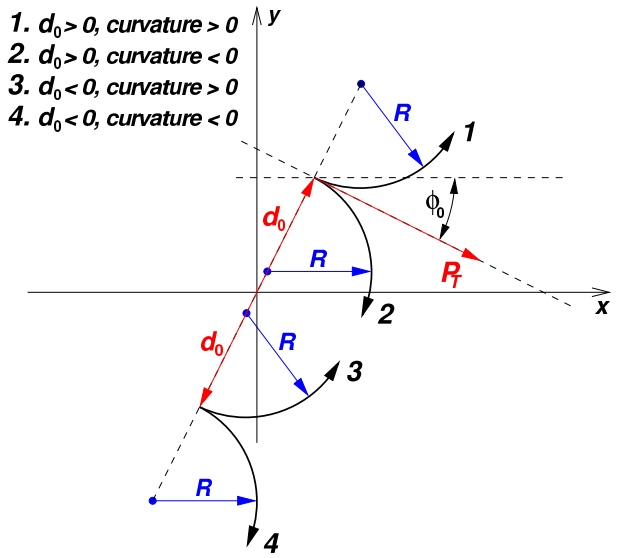

Figure 3.4: Illustration of helix track parametrization.

momenta:

$$p_T = \frac{cB}{2|C|}, \tag{3.6}$$

$$p_z = p_T \cot\theta \tag{3.7}$$

The CDF II tracking system is essentially divided in an inner silicon strip detector, aiming to more precise vertexes reconstruction, and an outer Drift Chamber that provides the necessary information for track's momentum measurement. As shown in Figure 3.5, the overall tracking volume covers up to $|\eta| = 2$ region, allowing track's reconstruction in a wide volume.

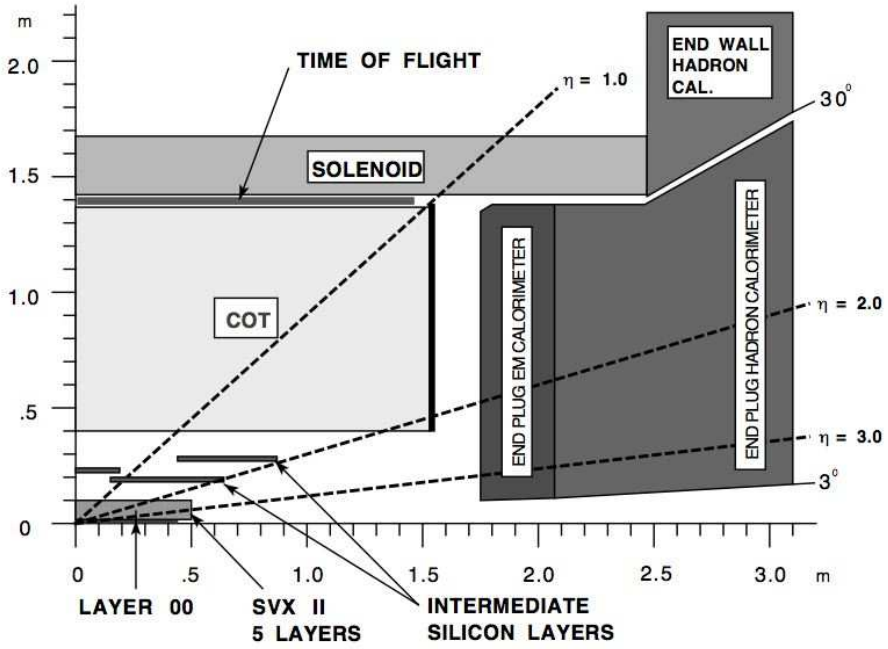

Figure 3.5: The r-z view of The CDF II tracking system.

Silicon Vertex Detector

As mentioned above, silicon tracking detectors are used to obtain precise measurements of the charged particle's path near the interaction point, and then a precise determination of the long lived particle's decay vertex.
The principle on which a silicon strip detector works is visualized on Fig.3.6: it can be summarized as a reverse-biased p-n junction. In a typical silicon micro-strip detector, over a lightly doped n-type silicon (n^-) substrate, roughly 300 μm thick, a series of finely spaced p-type silicon strips are inserted via implantation technique [32]. The opposite side is then equipped with a thin layer of strongly doped n-type silicon (n^+). A positive voltage is then applied to the n^+ side, depleting the bulk of free charge carriers (both electrons and holes) creating an electric field. When a charged particle

Layer	Radius $[cm]$		# of strips		Strip pitch $[\mu m]$		Stereo	Ladder Active, $[mm]$	
	stereo	$r-\phi$	stereo	$r-\phi$	stereo	$r-\phi$	angle	width	length
0	2.55	3.00	256	256	60	141	90 °	15.30	4×72.43
1	4.12	4.57	576	384	62	125.5	90 °	23.75	4×72.43
2	6.52	7.02	640	640	60	60	+1.2 °	38.34	4×72.43
3	8.22	8.72	512	768	60	141	90 °	46.02	4×72.43
4	10.10	10.65	896	896	65	65	-1.2 °	58.18	4×72.43

Table 3.2: SVX summary.

crosses the active volume (i.e. the n^- substrate), it creates a column of electron-hole pairs from ionization along the particle path. The presence of the electric field drifts

the holes to the p^+ implanted strips producing a well localized signal in $r-\phi$ plane. The inter-strip spacing is typically around 60 μm, non the less the position measurement accuracy that can be achieved at CDF II is of 12 μm. This can be done using weighting technique. In fact, the signal is usually detected not by a small cluster of adjacent strips: the hit position can be extracted by weighting the strip positions with the amount of charge collected by each strip.
The CDF II Silicon VerteX Detector, called SVX II [31], is composed by three different barrels 29 cm long each. Each barrel support five layers of double-sided silicon micro-strip detectors in the range of 2.5 to 10.7 cm from the beamline. The layers are numbered from 0 (innermost) to 4 (outermost). The Layers 0,1 and 3 combine an $r-\phi$ measurement on one side with the 90° stereo (r - z) on the other, while the Layers 2 and 4 combine an $r-\phi$ measurement with small angle stereo at 1.2° (Table 3.2). The active silicon crystals, usually called wafers, are supported by weight substrates

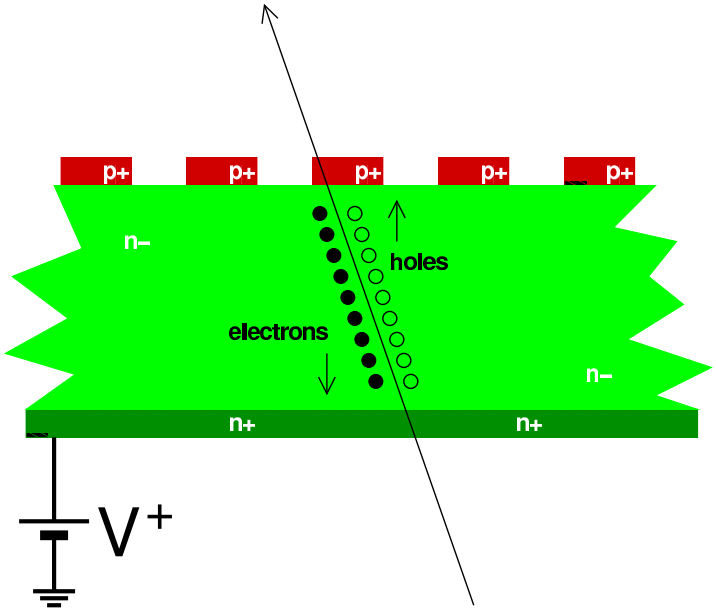

Figure 3.6: Sketch of a generic silicon micro-strip detector.

(Rohacell foam) in assemblies called ladders. The layout of these wafers is shown in Figure 3.7. There are four wafers connected by wire-bonds in each ladder. Twelve ladders of appropriate width compose a layer. Sixty ladders are mounted between two beryllium bulkheads making an SVX II barrel.
Each ladder is read out at both ends. The number of channels in the system (405,504) and the nature of the signals require that the electronics be physically mounted on the system. In fact the amount of cables that one should route out will be impossible to manage, more over a pre-amplification is needed to avoid noise increasing. The main limitation of the *built in* electronics is that more passive material is brought inside the detector, increasing the effect of Coulomb scattering and radiation lenght; the built in electronics also dissipates significant amount of heat (over 1 kW): to provide adequate cooling SVX II was designed to incorporate cooling channels into the bulkheads.

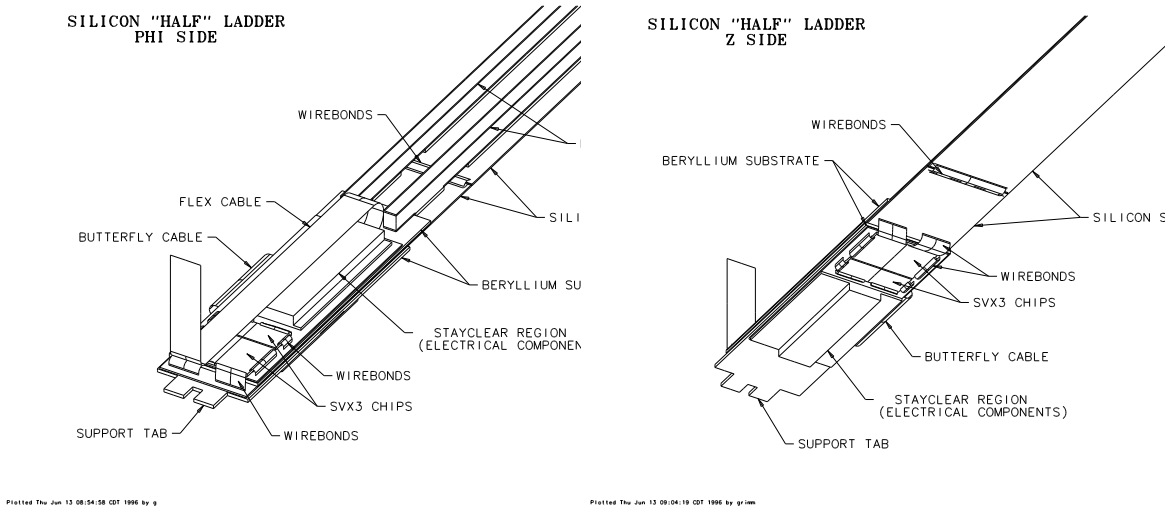

Figure 3.7: Perspective view of the top (r - ϕ) and bottom (r - z) side of Layer 0 ladder.

A measure of the SVX performances is the impact parameter resolution. Presently the resolution on the impact parameter is at about 27 μm, when using tridimentional track reconstruction the resolution[5] on impact parameter is around 70 μm.

Intermediate Silicon Layer and Layer 00

To reach better performances in terms of resolutions and tracking coverage two special sub detectors were subsequently added to the silicon tracker: the Intermediate Silicon Layer (ISL) and Layer 00 (L00) [33]. These two brand new detectors were not included in the *baseline project* for the CDF upgrade, turning onto some technical difficulties such space, time and money ... Due to these problems, the integration of the devices got relatively late.

ISL: In the central region a single ISL layer is placed at a radius of 22 cm. In the region $1.0 < |\eta| < 2.0$, two silicon layers are placed at radii of 20 and 28 cm (see Figure 3.5). Double sided silicon is used with 55 μm strip pitch on the axial side and 73 μm pitch on the stereo side with a 1.2° stereo angle. The read out is performed every other strip, in order to reduce the number of total read out channels, that count 268,800 units. This indeed affects the single hit resolution, which is about 16 μm on the axial side and 23 μm on the stereo side. Despite this fact ISL ladders are similar to the ones used for SVX.

L00: As can be seen in Figure 3.8, the L00 is a set of silicon strips assembled directly on the beam pipe. The design has six narrow and six wide groups of ladder in ϕ at radii 1.35 and 1.62 cm respectively, providing 128 read out channels for the narrower

[5]The quoted resolution has been obtained by tracks that have ISL hits on them. SVX stand-alone resolution is somewhat worse.

groups and 256 channels for the other groups. The silicon wafers are mounted on a carbon-fiber support which provides cooling also. L00 sensors are made of light-weight radiation-hard silicon (different from the ones used within SVX) and are single-sided with a 25(50) μm implant (readout) pitch. The ISL is intended to improve the tracking

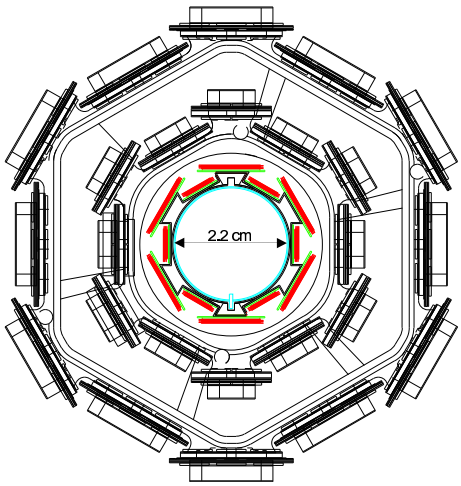

Figure 3.8: Transverse view of Layer 00, the innermost silicon layer.

resolution in the central region, while in the $1.0 < |\eta| < 2.0$ region should provide a useful tool for a silicon stand alone tracking in conjunction with SVX layers. Instead, L00, assembled directly on the beam pipe, allows to overcome the effects of multiple scattering for tracks passing through high density regions of SVX (where the bulkheads and readout electronics are located) making possible to improve vertexing resolutions.

Central Outer Tracker

In addition to the silicon detector a drift chamber is used at larger radii to improve the momentum resolution. In the region $|z| < 155$ cm and between the radii of 43 and 133 cm takes place the Central Outer Tracker, COT. The COT [31], is a cylindrical multi-wire open-cell drift chamber filled with an Argon-Methane and Isopropyl Alcohol (49.5:49.5:1) mixture gas used as active medium. The COT contains 96 sense wire layers, which are radially grouped into eight "superlayers" (See Figure 3.10). Each superlayer is divided in ϕ "supercells", each supercell has 12 sense wires and the maximum drift distance is approximately the same for all supercells. Therefore, the number of supercells in a given superlayer scales approximately with the radius of the superlayer. Half of the 30,240 sense wires within the COT run along the z direction ("axial"), while the others are blow at a small angle ($2\,^\circ$) with respect to the z direction ("stereo").
In a drift chamber detector a charged particle passing through the gas mixture leaves a trail of ionization electrons. These electrons are then drift toward sense wires of the cell where they are produced. The electrons drift is not only driven by an electrical field crated with this purpose, but also by the magnetic field present within the tracking volume. In such fields, electrons, originally at rest, move in the plane perpendicular to the magnetic field at an angle α with respect to the electric field lines. The value of α,

the so called Lorentz angle, depends on both the magnitude of fields and the properties of the gas mixture. In the COT $\alpha \simeq 35\,^\circ$.

Resolution-wise, the optimal situation is when the drift direction is perpendicular

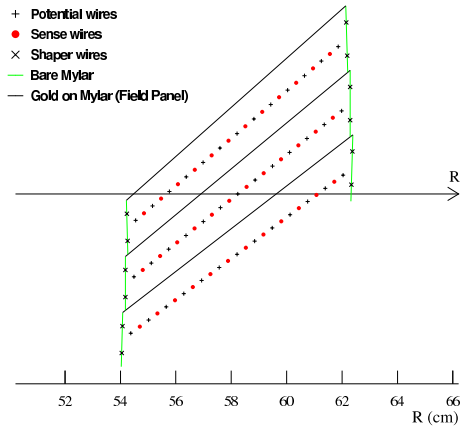

Figure 3.9: Transverse view of three cells from the COT superlayer 2. The arrow shows the radial direction or, equivalently, a very high p_T track trajectory. The electric field is roughly perpendicular to the field panels; the drift velocity would be vertical in this picture. The angle between wire-plane of the central cell and the radial direction is $35\,^\circ$.

to that of the track. Usually the optimization is done for high p_T tracks, which are almost radial. Therefore all COT cells are tilted of $35\,^\circ$ away from the radial, so that the ionization electrons drift in the ϕ direction. When the electrons get near the sense wire, the local field accelerates them causing further ionization. In brief an "avalanche" of ionized particles is produced, creating a signal (a hit) on a sense wire. Subsequently the signal is amplified and shaped by the electronics attached at the end of the wire. So the r - ϕ position of the track with respect to the sense wire is inferred by the arrival time of the signal.

There are other advantages in doing the wire-plane tilt. For example, the tilt allows to overlap in the radial view, which means that high p_T tracks must pass very close to at least one wire in each superlayer. This is taken advantage by the eXtremely Fast Tracker (XFT) in the Level-1 trigger, as will be described in Section 3.5. Also the large tilt provides a lever in resolving the left/right ambiguity. Indeed, a particle passing by a wire-plane leaves several hits, which are grouped into a track segment, but since there is no way of knowing whether an individual hit is on the left of the respective wire or on the right of it, there are actually two segments, one the mirror image of the other. The angle between the two track segments ($\tan^{-1}(2 \cdot \tan\alpha) \approx 54\,^\circ$) is large, making the pattern recognition problem much easier.

A measure of COT performance is the single hit position resolution. It has been measured to be about 140 μm, which translates into the transverse momentum resolution $\frac{\delta p_T}{p_T} \sim 0.15\% \frac{p_T}{GeV/c}$.

Another important application of the COT is particle identification. The signals collected in the sense wires are characterized by a leading edge that provides informa-

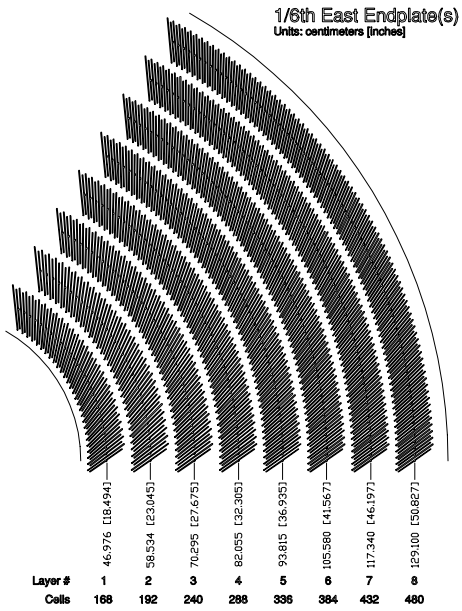

Figure 3.10: Layout of wire planes on COT end-plate.

tion about the arrival time of the pulse and a width (the width of the pulse, expressed in nanosecond) that is proportional to the amount of charge collected by the wire. After calibrating the width variations due to several effects (geometry, gas gain differences), the amount of charge collected by the wire can be related to the energy loss of charged particles in the COT gas volume: since the energy loss of a particle in the material, dE/dx, is related to the particle velocity, the COT can be used for identifying the charged particles species by extracting the particle mass from velocity and momentum measurements. This feature is very important for our analysis since the dE/dx measurement complements the TOF reduced particle identification power at higher momenta.

Tracking and Vertexing

Before proceeding in this overall Detector review, it's important to introduce the basic concepts of tracks reconstruction at CDF II. Several algorithms were developed at CDF to reconstruct tracks, some use only the COT information, other the silicon information only, others use both COT and silicon hits. The most used is the so called *Outside-In* algorithm [35]. The basic idea is to start the track reconstruction from the drift chamber and project the track into the silicon detector to find the hits that have to be used in the final determination of track's parameters.
Track reconstruction in the COT begins from finding matching track segments or just individual hits in the axial superlayers [36]. When the $r-\phi$ projection of the track is reconstructed we get the measurement of C, d_0 and ϕ_0 helix parameters. When looked at in $r-\phi$ plane, hits from stereo superlayers appear to be offset from the reconstructed helix projection. The amount of the offset is proportional to the z coordinate. Proper

matching of stereo superlayer segments/hits to existing $r-\phi$ track projection allows to extract z information of the track at 4 radial regions thereby measurement $\cot\theta$ and z_0 parameters of the helix.
It's crucial to mention that the global CDF coordinate system, introduced at the beginning of the Section 3.2.1 is anchored to the center of the COT, i.e. the COT cylinder axis is the z axis of the global CDF coordinate system, and the center of the COT is its origin. Positions of other detector components are measured[6] with respect to the COT reference frame and encoded in so-called *alignments tables*. Whenever a spatial measurement is done by a system other than the COT, it is usually done in the local reference frame and then converted into the global CDF (w.r.t. COT) reference frame, via the respective alignment table. One example of this procedure concerns the Silicon Vertex Detector, described in previous paragraph.
As said before, tracking can be performed using only the silicon information, so that a dedicated alignment effort has to be done in order to have high precision tracks measurement. In fact, every effort is made to place the SVX barrels in a coaxial manner. Remaining (small) spatial shifts are accounted for by barrel-to-barrel alignment. For the purpose of triggering[7] it is much more important to place SVX symmetrically around the beam than that of the z axis of the detector. This results in the fact that the SVX axis is offset from the COT axis by about the same amount that the beamline differs from the z axis of the detector.

To complete the helical fit for the track in the best way [36], SVX and COT information have to be combined, when all SVX hits (some of which may be fakes) are found. At this point, it is absolutely important to have a very good alignment table, so that the positions of the SVX hits, originally measured only with respect to the individual ladders, are translated correctly into the global (COT) reference frame. Then, using this information, SVX and COT hits can be combined to extrapolate the tracks parameters. The process starts when a track is reconstructed with the COT information only (The so-called COT-only track). This track, because the parameters uncertainties is more like a tube of radius σ, determined by the errors on the track parameters. As additional complication σ, does not have to be the same in ϕ and z directions.
Thereby the COT-only track is extrapolated through the SVX. As extrapolation proceeds from the outermost SVX layer toward the beampipe, the track error matrix is updated to reflect the amount of scattering material transversed. At each SVX layer, hits that are within a certain radius[8] are appended to the track and track re-fit is performed. A new track candidate is generated for each of the newly appended hits, but only the best two (in terms of the fit quality and the number of hit) are retained. Each of these candidates is then extrapolated further in, where the process is repeated.

[6] Measurement are performed mechanically, by means of optical survey, or , when the ultimate precision is needed and the possibility exists, with data .

[7] Certain triggers rely on the d_0 track parameter as measured by SVX. In case the beamline does not coincide with the SVX axis d_0 (and consequently, the triggers) became ϕ-dependent!

[8] Often the radius defined as some multiple of σ rather than an absolute number because σ changes as hits are being added.

At the end there may still be several candidates associated to the original COT-only track. In this case, a selection is done in the number of hits and then in terms of fit quality.

Precise determination of track parameters allows to distinguish which tracks came from what vertex and thereby to distinguish the *primary* vertex (PV) from the *secondary* vertex (SV), such as a B hadron or other long-lived particle decay vertex.

3.2.3 Muon Detectors

Thanks to their high penetration power, muons are separated from surrounding particles by the calorimeter, that acts as a shield on electromagnetic and hadronic matter. Muon identification can therefore be performed by extrapolating the tracks outside the calorimeter and matching them to tracks segments (called *stubs*) reconstructed in an external muon detector.
Figure 3.11 shows an overview of the coverage of the muon detectors. To this purpose, muon system has been equipped with several devices:

- Central MUon detector (CMU) consists of a set of 144 modules, each containing four layers of rectangular drift cells, operating in proportional mode. It is placed immediately outside the calorimeter and supplies a global coverage up to $|\eta|$ <0.6; ϕ measurement of muon position is guaranteed by azimuthal segmentation of the detector, while z coordinate is estimated on the basis of charge division.

- Central Muon uPgrade (CMP) consists of four layers of single-wire proportional drift tubes staged by half cell per layer and shielded by an additional 60 *cm* steel layer. It is arranged in a square box around the CMU, providing a ϕ-dependent η coverage (see Figure 3.11) according to the cylindrical structure of the inner detector. Contrary to CMU, this device supplies only ϕ information. For Run II, CMP benefits of an increased acceptance of $\sim$ 17%.

- Central Scintillator uPgrade (CSP) is a layer of rectangular scintillator counters placed on the outer surface of CMP.

- Central Muon eXtension (CMX) consists of a stack of eight proportional drift tubes, arranged in conical sections to extend the CMU/CMP coverage in the 0.6 < $|\eta|$ <1 region. Azimuthal acceptance has been improved by 45% for Run II; only a 30 ° ϕ-gap remains to be used by the solenoid cryogenic system.

- Central Scintillator eXtension (CSX) consists of a layer of scintillator counters on both sides of CMX. Thanks to scintillator timing, this device completes with z information the measurement of ϕ position of muons provided by CMX.

- Intermediate MUon detector (IMU) replaces the old Forward Muon Detector (FMU) to exploit the improved tracking capabilities and perform muon momentum measurement based only on the central solenoid field. In fact, during Run I the momentum of forward muons had to be measured by the FMU itself through

a toroidal magnet; steel toroids are now used to supply mechanical support and shielding to new detector. IMU consists of four staggered layers of proportional drift tubes and two layers of scintillator tiles, arranged as for the CMP/CSP system to extend triggering and identification of muons up to $|\eta| \leq 1.5$ and $|\eta| \leq 2$ respectively.

Due to their slow response, muon chambers are not able to work within the Run II inter bunch interval of 400 to 132 *ns*. However, detector occupancy is expected to be strongly reduced with respect to Run I thanks to the accelerator upgrades[9] and to stronger shielding from beam halo. Together with the high granularity of the muon devices, it would allow to integrate the collected signals over several beam crosses.

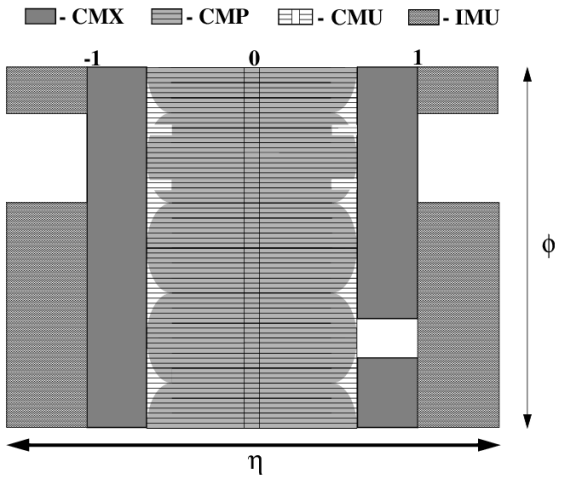

Figure 3.11: $\eta - \phi$ coverage of the Run II muon system.

3.2.4 Time-of-Flight Detector

The Time-Of-Flight system (TOF), expands the CDF's particle identification capability in the low momentum region. The TOF measures arrival time t of a particle with respect to the collision time t_0. The mass m of the particle is then determined combining the path length L and momentum p measured by the tracking system:

$$m = \frac{p}{c}\sqrt{\frac{(ct)^2}{L^2} - 1}. \tag{3.8}$$

The TOF consists of 216 CB-408 scintillator bars installed at a radius of about 138 *cm* (from the z axis) in the 4.7 *cm* space between the outer shell of the COT and the cryostat of the superconducting solenoid (see Figure 3.5). Bars are approximately 279 *cm* long and $4 \times 4\,cm^2$ in cross-section. With cylindrical geometry TOF provides 2π

[9]More than 95% of the ionization detected in the muon system during the Run I resulted to be originated by the Main Ring, that has been replaced by the Main Injector.

coverage in ϕ and roughly (-1;1) coverage in η.
Bars are read out at both ends by fine-mesh photomultipliers, PMT, (Hamamatsu R7761), capable of providing adequate gain even if used inside 1.4T magnetic field.

When a charged particle traverses the scintillator material, photons are emitted and they propagate towards the ends of the scintillator bar. The PMTs at the both ends of the bar collect the light and the front-end electronics measures the arrival time of the PMT pulse and the amount of charge collected (related to the number of photons produced). The physical location of the bar where the hit was registered provides the ϕ location of the hit; comparing the arrival times of the pulses at the two end of the bar determines the z position of the hit. The COT tracks are then extrapolated to the TOF system location to find the matches between the track trajectories and the hits in the TOF system. This associates the timing information from TOF with the tracking information from the COT. Usage of long attenuation length fast rises time scintillator in conjunction with these PMTs allowed to achieve specified resolution of 100-150 ps on TOF measurement for most particles.

Fig.3.13 (a) shows time-of-flight difference for K/π, p/π and K/p hypotheses and the separation power assuming resolution of 100 ps as a function of the momentum; for comparison the expected K/π separation power provided by dE/dx measurement in the COT is also shown. Figure 3.13 (b) early TOF performance is illustrated.
More details on TOF construction and performances can be found in Reference [33].
In conclusion, the combination of particle identification information from the COT and TOF detectors allows us to separate the particle based on their mass in practically all the P_t regions accessible at CDF.

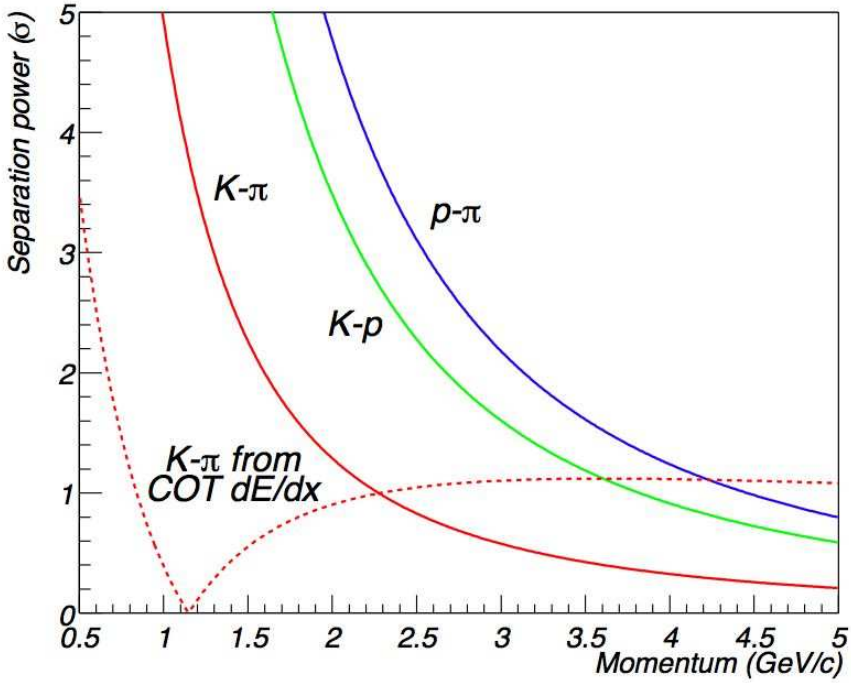

Figure 3.12: K/π, p/π and K/p difference over a path of 140 cm as a function of momentum, expressed in ps and separation power(σ), assuming resolution of 100 ps. The dashed line shows the K/π separation power from dE/dx measurement by the COT.

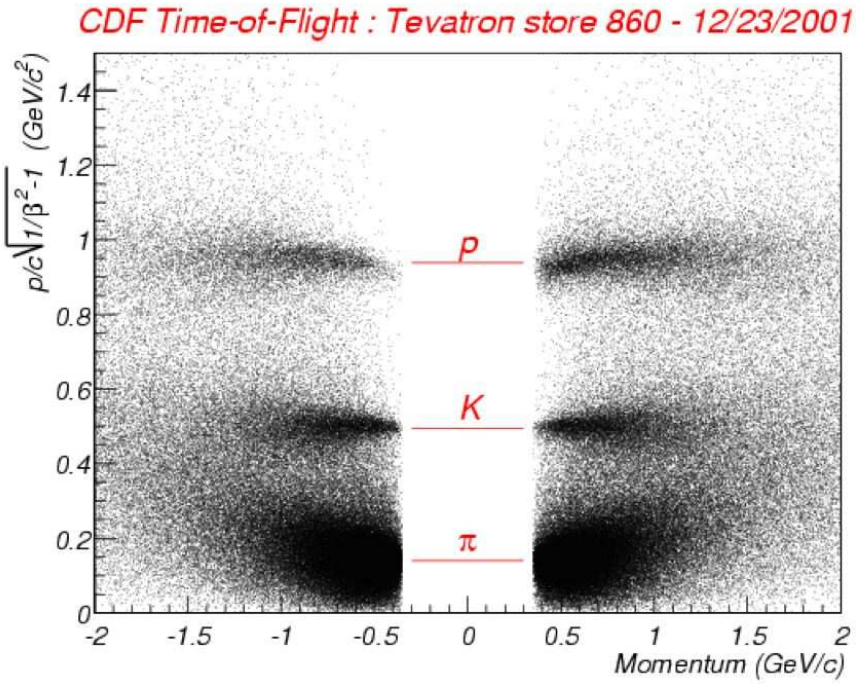

Figure 3.13: TOF reconstruction mass vs. momentum for positive and negative tracks. Cluster of data points corresponding to π, K and p are clearly visible. Data are from Tevatron store 860 (12/23/2001).

3.2.5 Calorimeter Apparatus

Even if not used in this analysis, the calorimeter system, together with the muon and tracking systems, is one of the main sub-detector apparatus of CDF II detector.
The CDF II calorimetry system has been designed to measure energy and direction of neutral and charged particles leaving the tracking region. In particular, it is devoted to jet reconstruction and it is also used to measure the missing energy associated to neutrinos.

Particles hitting the calorimeter can be divided in two classes, according to their main interaction with the matter: electromagnetically interacting particles, such as electron and photon, and hadronically interacting particles, such as mesons or barions produced in hadronization processes. To detect these two classes of particles, two different calorimetric parts have been developed: an inner electromagnetic and an outer hadronic section, providing coverage up to $|\eta|$ <3.64. In order to supply information on particle position, the calorimeter is also segmented in radial sections, called towers, projected toward the geometrical center of the detector. Each tower consists of alternating layers of passive material and scintillator tiles. The signal is read out via wavelength shifters WLS embedded in the scintillator and light from WLS is then carried by light guides to photomultiplier tubes. The central sector of the calorimeter, covering the region $|\eta|$ <1.1, was recycled from Run I, while brand new calorimeters (called plug calorimeters) were built up to cover the forward and backward regions.

The Central Calorimeter

Apart from upgrades on the readout electronics, needed to follow the increased collision rate, the central calorimeter is almost the same used during Run I [31] . The Central Electro-Magnetic calorimeter (CEM) is segmented in $\Delta\eta \times \Delta\phi$=0.11×15 ° projective towers consisting of alternate layers of lead and scintillator, while the Central and End Wall HAdronic calorimeters (CHA and CWA respectively), whose geometry tower segmentation matches the CEM one, use iron layers as radiators. A perspective view of a central electromagnetic calorimeter module (*wedge*) is shown in Figure 3.14 (a), where both the arrangement in projected towers and the light-gatering system are visible.
The projective geometry has been used in order to take advantage of the momentum conservation in the transverse plane: before the $p\bar{p}$ collision, the projection in the transverse plane w.r.t. the beam direction of the beam energy is zero, therefore this quantity have to be the same also after the collision took place. Thus, the for each tower the *transverse energy* E_T is defined as $E_T = E \cdot \sin\theta$, where E is the energy detected by the tower and θ is the angle between the beam axis and the tower direction, in the CDF detector coordinates system. Two position detectors are embedded in each wedge of CEM:

- The Central Electromagnetic Strip chamber (CES) is a two-dimensional stripwire chamber arranged in correspondence to maximum shower development ($\sim 5.9 X_0$).

	Thickness	number of layers	Resolution (E in GeV)
CEM	19 X_0	20-30 Pb:3mm,Scint.:5mm	$13.5\%\sqrt{E\sin\theta}\oplus 2\%$
PEM	21 X_0	22 Pb:4.5mm,Scint.:4mm + Preshower	$16\%\sqrt{E\sin\theta}\oplus 1\%$
CHA/WHA	4.7/4.5 λ_0	32/15 Fe:25/50 mm, Scint.:10 mm	$75\%/\sqrt{E\sin\theta}\oplus 3\%$
PHA	7 λ_0	23 Fe:51 mm, Scint.:6mm	$80\%/\sqrt{E\sin\theta}\oplus 5\%$

Table 3.3: Basic quantities characterizing CDF II calorimetry.

It measures the charge deposit of the electromagnetic showers, providing information on their pulse-height and position with a finer azimuthal segmentation than calorimeter towers. This results in an increased purity on electromagnetic object reconstruction.

- The Central Pre-Radiator (CPR) consists of two wire camber modules placed immediately in front of the calorimeter. It acts as pre-shower detector by using the tracker and the solenoid coil material as radiators, resulting to be a very useful tool in rejection of electron and photon background.

Calorimeter response is fast enough to match the time requirements imposed by Run II. However, wire chambers associated to CES and CPR may need to be integrated over several beam crossings; this will not be a problem since the high granularity of these devices guarantees a low detector occupancy.
Table 3.3 summarize the basic quantities of calorimeter detectors.

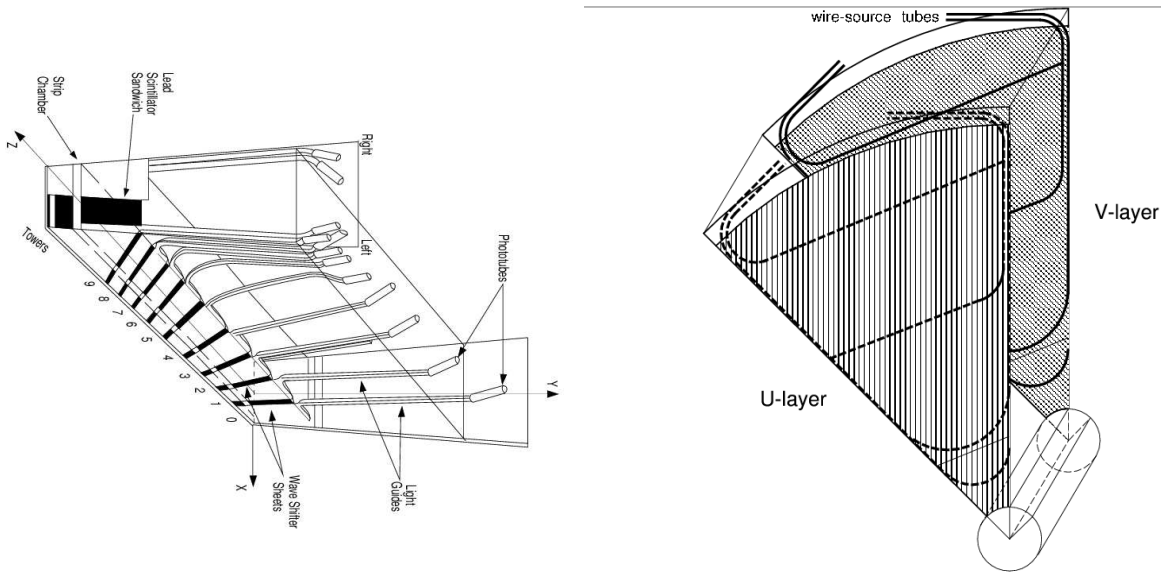

Figure 3.14: Perspective view of a CEM module (left) and of SMD (right).

The Plug Calorimeter

The plug calorimeter, covers the η region from 1.1 to 3.64. The new configuration, based on the same principles as the central calorimeter, allows the detector to operate in the Run II environment and makes experimental data more homogeneous. Both electromagnetic and hadronic sectors are divided in 12 concentric η regions, with $\Delta\eta$ ranging from 0.10 to 0.64, according to increasing pseudorapidity, each of them is segmented in 48 or 24 (for $|\eta| < 2.11$ or $|\eta| > 2.11$ respectively) projective towers. The actual size of these towers was chosen so that identification of electron in b-jets would be optimized.

Projective towers consist in alternating layers of absorbing material (lead and iron for electromagnetic and hadronic sector respectively) and scintillator tiles. The first layer of the electromagnetic tile is thicker (10 mm instead of 6 mm) and made of material with higher photon yield. They act as a pre-shower detector.
As in the central calorimeter, a Shower Maximum Detector (SMD) is also included in the plug electromagnetic calorimeter, at a radial depth of $\sim 6\ X_0$. The SMD consists of eight 45° azimuthal sectors, each covering six (or three) calorimetric towers in ϕ. Furthermore, each detector is segmented in two η regions in order to reduce detector occupancy. Within each region, 5 mm pitch scintillating strips are arranged on two layers (called U and V). Being parallel to either boundary of the sector, U and V strips from an angle of 45° among them (see Figure 3.14 (b)), providing a two dimensional measurement of the shower. The SMD is a useful tool to discriminate photons and electrons from pion background.

3.2.6 CLC

The Cherenkov Luminosity Counter (CLC), measures the average number of interactions per bunch crossing μ. Then instantaneous luminosity $\mathcal{L}$ is extracted using the following formula:

$$\mu \cdot f_{bc} = \sigma_{p\bar{p}} \cdot \mathcal{L} \tag{3.9}$$

where $\sigma_{p\bar{p}}$ is relatively well known total $p\bar{p}$ cross=section at $\sqrt{s} = 1.96\,TeV$ and f_{bc} is the rate of bunch crossings in the Tevatron.

The CLC exploits the effect, known as Cherenkov radiation. Particles traversing a medium at a speed higher than the speed of the light in this medium, radiate light into a cone around particle direction; cone's opening angle is the ratio of the two speeds.
The idea is to use an assembly of long gas-filled Cherenkov counters positioned in the Plug Calorimeter 3^d gap, so that they point toward the interaction region, as schematically shown in Figure 3.15. This arrangement allows to make the detector much more sensitive to the particles coming directly from the interaction point because their flight path in the gas of the counter is the longest, and therefore the amount of the light produced the largest.
Excellent timing resolution ($\sim 50\,ps$) and clever design allow the CLC to discern multiple interactions within the same bunch crossing and achieve an overall accuracy of

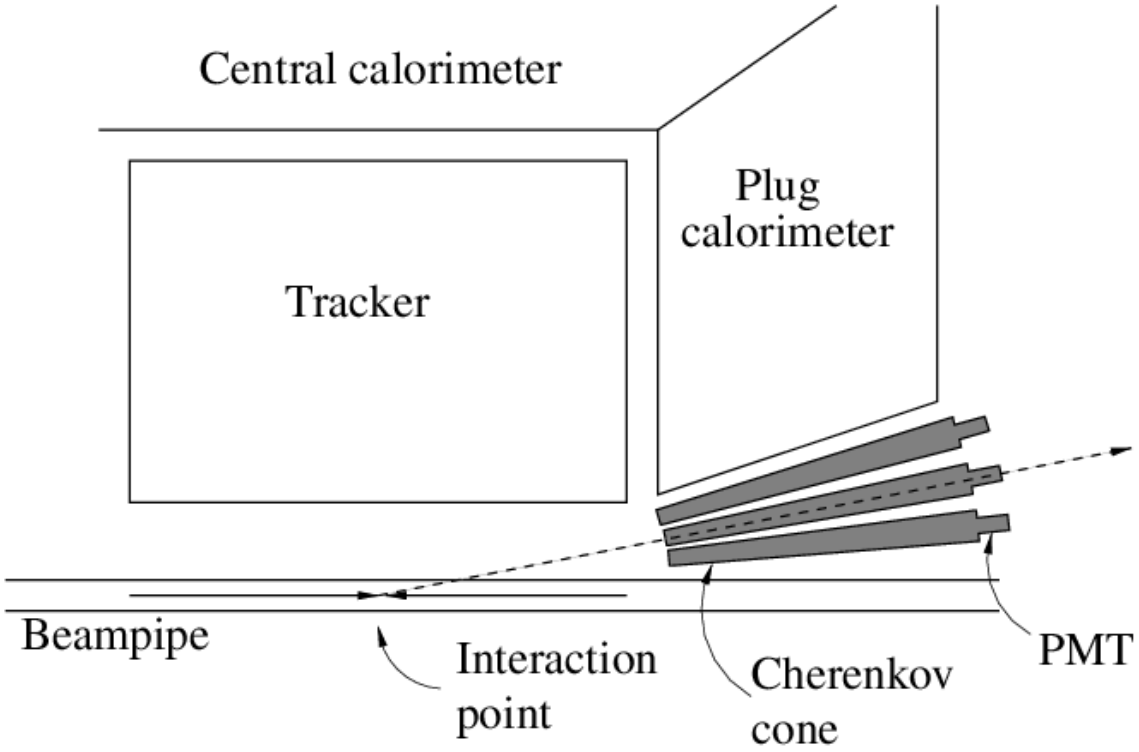

Figure 3.15: CLC geometry.

the luminosity measurement better than 5%.
Further information on the CLC design and performance is given in References [51] [52] [53].

3.3 The CDF II Trigger

At the Tevatron collider, protons and antiprotons collide every 396 ns. This collision rate is too high to record all the events: in fact, CDF has mass storage capability of $\sim 100\ Hz$, while the collision rate provides an output of roughly 2.5 MHz. Therefore a selection have to be performed to reduce the event rate. Moreover, even with a higher recording speed, keeping all the produced events would result in 300 TB of data in one week of running, that will be too much expensive in terms of computing time and resources. However, most processes of interest have cross-sections in range of 10-100 μb or smaller, i.e., at least three orders of magnitude smaller than the total $p\bar{p}$ cross-section. This fact allows one to perform a preliminary on-the-fly selection recording only the most interesting events: the trigger.

3.4 Triggering

CDF II is equipped with a 3-levels trigger. At each level, only part of the all available information is used to built some low resolution physical objects, called *primitives*, subsequently used to select the interesting events. At every level the primitive variables are reconstructed with more accuracy so that the trigger selections are more sophisticated and more efficient. The design of the fully pipelined data acquisition system and the three-level dead timeless trigger is pictured in Figure 3.16.
Level-1 trigger discards the majority of the events. Since it can take as long as 5.5 μs for the Level-1 to reach its decision, all front-end electronics are equipped with buffers 14 bunch crossing deep. If Level-1 does not reject an event it proceeds to the Level-2. The Level-2 does a more careful analysis of the information, taking longer time (few tens of microseconds). The entire detector is read out for the Level-3 decision only if Level-2 requirements are full-filled.

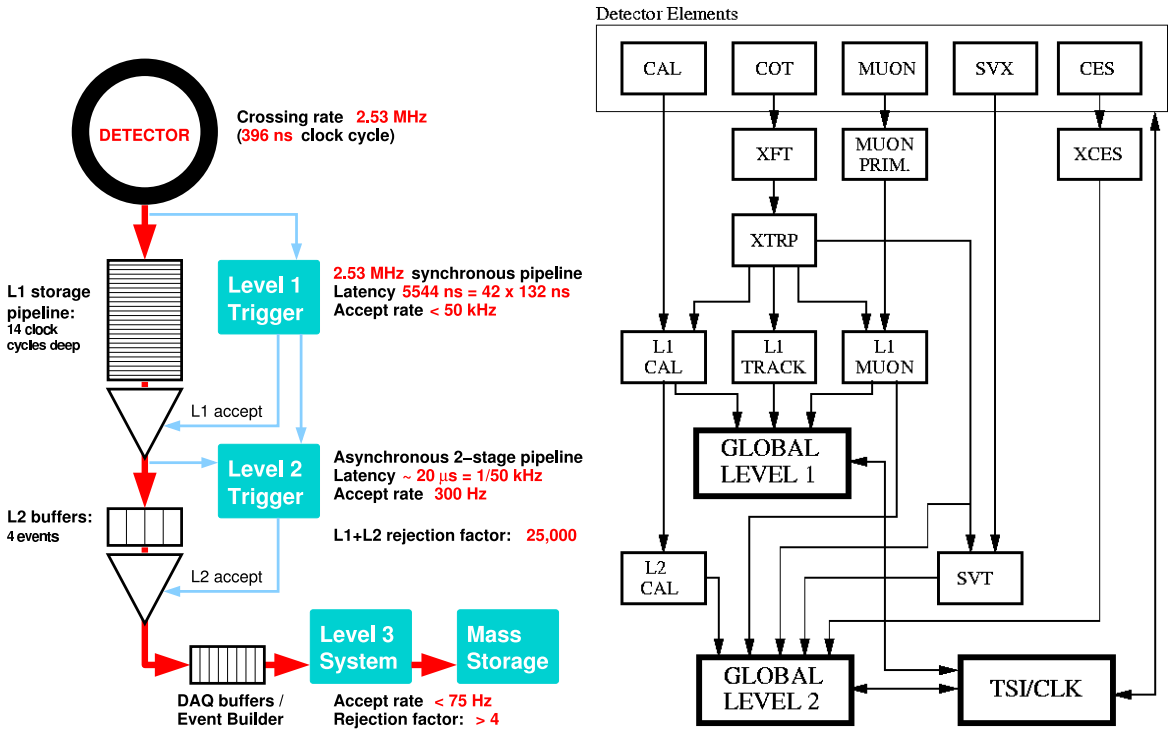

Figure 3.16: Block diagram detailing CDF DAQ and L1/L2 trigger system.

The Level-1/Level-2 trigger system is managed by the Trigger Supervisor Interface (TSI/CLK box in Figure 3.16 (b)). TSI also provides an interface between the triggers and the DAQ as well as global clock and a bunch crossing signal. In the case of Level-2 accept, the digitized output from all detector components is collected and transferred to the Event Builder. There, the event fragments obtained from different subsystems are organized into a properly ordered sequence, which is then fed to Level-3 computing

farm. At Level-3 the event undergoes fairly thorough reconstruction after which final requirements are applied. If these are satisfied the event gets written to a mass storage device.
At every level the decision process can follow different rules, depending on the physics process to be selected.

Below, we discuss CDF II trigger and data acquisition system, relevant to our analysis. The conceptual design of the entire system is presented in Reference [37] and an elaborate description is given in Reference [31].

3.5 The Level 1 Trigger

The Level-1 is a synchronous system with an event read-in and an accept/reject decision, made every bunch crossing. The decision is based on transverse energy in the calorimeters, tracks in the COT and stubs in CMU, CMX and CMP chambers. Level-1 uses rudimentary (no detailed reconstruction) versions of the above mentioned objects, called *primitives*.
In several cases tracks primitives are combined with calorimeter or muon primitives to form e, μ and jet objects as shown by arrows in Figure 3.16 (b).
To ensure the maximum speed, Level-1 uses custom designed hardware. The total rate of Level-1 accept is about few tens of KHz, a factor of few hundred smaller than the input rate of 2.5 MHz.
There are many algorithms (or, equivalently, individual triggers) at the Level-1 [38]. The rest of this Section will be devoted to introduce two important systems for L1-triggering, XFT and XTRP, which provide information to be incorporated into decision making process for several separate Level-1 triggers.

XFT and XTRP

At Level-1, the track reconstruction is performed by XFT [39], the eXtremely Fast Tracker, which identifies the track primitives (high p_T tracks[10] in $r-\phi$ view) using the four axial superlayers of the COT. Track identification is accomplished in two steps: segment finding and segment linking. In the finding step, all COT axial hits are classified as either "prompt" (drift time less then 44 ns) or "delayed" (44 ns < drift time < 132 ns). Then, a set of binary masks (predefined patterns of prompt/delayed hits) is applied in order to find all segments compatible with a valid track[11] passing through a given superlayer. For a successful match a "pixel" is set. This pixel represents the ϕ position of the segment plus a slope information in the two outermost axial superlayers (needed to resolve the charge). In the second step (linking) four pixels appearing to have come from the same track are identified and a crude estimate of track parameters is done. These tracks are reported to the XTRP (the eXTRaPolator unit) unit and a copy of them is preserved to be used in the Level-2.

[10]High p_T tracks are tracks with $p_T > 1.5$ GeV/c.
[11]The one that originates in the vicinity of the beamline and has high enough p_T .

XTRP, is responsible for quick extrapolating of the XFT tracks to other detector subsystems such as calorimetry and muon chambers (see Figure 3.16 (b)). Matching these tracks with electron towers (EM calorimeter) or muon stubs (muon chambers) allows the construction of more complex primitives and, therefore, an additional rejection at Level-1.

The XFT reports to XTRP the p_T, ϕ_{SL6} (ϕ at the COT superlayer 6) and charge information for each detected track. Different trigger paths can need muon or calorimeter information (L1MUON and L1CAL respectively). These are extracted by dedicated boards and sent to XTRP for the final Level-1 characterization and then to the Global Level-1 Board for the ultimate decision. Finally if an event is not rejected by the Level-1 trigger decision, it is automatically passed to the Level-2 system.

3.6 The Level 2 Trigger

The Level-2 is an asynchronous system which processes events accepted by the Level-1 in the time-ordered fashion. It uses Level-1 primitives as well additional data coming from the shower maximum strip chambers (CES) in the central calorimeter and the $r-\phi$ strips of the SVX as indicated in Figure 3.16 (b). There are three hardware subsystems building primitives at the Level-2: L2CAL, XSEC and SVT.
Briefly L2CAL hardware receives trigger towers from L1CAL and finds energy tower clusters by applying seed and shoulder thresholds. That is, starting from the tower with highest energy deposit (seed tower), nearest towers are subsequently added to the seed if their energy is higher than an fixed value (the shoulder threshold) creating, in that way, a cluster.
The XSEC system generates bitmap of strips above certain threshold in the shower maximum chambers (8 bits per 15 °). Then XFT track primitives are extrapolated by the XTRP to the CES radius and fed to the XSEC where they are matched with the strip bitmap, producing electron candidates.
The SVT uses SVX $r-\phi$ hits to extend XFT track primitives inside the SVX volume, closer to beamline. The SVT improves the XFT ϕ_0 and p_T resolutions and adds the measurement of the impact parameter d_0 (original XFT track primitives are beamline constrained). Acting into the impact parameter have is a very useful handle in order to select decay modes of heavy mesons.

As shown in Fig. 3.17, the impact parameter of decay products is strongly related to the decay length of the *mother* meson, therefore a selection based on the tracks impact parameter turns directly in to a proper time requirement.
This innovative system is the core of all the trigger systems for B physics, and will be described in further details in the next subsection.

3.6.1 SVT

The Silicon Vertex Tracker (SVT) [40][41][42][43] is the most significant addition to Level-2 trigger system from Run I. This is an innovative device that exploits the poten-

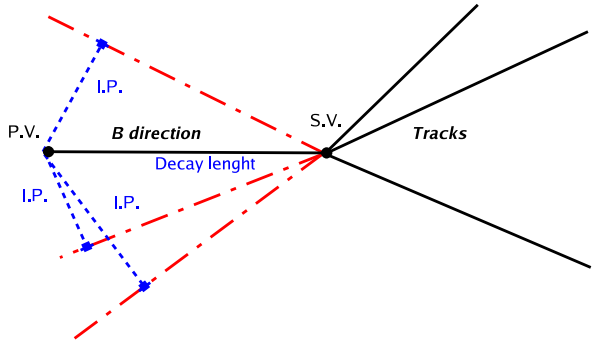

Figure 3.17: Schematic chart showing the correlation between the tracks I.P. and the decay length of a hypothetical B meson decay.

tial of a high precision silicon vertex detector to trigger on tracks significantly displaced from the $p\bar{p}$ interaction point. This can make accessible a large number of important processes involving decays of b-hadrons with a long lifetime.
SVT is a sophisticated device able to perform track reconstruction in the $r-\phi$ plane; its overall architecture is shown in Figure 3.18. The event flow can be summarized as follows: first, each of the 72 SVX II sectors[12] is read out by the *Hit Finder* , that performs a hit clustering on each layer contained in the sector. For each cluster found, the Hit Finder computes the centroid, representing the most probable intersection point between the trajectory of a particle and the layer that cluster belongs to. The outputs of the Hit Finder of each SVX II wedge are merged into one stream and fed both into an *Associative Memory* (AM) [45] and into a *Hit Buffer* [44], together with track primitives information from XFT. The task of the Associative Memory is to perform the first stage of the pattern recognition [46]: cluster centroids from the Hit Finder are mapped in *superstrips*[13]; then, all possible combinations of superstrips and XFT tracks are compared to a pre-established set of admissible combinations (*roads*), each corresponding to a set of four SVX II superstrips and an outer XFT track. Superstrip size results from a compromise between a precise pattern recognition which requires a large memory, and a coarse one, which introduces a lot of fake track candidates but small costs. The result from the pattern recognition performed by the Associative Memory is finally stored into the *Hit Buffer* [44] together with the SVX clusters and XFT tracks information. Now a road represents some kind of pipe where to perform a more detailed track reconstruction. The *Track Fitters* takes care of that, fitting the track information from the Hit Buffer by means of a linear approximated algorithm, consisting of a set of scalar products [47]. Hence, for each track, p_T, ϕ_0 and d_0 are computed.

For tracks with $p_T > 2\ GeV/c$ the SVT resolutions are found to be $\sigma_{d_0} = 35\mu m$, $\sigma_\phi = 1mrad$ and $\sigma_{p_T}/p_T = 0.003\ c/GeV$ [48]. In fact the width of the Gaussian fit for the distribution of measured track impact parameters is 47 μm. This is a combi-

[12] As described in the previous Chapter SVX II is composed by 3 barrels with 24 ϕ-wedges each.
[13] low resolution hits

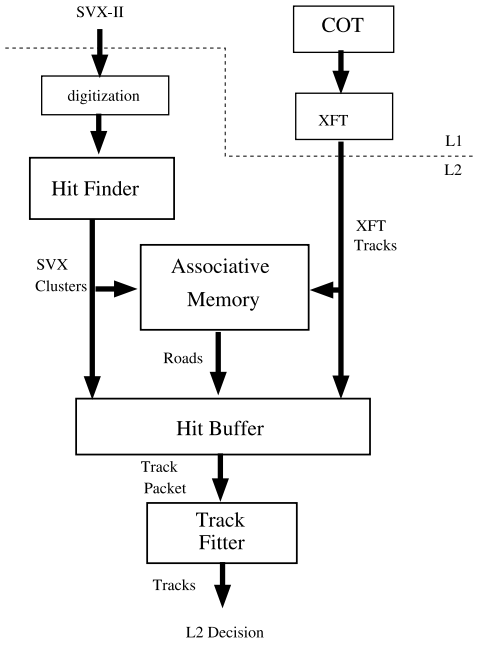

Figure 3.18: The SVT architecture.

nation of the intrinsic impact parameter resolution of the SVT measurement, and the transverse intensity profile of the interaction region. This profile is roughly circular and can be approximated by a Gaussian of $\sim 35\mu m$ resolution. Thus, the intrinsic SVT resolution is obtained by subtracting the beamline width from the width of the d_0 distribution by the use of the following relation:

$$\sigma_{SVT} = \sqrt{\sigma^2_{Measured} - \sigma^2_{Beam}} \tag{3.10}$$

At that time, all the track quantities refer to the origin of the coordinates system, *i.e.* the center of the COT. Clearly, the $p\bar{p}$ beam cannot be controlled with a infinite precision, and even if a lot of efforts have been done to keep it stable, usually it does not lie in the z axis and some kind of slope is present in both $r-\phi$ and $z-y$ plane projections. This problem, together with the fact that beam resolution in the z axis is around 30 cm, forced CDF to create a dedicated database where the beam properties are stored for each stable condition of data acquisition, the SVT alignment tables. The beam properties are measured in the first moments of data taking with stable beam condition.
Such a measurement is done looking at the correlation between the track impact parameter d_0 and the angular position ϕ_0. In absence on any bias there isn't any correlation between the two variables, while whenever the beam position differs from the nominal one a sinusoidal correlation appears in between d_0 and ϕ_0. This correlation is used to correct the track parameters and is used iteratively until it disappears (Fig.: 3.19). When the correcting factor are found they are written in the SVT alignment table and becomes available for the next events. Finally the SVT corrects the impact pa-

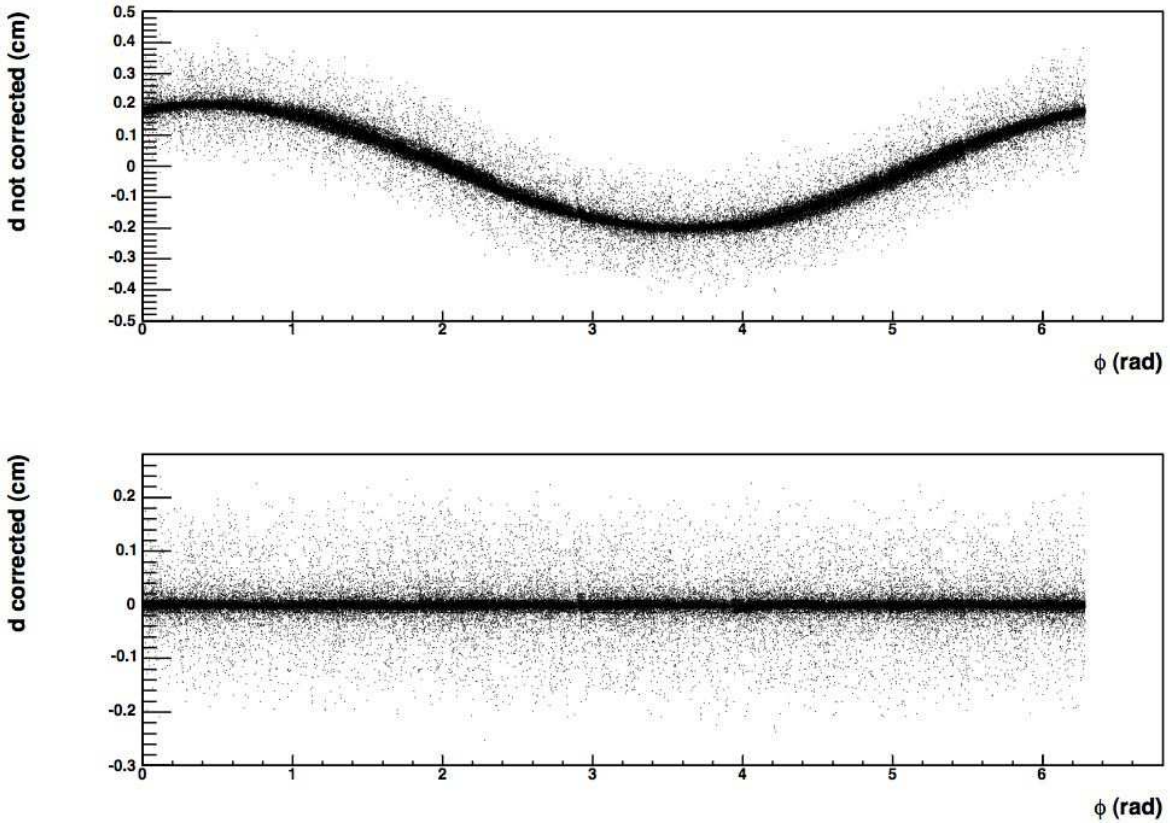

Figure 3.19: Impact parameter (d_0) vs azimuthal angle (ϕ_0) plot using SVT variables after (top) and before (bottom) beam position correction has been done.

rameter and angular position of each track for the beam position in order to operate the trigger selection in an unbiased way. All the Level-2 primitives are then sent to the Global Level-2 decision board, that perform the event rejection according to the different trigger requirements of every trigger path.

3.7 The Level 3 Trigger

When an event is accepted by Level-2, the entire detector is read out, and thereby a slot in all the detector buffers is emptied for the next event. The read out event fragments are put in the proper order by the Asynchronous Transfer Mode (ATM) switch based system known as the Event Builder [50], and then arranged event fragments are channeled to the Level-3.
Level-3 [50] is a farm of conventional PCs running Linux. The farm is split in a number of 16 sub-farms of identical architecture. Each sub-farm consists of a head node (also known as converter node) and 12-16 processor nodes. There are also eight so-called output nodes in the Level-3, each is shared by two sub-farms.
Figure 3.20 shows the implementation of the Level-3 farm. Data from the front end

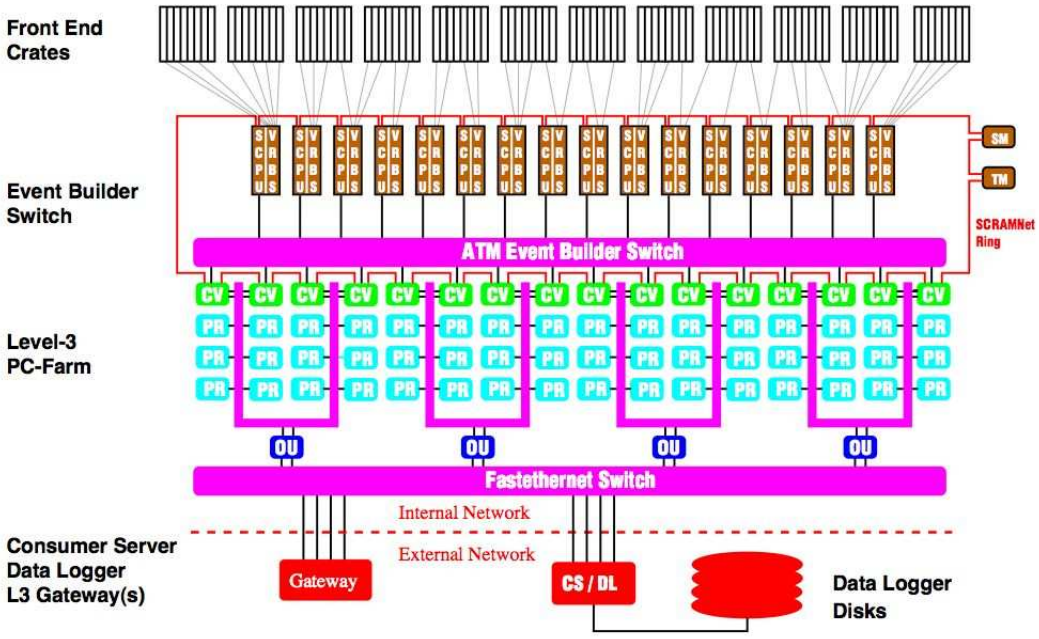

Figure 3.20: Event Builder and L3 operating principle. All the main components are shown: ATM switch (purple), converter nodes (green), output nodes (dark blue), Consumer Sever and data logging System (red).

crates is prepared by Scanner CPU's (SCPU) and fed into the ATM switch. On the other side it is the converter node that receives an ordered sequence of event fragments from the Event Builder. In the converter node these fragments are assembled in a block of data, called the *event record*, suitable for analysis by CDF software. From then on, the event record becomes the one and only piece of information about a particular event.

Each event record is fed to one of the processor nodes in the sub-farm, where event reconstruction is performed and final trigger requirements are applied. At this stage Level-3 takes advantage of the full detector information and improved resolution, not available at the lower trigger levels. Therefore tracks are reconstructed using tridimensional algorithms and both COT and SVX information, match is performed with the muon stubs or calorimetric deposit in order to identify muons and electrons candidates, and calorimetric energy is clustered with more detailed algorithms to generate jet candidates. Dedicated alignment tables and detector calibrations are applied at this level also. If an event satisfies Level-3 requirements, the corresponding event record gets passed to the output node which subsequently transfers it to the mass storage via the Consumer Server/Data Logger.

Parallel processing of many events by many nodes allows for much more time to look at a particular event and therefore for a more accurate decision whether to keep it or not. Level-3 provides an additional reduction by a factor of 4 bringing the total event

rate down to approximately 80 Hz.
It would be noted that the data acquisition system is taking data for (usually large but never exceeding duration of the store) continuous periods of time called *runs*. During the run, the detector configuration (including all the on-line calibration constants *etc.*) is almost stable, it can change however from one run to another, affecting or not the data being recorded. In any case, the events that pass Level-3 are stamped with run number, so that at a later time, information about detector configuration at the time the event was taken could be retrieved from the database.
The data flow from the Level-3 is segmented into ten streams. All the streams are written to tape in real time, as the data are taken, i.e. in on-line regime.
In a second time, data are retrieved from mass storage to be elaborated. At this stage the raw data banks are unpacked and collection of physics objects suitable for analysis, such as tracks, vertexes, muons, electrons, jets, are generated. This is similar to what is done at Level-3, except that it is done in a much more elaborate fashion, applying the most up-to-date calibrations and using the best measured beamlines.
Hence the data flow undergoes further categorizations and the ten data streams coming from the Level-3 output are separated in 35 data sets depending on the physics process one is interested in.

Chapter 4

Same Side Kaon Tagging Studies

This chapter resumes the most important results regarding the studies on the Same Side Kaon tagging. All the data and Monte Carlo samples described here and the corresponding selection strategies are relative to the work resumed in this chapter and have changed in the particle fraction measurement (see chapter 5).

Introduction

Mixing analyses require the knowledge of the B meson flavor both at the time of production and decay. For the determinaton of the flavor at the time of decay we rely on the charge of the decay products of the beauty meson. Establishing the flavor at production is significantly more complex and requires the development of complex algorithms.

Among the different approaches there is the so-called Same Side Tagging (SST) that determines the flavor of the meson at production time considering the charge of the fragmentation tracks around the meson itself. The SST relies on the fact that during fragmentation one of the particle around the B meson carries the partner quark of the one forming the B meson with the b quark. If this particle is charged and if we are able to distinguish it among all the others produced in the fragmentation and by the underlying event, we are also able to determine the B flavor at production time.

In the case of B_d one expects the tagging particle to be a π, while for B_u's both pions and Kaons can contribute. A small component due to protons is also present. In the case of the B_s, due to its strangeness, only strange particles can be tagging particles. Since this particle is expected to be mostly a Kaon, we call the SST algorithm for the B_s Same Side Kaon Tagging (SSKT).

The most relevant issue of the SSKT is the fact that there is no straightforward way to measure its dilution on data. This is only possible in presence of clear mixing signal, then the SSKT dilution can be fitted from data by the mixing fit itself.

While B_d mixing is established and B_u does not mix at all, B_s mixing is heavely pursued at CDF II but still not observed. This implies that SSKT dilution in B_s events is currently unknown. We describe here an attempt to evaluate it from Monte Carlo after tuning its fragmentation properties. No systematic error is presently assigned to

this procedure; we plan to do this in a second stage of this analysis.

In this study we consider at first B_u events that in principle should be tagged by SSKT and whose corresponding dilution can be measured on data; we will compare B_u data to B_u Monte Carlo in order to get an estimate of how well the Monte Carlo reproduces both kinematical spectra and tagging performances. We then consider B_s events on data and Monte Carlo, we will compare several kinematical distribution, in order to verify substantial agreement between data and Monte Carlo. In the end we will evaluate SSKT performances on Monte Carlo in order to establish updated projections on the SSKT capabibilities at CDF II for B_s mixing analysis.

4.1 Description of data samples

This study considers the following decay modes of Bu and B_s:

- $B_u \to D\pi$, $D \to K\pi$
- $B_s \to D_s\pi$, $D_s \to \phi\pi$,$\phi \to KK$

We use data collected with the two track trigger up to the summer 2004 shutdown excluding the compromised COT period. The B_CHARM stream was produced with generation 5.3 CDF offline reconstruction and skimmed in chdl04 (B_u) and chdl07 (B_s) datasets according the procedure described in [65]. At the time of this studies a few percent of the whole data set were missing in the skimmed samples, but this is not an issue for the present analysis.

Three Monte Carlo samples were generated with the PYTHIA event generator for a total of 20 M events. For each B meson type we forced the appropriate decay mode and decayed the meson with EvtGen. The second B in the event is left free to decay in any allowed final state. Realistic detector simulation based on GEANT 3 was then used. The Monte Carlo samples were produced following B Monte Carlo recommendation [66] after correcting the B excited states mass values. The following settings were used for the generation:

- MSEL = 1 (QCD generation);
- $p_T > 3$ GeV/c for partons involved in the hard scattering;
- Tune A of the underlying event [72];
- $B^{\star\star}$ rate fixed to 20% [70];
- The default value of $B^{\star\star}$ masses and widths were replaced according to results reported in [71]; $B_s^{\star\star}$ masses were replaced according to recently published results [70];
- Default Bowler fragmentation function was used;
- Generator filter requiring at least a b quark in the event;

Offline tracks were refitted using the KAL algorithm and corrected for energy loss in the detector material. The COT covariance matrix and magnetic field were rescaled according to standard prescriptions.

Cuts optimized for mixing analyses were applied both in data and Monte Carlo samples for signal selection [67] [68]. In Tab. 4.1 and Tab. 4.2 these cuts are shown respectively for B_u and B_s. After applying this selection we obtain ~ 5515 B_u events

Table 4.1: Selection cuts for $B_u \to D\pi$

$\chi^2_{r,\phi}(D)$	< 15
$\Delta R(D, \pi_B)$	< 2.0
$L_{x,y}(B \to D)$	$> -150\mu m$
$\chi^2_{r,\phi}(B)$	< 15
$L_{x,y}/\sigma_{L_{x,y}}(B)$	> 8
$p_T(\pi_B)$	> 1 GeV/c
$\lvert d_0(B)\rvert$	$< 80\mu m$

Table 4.2: Selection cuts for $B_s \to D_s\pi$

$\chi^2_{r,\phi}(D)$	< 14
$\Delta R(D, \pi_B)$	< 2.0
$L_{x,y}(B \to D)$	$> -200\mu m$
$\chi^2_{r,\phi}(B)$	< 15
$L_{x,y}/\sigma_{L_{x,y}}(B)$	> 7
$p_T(\pi_B)$	> 1.2 GeV/c
$\lvert d_0(B)\rvert$	$< 60\mu m$

[fig. 4.1] and ~ 315 B_s events [fig. 4.2].

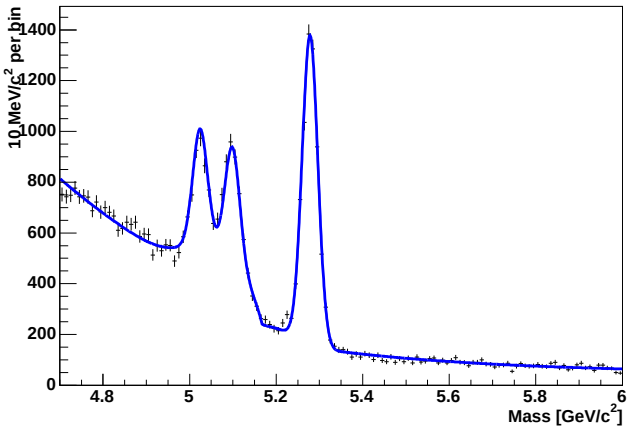

Figure 4.1: Invariant mass distribution for B_u events.

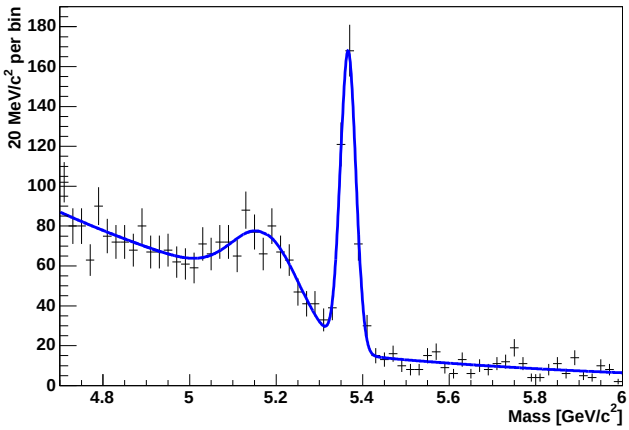

Figure 4.2: Invariant mass distribution for B_s events.

In the following sections we study same side flavor tagging using tracks found around the reconstructed B's. The common requirements for tracks used by all tagging algorithms considered later are listed below:

- Track must be in a cone $\Delta R < 0.7$ relative to the B meson direction ($\Delta R = \sqrt{\eta^2 + \phi^2}$).
- Track must have at least 3 axial silicon hits.
- Track $p_T > 450\ MeV/c$.
- $d_0/\sigma_{d_0} < 10$.
- $\Delta z_0 < 2$ cm between B candidate and track.

4.2 Particle Identification tools

The CDF II detector provides two means of charged particle identification: dE/dx in the COT and TOF. In our studies we use an algorithm that combines the two pieces of information in order to achive the best particle type separation [69].

Our primary goal is to separate the Kaons from the large Pion background. We define the combined PID Likelihood as:

$$L_{comb}(part) = p(TOF|part) \cdot p(dE/dx|part) \tag{4.1}$$

where 'part' is the assumed particle hypotesis. We do not consider at the moment the correlations between different particles in the same event. We select Kaons applying a cut on the Likelihood Ratio (LR_{comb}) defined as:

$$LR_{comb} = log\left(\frac{p(TOF|K) \cdot p(dE/dx|K)}{p(TOF|\pi) \cdot p(dE/dx|\pi)}\right) \tag{4.2}$$

4.2.1 Monte Carlo PID simulation

The Monte Carlo currently implements only a partial simulation of particle ID: dE/dx is not available, while full 5.3.4 TOF simulation exists and has been used in the production of our Monte Carlo samples.

In order to describe dE/dx in simulated events, we have implemented a parametrization in terms of resolution functions extracted directly from the data. dE/dx resolution functions are obtained from a large sample of of $D^{\star}$'s obtained with the two track trigger [69].

In the case of the TOF we need the simulation to extract the following information: the efficiency (the probability that given a track there is a matching hit in the TOF bars) and the time of flight measurement. We have used the TOF full simulation to describe the efficiency of the detector. The TOF measurement is instead implemented in terms of resolution functions extracted directly from the data [69] using an approach similar to that used in the dE/dx case.

We observe a residual discrepancy between the TOF efficiency measured in the Monte Carlo, ϵ_{tof}^{MC}, and the corresponding efficiency, ϵ_{tof}^{Data}, measured in the data. The ratio of these efficiencies is fairly constant with the track p as shown in fig. 4.3. We therefore degrade the Monte Carlo efficiency according to this measured constant ratio.

4.3 Data - Monte Carlo comparison in $B_u \rightarrow D\pi$ events

In this section we show comparisons of relevant distributions between data and Monte Carlo for B_u events.

All the plots in this section are sideband subtracted. Only the high mass region is considered for sideband subtraction due to partially reconstructed events contamination in the low mass sideband (fig. 4.1). Sideband events are rescaled to the number of expected background events in the signal region (2σ around the B_u fitted mass).

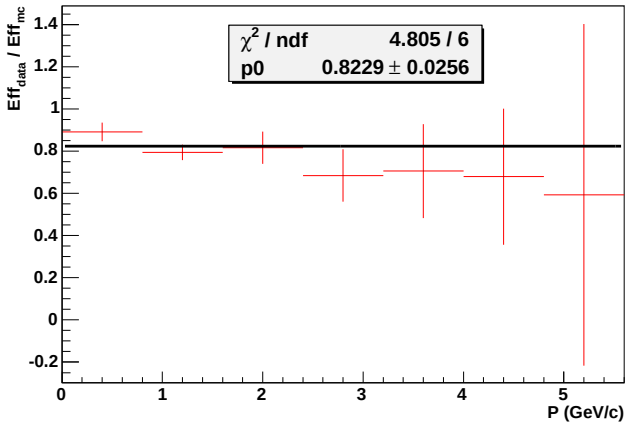

Figure 4.3: $\epsilon_{tof}^{Data}/\epsilon_{tof}^{MC}$ as a function of track momentum in B_u events.

All the plots in this section are also normalized to the number of B_u. As a consequence of this normalization, the plots using all the tracks around the B_u are not normalized to one but to the average number of tracks per B_u. The only exceptions are the *min* p_T^{rel} and the *max* p_L^{rel} distributions where at most one track is selected per B_u candidate.

Distributions related to tracks around the B_u are shown before and after applying PID selection. We observe an overall good agreement between Monte Carlo and data with a few exceptions discussed below in more detail.

In fig. 4.4 there is evidence of a difference in the p_T spectrum of the B_u candidate: Monte Carlo seems to be softer than data and a χ^2 test give a probability equal to 0 . The discrepancy however is sufficiently small to have only a small effect on SS(K)T dilutions and efficiencies. We have tried reweighing and found variations of the tagging efficiencies and dilutions well within the statistical errors (see section 5.1).

We also observe an overall small excess of tracks in data with respect to Monte Carlo, as shown in the multiplicity distribution (fig. 4.10). Furthermore the the p_T^{rel} (fig. 4.6) and p_L^{rel} (fig. 4.7) distributions appear softer in data than in Monte Carlo.Pile up effects should be further investigated as a possible source of these differences, such as the excited B^{**} states contribution.

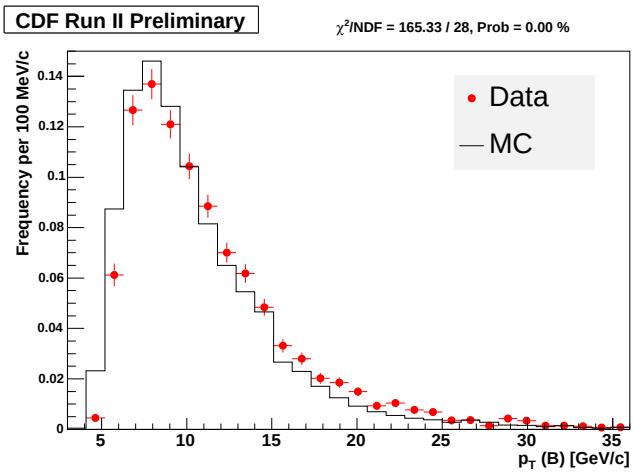

Figure 4.4: $p_T(B_u)$ spectrum: data (red) and Monte Carlo (black).

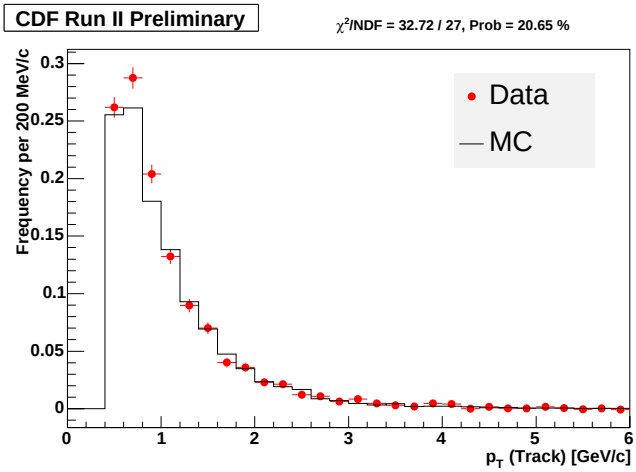

Figure 4.5: p_T spectrum of tracks in a cone $\Delta R = 0.7$ around the B_u meson; data (red) and Monte Carlo (black).

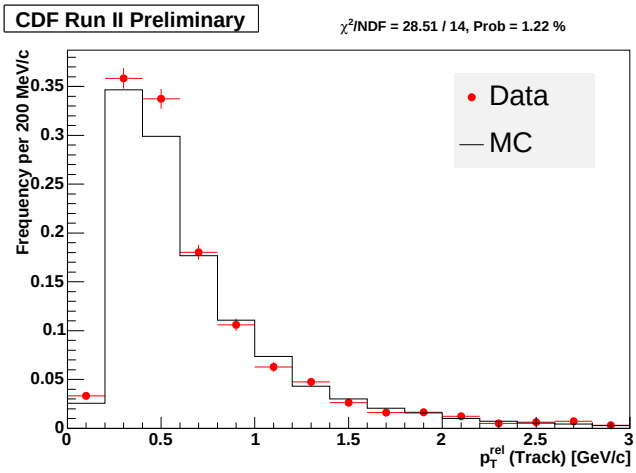

Figure 4.6: p_T^{rel} spectrum of tracks in a cone $\Delta R = 0.7$ around the B_u meson; data (red) and Monte Carlo (black).

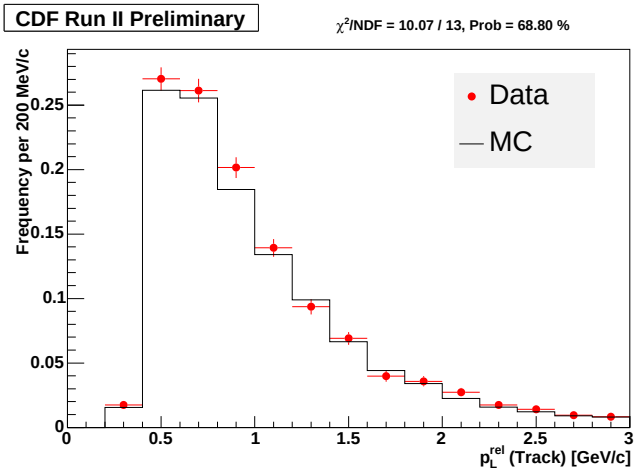

Figure 4.7: p_L^{rel} spectrum of tracks in a cone $\Delta R = 0.7$ around the B_u meson; data (red) and Monte Carlo (black).

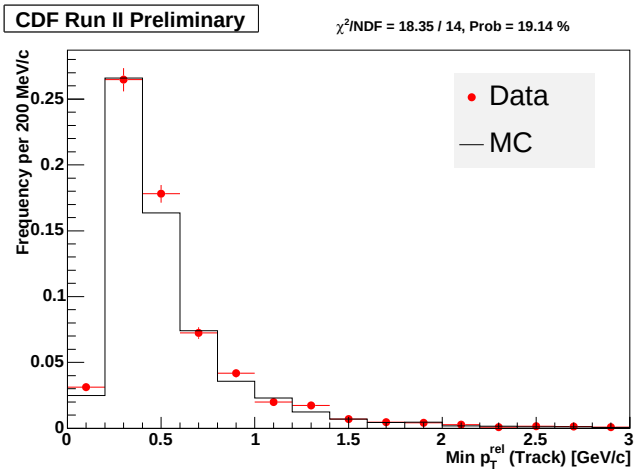

Figure 4.8: $Min\ p_T^{rel}$ spectrum of tracks in a cone $\Delta R = 0.7$ around the B_u meson; data (red) and Monte Carlo (black).

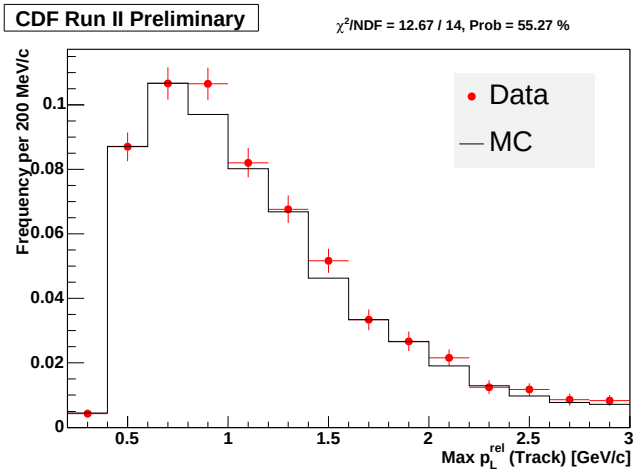

Figure 4.9: $Max\ p_L^{rel}$ spectrum of tracks in a cone $\Delta R = 0.7$ around the B_u meson; data (red) and Monte Carlo (black).

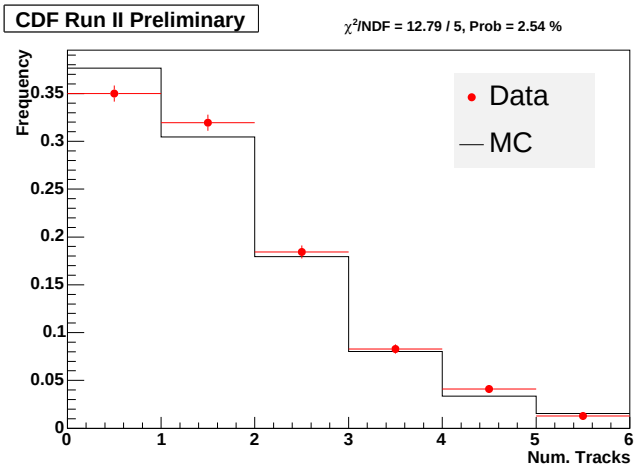

Figure 4.10: Track multiplicity in a cone $\Delta R = 0.7$ around the B_u meson; data (red) and Monte Carlo (black).

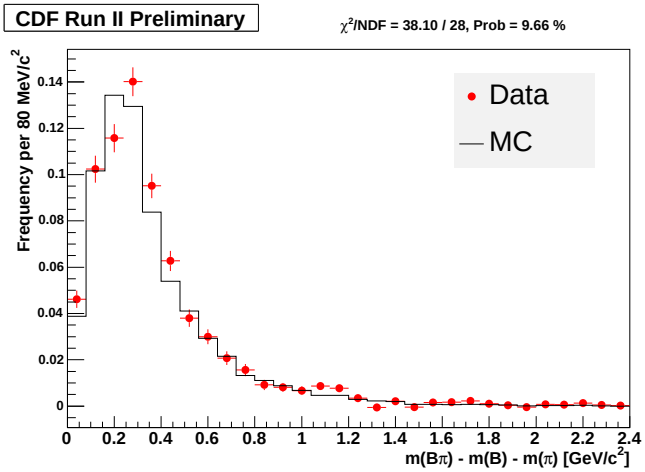

Figure 4.11: Right sign $m(B\pi) - m(B) - m(pi)$ distribution for B_u meson; data (red) and Monte Carlo (black).

The rest of this section is dedicated to data - Monte Carlo comparisons after applying PID selections. We distinguish between π and K mesons by cutting on LR_{comb} where LR_{comb} is the log of the combined likelihood ratio as defined previously in eq. (4.2). We also define LR_{tof} and $LR_{dE/dx}$ as the corresponding log likelihood ratios using only the TOF or dE/dx part respectively.

All distributions, except for the LR_{comb} distribution themselves, use tracks passing the cut $LR_{comb} > -2$. This cut has not been otimized, but is rather justified by observing fig. 4.12 and fig. 4.13. Indeed the cut is located about half way between the pion and kaon peaks. After $LR_{comb} > -2$ cut we observe in Monte Carlo the following particle type fractions: Pions = 43.6 %, Kaons = 35.8%, Protons = 20.6 %.

In fig. 4.12 we observe a small excess of particles on the π side (and a slight depletion in the kaon side) in the Monte Carlo relative to data. In addition the p_T (fig. 4.15), p_T^{rel} and p_L^{rel} distributions after the LR cut show a softer behavior in data than in Monte Carlo. All these features could be related to the fragmentation model properties in Monte Carlo that will be the subject of further stuides in a near future; similary also the $B_s^{\star\star}$ contribution will investigated.

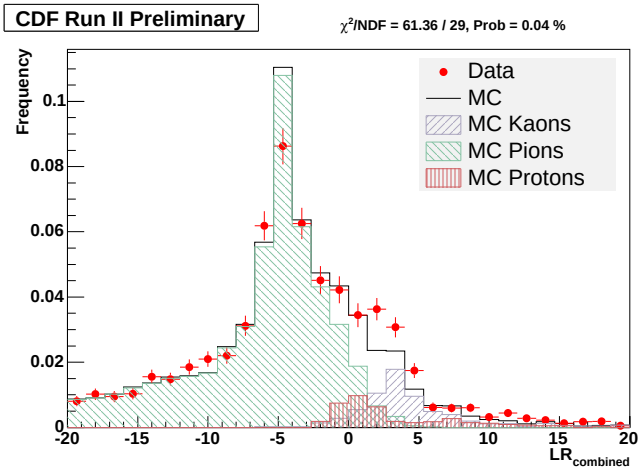

Figure 4.12: LR_{comb} distribution of tracks in a cone $\Delta R = 0.7$ around the B_u meson; data (red) and Monte Carlo (black).

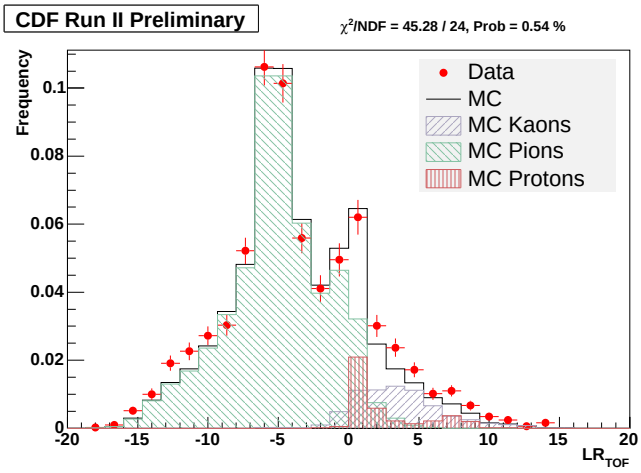

Figure 4.13: LR_{tof} distribution of tracks in a cone $\Delta R = 0.7$ around the B_u meson; data (red) and Monte Carlo (black).

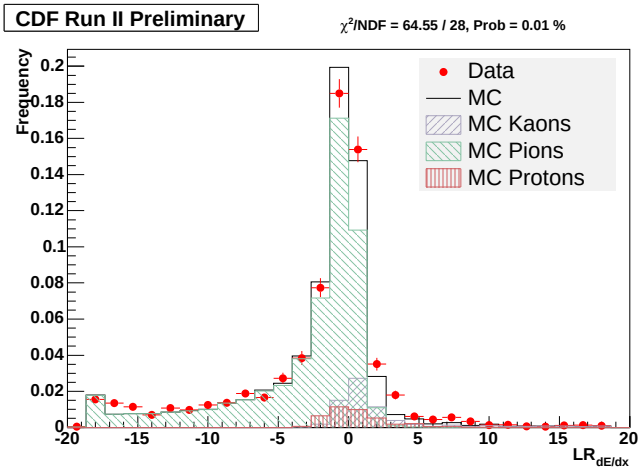

Figure 4.14: LR_{dedx} distribution of tracks in a cone $\Delta R = 0.7$ around the B_u meson; data (red) and Monte Carlo (black).

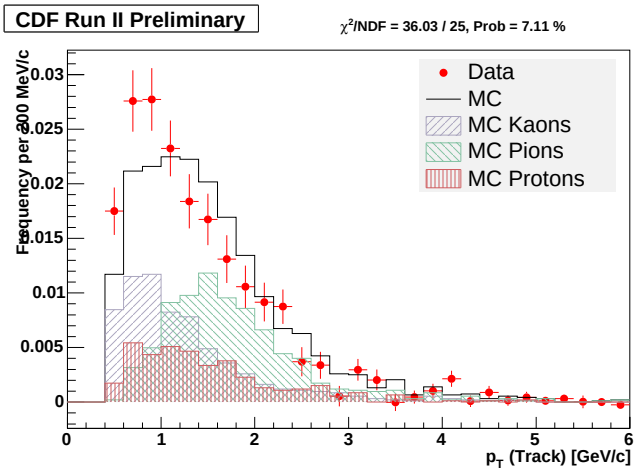

Figure 4.15: p_T spectrum of tracks passing $LR_{comb} > -2$ cut in a cone $\Delta R = 0.7$ around the B_u meson; data (red) and Monte Carlo (black).

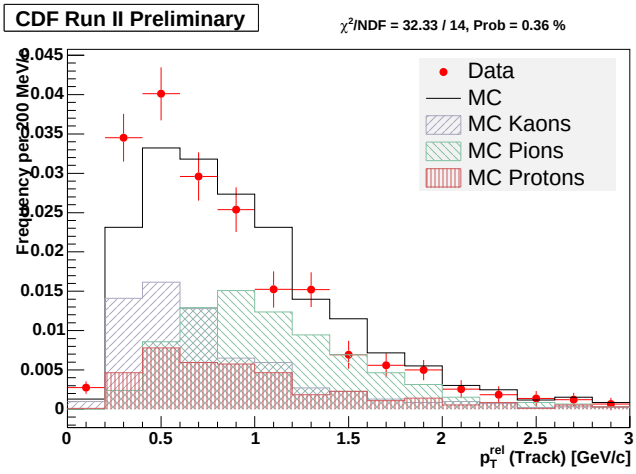

Figure 4.16: p_T^{rel} spectrum of tracks passing $LR_{comb} > -2$ cut in a cone $\Delta R = 0.7$ around the B_u meson; data (red) and Monte Carlo (black).

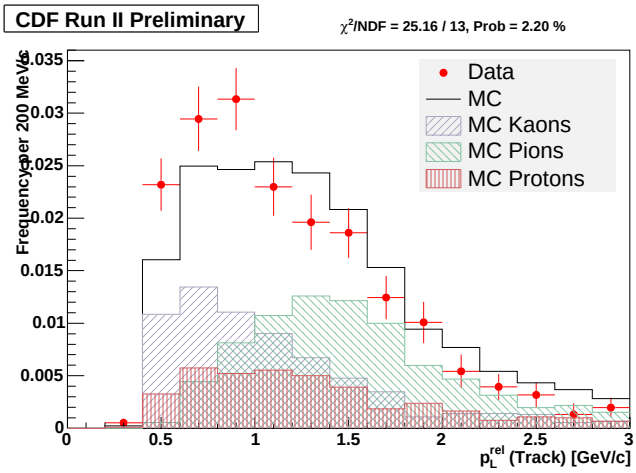

Figure 4.17: p_L^{rel} spectrum of tracks passing $LR_{comb} > -2$ cut in a cone $\Delta R = 0.7$ around the B_u meson; data (red) and Monte Carlo (black).

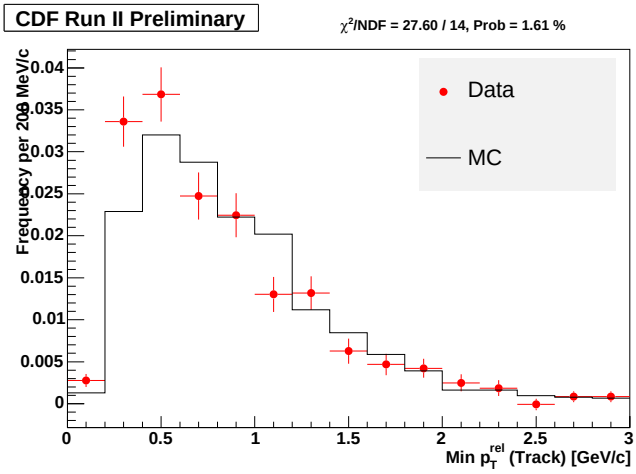

Figure 4.18: $Min\ p_T^{rel}$ spectrum of tracks passing $LR_{comb} > -2$ cut in a cone $\Delta R = 0.7$ around the B_u meson; data (red) and Monte Carlo (black).

In conclusion, we observe a reasonable agreement between data and Monte Carlo distributions. The main differences are observed after PID selections.

4.4 Data - Monte Carlo comparison in $B_s \to D_s\pi$ events

In the case of B_s events, we observe an overall good agreement between data and Monte Carlo, also after PID selections. We remind that in this case we don't expect any contribution from excited states, contrary to the B_u case. For the B_s a slightly harder LR_{comb} cut was used, $LR_{comb} > -1$. As usual all the following plots are sidebands subtracted (high mass sideband only) and normalized to the number of B_s. After $LR_{comb} > -1$ cut we observe in B_s Monte Carlo the following particle type fractions: Pions = 17.6 %, Kaons = 70.3%, Protons = 12.0 %.

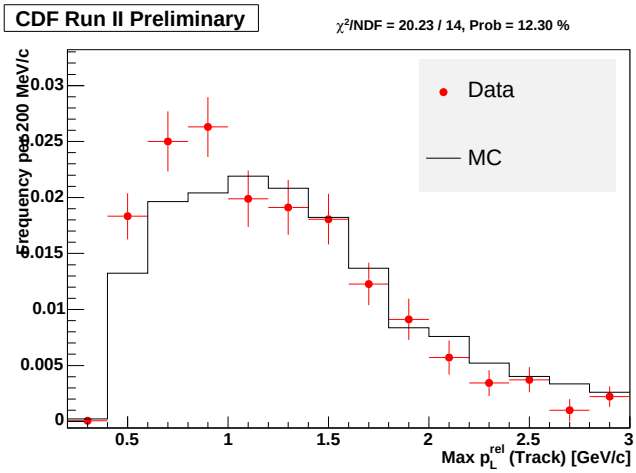

Figure 4.19: $Max\ p_L^{rel}$ spectrum of tracks passing $LR_comb > -2$ cut in a cone $\Delta R = 0.7$ around B_u meson; data (red) and Monte Carlo (black).

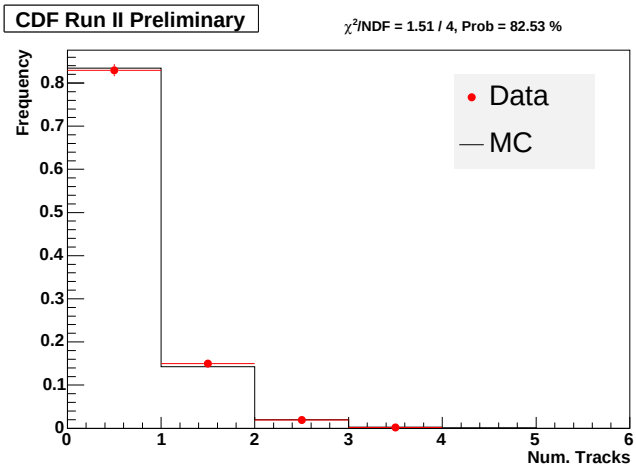

Figure 4.20: Track multiplicity in a cone $\Delta R = 0.7$ around the B_u meson for track passing $LR_{comb} > -2$ cut; data (red) and Monte Carlo (black).

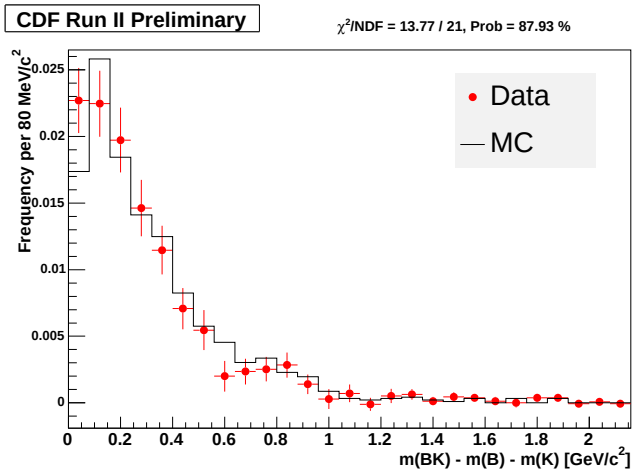

Figure 4.21: Right sign $m(BK)-m(B)-m(K)$ distribution for the B_u meson requiring $LR_{comb} > -2$ for kaon track; data (red) and Monte Carlo (black).

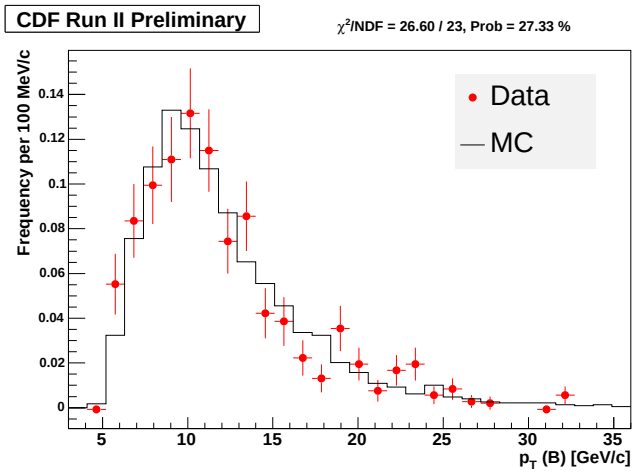

Figure 4.22: $p_T(B_s)$ spectrum: data (red) and Monte Carlo (black).

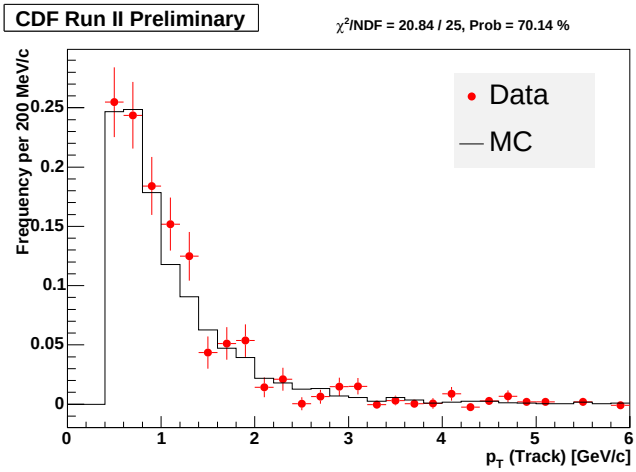

Figure 4.23: p_T spectrum of tracks in a cone $\Delta R = 0.7$ around the B_s meson; data (red) and Monte Carlo (black).

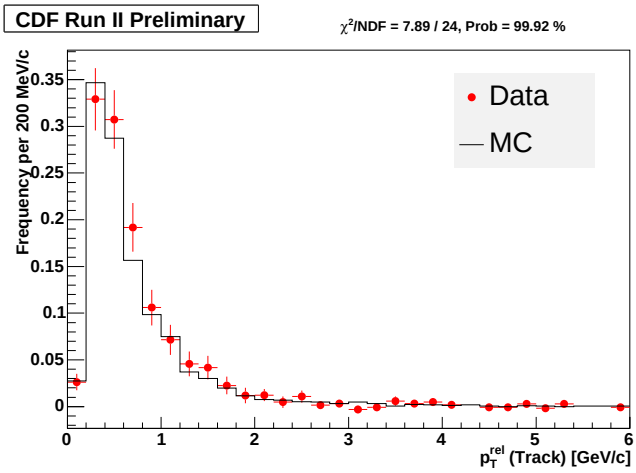

Figure 4.24: p_T^{rel} spectrum of tracks in a cone $\Delta R = 0.7$ around the B_s meson; data (red) and Monte Carlo (black).

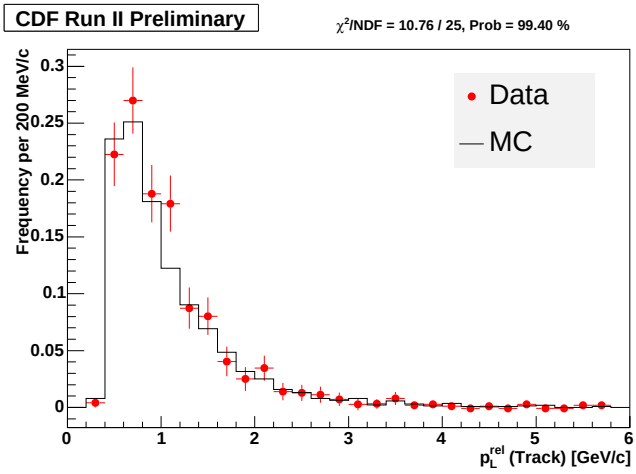

Figure 4.25: p_L^{rel} spectrum of tracks in a cone $\Delta R = 0.7$ around the B_s meson; data (red) and Monte Carlo (black).

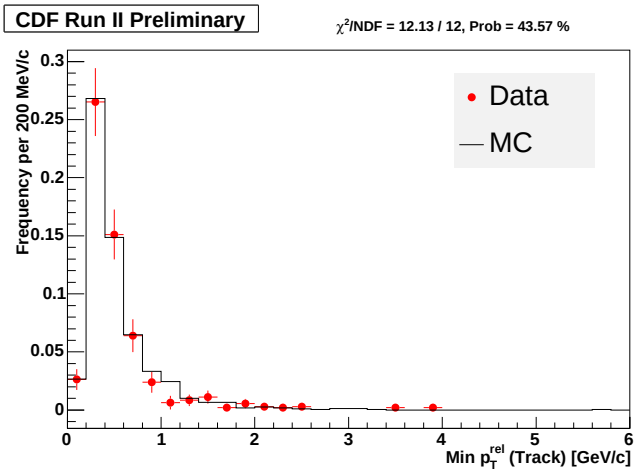

Figure 4.26: $Min\ p_T^{rel}$ spectrum of tracks in a cone $\Delta R = 0.7$ around the B_s meson; data (red) and Monte Carlo (black).

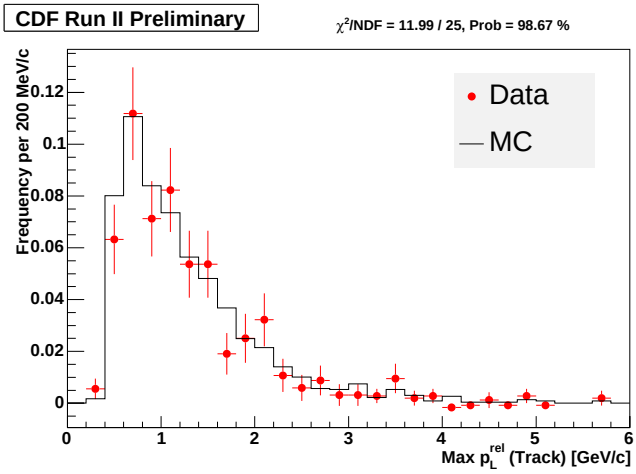

Figure 4.27: $Max\ p_L^{rel}$ spectrum of tracks in a cone $\Delta R = 0.7$ around the B_s meson; data (red) and Monte Carlo (black).

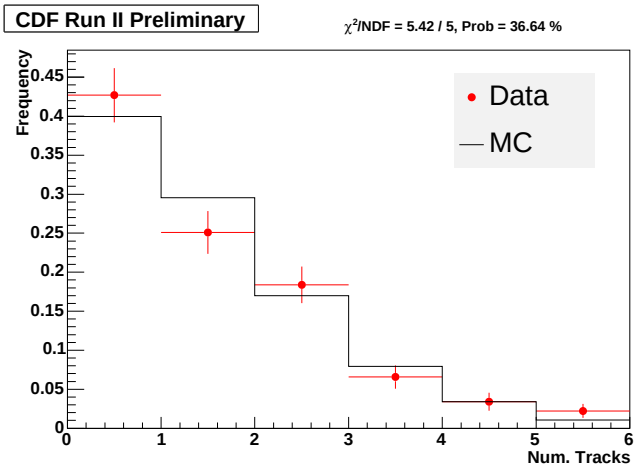

Figure 4.28: Track multiplicity in a cone $\Delta R = 0.7$ around the B_s meson; data (red) and Monte Carlo (black).

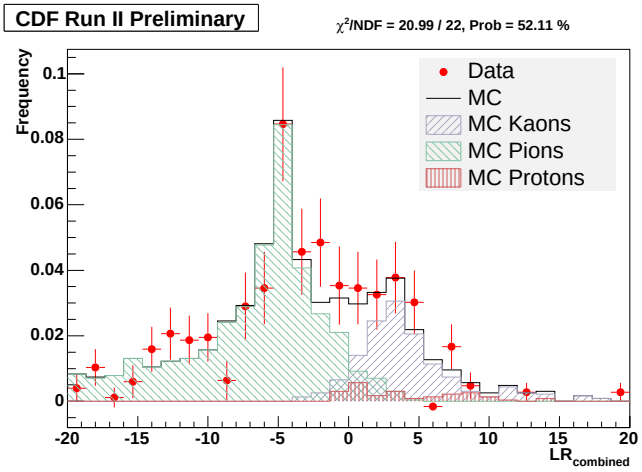

Figure 4.29: LR_{comb} distribution of tracks in a cone $\Delta R = 0.7$ around the B_s meson; data (red) and Monte Carlo (black).

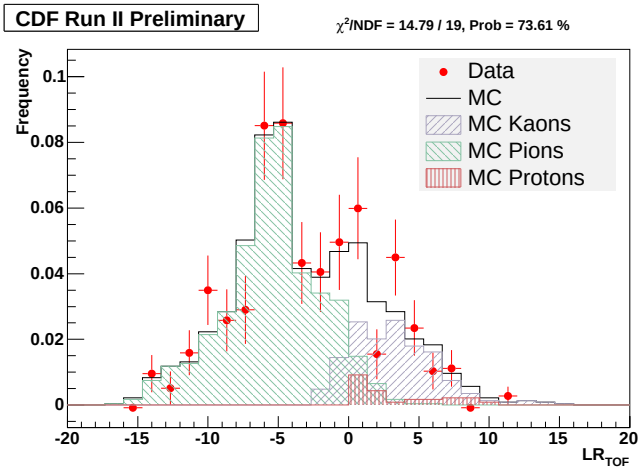

Figure 4.30: LR_{tof} distribution of tracks in a cone $\Delta R = 0.7$ around the B_s meson; data (red) and Monte Carlo (black).

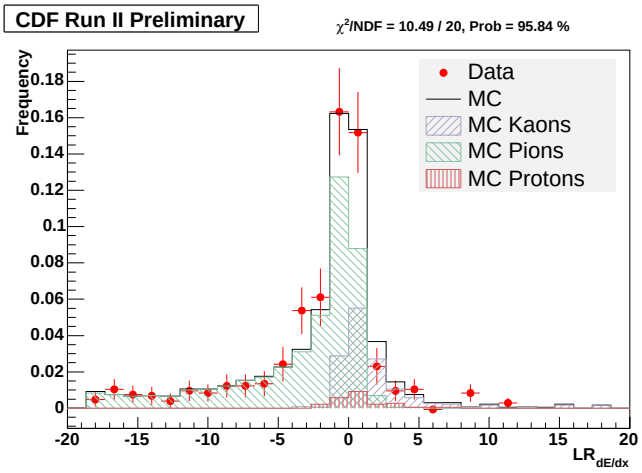

Figure 4.31: LR_{dedx} distribution of tracks in a cone $\Delta R = 0.7$ around the B_s meson after tof matching requirement; data (red) and Monte Carlo (black).

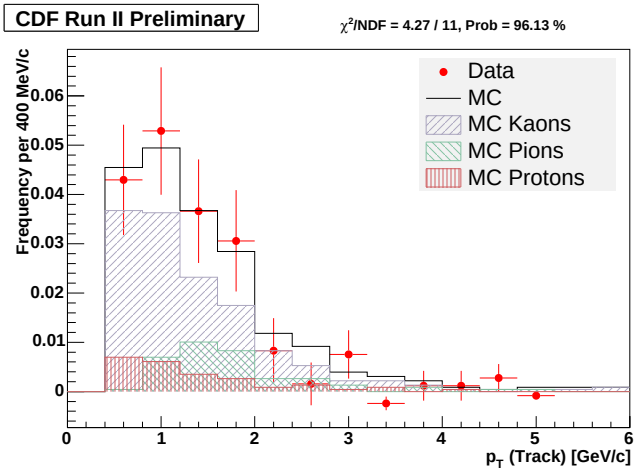

Figure 4.32: p_T spectrum of tracks passing $LR_{comb} > -1$ cut in a cone $\Delta R = 0.7$ around the B_s meson; data (red) and Monte Carlo (black).

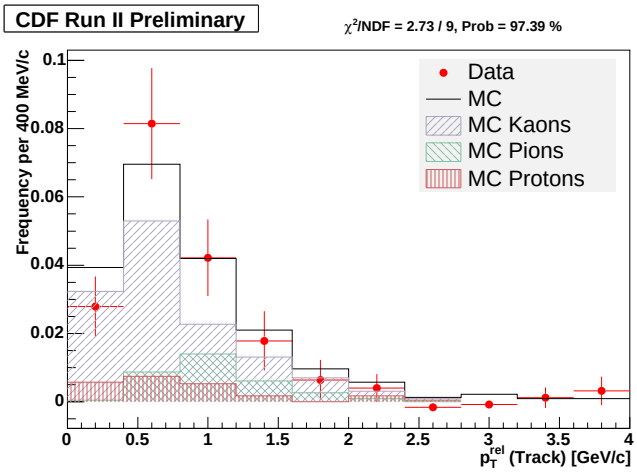

Figure 4.33: p_T^{rel} spectrum of tracks passing $LR_{comb} > -1$ cut in a cone $\Delta R = 0.7$ around the B_s meson; data (red) and Monte Carlo (black).

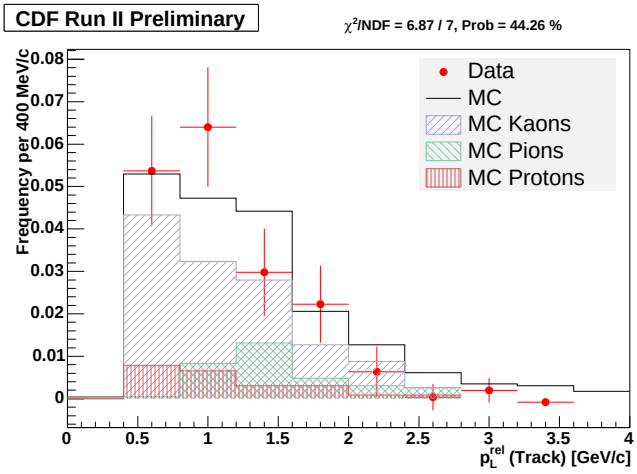

Figure 4.34: p_L^{rel} spectrum of tracks passing $LR_{comb} > -1$ cut in a cone $\Delta R = 0.7$ around the B_s meson; data (red) and Monte Carlo (black).

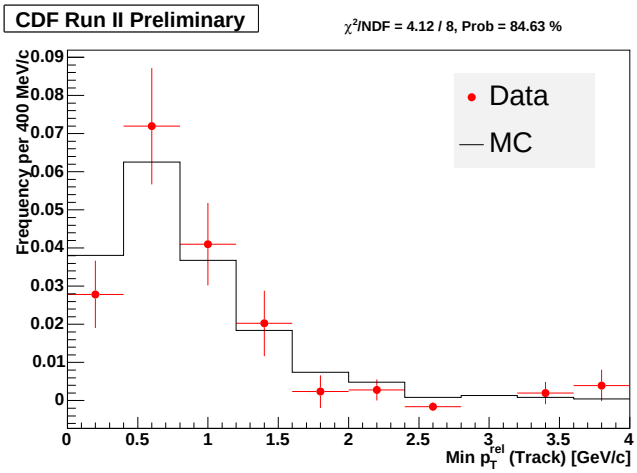

Figure 4.35: $Min\ p_T^{rel}$ spectrum of tracks passing $LR_{comb} > -1$ cut in a cone $\Delta R = 0.7$ around the B_s meson; data (red) and Monte Carlo (black).

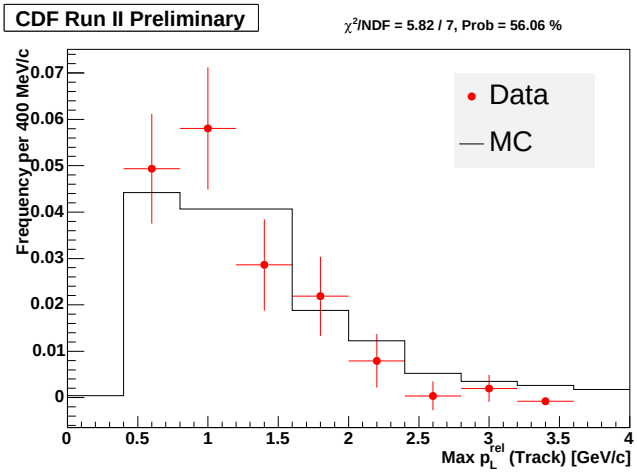

Figure 4.36: $Max\ p_L^{rel}$ spectrum of tracks passing $LR_{comb} > -1$ cut in a cone $\Delta R = 0.7$ around the B_s meson; data (red) and Monte Carlo (black).

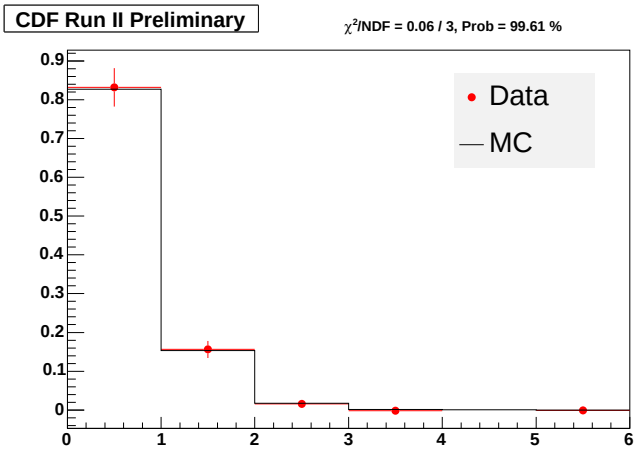

Figure 4.37: Track multiplicity in a cone $\Delta R = 0.7$ around the B_s meson for track passing $LR_{comb} > -1$ cut; data (red) and Monte Carlo (black).

4.5 Tagging Algorithms

The goal of Same Side Tagging algorithm is to determine the flavor of the B meson at production time using the information carried by the charge of fragmentation tracks around the meson itself. Two different approaches are considered in these studies:

- Attempt to select the fragmentation particle that carries the partner quark of the one forming the meson with the b quark;
- Use all charged particles around the B meson to extract some global estimator of the flavor at production.

As algorithm of the first class we considered:

- $min\ p_T^{rel}$, that is we choose as tagging track the one with the lowest p_T relative to the B meson flight direction. The tagger response is given by the sign of the track selected;
- $max\ p_L^{rel}$, that is we choose as tagging track the one with the highest p_L relative to the B meson flight direction. . The tagger response is given by the sign of the track selected. This is similar to the previous one, being just another way of defining the kinematical correlation between the B meson and the tagging track.

As algorithm of the second class, we considered:

- The tagger response is the sum of the charges of all the tracks inside the cone around the B meson.

In following subsections we present the tagging performances of all the three algorithms both in data and Monte Carlo for B_u events and only in Monte Carlo for B_s. In B_s data tagging efficiency only can be reported.

4.5.1 Tagging Performances in B_u

In this section we report the tagging results for B_u. Before applying PID selections, data and Monte Carlo agree very well for all the three algorithms; our results for $Min\ p_T^{rel}$ algorithm are in agreement with what found in [67]. Small discrepancies are observed after the $LR_{comb} > -2$ cut; in particular Monte Carlo turns out to be a bit less efficient than data while Monte Carlo dilutions are a bit lower than the corresponding values observed in data. Dilutions are anyway consistent within the statistical errors.

Table 4.3: $Min\ p_T^{rel}$ algorithms performance comparison between data and Monte Carlo without PID for $B_u \to D\pi$

$Min\ p_T^{rel}$	Data (%)	Monte Carlo (%)
ϵ	65.7 ± 0.6	63.2 ± 0.5
D	18.2 ± 1.6	19.8 ± 1.3
ϵD^2	2.17 ± 0.39	2.48 ± 0.32

Table 4.4: $Max\ p_L^{rel}$ algorithms performance comparison between data and Monte Carlo without PID for $B_u \to D\pi$

$Max\ p_L^{rel}$	Data (%)	Monte Carlo (%)
ϵ	65.7 ± 0.6	63.2 ± 0.5
D	24.3 ± 1.6	25.0 ± 1.3
ϵD^2	3.89 ± 0.50	3.96 ± 0.40

Table 4.5: ΣQ algorithms performance comparison between data and Monte Carlo without PID for $B_u \to D\pi$

ΣQ	Data (%)	Monte Carlo (%)
ϵ	53.1 ± 0.7	51.0 ± 0.5
D	28.3 ± 1.8	30.0 ± 1.4
ϵD^2	4.24 ± 0.53	4.59 ± 0.43

Table 4.6: $Min\ p_T^{rel}$ algorithms performance comparison between data and Monte Carlo selecting $LR_{PID} > -2$ tracks for $B_u \to D\pi$

$Min\ p_T^{rel}$	Data (%)	Monte Carlo (%)
ϵ	17.3 ± 0.5	17.1 ± 0.4
D	24.9 ± 3.1	25.7 ± 2.3
ϵD^2	1.07 ± 0.27	1.52 ± 0.25

Table 4.7: $Max\ p_L^{rel}$ algorithms performance comparison between data and Monte Carlo selecting $LR_{PID} > -2$ tracks PID for $B_u \to D\pi$

$Max\ p_L^{rel}$	Data (%)	Monte Carlo (%)
ϵ	17.3 ± 0.5	17.1 ± 0.4
D	28.5 ± 3.1	30.3 ± 2.4
ϵD^2	1.41 ± 0.31	1.57 ± 0.25

Table 4.8: ΣQ algorithms performance comparison between data and Monte Carlo selecting $LR_{PID} > -2$ tracks for $B_u \to D\pi$

ΣQ	Data (%)	Monte Carlo (%)
ϵ	16.0 ± 0.5	15.9 ± 0.4
D	28.2 ± 3.2	32.3 ± 2.4
ϵD^2	1.27 ± 0.30	1.66 ± 0.25

Effects of B^{**} fraction on tagging performances in B_u

In order to exploit the dilution dependence on excited B mesons we tried to vary the B^{**} and B_s^{**} fractions in Monte Carlo events. The relative B^{**} and B_s^{**} fraction is fixed. The excited states fraction is defined as $fracN^{**}N^{**} + N^{pr}$, where N^{**} is the number of excited states candidates and N^{pr} is the number of prompt B mesons: both numbers are evaluated *after* analysis cuts. In fig. 4.38 we show $Max\ p_L^{rel}$ dilution as a function of excited states fraction: a clear dependence is observed.

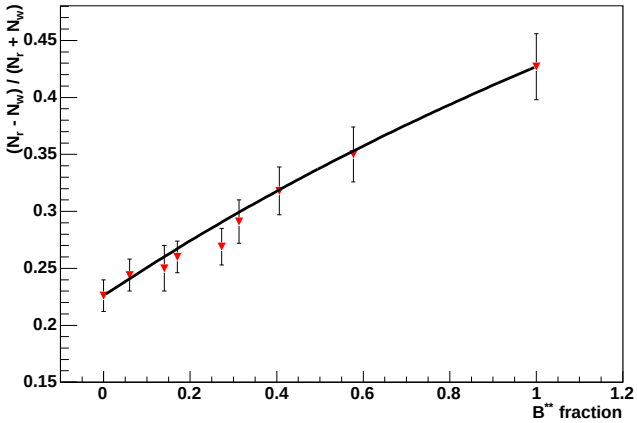

Figure 4.38: $Max\ p_L^{rel}$ dilution as a function of excited states fraction .

4.5.2 Tagging Performances in B_s MC

In the B_s case, although dilutions cannot be evaluated on data, we found a very good agreement between data and Monte Carlo efficiencies for all the three algorithms and both with and without the LR_{comb} selection for Kaons. We note that the Monte Carlo results indicate that we can obtain non-negligible dilutions with the $max\ p_L^{rel}$ and ΣQ algorithms also without PID selection. The Monte Carlo predicts that the $max\ p_L^{rel}$ algorithm is the one with the best performance after the PID selection with an estimated $\epsilon D^2 = 2.42 \pm 0.59\%$.

Table 4.9: $Min\ p_T^{rel}$ algorithms performance in Monte Carlo without PID for $B_s \to D_s\pi$

$Min\ p_T^{rel}$	Data (%)	Monte Carlo (%)
ϵ	57.0 ± 2.7	59.1 ± 1.0
D	–	11.1 ± 2.6
ϵD^2	–	0.73 ± 0.34

Table 4.10: $Max\ p_L^{rel}$ algorithms performance in Monte Carlo without PID for $B_s \to D_s\pi$

$Max\ p_L^{rel}$	Data (%)	Monte Carlo (%)
ϵ	57.0 ± 2.7	59.1 ± 1.3
D	–	19.0 ± 2.6
ϵD^2	–	2.13 ± 0.58

Table 4.11: ΣQ algorithms performance in Monte Carlo without PID for $B_s \to D_s\pi$

ΣQ	Data (%)	Monte Carlo (%)
ϵ	45.8 ± 2.7	46.5 ± 1.0
D	–	21.4 ± 2.9
ϵD^2	–	2.1 ± 0.58

Table 4.12: $Min\ p_T^{rel}$ algorithms performance in Monte Carlo selecting $LR_{PID} > -1$ tracks for $B_s \to D_s\pi$

$Min\ p_T^{rel}$	Data (%)	Monte Carlo (%)
ϵ	15.5 ± 2.0	15.7 ± 0.7
D	–	39.8 ± 4.7
ϵD^2	–	2.48 ± 0.60

Table 4.13: $Max\ p_L^{rel}$ algorithms performance in Monte Carlo selecting $LR_{PID} > -1$ tracks PID for $B_s \to D_s\pi$

$Max\ p_L^{rel}$	Data (%)	Monte Carlo (%)
ϵ	15.5 ± 2.0	15.7 ± 0.7
D	–	39.3 ± 4.7
ϵD^2	–	2.42 ± 0.59

Table 4.14: ΣQ algorithms performance in Monte Carlo selecting $LR_{PID} > -1$ tracks for $B_s \to D_s\pi$

ΣQ	Data (%)	Monte Carlo (%)
ϵ	14.6 ± 2.0	14.6 ± 0.9
D	–	44.7 ± 4.8
ϵD^2	–	2.91 ± 0.64

4.6 Conclusion

We presented a comparison between data and Monte Carlo in B_u and B_s events selected by the two track trigger of CDF. We compared several distributions of interest for tagging purposes.

In the B_u case the tagging performances of three different algorithms were found to be in rather good agreement with Monte Carlo predictions. In the case of the B_s the Monte Carlo gives a good description of all kinematical variables studied and of the tagger efficiencies. The tagging power of the ΣQ algorithm is estimated to be $\epsilon D^2 = 2.91 \pm 0.64\%$ after the selection of the Kaons with the CDF PID tools.

Chapter 5

Sample Selection

In this Chapter we will focus on the selection and reconstruction of B mesons candidates, the procedure used to extract the composition of the mass spectra of the candidates in order to separate signal events from background and the procedure used to collect the sample of particles produced in association with the B mesons. The data sample used in this thesis has been collected by the CDF detector between March 2002 and February 2006, and it corresponds to an integrated luminosity of about 1.3 fb^{-1}. We apply the CDF B Physics group Good Runs Selection (see appendix) on such data sample, defining an effective luminosity of 1.0 fb^{-1}.

5.1 B candidates selection

As already mentioned, we consider fully reconstructed decays of B^+, B^0 and B_s mesons[1]. The fully reconstructed decays, although have lower statistics, have several advantages respect to the partially reconstructed decays:

- The B signal is better separated respect to his background.
- The B candidate decay products are well defined and distinguished respect to the other particles in the event.
- The B candidates' momentum and direction are unequivocally determined; as we will see, this is important when defining a region of interest around the candidate to select the particles produced in association with the B mesons.

Two categories of B decays were considered: one is collected by the *di−muon* trigger path and characterized by a J/ψ meson in the final state, the other is collected by the *two−track* trigger path and characterized by a D meson in the final state.

In particular, in the *di−muon* trigger we analyzed the following exclusive decay modes:

– $B^+ \to J/\psi\, K^+$, with $J/\psi \to \mu^+\mu^-$;

[1]Through this thesis, references to a specific charge state imply the charge−conjugate state as well.

– $B^0 \to J/\psi\, K^{*0}$, with $J/\psi \to \mu^+\mu^-$ and $K^{*0} \to K^+\pi^-$;

– $B_s \to J/\psi\, \phi$, with $J/\psi \to \mu^+\mu^-$ and $\phi \to K^+K^-$;

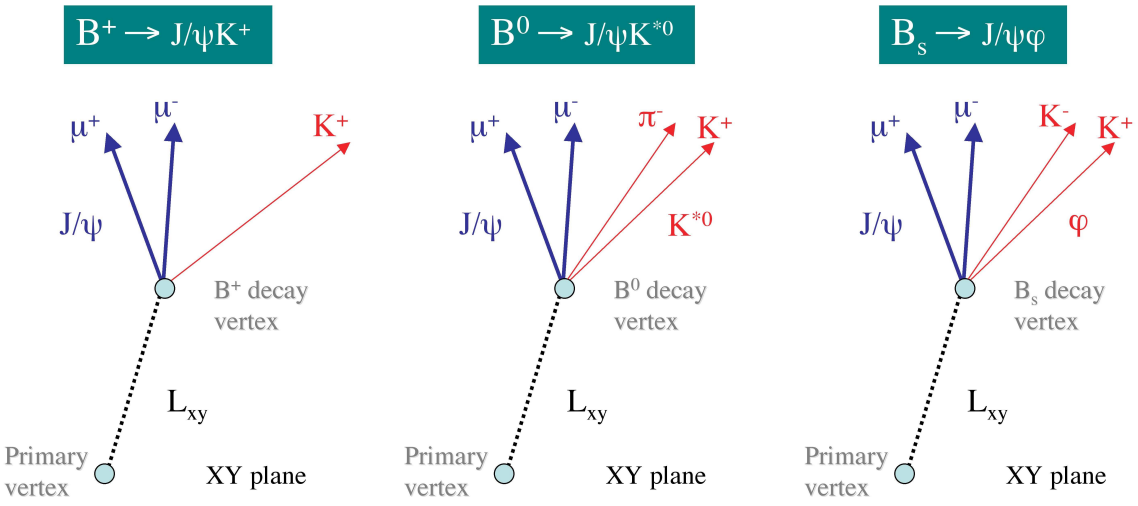

Figure 5.1: Picture of the J/ψ decay modes considered.

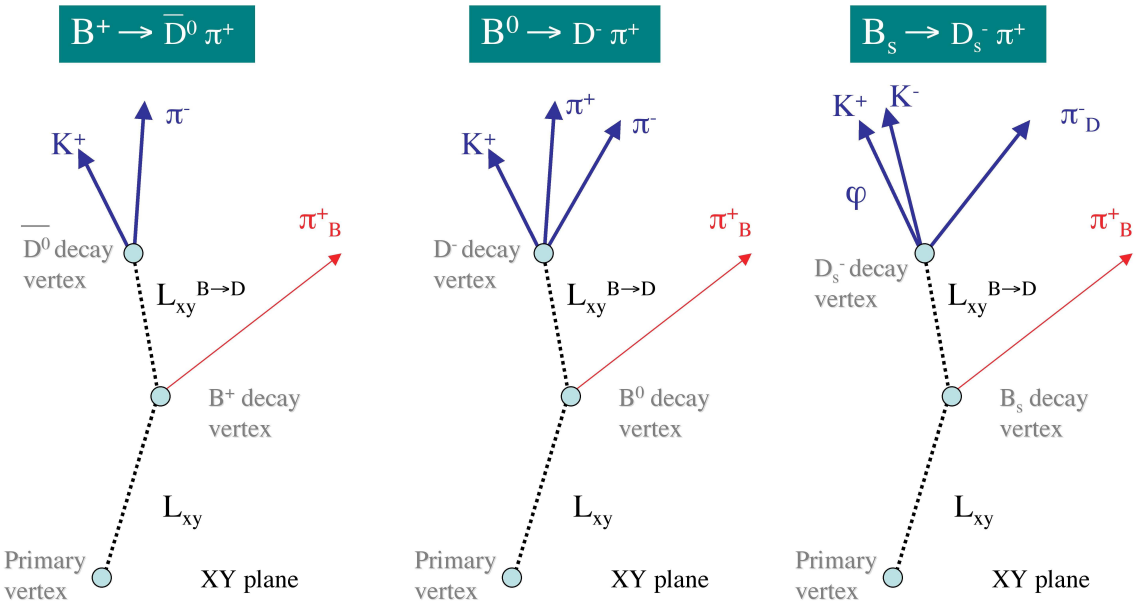

Figure 5.2: Picture of the hadronic decay modes considered.

while in the *two−track* trigger we analyzed the following exclusive decay modes:

– $B^+ \to \overline{D}^0 \pi^+$, with $\overline{D}^0 \to K^+\pi^-$;

– $B^0 \to D^- \pi^+$, with $D^- \to K^+\pi^-\pi^-$;

– $B_s \to D_s^- \pi^+$, with $D_s^- \to \phi\pi^-$ and $\phi \to K^+K^-$.

Fig.5.1 and Fig.5.2 show illustrations of the six decay topologies. Notice that while in the case of the *di−muon* trigger candidates (also called J/ψ *modes*), the decay topology is characterized by one single displaced vertex (the B decay vertex), in the case of the *two−track* trigger candidates we observe two distinguished displaced vertexes: one due to the B decay and another due to the D meson decay, notice also that the *two−track* trigger candidates are characterized by only hadrons in the final states, because of this they are also called *hadronic modes*.

In the rest of the thesis we will explicitly distinguish three different periods of data tacking; this is mainly because of the running conditions changed a lot in time and especially for the Particle IDentification devices, different calibrations and parameterization of the resolution functions have to be applied. The three periods, indicated respectively by the suffix *0d, 0h and 0i*, consist respectively of an integrated luminosity of 360 pb^{-1}, 410 pb^{-1} and 270 pb^{-1}. In the rest of the manuscript we will use the same notation, resumed in Tab.5.1, used at CDF to indicate each dataset for each running period.

	Integrated Luminosity	Hadronic modes	J/ψ modes
Period 1	360 pb^{-1}	xbhd0d	xpmm0d
Period 2	410 pb^{-1}	xbhd0h	xpmm0h
Period 3	270 pb^{-1}	xbhd0i	xpmm0i

Table 5.1: Datasets used in this analysis for each data taking period both for hadronic and J/ψ modes.

5.1.1 Trigger Path

Two different trigger paths are used to collect the B fully reconstructed decays: the *di−muon* trigger and the *two−track* trigger. Both are triggers based on the requirement of some conditions on charged tracks. In the rest of the thesis we will refer to those tracks as *trigger tracks*.

We will now briefly describe the two triggers strategies.

Di−Muon Trigger

The di−muon trigger path is used for selecting decay channels with J/ψ mesons in the final state. Muons are particles relatively clean to to be identified and the requirements of two opposite charge muons with an invariant mass close to the J/ψ mass already

provides a clear J/ψ signal. The di−muon triggers is a combination of the CMU−CMU and the CMU−CMX triggers, where CMU−CMU/CMX indicates that the first muon is always from the central muon system and the other is or again from the CMU or from the Central eXtention Muon system (for CMU and CMX description refer to chapter 3). The conditions required at each trigger level are:

1. Level 1
   - two XFT tracks with opposite charge;
   - each track is matched with two muon stubs;
   - each CMU (CMX) muon has $P_T^{XFT} > 1.5\ GeV/c$;
   - $\Delta\phi_6$(CMU,CMU) $< 135^o$;
   - no cut is applied in $\Delta\phi_6$(CMU,CMX);

1. Level 2
   - no requirements

1. Level 3
   - confirmation of Level 1 cuts on the fully reconstructed tracks (3−D offline quality);
   - $2.7 < M_{\mu\mu} < 4\ GeV/c$,

where $M_{\mu\mu}$ is the di−muon pair invariant mass. In addition, we require at least 3 $r-\phi$ hits in the silicon detector for both tracks.

Level 1 requirements are essentially based on the presence of two opposite charge tracks reconstructed, in the transverse plane, using the drift chamber (COT) information by the Level 1 processor XFT (see previous chapters for details). Those tracks are matched to the muon system information and kinematic cuts are then applied using XFT quantities. No selection is applied at level 2, while level 3 confirms Level 1 requirements on offline quality quantities; an invariant mass cut on the track couple is finally applied to focus on the J/ψ mass range.

Two−Track Trigger

For the first time at hadron collider's detector, a Level 2 trigger processor, the Silicon Vertex Tracker (SVT, see previous chapters) allows to select the long-lived heavy flavor particles by cutting on the track impact parameter with a precision similar to that achieved by the full event offline reconstruction. This strategy allows to select and collect huge samples of fully reconstructed heavy flavor events without the specific requirement of leptons in the final states. The two−track trigger is mainly used for the collection of the so called *hadronic modes*. The conditions required at each trigger level are:

1. Level 1

- two XFT tracks with opposite charge;
- each track has at least 4 XFT layers with hits;
- each track has $P_T^{XFT} > 2.04$ GeV/c;
- $\sum P_T^{XFT} > 5.5$ GeV/c;
- $0^o < \Delta\phi_6 < 135^o$;

1. Level 2

- each track is required to matched by the SVT;
- for each track $100\mu\text{m} \leq |d_0^{SVT}| \leq 1$ mm;
- each track has $P_T^{SVT} > 2.0$ GeV/c;
- $\sum P_T^{SVT} > 5.5$ GeV/c;
- $2^o < \Delta\phi_0 < 90^o$;

1. Level 3

- $|\Delta z_0| < 5$ cm;
- two−track vertex $L_{xy} > 200\mu$m;

where P_T^{XFT} is the transverse momentum as measured by the Level 1 processor XFT and $\Delta\phi_6$ is the opening angle at super−layer 6 of the COT, d_0^{SVT} is the impact parameter as measured in the SVT, Δz_0 is the distance between the two tracks along the beam axis and L_{xy} is the distance, in the transverse plane, of the two−tracks vertex with respect to the primary vertex.

Also for the two−track trigger, Level 1 requirements are based on the processor XFT; in this case kinematic cuts are more selective respect to the di−muon trigger due to the absence of additional information from the muon detectors. The novelty is the possibility, exploited at Level 2 by the SVT, to apply requirements on the impact parameter of the tracks (long−lived particle decay products are expected to have impact parameters respect to the interaction vertex significantly different from zero).

5.1.2 Offline Reconstruction and Selection

CDF II has a limited particle identification capability and therefore the candidate reconstruction strategy is based only on tracking information: tracks are assigned pion or kaon mass hypotheses and combined together to form meson candidates.

Candidates for each particle decay tree are reconstructed according a *bottom−up* strategy. This means that, for example, in the case of $B^+ \to \overline{D}^0 \pi^+$, $\overline{D}^0 \to K^+\pi^-$, at first we look for a track pair vertex that is compatible with a $\overline{D}^0$ decay, typically, to suppress the combinatorial background, the invariant mass of the track pair is required to lie in a mass range centered in the D^0 mass; we then combine the given D candidate with an additional charged track (new vertex) to reconstruct a new candidate compatible with a $B^+ \to \overline{D}^0 \pi^+$ decay. To make up higher level candidates

like $B, J/\psi, K^{*0} or D$, tracks are fitted to a secondary vertex applying mass and pointing constraints, at the same time they are forced to comply with the proper vertex topology.

From this secondary vertex fits we can extract higher level information regarding the candidates. Considering again the $B^+ \to \overline{D}^0 \pi^+$, $\overline{D}^0 \to K^+\pi^-$, Fig.5.2 left, the corresponding topology has a two−prong ($\overline{D}^0 \to K^+\pi^-$) vertex and a single displaced track, the B meson daughter pion, π_B; the following quantities are available to select such decays: mass, transverse decay−length L_{xy}, transverse impact parameter d_0 of the higher level candidates (B and D), $\chi^2_{r-\phi}$ of both D and B meson vertex fits, transverse momenta P_T of both D and B mesons, the significance of the transverse decay−length $L_{xy}/\sigma_{L_{xy}}$ of the D and B mesons with respect to the primary interaction vertex, the displacement in the transverse plane $L_{xy}^{B\to D}$ of the D meson vertex with respect to the B meson vertex, the transverse momentum of the B meson daughter pion $P_T(\pi_B)$, the $\Delta R(D,\pi_B) \equiv \sqrt{\Delta\phi(D,\pi_B)^2 + \Delta\eta(D,\pi_B)^2}$ between the D meson and the B daughter pion, and the B meson impact parameter with respect to the primary vertex, $d_0(B)$.

Similar quantities are available also for J/ψ modes, keeping in mind that the corresponding topology is characterized by a *single* three−prong or four−prong secondary vertex due to the B meson decay and no additional secondary vertex due to B daughters decay is expected as shown in Fig.5.1.

Because candidate reconstruction is track based, special care is taken to ensure that the used tracks are of high quality. We therefore apply track quality requirements on the trigger tracks and the other tracks of the event, so that the track parameters and their error estimates are accurate. A very simple way to reduce the number of fake tracks is to require a minimum number of hits in the drift chamber and in the silicon detector.

After candidates have been reconstructed, additional cuts are applied in order to achieve an *optimized selection* of the final sample and further reduce the combinatorial background. The goal of an optimization procedure is maximizing or minimizing a certain variable (depending on the analysis being performed). We aim for the measurement of particle species fractions produced in association with B mesons in order to better understand the flavor tagging of the B mesons for B mixing and time−dependent CP violation measurement. We then decided to apply the same cuts used in [57] where a data−Monte Carlo comparison is performed in order to develop a Same Side Kaon Tagging algorithm for B_s mixing measurement. Those cuts are selected in order to optimize the figure of merit $S/\sqrt{S+B}$, that is strictly related to the B_s oscillation significance through the equation [3]:

$$\mathcal{S}(\Delta m_s) = \frac{S}{\sqrt{S+B}} \sqrt{\frac{\epsilon \mathcal{D}^2}{2}} e^{-\frac{1}{2}\sigma_{ct}^2 \Delta m_s^2} \tag{5.1}$$

Where S and B are the number of signal and background events respectively; ϵ is the probability to get an answer from the tagging algorithm about the flavor of the B meson; $\mathcal{D}$ is the dilution of the flavor tagging algorithm defined as $1 - 2P_{wrong}$ (P_{wrong} is the probability that the algorithm wrongly identifies the flavor of the B); σ_{ct} is the proper time resolution.

Tabs.5.2 and 5.3 summarize the list of selections respectively for J/ψ modes and hadronic modes.

		$B^+ \to J/\psi\, K^+$	$B^0 \to J/\psi\, K^{*0}$	$B_s \to J/\psi\, \phi$
Min B vtx prob		0.001	0.0001	0.001
Max $\chi^2_{xy}(B)$		–	225	225
Min $P_T(B)$	[GeV/c]	5	5	4
Min $L_{xy}/\sigma_{L_{xy}}(B)$		4.5	4.5	3
Max $\sigma_{L_{xy}}(B)$	[cm]	0.04	0.04	0.04
Min $P_T(K^+, K^{*0}, \phi)$	[GeV/c]	1	1	1
Max $\lvert m(K\pi) - M_{K^*}\rvert$	[MeV/c^2]	–	50	–
Max $\lvert m(KK) - M_\phi\rvert$	[MeV/c^2]	–	–	10

Table 5.2: List of selection cuts for the J/ψ modes.

		$B^+ \to \overline{D}^0\, \pi^+$	$B^0 \to D^-\, \pi^+$	$B_s \to D_s^-\, \pi^+$
Max $\chi^2_{xy}(B)$		15	15	15
Min $P_T(B)$		5.5	5.5	5.5
Min $L_{xy}/\sigma_{L_{xy}}(B)$		8	11	7
Max $\sigma_{L_{xy}}(B)$	[cm]	–	–	0.04
Max $\lvert d_0(B)\rvert$	[cm]	0.008	0.011	0.006
Max $\chi^2_{xy}(D)$		15	15	14
Min $L_{xy}/\sigma_{L_{xy}}(D)$		–	–	2
Min $D_{xy}(B \leftarrow D)$	[cm]	-0.015	-0.03	-0.02
Min $P_T(\pi_B)$	[GeV/c]	1	1.2	1.2
Max $\Delta R(D, \pi_B)$		2	1.5	–
Max $m(KK)$	[MeV/c^2]	–	–	$[1.013, 1.028]$

Table 5.3: List of selection cuts for the hadronic modes.

5.2 B candidates yield estimation

To estimate the sample composition and the B meson yield we perform an unbinned maximum likelihood fit on the reconstructed invariant mass distribution of the candidates. We decide to setup such a fit not only to estimate the yield of our B samples, but mainly because, as we will see in next chapters, it is the basis for the particle factions fit in order to separate signal from background contributions.

This procedure requires to properly model the signal and the background contributions to the invariant mass spectrum. Signal decays, that are fully reconstructed and recognized identifying a resonance peak in the invariant mass distribution, are expected to distribute according to a Gaussian function centered at the nominal B meson mass with a width depending on the detector characteristics. At CDF mass resolutions of B mesons are found to be $\sigma_m \approx 10 - 20$ MeV/c^2. On the other hand, both J/ψ

and, in particular, hadronic modes present a non trivial structure in the mass region close to the signal resonance. Therefore an effort has been done to understand which are the dominant contributions to the background and how these contribution can be described. Three sources of background can be defined:

1. The main background source at CDF is due to B meson candidate formed with at least one track not coming from a B decay. The track kinematics fakes a B meson daughter tracks to produce background that spans along a wide mass region, signal region included.

2. In smaller amount, partially reconstructed $b-$hadrons are sources of background. In the decay chains of these $b-$hadrons, neutral particles, that cannot be reconstructed by tracking system, can be produced; at the same time the invariant mass of the remaining $b-$hadron daughter tracks happens to be close enough to our signal region. The same effect can happen when a charged daughter of such $b-$hadrons has been missed by the tracking system due to inefficiency. These partially reconstructed backgrounds lie at lower mass region then the signal due to the missing energy of the lost daughter track.

3. The last background source corresponds to mis$-$reconstructed B meson decays where a particle has been wrongly identified, i.e., a kaon has been identified as a pion. Due to the relative small mass difference among the possible $b-$hadron daughter tracks when compared to the momentum of such particles, this background source tends to lie in the signal region.

Along this thesis we will refer to the first background as *combinatoric background* and the last two sources will be called *physics background* because they are real $b-$hadrons.

In next sections we will describe in detail the procedure and the set-upping of the unbinned maximum likelihood fits for each decay mode; however, for simplicity, in Tab.5.4, the estimated yields on the combination of the three dataset periods for each decay mode are reported.

Channel	Secondary Decays	yield
$B^+ \to J/\psi\, K^+/\pi^+$	$J/\psi \to \mu^+\mu^-$	18302 ± 267
$B^0 \to J/\psi\, K^{*0}$	$J/\psi \to \mu^+\mu^-$, $K^{*0} \to K^+\pi^-$	7564 ± 135
$B_s^0 \to J/\psi\, \phi$	$J/\psi \to \mu^+\mu^-$, $\phi \to K^+K^-$	1329 ± 49
$B^+ \to \overline{D}^0\, \pi^+$	$\overline{D}^0 \to K\pi$	30005 ± 272
$B^0 \to D^-\, \pi^+$	$D^- \to K^+\pi^-\pi^-$	25801 ± 277
$B_s \to D_s\, \pi$	$D_s \to \phi\pi$, $\phi \to K^+K^-$	1510 ± 52

Table 5.4: Estimation of the yield of each decay mode considered in this thesis; numbers refer to the combination of the three data taking periods.

5.2.1 J/ψ modes

An extensive study of the J/ψ modes mass spectra has been performed in [58] using Monte Carlo samples. In Fig.5.3 all the contributions to the mass spectra are shown (with the exception of the combinatoric background): it is evident that the mass range can be chosen to avoid a large amount partially reconstructed decays. In particular, we fitted the $B^+ \to J/\psi\, K^+$ and the $B^0 \to J/\psi\, K^{*0}$ spectra in the mass range $(5.18-5.39)$ GeV/c while for the $B_s \to J/\psi\, \phi$ spectrum we focused on the mass range $(5.27-5.47)$ GeV/c.

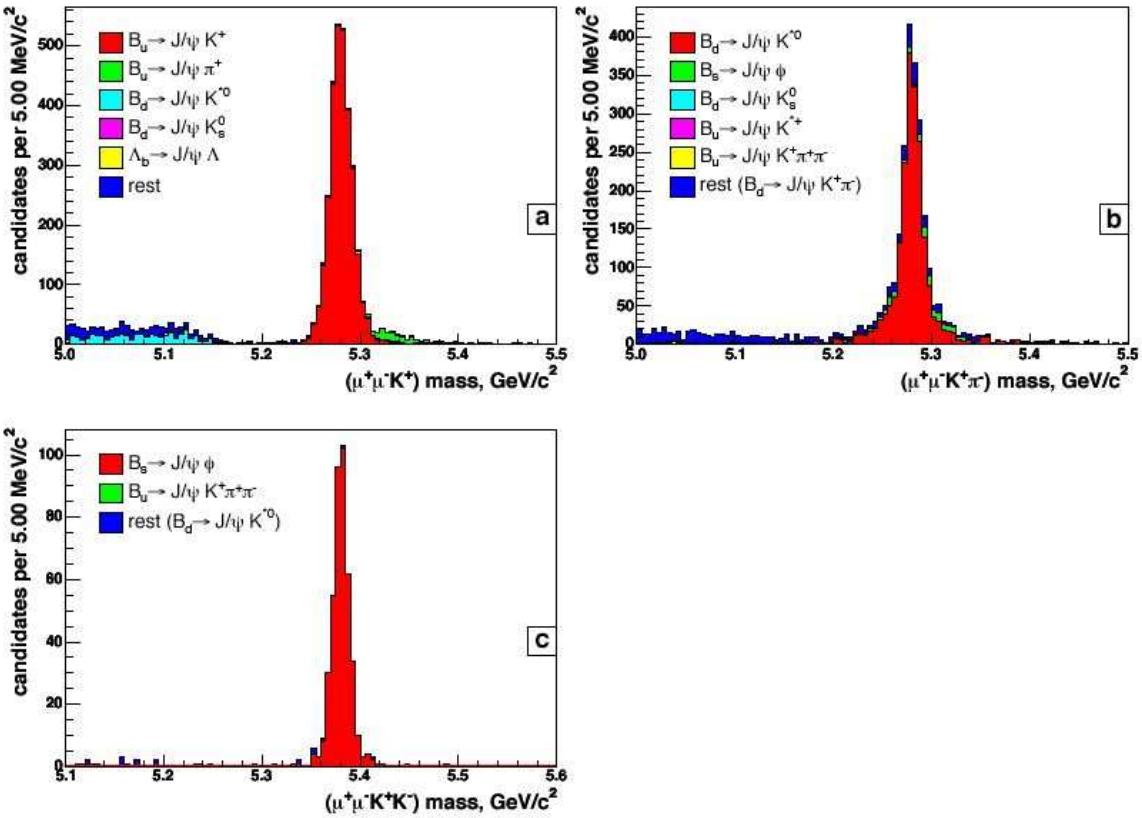

Figure 5.3: Mass spectrum when reconstructing the $B^+ \to J/\psi\, K^+$ (a), $B^0 \to J/\psi\, K^{*0}$ and $B_s \to J/\psi\, \phi$ decay in the $b \to J/\psi X$ Monte Carlo.

In the case of the $B^+ \to J/\psi\, K^+$, after applying the selection on the mass range, the only significant physics background is represented by the $B^+ \to J/\psi\pi$ decay, this contribution is parameterized by Monte Carlo.

For the $B^0 \to J/\psi\, K^{*0}$ mode, again after the mass range selection, the main physics background contribution is due to the self−reflection caused by the swapping of the mass assignment $K \leftrightarrow \pi$ in the K^{*0} reconstruction; the mass template of this background is parameterized by Monte Carlo. As shown in [58], the $B_s \to J/\psi\, \phi$, $\phi \to K^+K^-$ with K^- assigned the π mass is strongly suppressed by the cut on the mass of the reconstructed K^{*0} (see Tab.5.2) and the reminder of this reflection is negligible.

Finally, the only significant component of the $B_s \to J/\psi\,\phi$ physics background, represented by $B^0 \to J/\psi\,K^{*0}$ with the K and π from the K^{*0} both reconstructed with K mass assignment, is negligible after the selection cut on reconstructed ϕ mass (see Tab.5.2).

$B^+ \to J/\psi\,K^+$ description

In the mass range considered, $(5.18, 5.39)$ GeV/c^2, three components are parameterized: the signal $B^+ \to J/\psi\,K^+$, the Cabibbo suppressed mode $B^+ \to J/\psi\,\pi^+$ and the combinatoric background. The signal is modeled with the sum of two Gaussians with the respective means fixed to be the same. The mass distribution of the $B^+ \to J/\psi\,\pi^+$ component is parametrized with a Gaussian plus an asymmetric Gaussian whose parameters are extracted by Monte Carlo and then fixed in the unbinned maximum likelihood fit. The combinatoric background is described with a first order polynomial. The templates used in the fit are listed for simplicity in Tab. 5.5.

The combinatoric background fraction $f_{\rm comb}$, the $B^+ \to J/\psi\,\pi^+$ fraction $f_{J/\psi\pi}$ and all shape parameters, with the exception of the $B^+ \to J/\psi\,\pi^+$ template, are floated as free parameters to be determined by the unbinned maximum likelihood fit.

Fit component	Template
$B^+ \to J/\psi\,K^+$	$f\,G(m;\mu,\sigma) + (1-f)\,G(m;\mu, r\,\sigma)$
$B^+ \to J/\psi\,\pi^+$	$G(m;\mu_1,\sigma_1) + r\,AG(m;\mu_2,\sigma_2^L,\sigma_2^R)$
Comb. bkg	$P_1(m;a,b)$

Table 5.5: Templates used in the mass fit of $B^+ \to J/\psi\,K^+$ mode. G is a Gaussian, while AG an asymmetric Gaussian and P_1 a first order polynomial.

Tab. 5.6 reports the fit result for the whole dataset (the combination of the three data taking periods).

Fig. 5.4 shows the invariant mass distributions with the corresponding fit projections superimposed for the three data taking periods and for the whole dataset. The corresponding estimated signal yield is also reported. The four fits have a goodness that can be quantified, respectively, $\chi^2/\text{ndf} = 66.8/70$ (prob = 59%), $\chi^2/\text{ndf} = 58.4/70$ (prob = 84%), $\chi^2/\text{ndf} = 66.7/70$ (prob = 59%), and $\chi^2/\text{ndf} = 61.7/70$ (prob = 84%).

Fit component	Fit parameter	Value
$B^+ \to J/\psi\,K^+$	μ	5.27858 ± 0.00011
	σ	0.00951 ± 0.00046
	r	1.800 ± 0.076
	f	0.732 ± 0.077
Comb. bkg	a	-17.0 ± 2.7
	b	102 ± 16
	$f_{J/\psi\pi}$	0.0341 ± 0.0097
	$f_{\rm comb}$	0.3135 ± 0.0091

Table 5.6: Mass fit result for the whole dataset. Parameters are defined in Tab. 5.5.

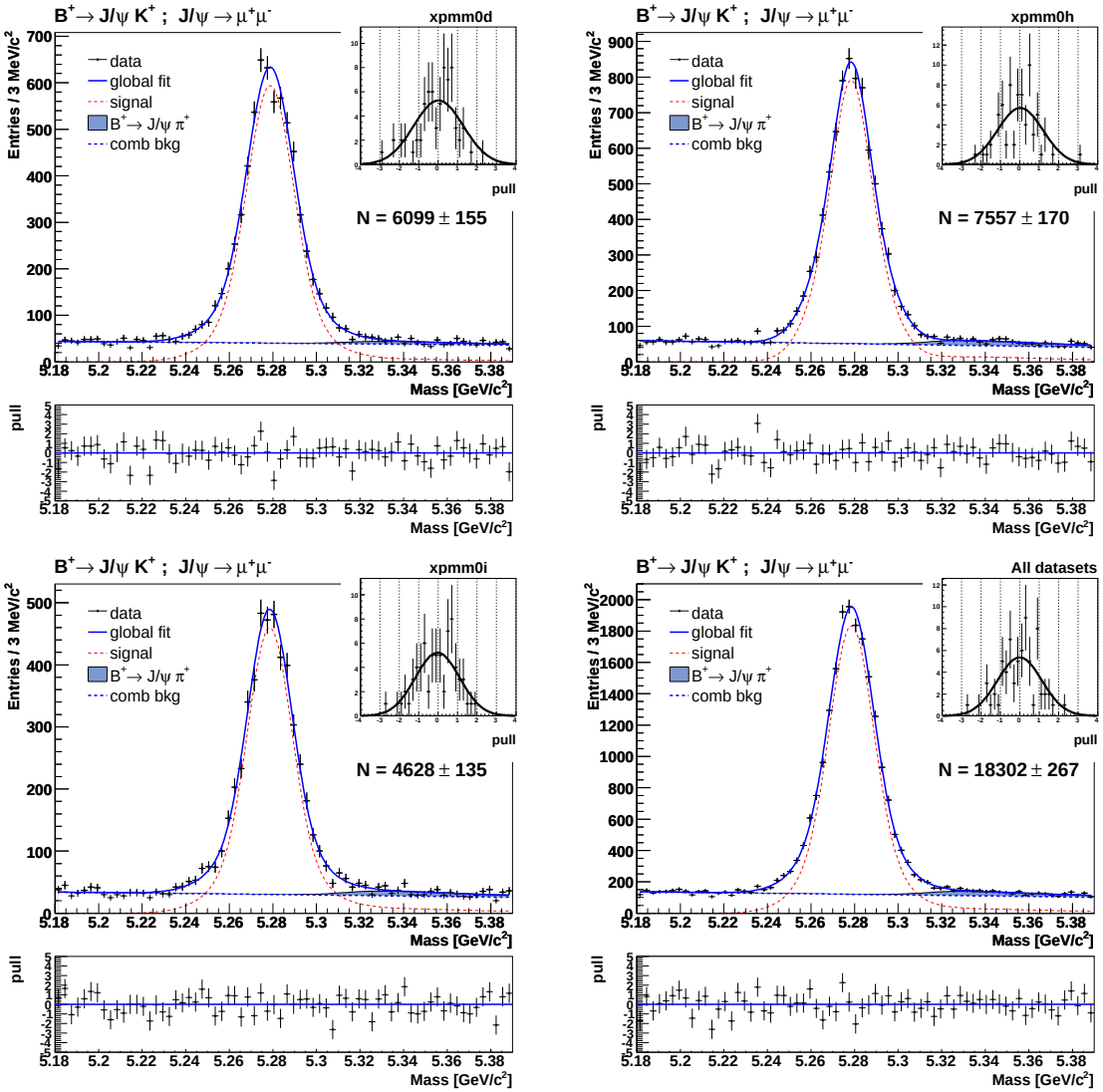

Figure 5.4: Mass fits for the $B^+ \to J/\psi\, K^+$ mode in different data-taking periods and for the whole dataset: xbhd0d (upper left), xbhd0h (upper right), xbhd0i (lower left), full dataset (lower right). The quoted yields include also the Cabibbo suppressed component $B^+ \to J/\psi\, \pi^+$, which lies under the upper tail of the signal peak.

$B^0 \to J/\psi\, K^{*0}$ description

The fit is performed in the mass region $(5.18, 5.39)$ GeV/c^2. Also in this case, three components are considered in the unbinned fit : the signal $B^0 \to J/\psi\, K^{*0}$, the combinatoric background and $B^0 \to J/\psi\, K^{*0}$ events which enter the mass window , although K^{*0}'s legs have been assigned the wrong mass hypothesis (swapped).

The signal contribution is parameterized by the sum of two Gaussians centered at the same mean while the combinatoric background is modeled with a first order

polynomial. The shape of the mass distribution of events with a swapped K^{*0} is fixed by Monte Carlo and is described by the sum of two Gaussians. Tab. 5.7 summarizes the functions used as templates of the fit.

Fit component	Template
$B^0 \to J/\psi\, K^{*0}$	$f\, G(m;\mu,\sigma) + (1-f)\, G(m;\mu, r\,\sigma)$
swapped K^{*0}	$f\, G(m;\mu,\sigma) + (1-f)\, G(m;\mu, r\,\sigma)$
Comb. bkg	$P_1(m;a,b)$

Table 5.7: Templates used in the mass fit of $B^0 \to J/\psi\, K^{*0}$ mode. G indicates a Gaussian, while P_1 is a first order polynomial.

Fit results corresponding to each floating parameter of the unbinned maximum likelihood fit are reported in Tab. 5.8, those results correspond to the fit using all the three data taking periods. The fraction of swapped K^{*0} has been fixed to 22.7% of the signal, as extracted by Monte Carlo.

Fit component	Fit parameter	Value
$B^0 \to J/\psi\, K^{*0}$	μ	5.27917 ± 0.00017
	σ	0.0065 ± 0.0015
	r	1.96 ± 0.17
	f	0.54 ± 0.24
Comb. bkg	a	-16.55 ± 0.60
	b	100.7 ± 3.7
	$f_{\rm comb}$	0.6058 ± 0.0065

Table 5.8: Mass fit result for the whole dataset. Parameters are defined in Tab. 5.7.

Fig. 5.5 shows the invariant mass distributions with the corresponding fit projections superimposed for the three different data taking periods and for the whole dataset. The corresponding estimated signal yield is also reported. The four fits have goodness that can be quantified, respectively, $\chi^2/\text{ndf} = 76.6/70$ (prob = 28%), $\chi^2/\text{ndf} = 44.5/70$ (prob = 99%), $\chi^2/\text{ndf} = 48.8/70$ (prob = 97%), and $\chi^2/\text{ndf} = 48.2/70$ (prob = 98%).

$B_s \to J/\psi\, \phi$ description

The $B_s \to J/\psi\, \phi$ mass spectrum is fitted in the mass region $(5.27, 5.47)$ GeV/c^2. The spectrum shows a quite simple structure: a signal peak over a flat combinatoric background. The signal is modeled with a Gaussian, while the background is parameterized again by a first order polynomial (Tab. 5.9).

Fit component	Template
$B_s \to J/\psi\, \phi$	$G(m;\mu,\sigma)$
Comb. bkg	$P_1(m;a,b)$

Table 5.9: Mass fit templates for $B_s \to J/\psi\, \phi$. G indicates a Gaussian, P_1 a first degree polynomial.

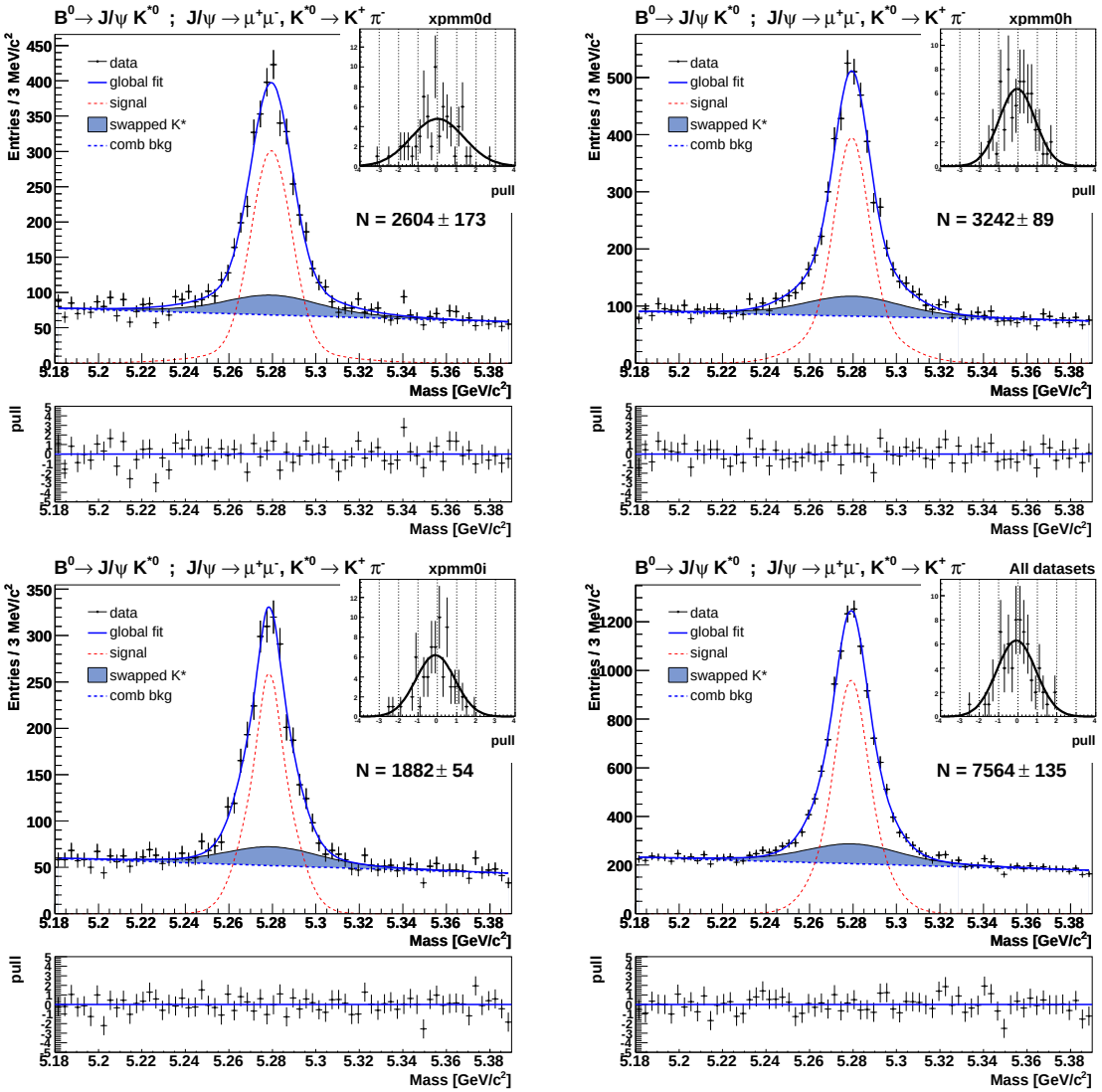

Figure 5.5: Mass fits for the $B^0 \to J/\psi\, K^{*0}$ mode in different data-taking periods and for the whole dataset: xbhd0d (upper left), xbhd0h (upper right), xbhd0i (lower left), full dataset (lower right).

All parameters are left free to be floated by the unbinned fit. The result on the whole dataset is reported in Tab. 5.10.

Fig. 5.6 shows the invariant mass distributions with the corresponding fit projections superimposed for each of the three data taking periods and for the whole dataset. The corresponding estimated signal yield is also reported. The four fits have goodness that can be quantified, respectively, $\chi^2/\text{ndf} = 57.0/50$ (prob = 23%), $\chi^2/\text{ndf} = 77.9/50$ (prob = 0.70%), $\chi^2/\text{ndf} = 31.1/50$ (prob = 98%), and $\chi^2/\text{ndf} = 49.7/50$ (prob = 48%).

Fit component	Fit parameter	Value
$B_s \to J/\psi\,\phi$	μ	5.36673 ± 0.00034
	σ	0.00871 ± 0.0034
Comb. bkg	a	-4.5 ± 2.1
	b	28 ± 13
	$f_{\rm comb}$	0.699 ± 0.010

Table 5.10: Mass fit result for the whole dataset. Parameters are defined in Tab. 5.9.

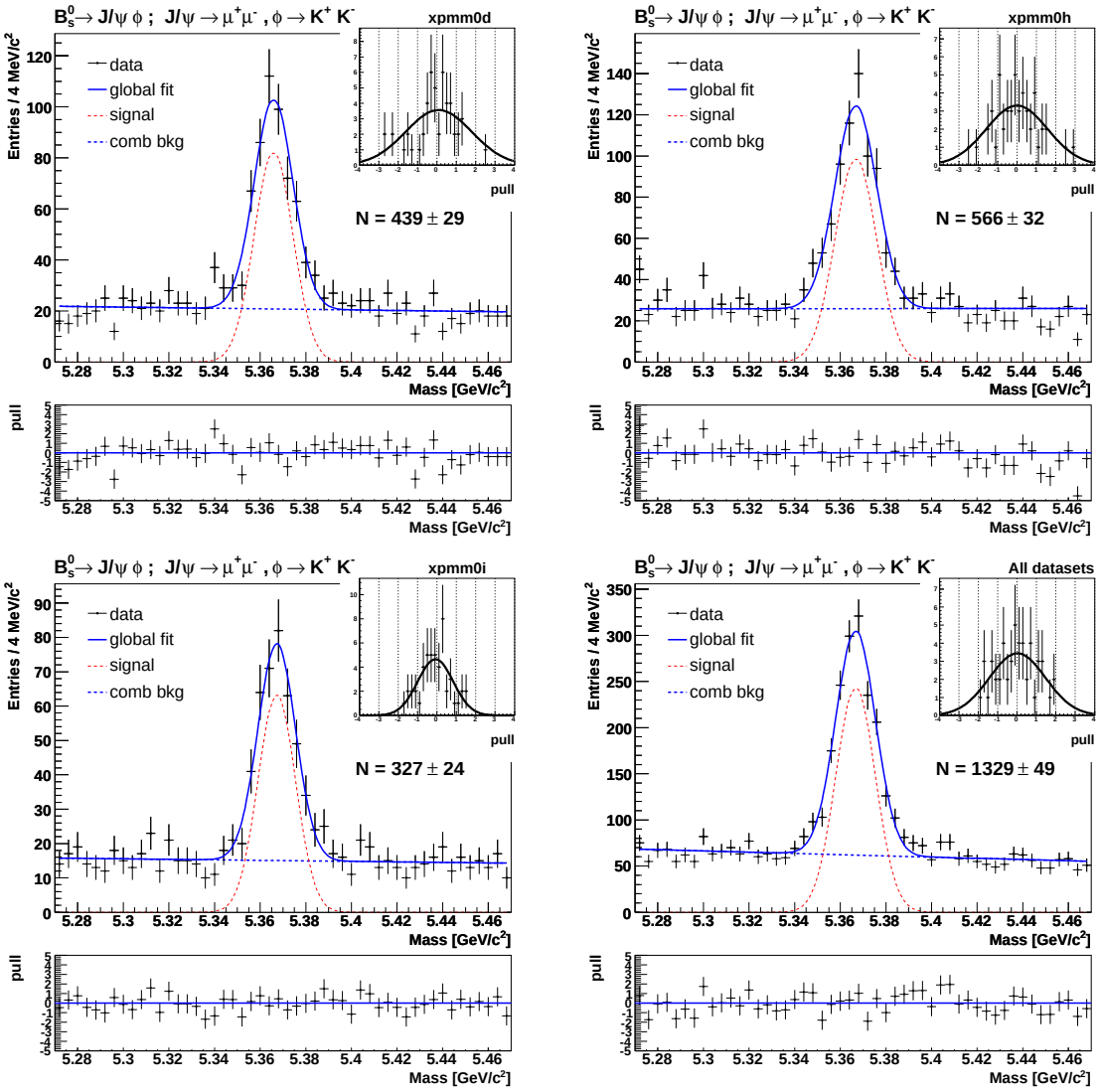

Figure 5.6: Mass fits for the $B_s \to J/\psi\,\phi$ mode: xbhd0d (upper left), xbhd0h (upper right), xbhd0i (lower left), full dataset (lower right).

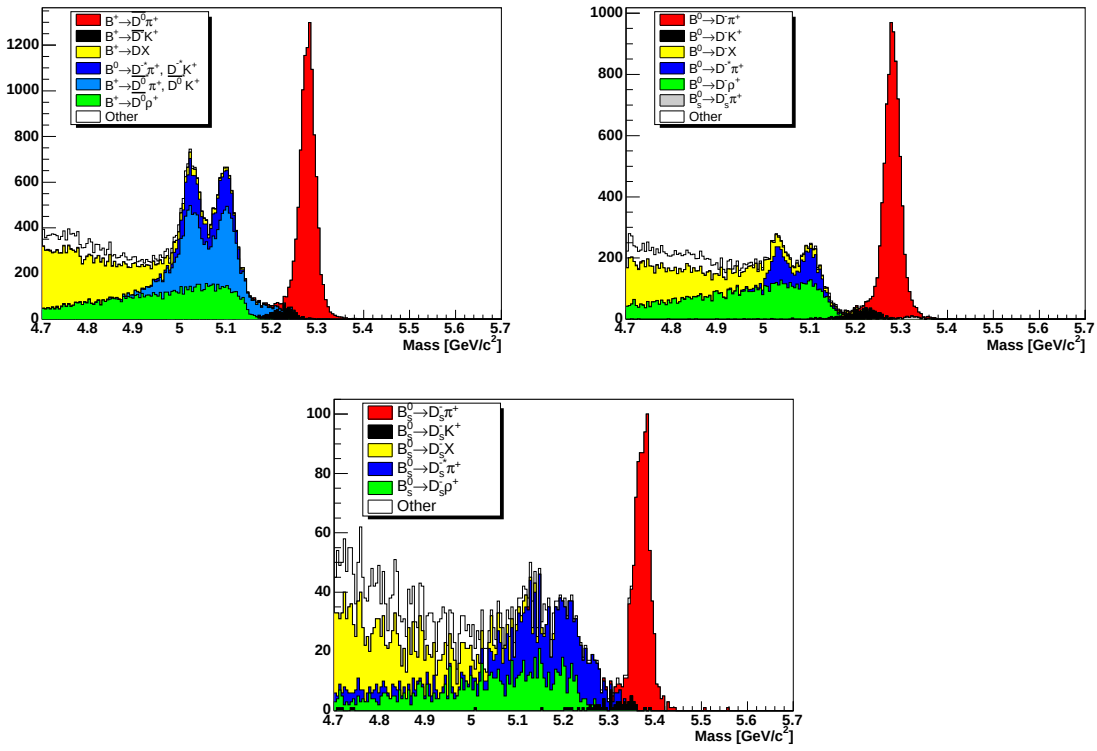

Figure 5.7: Inclusive Monte Carlo mass distributions for the three hadronic decay mode studied in this analysis. (upper left) $B^+ \to \bar{D}^0\pi^+$; (upper right) $B_d^0 \to D^-\pi^+$; (bottom) $B_s^0 \to D_s^-\pi^+$. Contributions from partially reconstructed B decays are also shown.

5.2.2 Hadronic modes

Hadronic signals collected within the two−track trigger present a complex structure in the mass region close to the signal resonance (see for example Fig.5.8). Therefore an effort have been done to understand which are the dominant contributions of the background an how those contributions can be described. A detailed description of such a study can be found in [59].

The resonance peaks close to the signal one suggest that most of the background is produced from B not completely reconstructed or with wrong mass assignment to the tracks. Then, to understand the B background contribution a sample of inclusive b decays is needed. For this purpose an inclusive Monte Carlo sample with a mixture of B mesons (38.9% B_u, 38.9% B_d, 10.7% B_s ,11.6% Λ_b) has been generated.

Figure 5.7 shows the mass distributions of the inclusive simulation for the five reconstructed decay modes.

These distributions, compared to the mass distributions obtained from data (Fig. 5.8), show that the partially reconstructed B mesons generate the complex structure at the low mass region with respect to the signal peak (the red one in the 5.7 plots). In all the cases the main contribution appears coming from decay modes involving the

excited state of D mesons ($D^\star$). In all the decay channels ($B_d^0 \to D^-\pi^+$; $B^+ \to \bar{D}^0\pi^+$; $B_s^0 \to D_s^-\pi^+$), the $D^\star$ modes are responsible for the double peak structure on the right side of the signal peak. In fact, when an excited D meson state is involved, it decays on a more stable D state emitting a neutral pion or a γ. Because the conservation of the angular momentum, the $D^\star$ meson comes from the B meson in a polarized state. Therefore the final D meson, in the presence of a γ emission, can carry only a quantized fraction of the total momentum, resulting in the *double-horn* structure in the low mass region.
Looking at the specific decay modes, the inclusive simulation help to determine the main contributions and classifying them.
In the $B^\pm$ mass distribution (Fig. 5.7 (upper left)) the dominant contribution is played by the excited D modes. Here an enhancement is provided by two different excited D modes, the charged ($D^{\star-}$) and the neutral one ($D^{\star 0}$). Both of them decay in a $D^0\pi$ mode, where the pion can be neutral or charged. Therefore reconstructing the $D^0\pi^\pm$ invariant mass distribution we get contamination from the $B^\pm \to D^{\star 0}\pi^\pm$ and also from the $B_d^0 \to D^{\star\pm}\pi^\mp$. Then, both the neutral and charged excited D generate the *double horn* phenomenon when a photon is lost, enhancing the resonant peaks close to the signal one. As for the other neutral modes a $D^0\rho^+$ contribution is present, but in this case it has been grouped with the D^0X continuum background to form a single mass template.
In the $B_d^0 \to D^-\pi^+$ mode the dominant contributions can be classified in the already quoted $D^{\star-}$ modes, where a neutral particle is lost during reconstruction, the $D^-\rho^+$ and the D^-X decay modes. $B_d^0 \to D^-\rho^+$ decay mode has a Branching ratio roughly 2 times bigger than the signal mode, therefore its contribution is supposed to be high when the D tracks fire the trigger. The $\rho^\pm$ resonance decay almost any times in a $\pi^0\pi^\pm$ modes, then the charged pion is reconstructed together with the charmed meson while the neutral pion is lost. Then the mass distribution of the $D^\mp + \pi^\pm$ appears as a smeared distribution at lower mass values with respect to the signal resonance (see Fig. 5.7 (upper right)). The D^-X mode (called also continuum) takes into account for all the B decays modes not involving the signal, the Cabibbo suppressed D^-K^+ and the previous $D^-\rho^+$ modes. Therefore it includes also the semileptonic modes, which do not contribute in a significant way, and all other multi bodies modes. Within these contributions there isn't any dominant decay mode, therefore they have been grouped together. Finally $B_s^0 \to D_s^-\pi^+$ contamination, even if almost negligible, is present in the high mass region under the signal peak and has been taken into account.
The $B_s^0 \to D_s^-\pi^+$ mode presents the same dominant contribution observed in the B_d^0 case. $D_s^{\star-}\pi^+$ and $D_s^-\rho^+$ contributions are the main decay modes. Anyway in this case the statistic is not enough to clearly distinguish the *double-horn* structure from the excited D_s state, therefore the mass distribution of the $D_s^{\star-}\pi^+$ contamination appears like a smeared Gaussian close to the signal peak. The $D_s^-\rho^+$ contribution is similar to what has been seen in the B_d^0 case (see Fig. 5.7 (bottom)). Finally residual D_s^-X modes have been collected within a single group and used to create a single template. Templates for all physical background have been defined in Monte Carlo samples. We used the same functional forms as in [60], but we determined again the parameters by

refitting the distributions given by our event selection.

$B^+ \to \overline{D}^0 \pi^+$ description

The components considered in the unbinned fit, are the signal $B^+ \to \overline{D}^0 \pi^+$, the Cabibbo suppressed decay $B^+ \to \overline{D}^0 K^+$, the combinatoric background and the physics backgrounds, given by partially reconstructed B mesons with a D in the final state. As already mentioned, the main component of the physical backgrounds is $B \to D^* \pi$.

Tab. 5.11 lists the mass templates used in the fit for each component. The signal and the Cabibbo suppressed mode are parameterized with the sum of two Gaussians. The two-peak structure of the $B \to D^* \pi$ component is modeled with a central Gaussian plus two narrower Gaussians symmetrically disposed around the central Gaussians. The generic $b \to DX$ background is modeled with a negative slope straight line, dumped by an error function. The combinatoric background is described by an exponential function plus a constant.

Fit component	Template
$B^+ \to \overline{D}^0 \pi^+$	$f\, G(m;\mu,\sigma) + (1-f)\, G(m;\mu, r\,\sigma)$
$B^+ \to \overline{D}^0 K^+$	$f\, G(m;\mu,\sigma) + (1-f)\, G(m;\mu, r\,\sigma)$
$B \to D^* \pi$	$(1-f)G(m;\mu;\sigma_1) + \frac{f}{2}G(m;\mu-\delta;\sigma_2) + \frac{f}{2}G(m\ ;\mu+\delta;\sigma_2)$
$b \to D\, X$	$(1 - s(m-c))\,\mathrm{erfc}(\frac{m-\mu}{\sigma})$
Comb. bkg	$(1-f)\, e^{-s(m-\mu)} + f\, P_0(m;a)$

Table 5.11: Mass fit templates for $B^+ \to \overline{D}^0 \pi^+$.

The combinatoric background fraction ($f_{\rm comb}$), the $B \to D^* \pi$ fraction ($f_{D^*\pi}$) and the relative fraction of $b \to DX$ to $B \to D^* \pi$ (κ_{DX}) are left to be floated by the fit along with the template parameters reported in Tab. 5.12. The $B^+ \to \overline{D}^0 K^+$ fractions is fixed at 6.5 % (according what found in Monte Carlo). Tab. 5.12 also shows the parameters values at the convergence point.

Fig. 5.8 shows the invariant mass distributions with the corresponding fit projections superimposed for the three data taking periods and for the whole dataset. The corresponding estimated signal yield is also reported. The four fits have goodness that can be quantified, respectively, $\chi^2/\mathrm{ndf} = 148.6/130$ (prob = 12%), $\chi^2/\mathrm{ndf} = 191.1/130$ (prob = 0.04%), $\chi^2/\mathrm{ndf} = 187.0/130$ (prob = 0.08%), and $\chi^2/\mathrm{ndf} = 278.5/130$ (prob $= 10^{-12}$%).

Fit component	Fit parameter	Value
$B^+ \to \overline{D}^0 \pi^+$	μ	5.27800 ± 0.00014
	σ	0.01508 ± 0.00065
	r	1.86 ± 0.12
	f	0.784 ± 0.072
$B \to D^* \pi$	f	0.8667 ± 0.0098
	μ	5.06182 ± 0.00026
	δ	0.03676 ± 0.00025
	σ_2	0.01791 ± 0.00034
Comb. bkg	f	0.087 ± 0.026
	s	2.67 ± 0.11
	a	107 ± 32
	f_{comb}	0.4143 ± 0.0098
	$f_{D^*\pi}$	0.1557 ± 0.0021
	κ_{DX}	1.861 ± 0.080

Table 5.12: Mass fit result for the whole dataset. Parameters of each fit component are defined in Tab. 5.11.

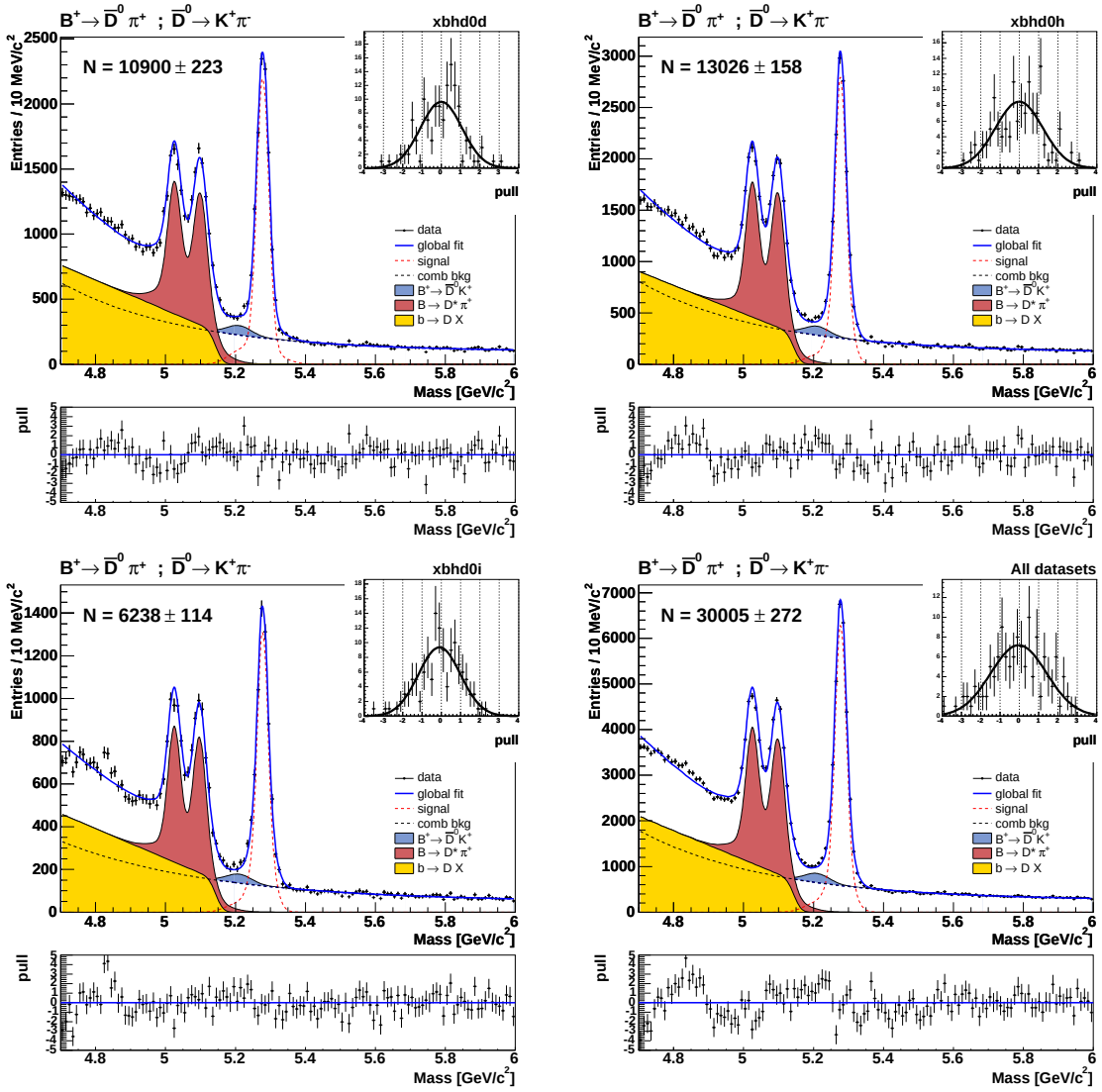

Figure 5.8: Mass projections of the $B^+ \to \overline{D}^0 \pi^+$ fit: xbhd0d (upper left), xbhd0h (upper right), xbhd0i (lower left), full dataset (lower right). The quoted yields include also the Cabibbo suppressed mode $B^+ \to \overline{D}^0 K^+$.

$B^0 \to D^- \pi^+$ description

The components considered in the unbinned fit, are the signal , given by $B^0 \to D^- \pi^+$ and the Cabibbo-suppressed mode $B^0 \to D^- K^+$, the reflections $B_s \to D_s^- \pi^+$, $D_s^- \to \phi\pi^-$ and $\Lambda_b \to \Lambda_c^- \pi^+$, $\Lambda_c^- \to \bar{p} K^- \pi^+$ which present the same topology as the signal and enter the signal mass region (when reconstructed with wrong mass assignments to the tracks) , the partially reconstructed decays $B \to D^* \pi$, $B \to D \rho$, and $b \to D X$, and finally the combinatoric background.

Fit component	Template
$B^0 \to D^- \pi^+$	$f\, G(m;\mu,\sigma) + (1-f)\, G(m;\mu, r\,\sigma)$
$B^0 \to D^- K^+$	$e^{s(m-c)}\,\mathrm{erfc}(\frac{m-\mu}{\sigma})$
$B_s \to D_s^- \pi^+$	$AG(m;\mu,\sigma^L,\sigma^R)$
$\Lambda_b \to \Lambda_c \pi^+$	$f\, AG(m;\mu_1,\sigma_1^L,\sigma_1^R) + (1-f)\, AG(m;\mu_2,\sigma_2^L,\sigma_2\ ^R)$
$B \to D^* \pi$	$(1-f)G(m;\mu;\sigma_1) + \frac{f}{2}G(m;\mu-\delta;\sigma_2) + \frac{f}{2}G(m;\ \mu+\delta;\sigma_2)$
$B \to D \rho$	$e^{s(m-c)}\,\mathrm{erfc}(\frac{m-\mu}{\sigma})$
$b \to D X$	$\frac{2}{(a-b)^2}\,(a-m)$
Comb. bkg	$(1-f)e^{-s(m-\mu)} + fP_0(m;1)$

Table 5.13: Mass fit templates for $B^0 \to D^- \pi^+$.

The functions used to parameterized each component in the mass fit are listed in Tab. 5.13. We use the sum of two Gaussians for $B^0 \to D^- \pi^+$, an exponential tail dumped by the complementary error function for $B^0 \to D^- K^+$ and $B \to D \rho$. The B_s and Λ_b components are modeled with an asymmetric Gaussian and the sum of two asymmetric Gaussians, respectively. $B \to D^* \pi$ presents the characteristic two-horn shape like in the case of B^+ and is parameterized by three Gaussians. The continuum $b \to D X$ background is described by a straight line with a cutoff at 5.15 GeV/c^2, the combinatoric background by a exponential plus a constant.

The parameters floated in the fit are shown in Tab. 5.14. $f_{\rm comb}$ and $f_{D^*\pi}$ are the fractions of combinatoric background and $B \to D^* \pi$ events. $\kappa_{D\rho}$ and κ_{DX} are the relative fractions of $B \to D \rho$ and $b \to D X$ with respect to $B \to D^* \pi$. B_s and Λ_b fraction are fixed at 0.8% and 4.5% with respect to the signal (based on what found in MC).

Fig. 5.9 shows the invariant mass distributions with the corresponding fit projections superimposed for the three data taking periods and for the whole dataset. The corresponding estimated signal yield is also reported. The four fits have goodness that can be quantified, respectively, χ^2/ndf = 137.3/130 (prob = 31%), χ^2/ndf = 153.9/130 (prob = 7.5%), χ^2/ndf = 155.6/130 (prob = 6.3%), and χ^2/ndf = 210.0/130 (prob = 10^{-3}%).

Fit component	Fit parameter	Value
$B^0 \to D^- \pi^+$	μ	5.27856 ± 0.00016
	σ	0.01572 ± 0.00036
	r	2.45 ± 0.13
	f	0.852 ± 0.022
$B \to D^* \pi$	μ	5.06617 ± 0.00095
Comb. bkg	f	0.341 ± 0.019
	s	2.99 ± 0.10
	f_{comb}	0.506 ± 0.013
	$f_{D^*\pi}$	0.0320 ± 0.0025
	$\kappa_{D\rho}$	5.45 ± 0.60
	κ_{DX}	3.65 ± 0.39

Table 5.14: Results of the mass fit for the whole dataset. Parameters of each fit component are defined in Tab. 5.13.

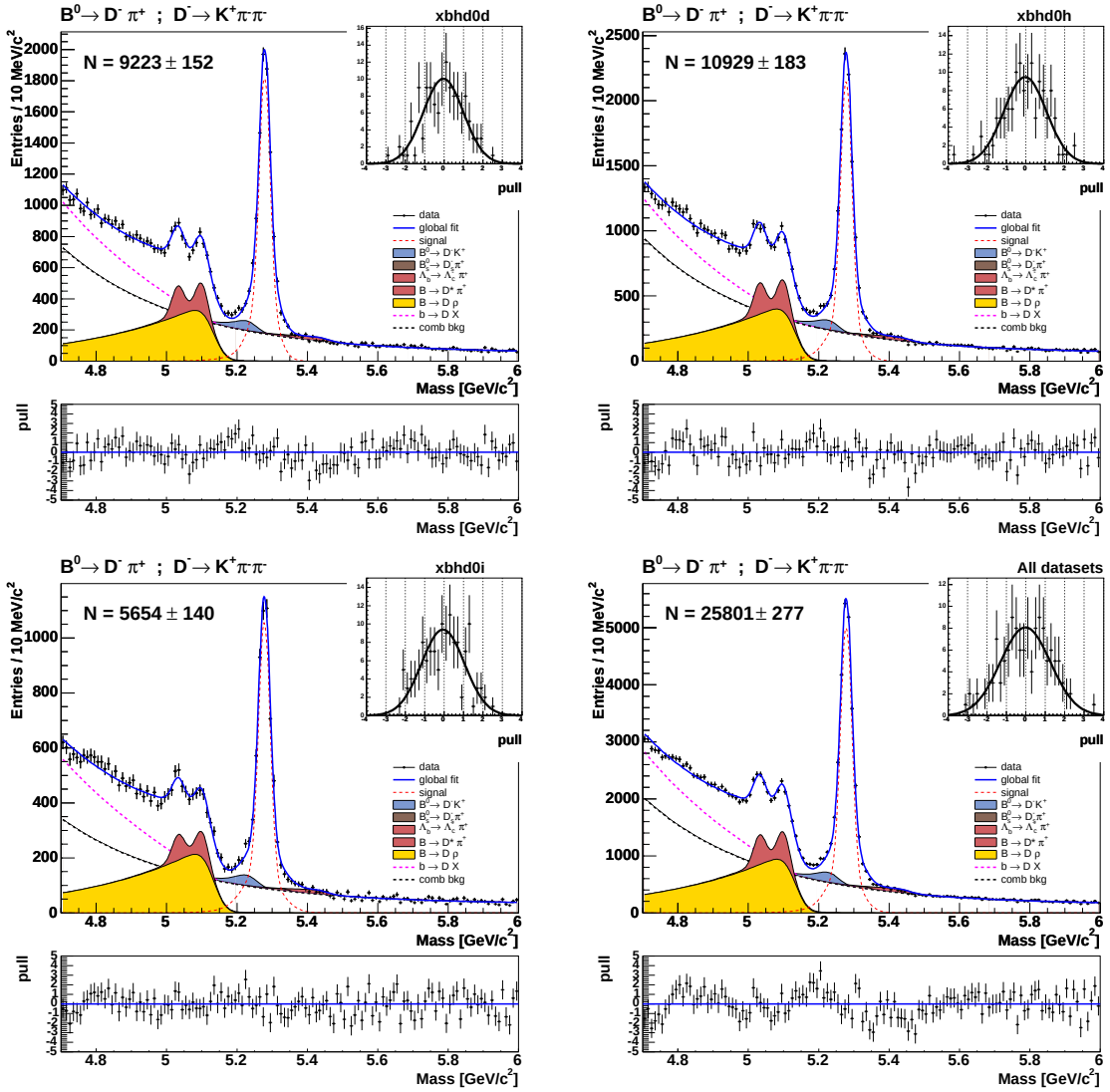

Figure 5.9: Mass fits for the $B^0 \to D^- \pi^+$ mode: xbhd0d (upper left), xbhd0h (upper right), xbhd0i (lower left), full dataset (lower right).

$B_s \to D_s^- \pi^+$ description

Finally, in the unbinned fit of the invariant mass spectra of the $B_s \to D_s^- \pi^+$candidates we consider: the signal ($B_s \to D_s^- \pi^+$ and $B_s \to D_s^- K^+$), the partially reconstructed $B_s \to D_s^* \pi$, $B \to D \rho$, and $b \to D X$, and the combinatorial background.

$B_s \to D_s^- \pi^+$ is parameterized by the sum of two Gaussians, $B_s \to D_s^- K^+$ by an asymmetric Gaussian, $B_s \to D_s^* \pi$ by a single Gaussian, $B \to D \rho$ by an exponential multiplied by the complementary error function, $b \to D X$ by a straight line, and the combinatoric background by an exponential plus a first order polynomial (see Tab. 5.15).

Fit component	Template
$B_s \to D_s^- \pi^+$	$f\, G(m;\mu,\sigma) + (1-f)\, G(m;\mu, r\,\sigma)$
$B_s \to D_s^- K^+$	$AG(m;\mu,\sigma^L,\sigma^R)$
$B_s \to D_s^* \pi$	$G(m;\mu,\sigma)$
$B \to D \rho$	$e^{s(m-c)}\,\mathrm{erfc}(\frac{m-\mu}{\sigma})$
$b \to D X$	$\frac{2}{(a-b)^2}\,(a-m)$
Comb. bkg	$(1-f)\, e^{-s(m-\mu)} + f\, P_0(m;1)$

Table 5.15: Mass fit templates for $B_s \to D_s^- \pi^+$.

The signal and $f_{D_s^*\pi}$ fractions are left free to be floated by the fit. Tab. 5.16 reports the result for the combination of the three data taking periods.

Fit component	Fit parameter	Value
$B_s \to D_s^- \pi^+$	μ	5.36706 ± 0.00064
	σ	0.0132 ± 0.0019
	r	2.05 ± 0.21
	f	0.66 ± 0.15
$B_s \to D_s^* \pi$	μ	5.1597 ± 0.0032
Comb. bkg	f	0.30 ± 0.01
	s	1.99 ± 0.24
	f_{sig}	0.1298 ± 0.0043
	$f_{D_s^*\pi}$	0.1976 ± 0.0083

Table 5.16: Mass fit result for the whole dataset. Parameters of each fit component are defined in Tab. 5.15.

Fig. 5.10 shows the invariant mass distributions with the corresponding fit projections superimposed for the three data taking periods and for the whole dataset. The corresponding estimated signal yield is also reported. The four fits have goodness that can be quantified, respectively, $\chi^2/\mathrm{ndf} = 129.3/101$ (prob = 3.0%), $\chi^2/\mathrm{ndf} = 129.4/107$ (prob = 6.9%), $\chi^2/\mathrm{ndf} = 100.2/92$ (prob = 26%), and $\chi^2/\mathrm{ndf} = 173.1/128$ (prob = 0.50%).

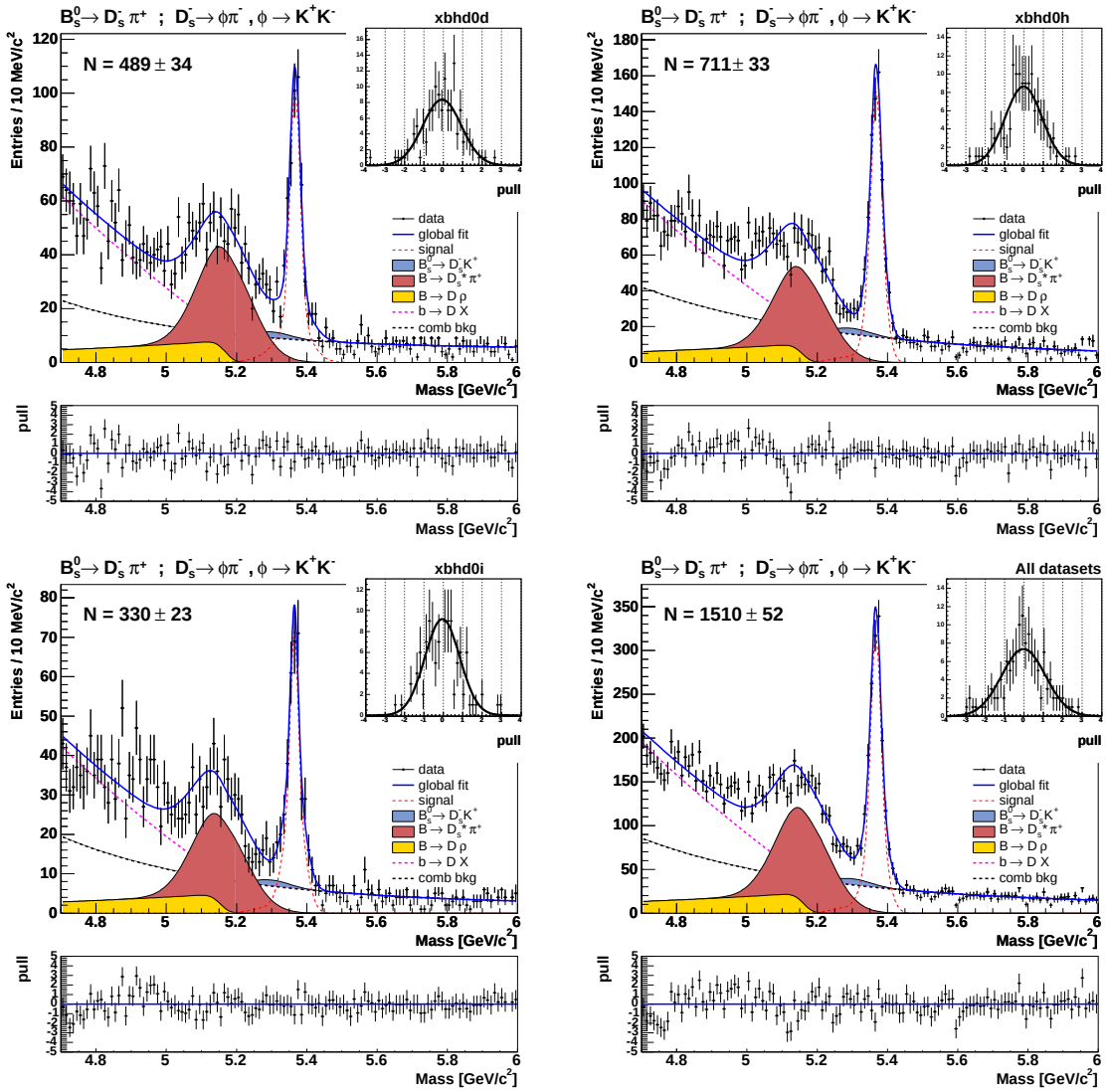

Figure 5.10: Mass fits for the $B_s \to D_s^- \pi^+$ mode: xbhd0d (upper left), xbhd0h (upper right), xbhd0i (lower left), full dataset (lower right).

5.3 Additional Tracks

Once our B meson candidates have been reconstructed and selected, and a procedure based on a maximum likelihood fit has been developed in order to disentangle signal events from background contributions, we are ready to select a set o tracks associated with the B meson formation.

At a glance, the tracks associated with these particles are expected to be relatively close to the B meson and are characterized by small impact parameter (as they are originated from the primary vertex as the B meson). In particular, we decide to use the same track selection adopted in the SSKT algorithm [57] in order to directly compare our results to the Monte Carlo used in the development of the algorithm. In summary, we look for all the tracks in the event that satisfy the following requirements:

- The track is not a decay product of the B candidate. This is a simple and important requirement, considering that decay products are not tracks associated with the meson formation. In particular, this requirements fully exploits the fully reconstructed characteristics of our B sample where, for each candidate, the decay products are unequivocally determined.

- The track is within the cone $\Delta R \equiv \sqrt{\Delta\eta^2 + \Delta\phi^2} < 0.7$ around the B candidate direction in order suppress the contamination from random tracks or particles related to the other $b-$hadron of the event. The value of the ΔR selection is motivated by studies done at CDF [61] showing the the fragmentation products of b quarks are contained in a cone $\Delta R = 0.6$ around the B mesons. As shown in Fig.5.11, the track density in the fully reconstructed $B^+ \rightarrow J/\psi\, K^+$ events (both in data and Pythia Monte Carlo) is higher in the $\Delta\phi - \Delta\eta$ plane around the reconstructed B compatible with the selected cone, track activity of the other $b-$hadron is also visible [63]. Also for the ΔR selection, the fact that the B candidate is fully reconstructed allows a better determination of the meson flight direction.

- The track has at least 3 silicon hits. This requirement, that in practice guarantees a better quality of track parameters, helps to suppress particles not originating from the primary vertex: long lived particles are expected to decay outside or in the middle of the SVX detector and have much lower probability of passing this selection.

- $|z_0^{trk} - z_{PV}| < 2$ cm, where z_0^{trk} and Z_{PV} are respectively the origin of the track and the origin of the primary vertex of the B along the beam axis. This requirements is necessary to ensure that the track and the B candidate come from the same interaction point. As shown in Fig.5.12, several pile$-$up tracks are produced in $p\bar{p}$ collisions that represent a background of our tracks of interest [63].

- The impact parameter significance of the track satisfies $|d_0/\sigma_{d_0}| < 4$. It is obvious that this selection reject secondary vertexes and enhance the sample of prompt tracks.

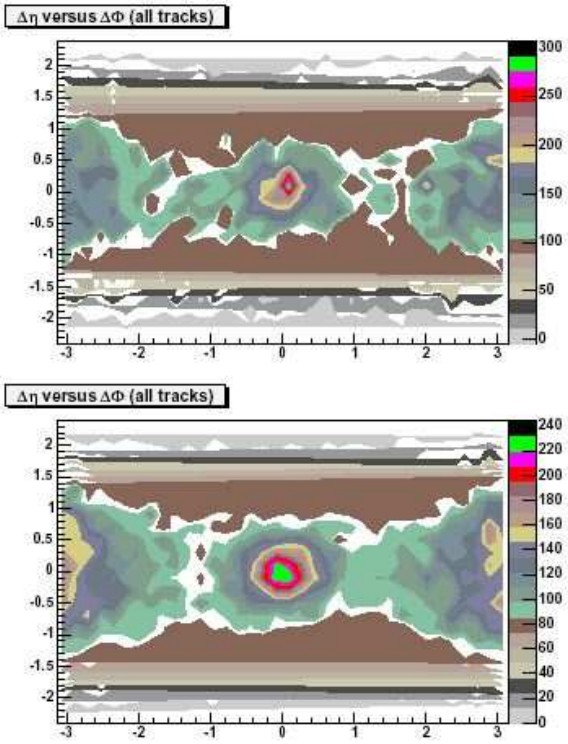

Figure 5.11: The track activity in the $\Delta\phi - \Delta\eta$ plane around the B meson in data (top) and Pythia Monte Carlo (bottom) for $B^+ \to J/\psi\, K^+$ events. The activity of the other b-hadron is also visible.

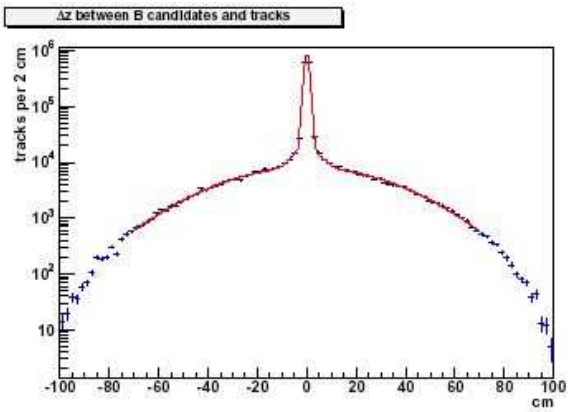

Figure 5.12: The distribution of $|z_0^{trk} - z_{PV}|$ in $B^+ \to J/\psi\, K^+$ data events. The parameterization consists of two narrow gaussians to describe the signal (track and B originating from the same vertex) and the broad gaussian to describe the contribution of tracks originates from other interactions.

- The track has $P_T > 0.45$ GeV/c and $P_T < 6.0$ GeV/c. As we will see, a fitting P_T range must be defined: the lower cut is used to select higher quality tracks that reach the outer layer of the drift chamber, while the upper cut is chosen to be in a region where the P_T distribution of the selected tracks starts to be poorly populated.
- The track has $|\eta| < 1$. Again this is a cut to have better reconstruction quality, both on the track parameters and on the particle identification information.
- The track, obviously, has dE/dx and TOF information. This is essential for our fit, considering they they are the only source of separation power between each particle type.

The sample of tracks satisfying the above criteria are expected to be enriched in particles produced in association with the B formation and it represents the sample used in our measurement of the particle content.

Chapter 6

Particle Fractions Estimation: the Statistical Method

In this Chapter we will introduce the formalism and the statistical methods that will be used to estimate the the particle content around the B mesons.

6.1 Introduction

It has been shown in some toy problems [64] that strong biases may occur in a multi-component Maximum Likelihood fit whenever the templates, i.e. the functions, used to parameterize the probability distributions used in the fit are not fixed but depend on event observables. An interesting example of such a problem in the practice of experimental High Energy Physics is the statistical separation of different kinds of particles on the basis of limited–precision measurements of particle–dependent quantities, like Time–of–Flight or energy loss (dE/dx).
In this Chapter we will show how the bias may occur in the particle fractions estimation; we will then describe to different approaches to obtain an unbiased estimation of the content of each particle type and finally we will generalize the method to disentangle the distributions of kinematical variables of each particle species.

6.2 Particle Fraction Estimation

Consider a mixture of known particle types, for example *Pions*, *Kaons*, *Protons* and *Electrons* . We indicate by f_π, f_K, f_P and f_e respectively the unknown fractions of each particle type contained in the sample. Using Particle Identification *PID* information we want to estimate f_π, f_K, f_P and f_e and possibly obtain distributions of relevant kinematical variables for different particle types.

We will consider two methods for particle identification, both available to CDF: one is based on the measurement of the energy loss of charged particles in the gas of the COT (dE/dx), the other is based on the measurement of the Time−of−Flight (TOF) of the particle from the production vertex to the scintillator bars just outside the COT.

A tricky feature of *PID* devices based on the above principles is that the separation power between different particles is strongly momentum dependent. This is shown in Fig. 6.1 where the dE/dx mean response of different particles is plotted as a function of momentum. Assuming that the resolution of the measurement is constant, the separation power dramatically changes in a short momentum range as shown in Fig. 6.2 (left). A similar situation occurs for Time−of−Flight though the momentum dependence is different.

As a consequence of this, the *pdf*'s that enter in the expression of the likelihood and describe the response of the *PID* devices for different particle types are strongly momentum dependent, Fig. 6.2 (right), and we need to be very careful in order to avoid the effect described in [64]. A multicomponent Maximum Likelihood fit may be affected by strong biases whenever the dependence on event observables of the *pdf*'s used in the likelihood is not correctly taken into account. Therefore care must be taken to properly define the likelihood function as discussed below.

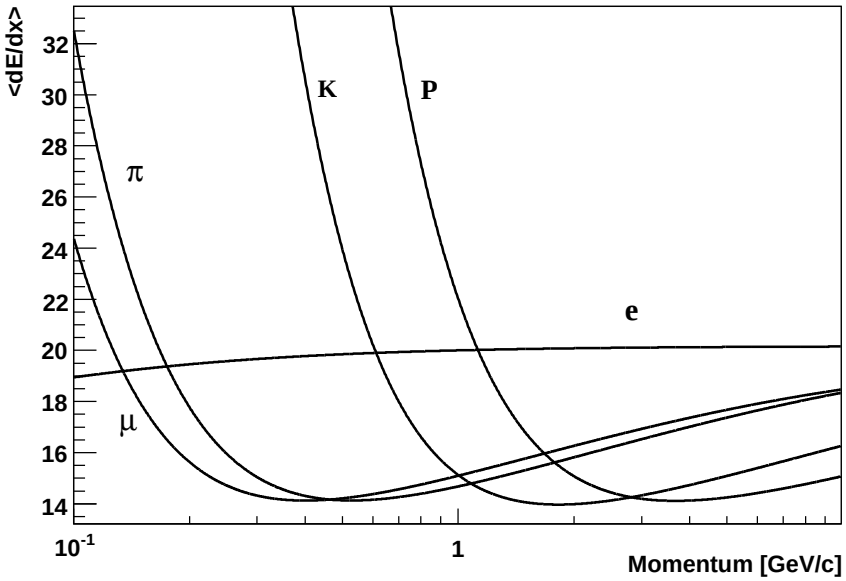

Figure 6.1: Mean dE/dx response of the CDF COT for different particle types as a function of momentum.

6.2.1 Avoiding a strong bias in the particle fraction estimation

Consider, for simplicity, only the PID information provided by a dE/dx measurement. Our observables are then the dE/dx (pid) and the momentum of the track (mom).We will indicate as *type* the particular particle hypothesis. Unfortunately, we cannot simply write the Likelihood function as:

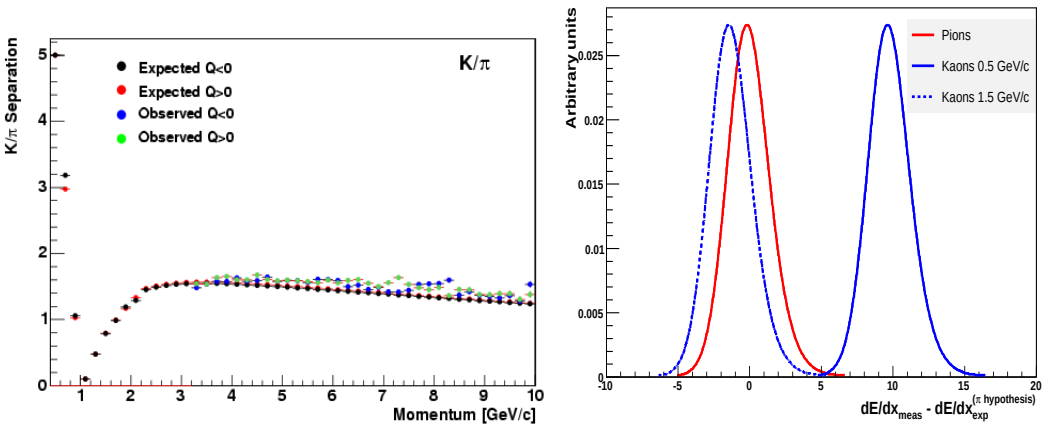

Figure 6.2: Left: K/π separation as a function of momentum using the dE/dx measurement in the CDF COT. Right: $\frac{dE}{dx}_{(Measured)} - \frac{dE}{dx}^{(\pi hypothesis)}_{(Expected)}$ for π (red) and K (blue) in different momentum ranges.

$$L(f_j) = \prod_i \Big(\sum_{j=\pi,K,P} f_j P(pid_i | mom_i, type_j) \Big). \tag{6.1}$$

Using expression (6.1) may give a strongly biased result on the particle fractions f_j if our additional variable, the momentum, has different distributions depending on the particle type (see next section). As discussed in[64], whenever the templates used in a multi–component fit depend on additional observables, to avoid the bias it is necessary to use the correct, complete Likelihood expression, including the explicit distributions of all observables for all classes of events. In our particular case, the above implies that we need to include in our Likelihood the momentum distributions of each particle type. We should also notice that in practice those distributions are almost always different.

We then write the correct Likelihood function as:

$$\begin{aligned} L(f_j) &= \prod_i \Big(\sum_{j=\pi,K,P} f_j P(pid_i, mom_i | type_j) \\ &= \prod_i \Big(\sum_{j=\pi,K,P} f_j P(pid_i | mom_i, type_j) \\ &\qquad \times P(mom_i | type_j) \Big), \end{aligned} \tag{6.2}$$

with the condition:

$$\sum_{j=\pi,K,P} f_j = 1. \tag{6.3}$$

A toy study

To show the effect of the use of the incorrect likelihood expression (6.1) we generated a sample of different particle types with known composition as follow:

- PID variable is distributed, for each particle, according to a typical resolution function (i.e. the template used in the fit) defined as:

$$PID_{\text{measured}} - PID_{\text{expected}}(mom) \tag{6.4}$$

Note the dependence on momentum of the expected PID.

This distribution represents:

$$P(pid_i|mom_i, type_j) \tag{6.5}$$

in Eq. (6.2).

- Momenta of the particles are distributed according a Gaussian $N(\mu_j, \sigma_j)$, where $j = \pi, K, P$ (electrons are not considered in this toy study) and:

$$\mu_\pi = 1.00, \quad \mu_K = 1.25, \quad \mu_P = 1.25,$$

$$\sigma_\pi = \sigma_K = \sigma_P = 0.50.$$

Those distributions obviously represent:

$$P(mom_i|type_j) \tag{6.6}$$

of equation (6.2).

- Particle fractions where fixed to:

$$f_\pi = 50\%, \quad f_K = 35\%, \quad f_P = 15\%.$$

We then used an unbinned Maximum Likelihood fit to estimate the particle fractions of the sample using the Likelihood function described in Eq. (6.2) where:

$$P(mom_i|type_j) = N(\mu_j, \sigma_j). \tag{6.7}$$

In Fig. 6.3 (left) the distribution of the estimators for f_π and f_P are shown for thirty toy samples of ten thousand particles each. As expected, the fractions returned by the fit are well centered on the true values given by the input.

Conversely, the same distributions obtained with the incomplete Likelihood function of Eq. (6.1) (Fig. 6.3, right) are affected by a bias much larger than the nominal statistical uncertainty of those measurements, due to the difference in the momentum distribution of each particle type. This demonstrates that the effect predicted in [64] is actually very significant in real–life problems of Particle Identification.

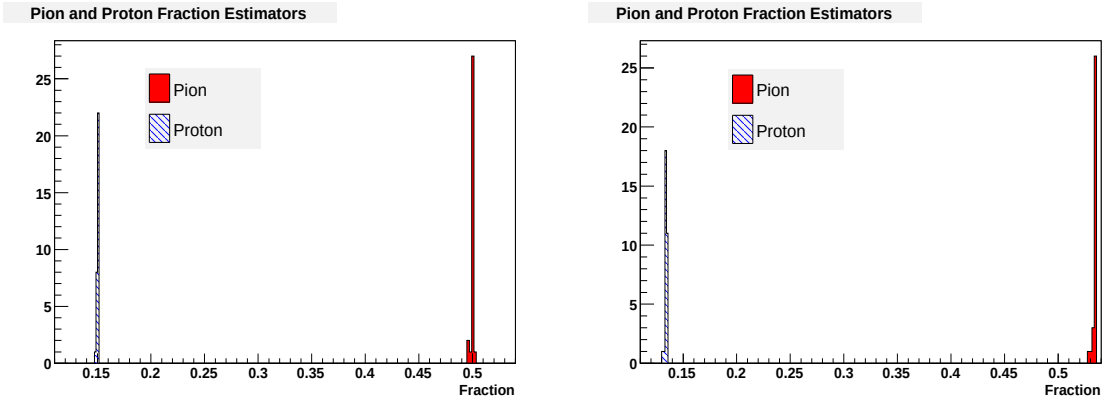

Figure 6.3: The Pion and Proton fraction estimator distributions when the complete (left) and incomplete (right) Likelihood expression is used.

6.3 What if the distributions of additional observables are unknown?

Writing the complete Likelihood function is relatively straightforward in principle. On the other hand, in practice, we often have poor information about the distributions of the additional observables ($P(mom|type_j)$ in our example). Sometimes they are completely unknown. This is the case, for example, of the particles produced during the hadronization of B mesons: the momentum distribution of each particle type is unknown and the correct Likelihood function as defined in (6.2) cannot be constructed.

In [73] it was shown that a possible solution is to use a series expansion of the unknown distributions. The momentum term of the Likelihood function (6.2) is then written as:

$$P(mom_i, type_j) = \sum_m a_{mj} U_m(mom_i) \tag{6.8}$$

and

$$L(f_j) \rightarrow L(f_j, a_{mj}) \tag{6.9}$$

Where m is the order and U_m are the base vectors used for the series expansion. The a_{mj} terms are treated as free parameters to be determined by the fit.

Coming back to our toy sample, we considered Orthogonal Polynomials as a basis for the expansion. Amongst a number of possibilities, we selected Second Type Chebyshev Polynomials (denoted by U_m).

We then replaced in expression (6.2) the term Eq. (6.7) with Eq. (6.8) and we performed again the unbinned Maximum Likelihood Fit, this time by fitting also the parameters of the polynomial expansion. As shown in Fig. 6.4, now the bias is brought back to zero, as it was when we assumed perfect knowledge of the individual momentum distributions of each particle type.

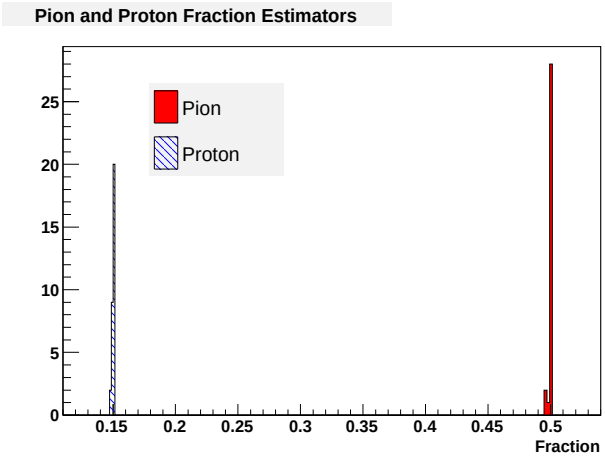

Figure 6.4: The Pion and Proton fraction estimator distributions using a Series Expansion as a parameterization of the momentum distribution.

We have been able to avoid the bias in the fraction fit, without any particular assumption on the functional form of the momentum distributions. In such a way we simulated the practical case where no information is known about the additional observable distributions. Please notice also that just the first seven terms of the Second Type Chebyshev Expansion were needed in order to parametrize each particle type momentum distribution. Another interesting aspect is that comparing Fig. 6.4 to Fig. 6.3 no significant degradation in the resolution of the estimator is observed, although the number of parameters is increased. In Fig. 6.5 the projections of the fit to the toy sample are shown.

Note that the maximization of (6.2) combined with (6.8) is not only an unbiased estimation of the particle content of the sample, but it provides also an approximation of the momentum distributions of each particle type in the form of a Series Expansion of order m of the true distributions.

The use of a Series Expansion is a general approach to avoid the bias in maximum likelihood fits when the *pdf* of one or more observables is unknown; on the other hand, if the number of free parameters to be determined by the fit is high, convergence problems may arise during maximization.

A different possible strategy, used for example in [74], is based on the idea that if the fit is performed in small momentum intervals, the bias due to the use of the likelihood function (6.1) is small and it goes to zero as the momentum interval width decreases. This approach requires an independent maximum likelihood fit in *each* momentum bin.

In next sections we take this idea to the extreme and use very small momentum bins and in each one of them we perform a separate fit to estimate particle fractions. In this way any bias caused by momentum dependence of the *pdf*'s is negligible and we show that we can extract the unknown momentum distributions of each particle type in a completely data driven mode without any assumption on the corresponding functional forms.

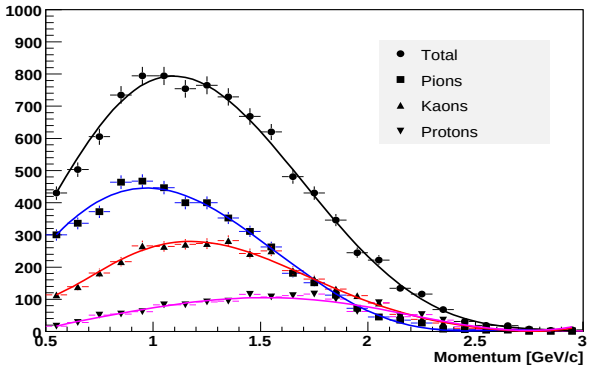

Figure 6.5: The momentum projections for each particle type superimposed on the corresponding generated distributions.

6.4 The Likelihood Function

Once we have restricted ourselves to particles contained in a sufficiently small momentum bin, the likelihood function we need to maximize in order to extract the fractions of each particle type takes the form:

$$Log(L) = \mathcal{L} = \sum_{i=0}^{N} Log(\sum_{j=1}^{M} N_j pdf_j(R_i)) \tag{6.10}$$

where N is the total number of particles in a particular momentum bin, M is the number of different particle species, N_j is the number of particles of type j and R_i is the PID response.

The likelihood must be maximized with respect to the free parameters N_j with the constraint:

$$N = \sum_{j=1}^{M} N_j \tag{6.11}$$

The discriminating power comes from the fact that the PID response has different distributions for different particle types (pdf_j). The bias in the fraction estimation is avoided because, once we restrict ourselves to sufficiently small momentum bins, the pdf_j do not depend on any other quantity but the particle type.

6.5 An iterative procedure to estimate the particle fractions

In next sections we will introduce an iterative procedure, called *Channel Likelihood* (CL), for parameter estimation. It was shown that this method is asymptotically equivalent to the Maximum Likelihood. The Channel Likelihood can be used to provide simultaneously, an unbiassed estimation of the particle fractions in the example

described before and a good estimation of the momentum distribution of each particle type.

6.5.1 The *Channel Likelihood method*

In [75] an extension of Maximum Likelihood analysis for multibody final states is presented. We will here briefly review the method, called *Channel Likelihood*.

Suppose we have a sample of N events that is a mix of M classes, or types of events. Each event i is described by a set of discriminating variables that we will indicate with the vector $\vec{R}_i$. We then know the analytical expression of the *p.d.f.* of the $\vec{R}_i$ variables for each class of events that will be indicated as $pdf(\vec{R})_j$ where $j = 1, 2, ..., M$.

Our goal is the estimation of the number of events of each class, N_j, in the intial sample N with the obvious constraint:

$$\sum_{j=1}^{M} N_j = N \tag{6.12}$$

We can define the *relative* probabilty of event i having come from class j:

$$N_j pdf(\vec{R}_i)_j \tag{6.13}$$

and the normalization for the event i:

$$\sum_{j=1}^{M} N_j pdf(\vec{R}_i)_j \tag{6.14}$$

Combining (6.13) and (6.14) we define the weight w_{ij} of event i for the class j:

$$w_{ij} = \frac{N_j pdf(\vec{R}_i)_j}{\sum_{k=1}^{M} N_k pdf(\vec{R}_i)_k} \tag{6.15}$$

that is the probability for event i to come from class j.

Notice that $\sum_{j=1}^{M} w_{ij} = 1$ for any given event i; notice also that in the ideal case, where there is no overlap between different classes, w_{ij} would be zero except for one class j (the right one) where $w_{ij} = 1$.

We can now write the N_j as:

$$N_j = \sum_{i=1}^{N} w_{ij} \tag{6.16}$$

We are now able to define the iterative process that provides an estimation of the N_j in our data sample. Starting from a first guess on those parameters, N_j^0 we can define an iterative procedure expressed by:

$$N_j^n = \sum_{i=1}^{N} \frac{N_j^{n-1} pdf(\vec{R}_i)_j}{\sum_{k=1}^{M} N_k^{n-1} pdf(\vec{R}_i)_k} \tag{6.17}$$

where at every step n of the iteration, we estimate the N_j^n that will be used as input values for the step $n+1$.

The procedure converges to the set of N_j that are the solutions of the equations:

$$N_j = \sum_{i=1}^{N} \frac{N_j pdf(\vec{R}_i)_j}{\sum_{k=1}^{M} N_k pdf(\vec{R}_i)_k} \tag{6.18}$$

or the equivalent:

$$1 = \sum_{i=1}^{N} \frac{pdf(\vec{R}_i)_j}{\sum_{k=1}^{M} N_k pdf(\vec{R}_i)_k} \tag{6.19}$$

After the solution has been found, we can use the w_{ij} to weight events when making plots respect to a variable belonging to $\vec{R}$.

In [75] it has also shown that this method is asymptotically equivalent to the Maximum Likelihood, i.e., the equation system (6.19) is the same that we are supposed to solve in order to maximize the Log-Likelihood respect to the parameters N_j:

$$Log(L) = \mathcal{L} = \sum_{i=0}^{N} Log(\sum_{j=1}^{M} N_j pdf(\vec{R}_i)_j) \tag{6.20}$$

the Channel Likelihood (CL) is then an optimal method for parameters estimation.

Notice also that , from the equivalence between CL and Maximum Likelihood, once the N_j are estimated, to evaluate the statistical error of our parameters we can write the inverse of the covariance matrix V_{jl}^{-1} of the fit as:

$$V_{jl}^{-1} = \frac{\partial(-\mathcal{L})}{\partial N_j \partial N_l} = \sum_{i=0}^{N} \frac{pdf(\vec{R}_i)_j pdf(\vec{R}_i)_l}{\left(\sum_{k=1}^{M} N_k pdf(\vec{R}_i)_k\right)^2} \tag{6.21}$$

The Channel Likelihood method has been used in several analysis, see for example [76], [77] and more recently [78]. In [79] a similar method is used for unfolding experimental distribution to get the best estimate of the true ones, in the same work it is also argued that the method can be directly derived from the Bayes' theorem.

We will now come back to our example and we will see how the Channel Likelihood method can be used in the particle type fractions estimation.

We already argued that the bias due to the maximization of the Likelihood function (6.1) can be neglected if the fit is performed in a narrow momentum bin. The idea is

to divide our sample in a relatively high number of momentum interval and perform in each bin a fit using the CL method.

This approach has several advantages: no functional shape is assumed for the spectra, the method, provided the *PID* templates, is completely data driven; all the fit can be performed in parallel, that is the iteration can be done in all bins at the same time; the algorithm is fast and it is stable respect to the initial guess on the N_j.

Using the same notation introduced in this section, N_j is the number of particles of type j where $j = \pi, K, P, e$; we then define the iteration in each momentum bin Δmom as:

$$N^{n+1}_{j,\Delta mom} = \sum_{i=1}^{N} \frac{N^n_{j,\Delta mom} pdf(pid_i|mom_i)_j}{\sum\limits_{k=\pi,K,P,e} N^n_{k,\Delta mom} pdf(pid_i|mom_i)_k} \tag{6.22}$$

Once we obtain the converge of the iterative process, we can write, for each particle type:

$$f_j = \frac{N_j}{N} = \frac{1}{N} \sum_{\Delta mom} N_{j,\Delta mom} \tag{6.23}$$

observing that each bin content is fitted independently, the corresponding statistical uncertainty is:

$$\sigma(f_j) = \frac{\sqrt{\sigma^2(N_j)}}{N} = \frac{1}{N} \sqrt{\sum_{\Delta mom} \sigma^2(N_{j,\Delta mom})} \tag{6.24}$$

Notice that the because we are performing the fit in each momentum bin and in principle we could use a high number of bins, the arrays of $N_{j,\Delta mom}$ can be interpreted as an *histogram* that reasonably approximate the true momentum distributions of each particle type: we obtained an unbiased estimation of the particle composition even if the $pdf(mom_i|type_j)$ were unknown and, at the same time, a reasonable estimation of the $pdf(mom_i|type_j)$ themselves.

6.5.2 The Chanel Likelihood as an Iterative Method

Let's now think in more detail about what we are actually doing. Given the Likelihood function (6.20) the Maximum Likelihood principle states that the set of parameters N_j that maximize (6.20) are an optimal estimation of the true values. In practice the maximization of (6.20) means solving, respect to N_k, the *non linear* system of equations (6.19). There are several numerical methods to solve non linear systems of equations and, among them, a well known and defined class is represented by the *iterative methods*. We will now describe some general features of such methods following the notation of [81] (a very comprehensive reference on the theory and the mathematics of iterative solution of nonlinear equations).

Let $F(\vec{x})$ be a n-dimensional function, $F : D \subset R^n \to R^n$, where $\vec{x}$ is the vector of the n variables, for simplicity through the rest of the note we will write x instead of $\vec{x}$

keeping in mind that we are referring to a vector of variables. Let x^* be the solution of the equation $F(x) = 0$, i.e. the *root* of F. A general iterative method to find x^* is the so called *parallel-chord method* whose iteration is defined as:

$$x^{h+1} = x^h - A^{-1}F(x^h) \tag{6.25}$$

where $h = 0, 1, ...$ is the iteration index and A is a *non singular* matrix. A crucial point for what follows is represented by the arbitrary nature of the matrix A in equation (6.25), we should in fact observe that, given the parallel-chord method and, of course, the F whose we want to evaluate the root, the iteration is defined by A.

There are many possible choices for the matrix A but the underling requirement is that the iteration (6.25) be at least *locally convergent*; this means that when the starting values of the iteration, x^0, are sufficiently close to x^* then $lim_{h\to\infty}x^h = x^*$.

A sufficient (and in practice necessary) condition for the local convergence is in fact a condition on the choice of the matrix A and, when $F^{'}(x^*)$ exists, it is expressed by:

$$\rho(I - A^{-1}F^{'}(x^*)) < 1 \tag{6.26}$$

where I is the identity matrix and ρ denotes the spectral radius of the matrix [1].

Since x^* is unknown, it is not obvious to choose A in advance such that (6.26) holds. On the other hand an ideal choice would be $A = F^{'}(x^*)$: in such a way ρ is equal to zero. We could then consider iterations where matrix A is not fixed but it can vary from step to step and $lim_{h\to\infty}A_h = F^{'}(x^*)$.

A well known case of such a choice is the so called *Newton method* whose iteration is defined by:

$$x^{h+1} = x^h - F^{'}(x^h)^{-1}F(x^h) \tag{6.27}$$

It is interesting to notice that a special form of the function F:

$$F(x) = Ax - G(x) \tag{6.28}$$

where A is again a non singular matrix and $G : D \subset R^n \to R^n$ is a non linear function, leads to the so called *Picard iteration*:

$$x^{h+1} = A^{-1}G(x^h) \tag{6.29}$$

If we choose $A = I$, the iteration (6.29) reduces to:

$$x^{h+1} = G(x^h) \tag{6.30}$$

that provides the root of:

$$F(x) = x - G(x) \tag{6.31}$$

We can now observe that (6.17) is an iteration of the form (6.30) while (6.18), the system that we are supposed to solve to maximize the Likelihood (6.20), is of the

[1]The spectral radius is defined as the maximum of the *absolute* value of the eigenvalues of a matrix

form (6.31): we are not surprised, the Channel Likelihood method is a particular case of iterative methods to solve the system (6.18), i.e. it is a Picard iteration with the *particular* choice $A = I$.

6.6 A Toy Monte Carlo study of the Channel Likelihood

We test our method on toy Monte Carlo samples. Each sample consists of 3500 particles. Different P_T spectra used to generate each particle type are taken from Pythia and the corresponding fractions are fixed at:

$$f_\pi = 0.74, \quad f_K = 0.17, \quad f_P = 0.07, \quad f_e = 0.02 \tag{6.32}$$

We then divide the sample into 50 momentum bins from 0.45 GeV/c up to 6.0 GeV/c. A maximum likelihood fit is made in each momentum bin to estimate the fractions of each particle species. Empty bins are ignored. We repeat the fit on 100 toy samples and plot the distributions of the residuals of the estimates.

Fig.6.6 and Fig.6.7 show the plots of the residuals of the estimators of the total fractions of Pion, Kaon, Proton and Electron, summed over all momentum bins. No significant bias is observed (a small shift can be noticed for the electron estimator, but it is less than one σ). Fig.6.8 shows the plots of the residuals of the estimators as a function of the bin number (i.e. momentum). In each plot, each point represents the mean value, while the error bar represents the width of the distribution of the residual. We observe no significant bias in all cases.

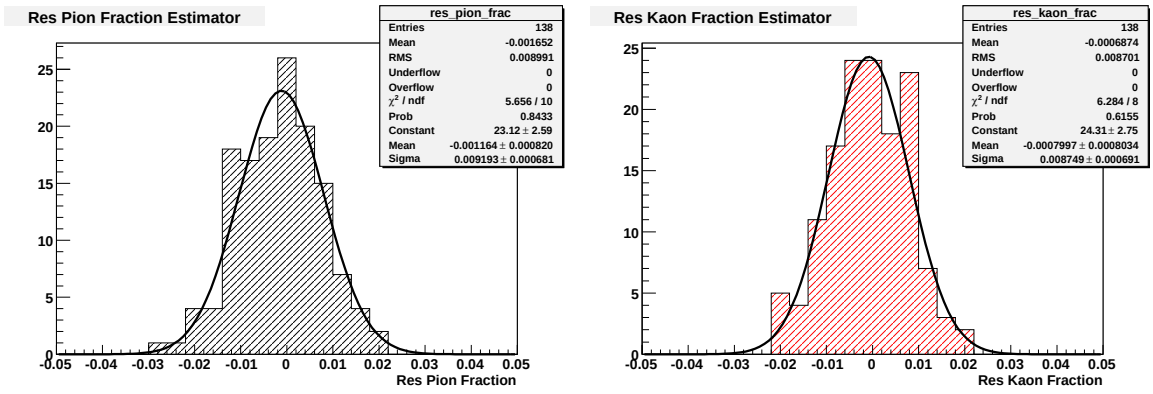

Figure 6.6: $Fraction_{meas}$ - $Fraction_{true}$ distributions (integrated on all momentum bins) for 100 toy samples: left Pions, right Kaons.

Examples of momentum distributions obtained from the fit are shown in Fig.6.9. A very good agreement between the true distributions (filled histograms) and the fit (dots) is observed for all particle types. The fits provide a very good estimation of the unknown distributions.

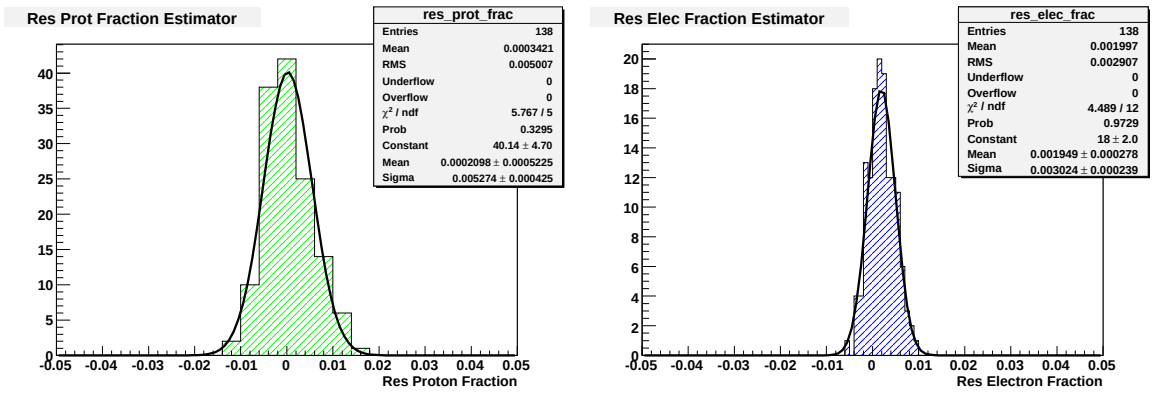

Figure 6.7: $Fraction_{meas}$ - $Fraction_{true}$ distributions (integrated on all momentum bins) for 100 toy samples: left Protons, right Electrons.

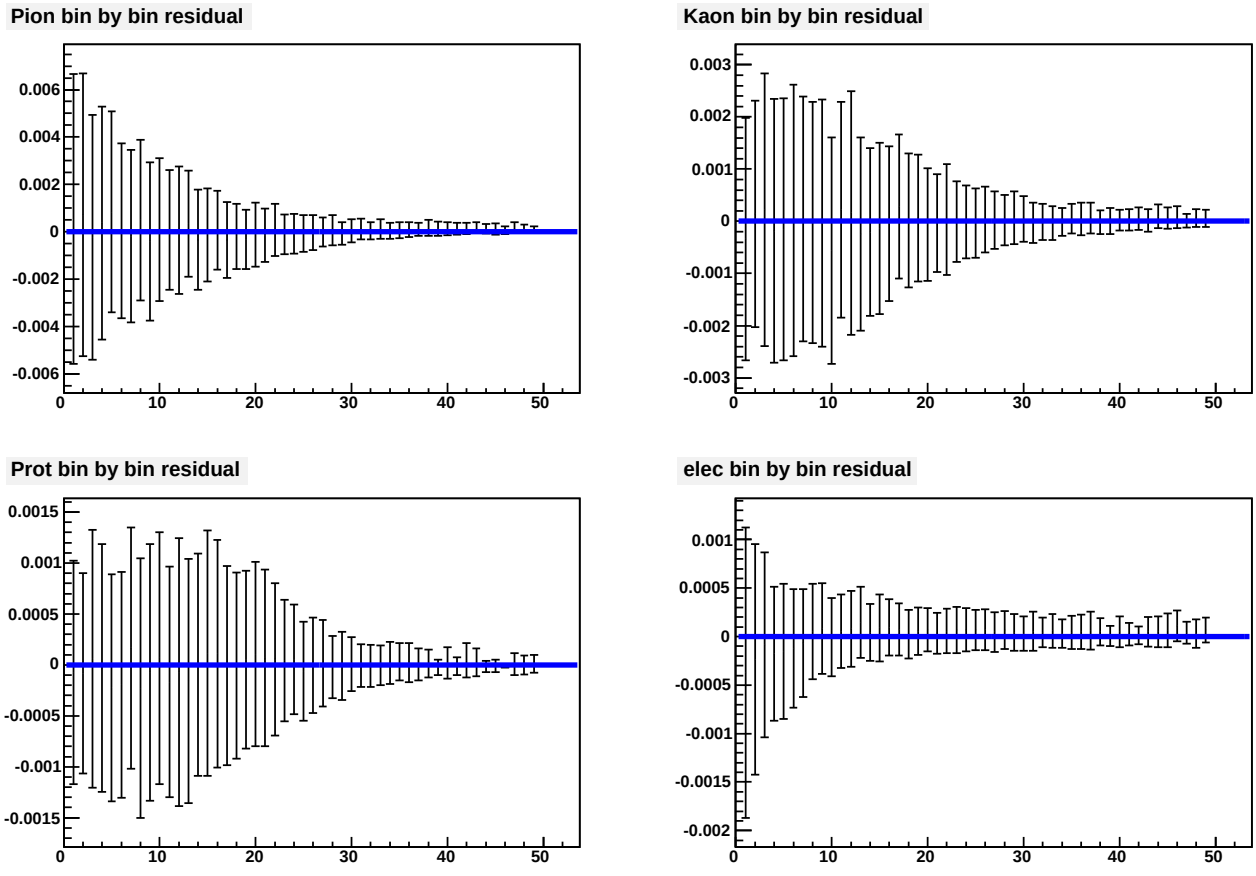

Figure 6.8: Mean and width of the $Fraction_{meas}$ - $Fraction_{true}$ distributions in each momentum bin.

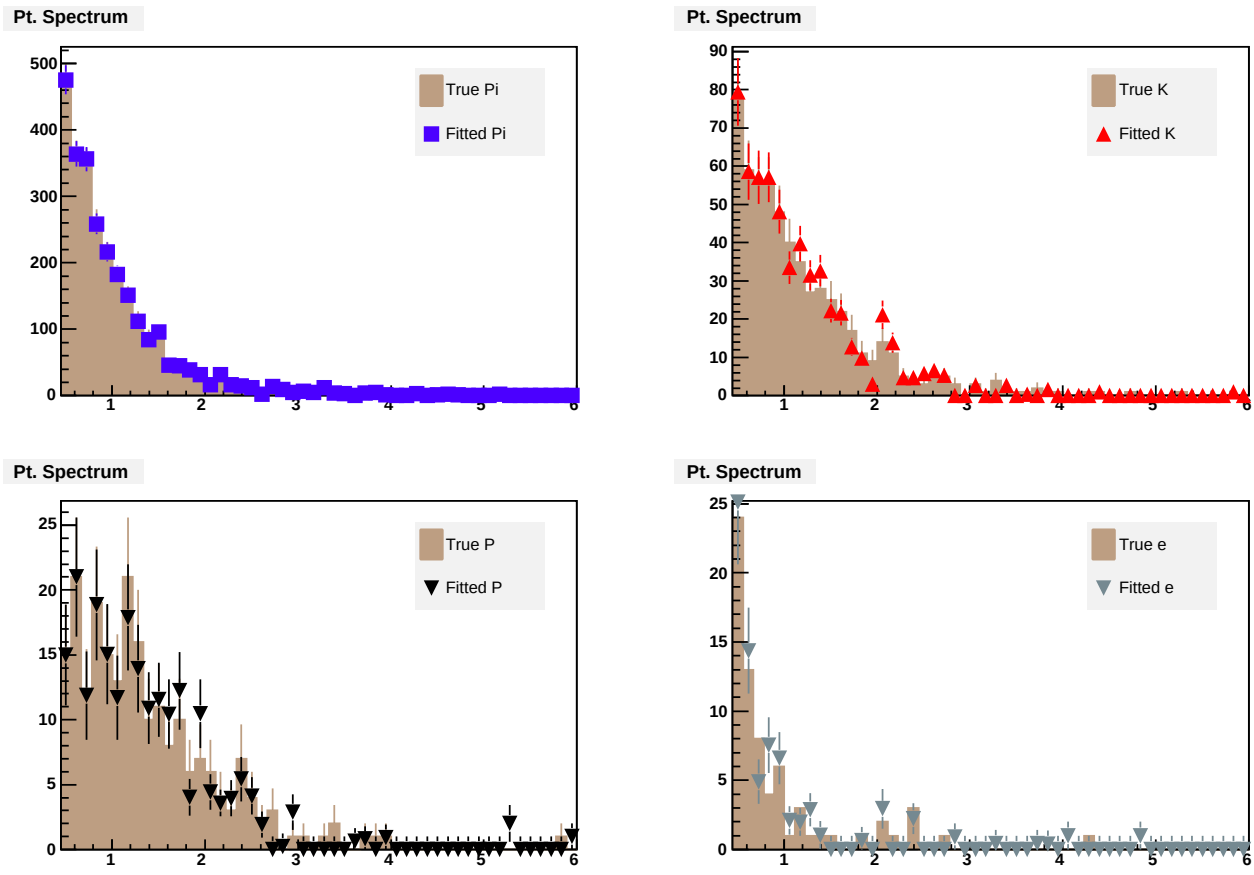

Figure 6.9: Overlay of the toy momentum distributions (filled histograms) and the ones resulting form the CL fits (dots) where the distributions are considered unknown.

6.6.1 The Single Event case

Performing the fits in small momentum bins may arises an obvious question: is the result strongly affected by the number of bins, or equivalently, is our procedure robust when the bin is poorly populated?

Actually checking the robustness of the fit when the number of bins is very high is equivalent to test its behavior when a bin has just *one* event.

To check this extreme case, *fixed* a certain momentum bin, we generated 200 new toy samples with, on average, just one event per sample. The particle fractions where fixed to the same values of the previous sections.

In Fig.6.10 the residuals of each particle specie do not show any particular shift respect to zero: the procedure seems to be corrected even if just one event is used as input of the fit.

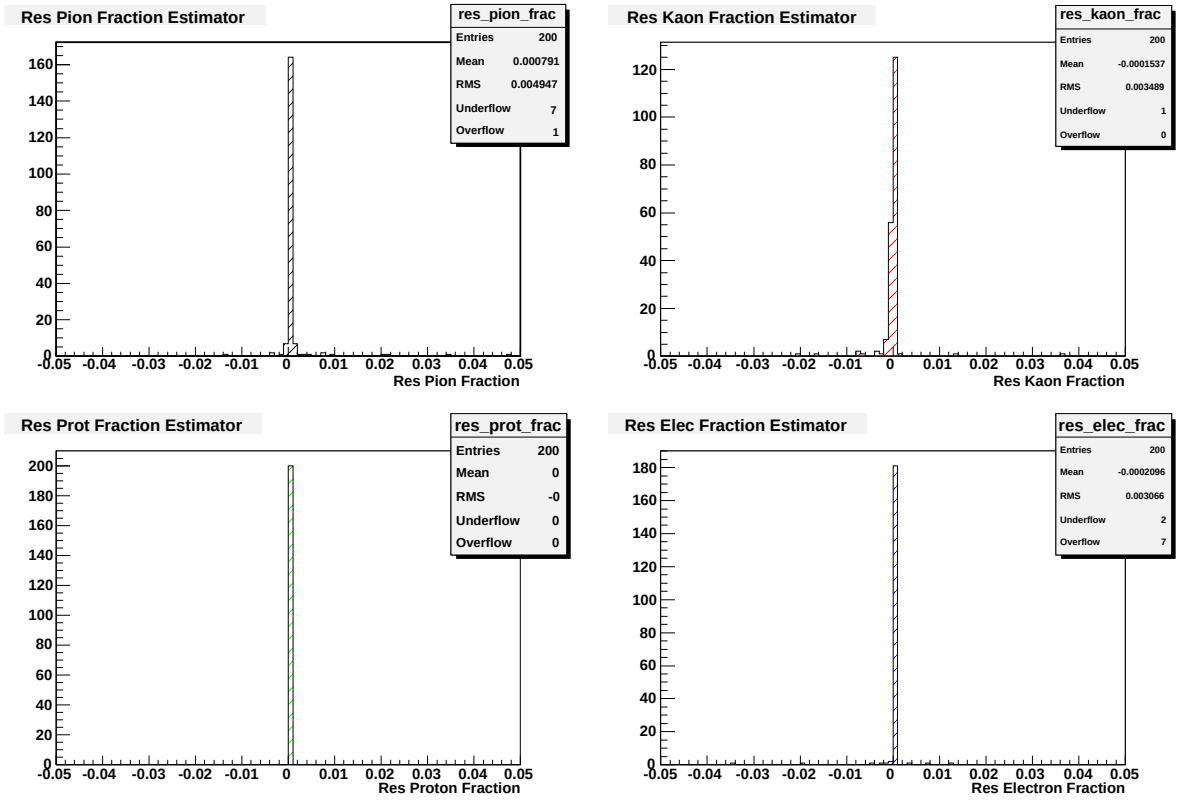

Figure 6.10: $Fraction_{meas}$ - $Fraction_{true}$ distributions for 200 toy samples with just one event per sample, from left to right ant top to bottom respectively: Pions, Kaons, Protons and Electrons.

6.7 The 2-Dimensional case

The method can be easily generalized, at least in principle, to a multidimensional case.

If, for example, our PID information is obtained by the measurement of the Time of Flight, the expression of the expected TOF (TOF_{exp}) is actually a function of two observables:

$$TOF_{exp}(mom, L) = \frac{L}{c}\sqrt{1 + (m_j/mom)^2} \tag{6.33}$$

where L is the length traveled by the particle (also called $arclength$), c is the speed of light, m_j is the mass of the particle type j and mom is again the momentum of the particle.

The distributions of both momentum and arclength can be different for different particle species and are unknown in general. Therefore both observables could be a source of bias in the estimation of particle fractions.

The consequence is that, since now we have two observables to deal with, we need to build a 2−dimensional grid of bins in mom and L and estimate particle fractions independently in each bin.

In Fig.6.11 the true 2-dimensional distributions of mom and L are shown superimposed to the result of the fit. The agreement is clearly very good also in this case.

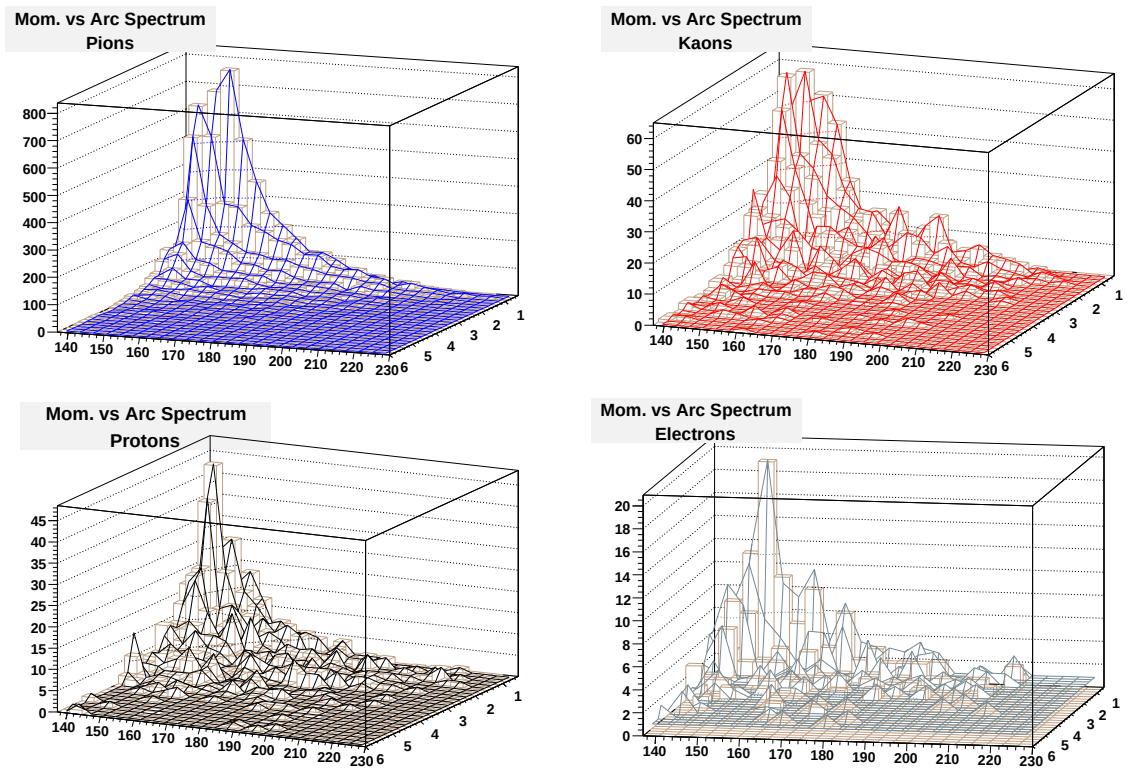

Figure 6.11: Momentum versus Arclength distributions from Pythia MC (histograms) and the fitter (surface): left Pions, right Kaons.

6.8 Extracting distributions of other quantities

Besides obtaining momentum and arclength distributions, we are typically interested in obtaining plots of many additional kinematical variables for the different particle species. A method to achieve this is a technique known as *sPlot* and is based on estimating particle fractions as described above and their covariance matrix [80].

Using the same notation introduced in the CL method, the aim of the *sPlot* formalism is to unfold the true distribution (denoted in boldface $\mathbf{M_j}(\mathbf{x})$) of a control variable x that is not used as discriminating variable in a Maximum Likelihood fit for events of the j^{th} species, from the sole knowledge of the discriminating variables $pdf(\vec{R})_j$ and the yields N_j estimated by the fit. If the the two sets of variable x and $\vec{R}$ are uncorrelated and denoted $\tilde{M}_j$ an estimate of $\mathbf{M_j}$ we can write the expectation value of $\tilde{M}_j$:

$$\begin{aligned}\left\langle N_j \tilde{M}_j(\bar{x}) \right\rangle &= \int d\vec{R}dx \sum_{l=1}^{M} N_l \boldsymbol{M_l}(x) pdf(\vec{R})_l \delta(x-\bar{x}) w_{ij} \\ &= N_j \sum_{l=1}^{M} N_l \boldsymbol{M_l}(x) \int d\vec{R} \frac{pdf(\vec{R_i})_j pdf(\vec{R_i})_l}{\sum\limits_{k=1}^{M} N_k pdf(\vec{R_i})_k}\end{aligned} \tag{6.34}$$

We may now observe that the integral in the right hand side of (6.35) is related to the inverse of the covariance matrix, given by the second derivatives of $-\mathcal{L}$:

$$V_{jl}^{-1} = \frac{\partial(-\mathcal{L})}{\partial N_j \partial N_l} = \sum_{i=0}^{N} \frac{pdf(\vec{R_i})_j pdf(\vec{R_i})_l}{\left(\sum\limits_{k=1}^{M} N_k pdf(\vec{R_i})_k \right)^2} \tag{6.35}$$

and on average:

$$\left\langle \boldsymbol{V}_{jl}^{-1} \right\rangle = \int d\vec{R} \frac{pdf(\vec{R_i})_j pdf(\vec{R_i})_l}{\sum\limits_{k=1}^{M} N_k pdf(\vec{R_i})_k} \tag{6.36}$$

therefore, (6.35) can be rewritten:

$$\left\langle \tilde{M}_j(\bar{x}) \right\rangle = \sum_{l=1}^{M} N_l \boldsymbol{M_l}(\bar{x}) \left\langle \boldsymbol{V}_{jl}^{-1} \right\rangle \tag{6.37}$$

inverting this matrix equation, one recovers the distribution of interest:

$$N_j \boldsymbol{M_j}(\bar{x}) = \sum_{l=1}^{M} \left\langle \boldsymbol{V}_{jl} \right\rangle \left\langle \tilde{M}_j(\bar{x}) \right\rangle \tag{6.38}$$

We can now defining the covariance-weighted quantity sw_{ij} defined by:

$$sw_{ij}(\vec{R}) = \frac{\sum_{l=1}^{M} V_{jl} pdf(\vec{R}_i)_l}{\sum_{k=1}^{M} N_k pdf(\vec{R}_i)_k} \tag{6.39}$$

Events can now be weighted using (6.39) and the distribution of the control variable x can be obtained as an histogram that, on average, reproduces the true binned distribution:

$$\left\langle N_j \tilde{M}_j(x) \right\rangle = N_j \boldsymbol{M_j}(x) \tag{6.40}$$

Notice that (6.35) is asymptotically true, but even in the case of low statistics, where the equivalence between the covariance matrix and the inverse of the Likelihoodś Hessian is not valid anymore, the use of the integral in the right hand side of (6.35) instead of the inverse of the covariance matrix returned by the fit is still correct. Notice also that, coming back to our particle fractions fit, we are already evaluating (6.35) in each bin to estimate the statistical uncertainty of the fit parameters: we can easily produce *sPlots* of kinematical variables that are not used in the fit.

The main requirement for the *sPlot* technique to actually work is that the kinematical variables we wish to plot be uncorrelated with the *pdf*'s that describe the response of the *PID*. In our case we do not need to worry because any dependence of the *pdf*'s from kinematical variables is $frozen$ by our strategy to perform a separate fit in each momentum and arclength bin.

To test this feature, we use a Pythia Monte Carlo sample of $B^- \to D^0\pi^-$, such a sample will provide a reasonable description of all the kinematical variables associated with a given particle and the correlations among them. We then fit the composition of the particles produced in the vicinity of the B^- meson. A parametric simulation of dE/dx and TOF is used.

We observe that momentum and arclength can be replaced by P_T and η with no loss of information. The advantage is that η distributions for different particle types are very similar. This in shown in Fig.6.12 where η distributions for different particle types are overlaid. No significant difference is observed and this allows us to factorize the η distribution and eliminate it from the Likelihood. This is a big simplification since it allows us to avoid $2-$dimensional binning and consider P_T as the only unknown variable.

Tab.6.8 reports the total fraction of each particle type, and Fig.6.13 shows the P_T distributions resulting from the fit.

	π	K	P	e
True fraction	0.828	0.112	0.0557	0.0039
Fitted fraction	0.829 ± 0.002	0.111 ± 0.001	0.0557 ± 0.0006	0.0044 ± 0.0003

Table 6.1: Pythia Monte Carlo fractions (true fractions) and fitter result

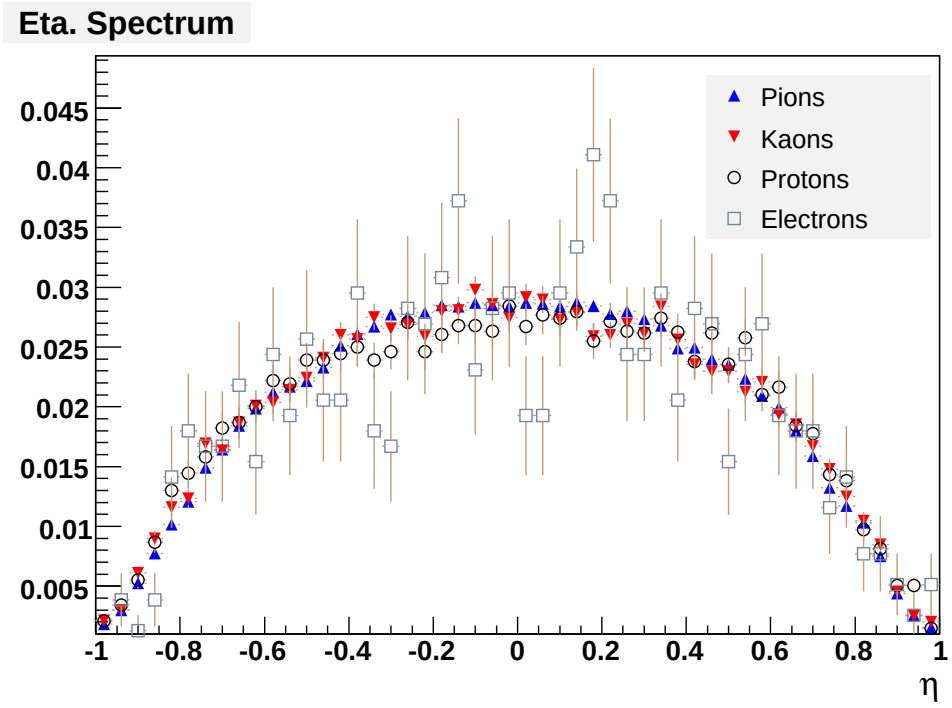

Figure 6.12: Overlay of Pythia η distributions of each particle type.

Using the particle fractions and the covariance matrices estimated in each P_T bin we can produce the *sPlots* of other kinematical variables.

Figures 6.14 − 6.18 show examples of distributions of a number of kinematical variables obtained in this way. In all cases a very good agreement is observed between the *true* distributions and the corresponding fit, even in those cases where high correlation with the P_T of the particle is expected.

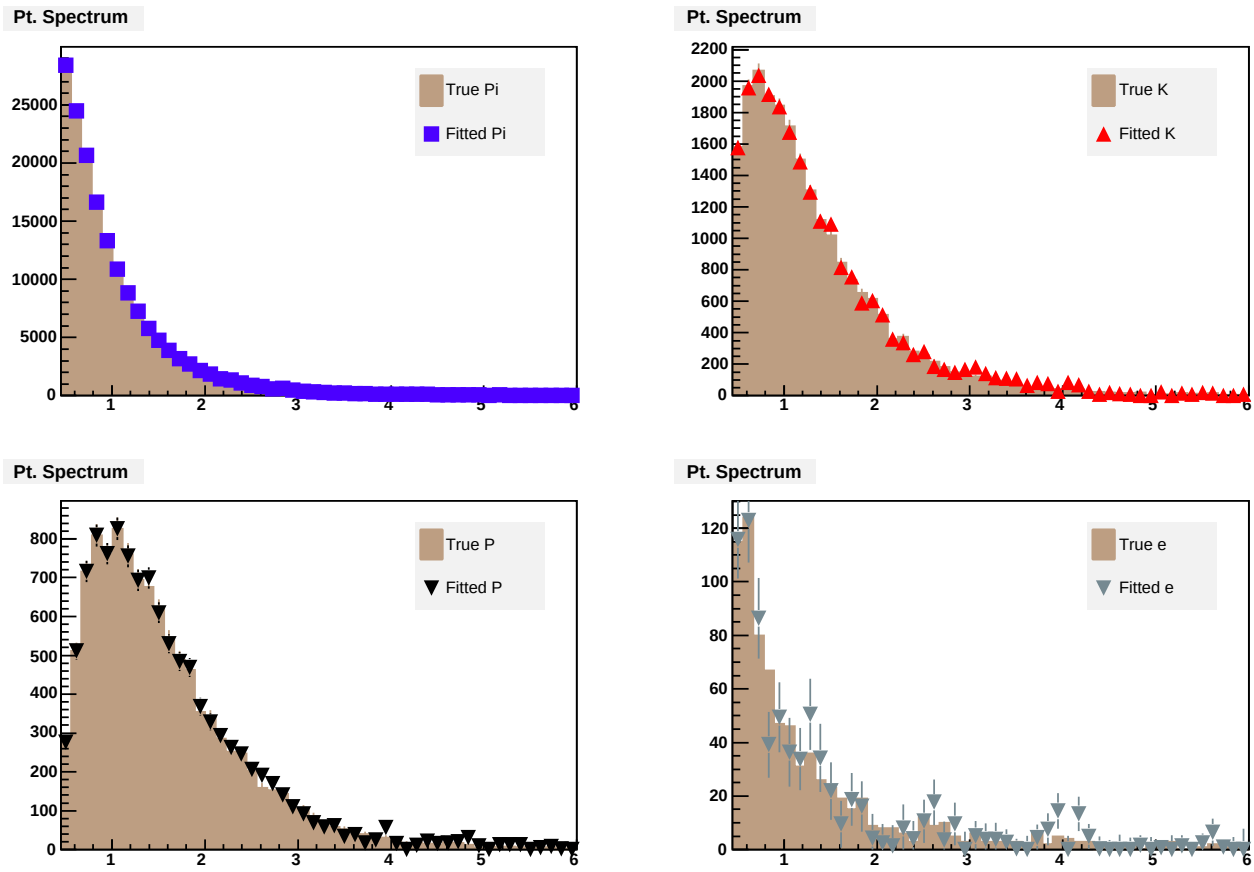

Figure 6.13: Overlay of the MC P_T distributions (filled histograms) and the result from the fit (dots) of each particle species.

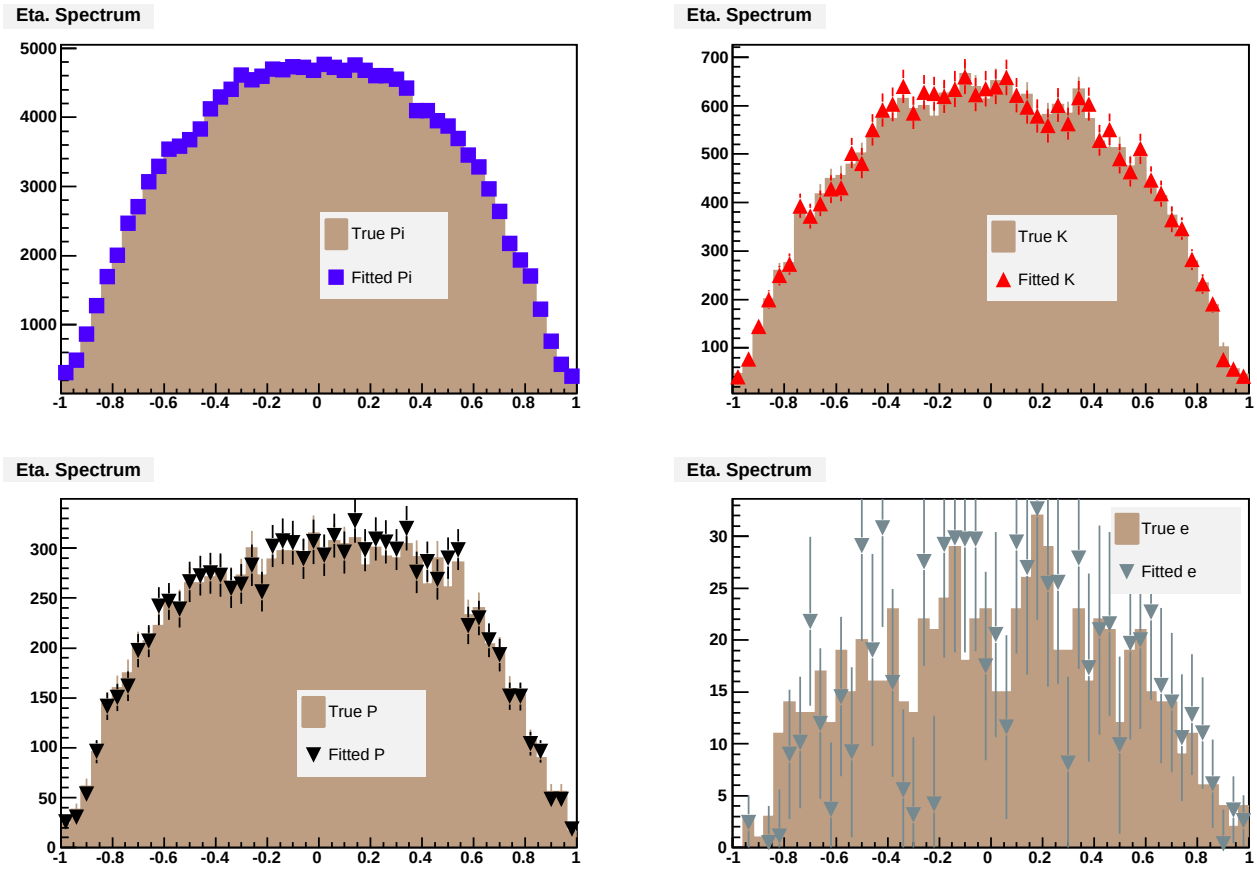

Figure 6.14: Pythia MC η distributions overlaid to the corresponding data *sPlot* of each particle species.

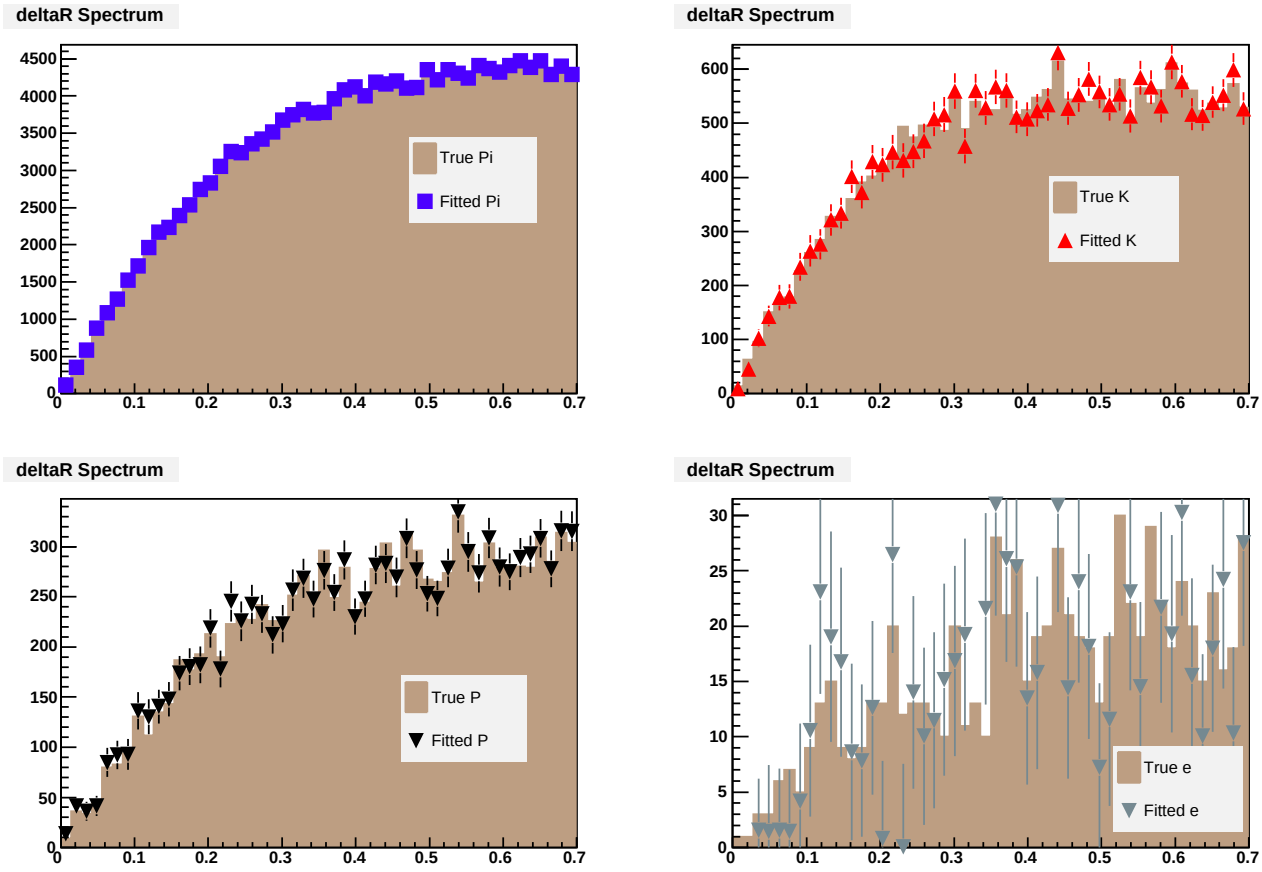

Figure 6.15: Pythia MC $\Delta R = sqrt\Delta\eta^2 + \Delta\phi^2$ distributions overlaid to the corresponding data *sPlot* of each particle species.

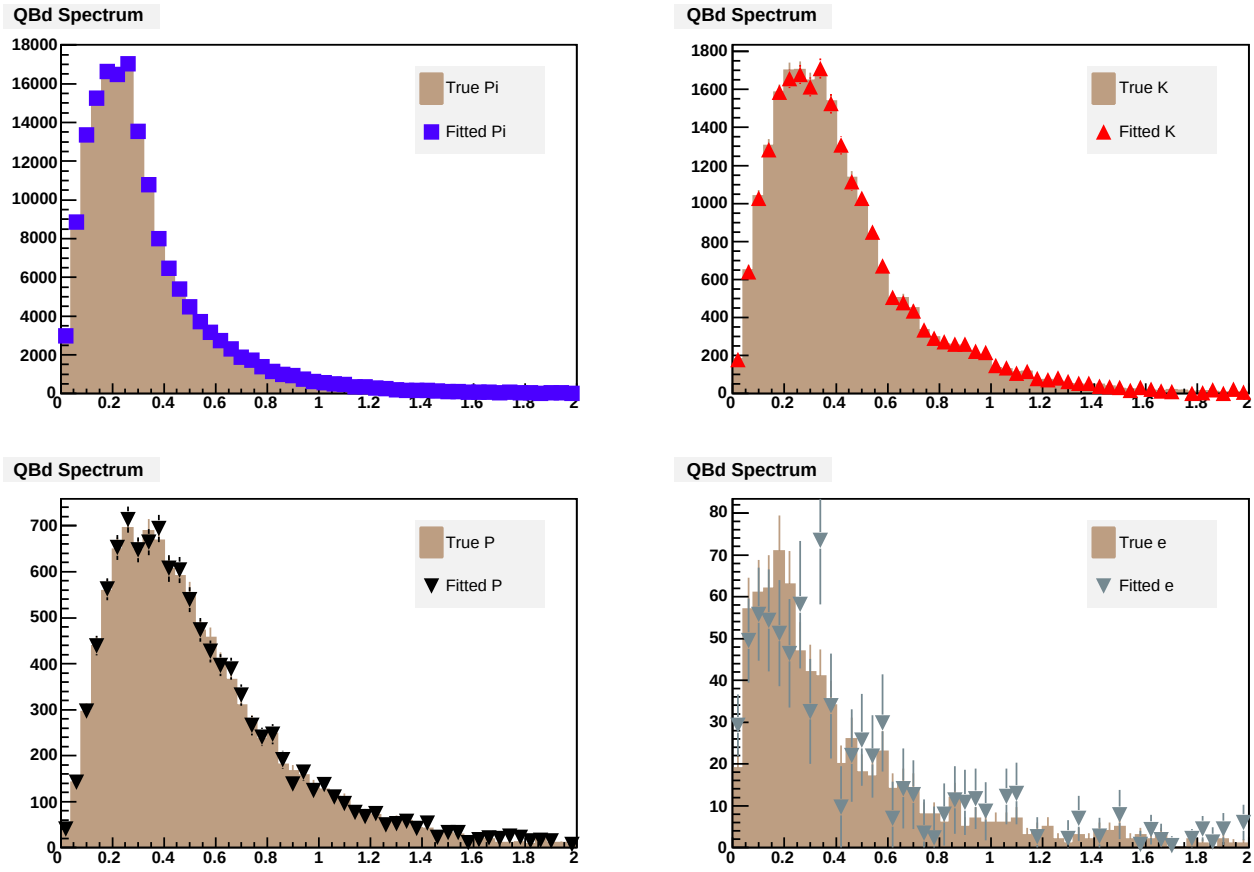

Figure 6.16: Pythia MC $M(B\pi) - M(B) - M(\pi)$ distributions overlaid to the corresponding data *sPlot* of each particle species.

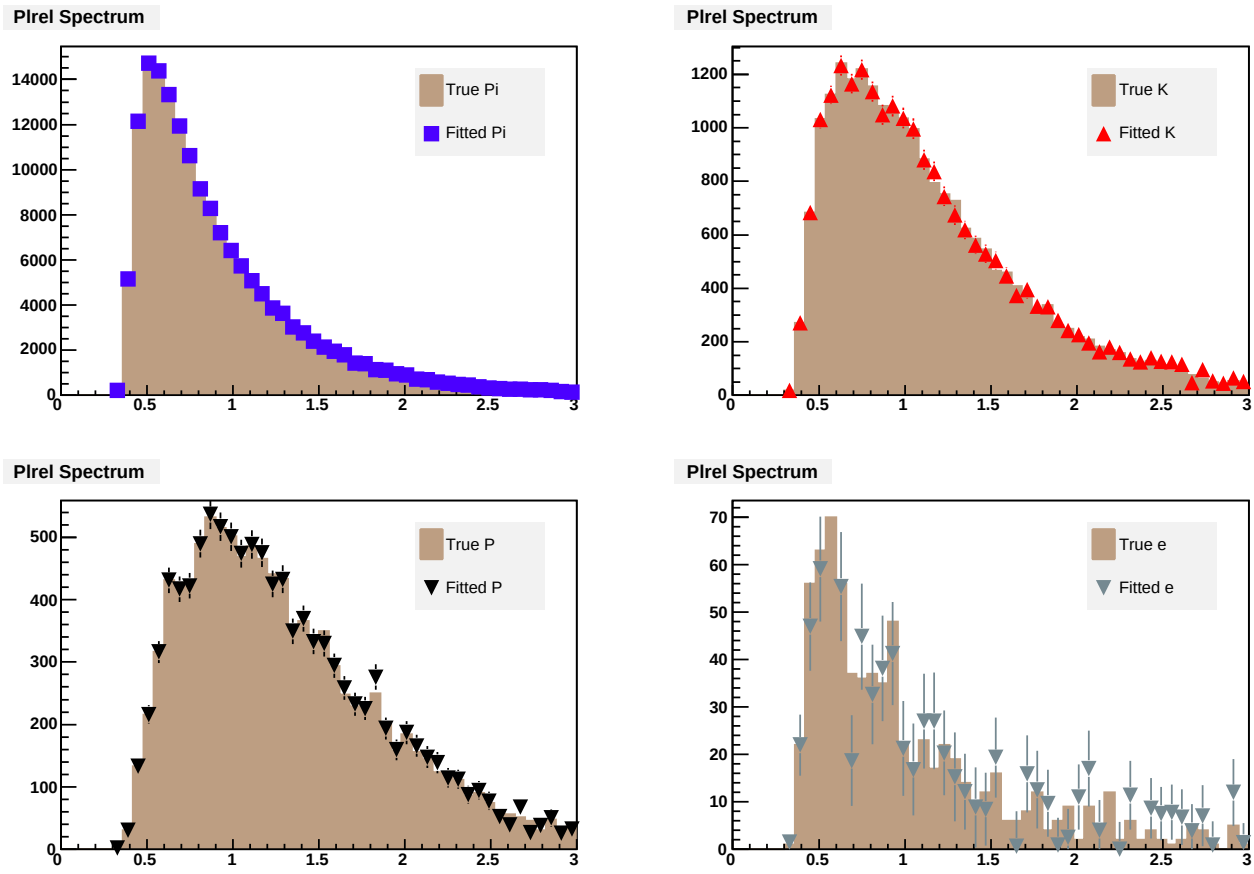

Figure 6.17: Pythia MC P_{Lrel} distributions overlaid to the corresponding data *sPlot* of each particle species. With P_{Lrel} we indicate the longitudinal component of the particle momentum respet to the flight direction of the B meson.

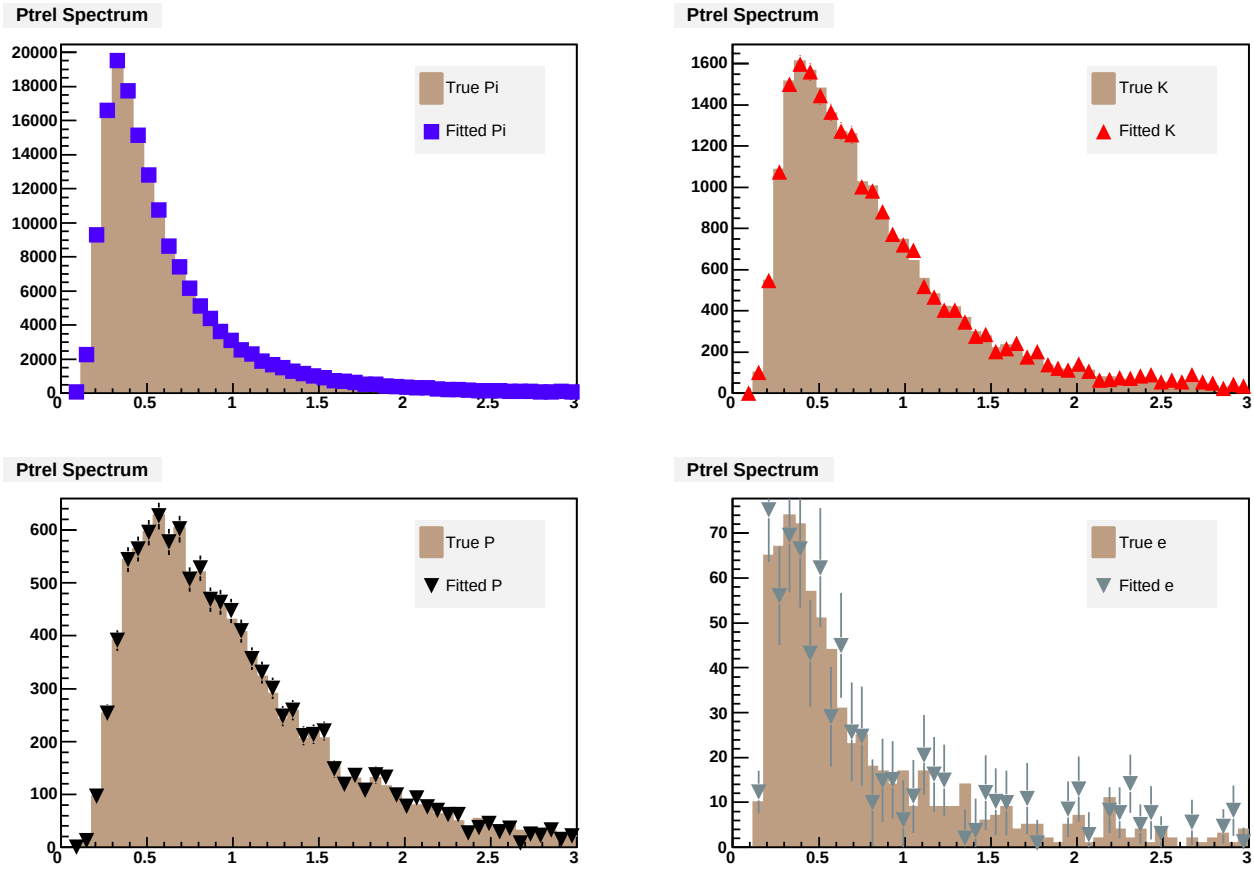

Figure 6.18: Pythia MC P_{Trel} distributions overlaid to the corresponding data *sPlot* of each particle species.With P_{Trel} we indicate the transversal component of the particle momentum respet to the flight direction of the B meson.

Chapter 7

Particle Fractions Measurement

In the previous chapter we described the techniques we developed for this analysis. In this chapter we will present the measurement of the composition of the particles produced during the formation of the B^0, B^+ and B_s mesons. A description of the sample used for this measurement can be found in chapter5.

7.1 What we measure (and do not)

Before describing and showing experimental results, we have to define in more detail what we are actually going to measure.

We will provide the fractions of particle types produced during the B meson formation without considering detector efficiency or particles decaying in flight. This is mainly because we would like to provide additional information in order to improve and have a better understanding of flavor tagging algorithms. In practice, when we want to determine the B flavor at production time looking at the tracks around it, we have to take a decision making use of the reconstructed tracks only. Additional effects, like track reconstruction efficiency and/or particles decaying in flight, cannot be considered.

At the same time, in order to compare data to Monte Carlo predictions, we prefer to correct the Monte Carlo to reproduce such effects without the application of any kind of corrections to data.

Notice that the majority of the particles that are reconstructed as the tracks in the detector belong to one of the five species: π, K, P, e and μ. Our particle identification capabilities allow to distinguish between all these types with the exception of muons and pions that, having similar masses, are practically indistinguishable using the measurement of the time-of-flight and energy loss thruough the TOF and COT detectors: as a conqsequence of this, in all the quoted results the measurement marked as for the pions should be understood as *including the muon contribution.*

Moreover, we will provide *raw* fractions in the sense specified before: given a B sample we developed a method that, on a statistical basis, estimates the number of π, K, P and e that on average are produced in association with the B and the corresponding kinematical properties .

Such results can depend on the reconstructed B decay mode due to the different kinematics of the decay products and/or the particular kinematics selections of the given B signal. As a consequence of this, they cannot be used as an absolute estimate of the particle type composition.

7.2 The Strategy

We will now define the strategy that will be followed to achieve our measurement. This strategy is based on the method described in chapter 6 where fits are performed in small momentum bins using the Channel Likelihood technique for the maximization of likelihoods.

- First of all we have to establish a method that allows to separate B meson signal (S) tracks from the background (B) contributions.

  In chapter 5, we developed a machinery that, using a Maximum Likelihood fit, is able to estimate the yield of signal B events and the corresponding background composition. We then selected a sample of tracks, as described in chapter 5, that is a mixture of charged particles produced during the formation of signal B events or produced in association with B background candidates. At each track corresponds a particular reconstructed B candidate; notice that the relation is not biunivocal because several tracks can share the same B candidate or a B candidate could have no tracks satisfying selection requirements in its vicinity.

  To statistically separate signal tracks from background ones, we apply the same strategy described in chapter 5 making use of a maximum likelihood fit. The discriminating varible between the two classes of tracks is then the mass of the corresponding B candidate: we perform a fit of the invariant mass distribution of the reconstructed B candidates when each event is a track found in its vicinity; the resulting mass distribution will then have the multiplicity of the tracks and not the multipllicity of the B candidates as in chapter 5. This procedure allows to estimate the composition in terms of signal and background and the corresponding probability distribution functions of the charged particle sample.

  Once the above mass fits are performed, the mass tempaltes of the track sample are determined and frozen for each decay mode, both for signal and background. As example we report in Fig.7.1 the projection of the Maximum Likelihood fit of the invariant mass distribution with the candidate multiplicity as obtained in chapter 5 (upper left) and the corresponding fit with track multiplicity (upper right) for $B^+ \to J/\psi\, K^+$ events.

  In particular, only in the case of the hadronic modes due to the complicated mass shape, we first fit the mass distribution in a wide range (the same of chapter 5) in order to estimate the contribution of the physical backgrounds; we then fix those contributions and we fit again the mass distribution in a smaller range where only signal parameters and combinatoric background parameters are left free to float

in the Maximum Likelihood fit (Fig.7.1 bottom, the $B^+ \to \overline{D}^0 \pi^+$ mass fit with the track multiplicity in the restricted range).

Given the above procedure, we finally determine the signal track mass *pdf* and the background track mass *pdf* denoted respectively by $\mathcal{M}^S$ and $\mathcal{M}^B$.

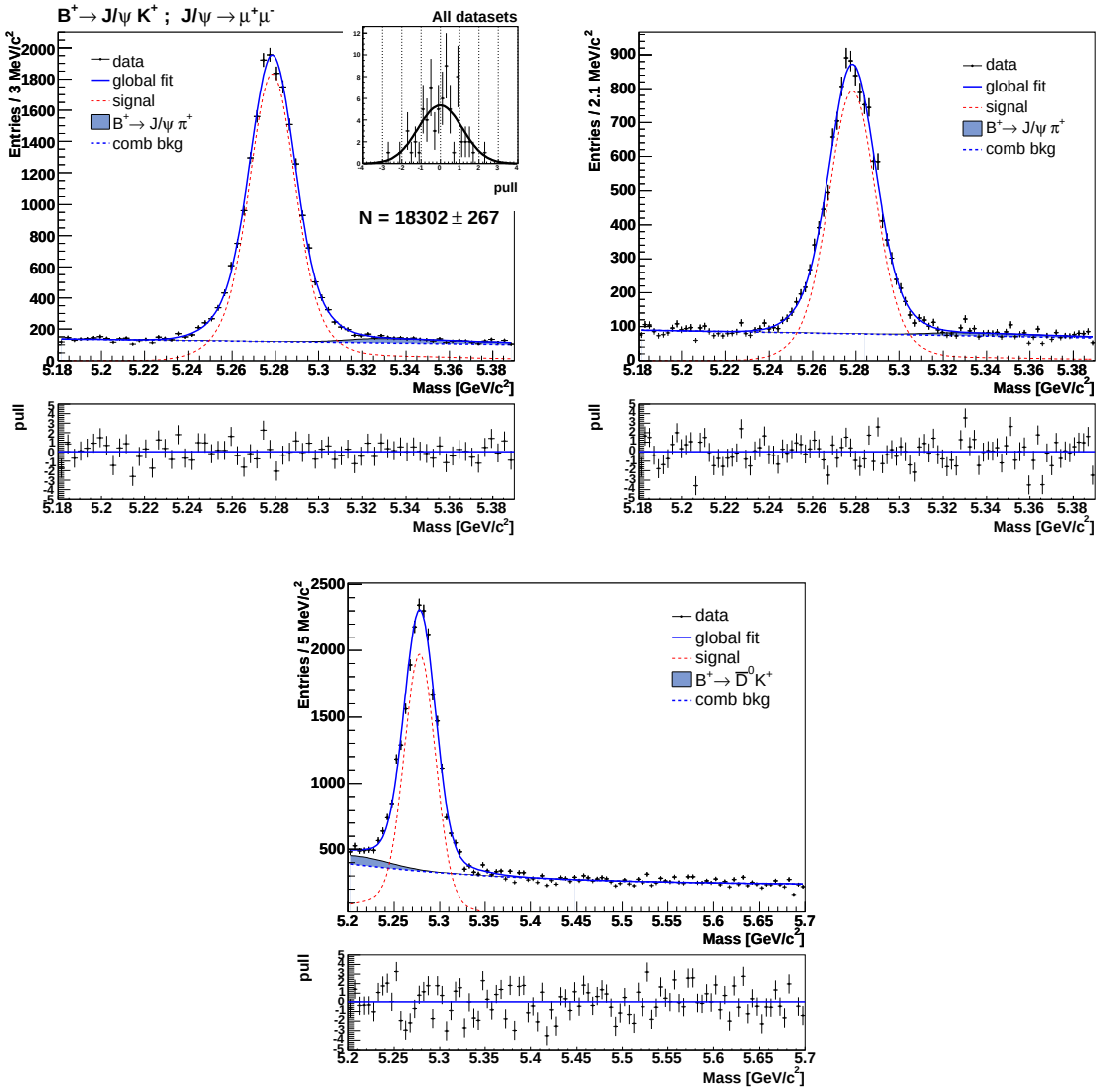

Figure 7.1: Projections of the $B^+ \to J/\psi\, K^+$ mass distribution fits when each entry corresponds to: a B candidate (upper left);a charged particle around a B candidate (upper right). Projection of the $B^+ \to \overline{D}^0 \pi^+$ mass fit in a narrow mass range around the signal when each entry correspond to a charged particle around the B.

- Once we have determined a procedure to separate signal from background tracks, we can proceed to the particle species fit using the Channel Likelihood method. The separation power between each particle type is provided by the use of TOF

and dE/dx measurements in the CDF detector. If we were to know the particle type beforehand, the measured TOF and dE/dx subtracted the corresponding expected value, are distributed according to the resolution function determined in [83] [84]. We then write the probability density function of a certain track with a given momentum and arclength to be of type j, both for TOF and dE/dx, as:

$$\begin{aligned} Res(TOF)_j &= TOF_{measured} - TOF_j^{expected} \\ Res(dE/dx)_j &= dE/dx_{measured} - dE/dx_j^{expected} \end{aligned} \tag{7.1}$$

Our observables will then be *for each track*: the mass of the corresponding B candidate, the measured TOF, the momentum, the artclength of the track from the interaction vertex to the TOF detector and the measured dE/dx.
As argued in the previous chapter and clearly shown in Fig.6.12, after having observed that momentum and arclength can be replaced by P_T and η with no loss of information, the η distribution can be factorized from the Likelihood function. It is reasonable to make the same assumption on data.
We will then divide our sample of tracks in P_T bins (the number of bins will vary from 50 to 25 depending on the statistics of each decay channel) from 0.45 to 6,0 GeV/c. In each bin we want to estimate the number of particles of each type, 4 types for signal events and 4 types for background ones for a total of 8 parameters, respectively: N_π^S, N_K^S, N_P^S, N_e^S, N_π^B, N_K^B, N_P^B, N_e^B.
In each P_T bin ΔP_T, following what shown in chapter 6, we define the iteration:

$$(N_{j,\Delta P_T}^C)^{n+1} = \sum_{i=1}^{N} \frac{(N_{j,\Delta P_T}^C)^n \mathcal{M}^C(mass_i) Res(TOF_i)_j Res(dE/dx_i)_j}{\sum_{C=S,B} \sum_{l=\pi,K,P,e} (N_{l,\Delta P_T}^C)^n \mathcal{M}^C(mass_i) Res(TOF_i)_l Res(dE/dx_i)_l} \tag{7.2}$$

where $(N_{j,\Delta P_T}^C)^{n+1}$ is the number of charged particles of type j of signal, $C = S$, or background, $C = B$, as determined at the iteration step $n + 1$ in the interval ΔP_T.
Once the iterations have converged, for each P_T bin we obtain the eight estimates of $N_{j,\Delta P_T}^C$ with the corresponding statistical uncertainties evaluated by the covariance matrix defined as eq.(6.21). Those values are then used to produce eight histograms (an examle is shown in Fig.7.2): each histogram represents a good estimate of the P_T spectrum of the corresponding particle type. Finally, each particle type fraction and the corresponding statistical uncertainty are extracted using the relations 6.23 and 6.24.

- In principle, the Channel Likelihood method (CL, in the following) provides both the P_T distribution and the total number of each particle species, from which the relative fractions can be easily computed as previously mentioned: for high statistics modes this gives a very accurate result; however, in the case of rarer

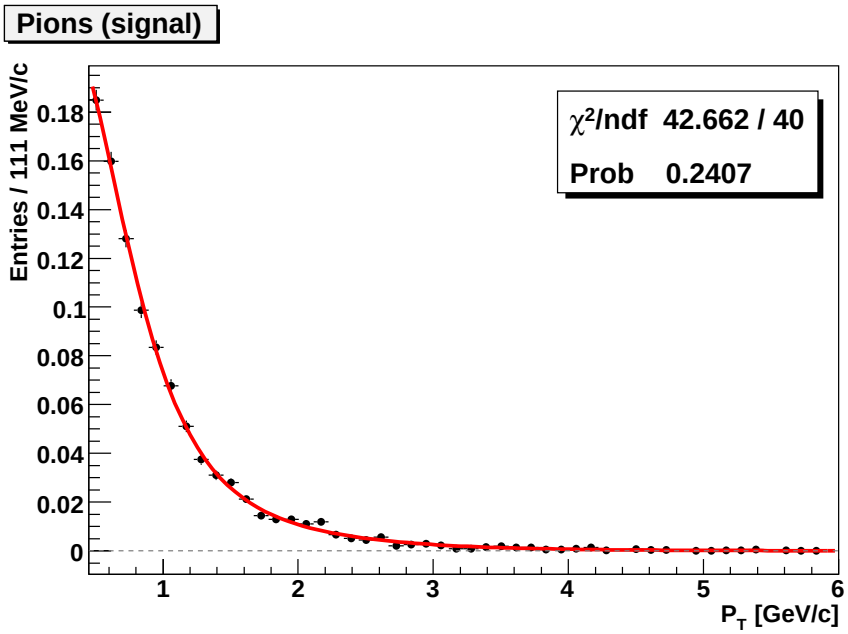

Figure 7.2: P_T distribution of pions produced around $B^+ \to \overline{D}^0 \pi^+$ events extracted using the CL procedure. The fit to the distribution using the functional form (7.5) is overimposed.

decays, as the B_s modes, the P_T bins are poorly populated and, in particular, it may occur to have a significant number of empty bins along the spectrum. Obviously, empty bins are not considered in the iterative procedure, and this may cause a bias on the total fraction of particle species and an underestimation of the corresponding statistical uncertainty.
To obtain a more accurate estimate of the fractions we fit the P_T distributions obtained by the Channel Likelihood with appropriate functions (see Fig.7.2). We then use those shapes as *pdf* in a Maximum Likelihood fit (ML, in the following) on the whole P_T range. The likelihood maximization is performed by the standard MINUIT package [82]. The overall procedure followed for the particle fractions measurement can be resumed in two steps: at first, the CL method is used as a procedure to extract the unknown P_T distributions $\mathcal{P}(P_T)$; second, these distributions are plugged in a ML fit to estimate the particle fractions on the whole P_T spectrum; notice that the bias discussed in chapter 6 is avoided since we are using the correct likelihood expression (6.2) that includes the P_T *pdf* of each particle species. The corresponding log-likelihood to be maximized will be:

$$Log(L) = \mathcal{L} = \sum_{i=0}^{N} \Big(\sum_{j=\pi,K,P,e} f_j^S \mathcal{M}^S(mass_i) Res(TOF_i)_j Res(dE/dx)_j \mathcal{P}^S(P_T)_j \quad (7.3)$$
$$+ \sum_{j=\pi,K,P,e} f_j^B \mathcal{M}^B(mass_i) Res(TOF_i)_j Res(dE/dx)_j \mathcal{P}^B(P_T)_j \Big)$$

with the conditions:

$$\sum_{j=\pi,K,P,e} f_j^S = 1 \qquad \sum_{j=\pi,K,P,e} f_j^B = 1 \tag{7.4}$$

In next sections, it will be also shown that, as expected, the CL and the ML results will provide compatible results.

7.3 Fitter validation

To check the behavior of both the CL and ML fitters, we performed some pseudo-experiment studies for all the decay modes considered in the measurement.

Our pseudo-experiment samples (also called *toy-samples*) are generated to reproduce as much as possible the same characteristics of the data samples: we apply our fitting procedure on data to extract all the distribution templates and the particle species fractions; we then fix all the estimated parameters to generate the toy-samples. Signal and background events are distributed according to the mass shape fitted on data; particle species fractions and P_T spectra for both signal and background tracks are generated according to the distributions extracted from data. 2000 toy-samples were generated for each decay mode; each toy-sample has a statistics compatible with the corresponding data sample. We then apply the CL and the ML procedures described in the previous section to each sample.

For simplicity, we report here the results of $B_s \rightarrow D_s^- \pi^+$ case: due to the low number of reconstructed B_s events, we expect this to be the more pathological case, where all the limitation of low statistics (if any) should arise in the pseudo-experiments study.

Each point of the plots in Fig.7.3 represents, for a given P_T bin and a given particle species, the mean value of the $N_{fit} - N_{true}$ residual distribution resulting from the 2000 pseudo-experiments[1]. The error bar associated to the point is the corresponding $N_{fit} - N_{true}$ RMS. No significant bias is observed in the residual distributions both for signal and background tracks of each species.

No significant bias is also observed in the residual distribution of the particle fractions integrated on the whole P_T range ($(f^{fit} - f^{true})$) as shown in fig.7.4. In this case the 2000 toy-samples are fitted using the ML procedure.

[1] N_{true} is the number of generated particles of the given type and N_{fit} is the corresponding fitted number extracted by the CL procedure in the given P_T bin.

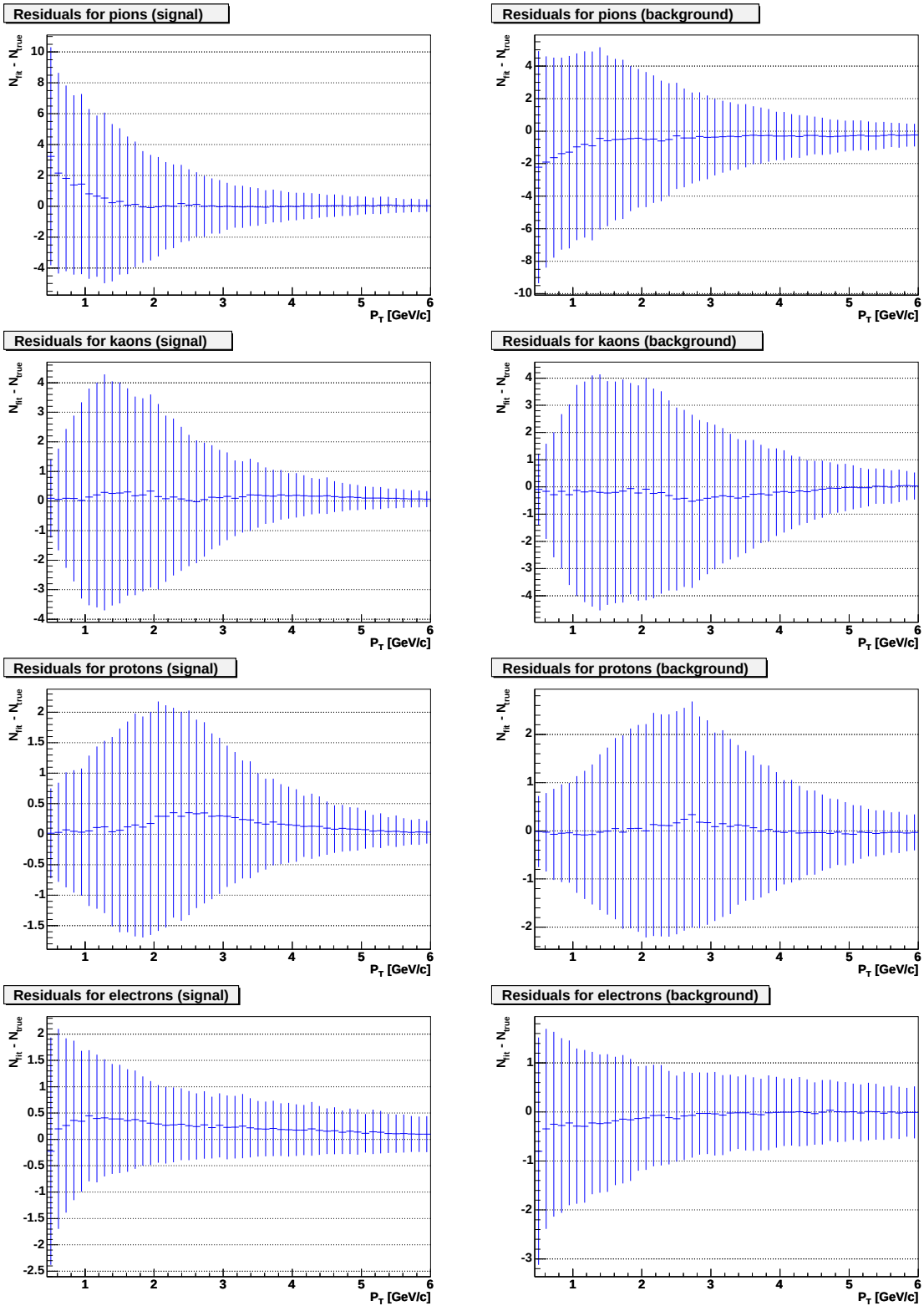

Figure 7.3: $B_s \to D_s^- \pi^+$. Residuals of the particle content estimators in each P_T bin resulting from application of the CL to 2000 toy-samples of $B_s \to D_s^- \pi^+$ events. Each point represents the mean value of the residual in a given bin while error bar is the corresponding RMS.

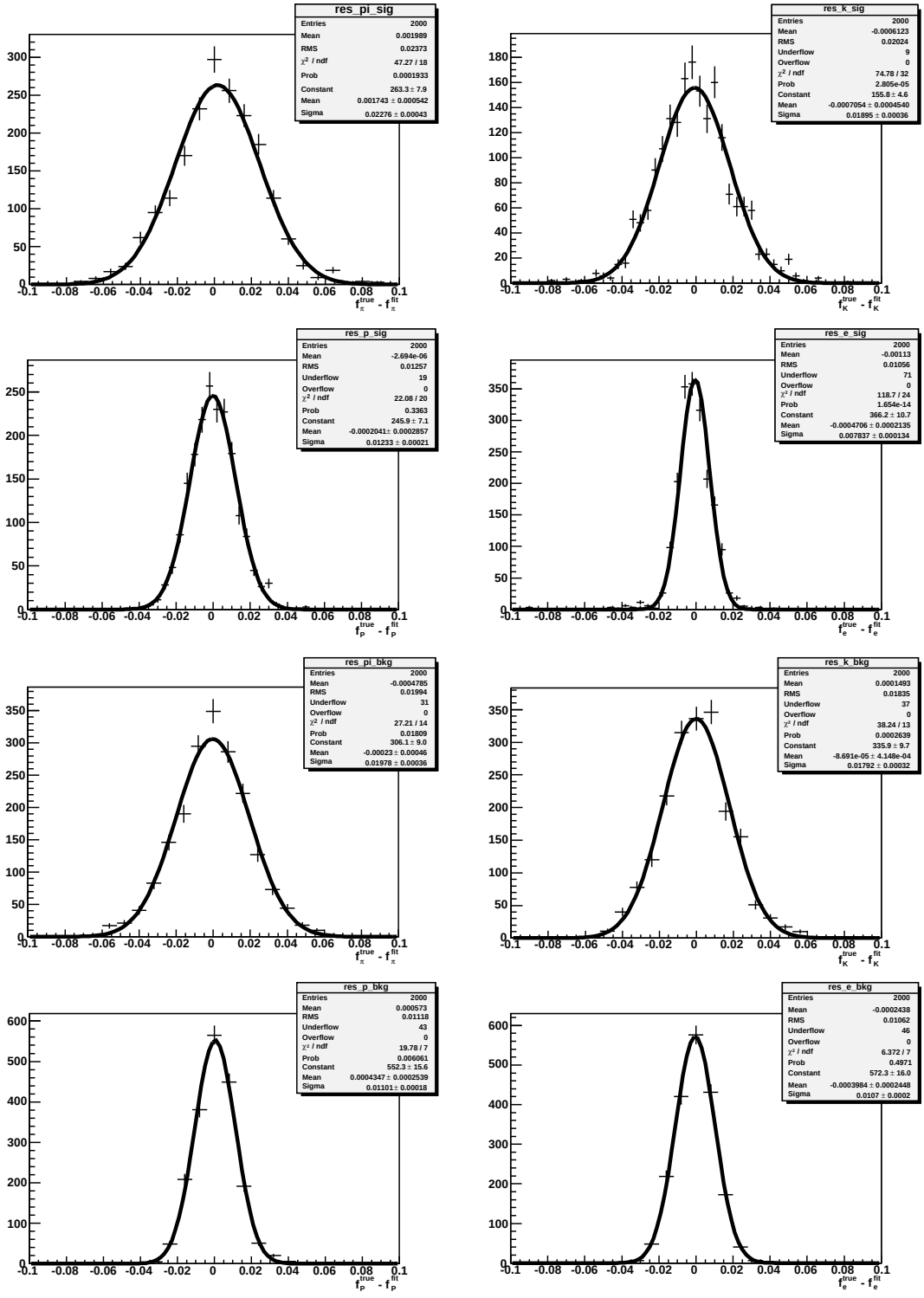

Figure 7.4: $B_s \to D_s^- \pi^+$. Residuals of the particle fraction estimators on the whole P_T range resulting from the application of the ML procedure to 2000 toy-samples of $B_s \to D_s^- \pi^+$ events.

7.4 Measurement of the particle content

We first apply the CL method separately to the datasets relative to the three data taking periods, both for hadronic and J/ψ modes, to check that results are consistent among them. As shown in more detail in next sections, form the comparison we conclude that the P_T spectra and the particle composition of the three data taking periods are compatible with each other within the errors.

Therefore we merge the datasets and apply the method to the whole sample. We notice that, as expected, spectra of different particles are significantly different in all the considered decay modes. Moreover, a not negligible difference appears also between signal and background spectra of the same kind of particles.

In order to have an accurate estimate of the particle fractions and to cross-check the CL result with the ML fit, we need the templates of the P_T spectra. Therefore, we found that the pion, kaon and proton P_T distributions resulting from the CL fit can be suitably parameterized (for all the decay modes, both signal and background) by the function:

$$a_0 \, (P_T - a_1) \, e^{-P_T/a_2} + a_3 \, (P_T - a_4) \, e^{-P_T/a_5} \ , \tag{7.5}$$

where $a_0 ... a_5$ are free parameters determined by a binned fit of the P_T histograms. Whereas for electrons we used (again for each decay modes, both signal and background) the function:

$$b_0 \, {P_T}^{b_1} \ . \tag{7.6}$$

where b_0 and b_1 are determined by a binned fit.

In the following sections we repeat the same exercise for all the decay modes.

7.4.1 $B^+ \to J/\psi \, K^+$

We divide the P_T range 0.45-6 GeV/c into 50 bins and the CL procedure is performed in each bin. Results are shown in Fig. 7.5: the distributions obtained in `xpmm0d`, `xpmm0h`, and `xpmm0i` datasets are normalized to one and superimposed. Uncertainties are statistics only and have been calculated bin per bin from the fit covariance matrix.

The resulting P_T spectra merging the three datasets, normalized to unity, are shown in Fig. 7.6 with the correspondig fitted function superimposed. The results on the particle composition are listed in the upper half of Tab. 7.1.

Fig. 7.7 shows the mass and P_T projections of the ML fit. The reduced χ^2 of the projections are: $\chi^2/\mathrm{ndf} = 173/100$ and $\chi^2/\mathrm{ndf} = 98/83$.

Tab. 7.1 summarizes the results for the $B^+ \to J/\psi \, K^+$ channel. It reports the results obtained with both the CL and ML methods for the different datasets along with the final result over the whole sample.

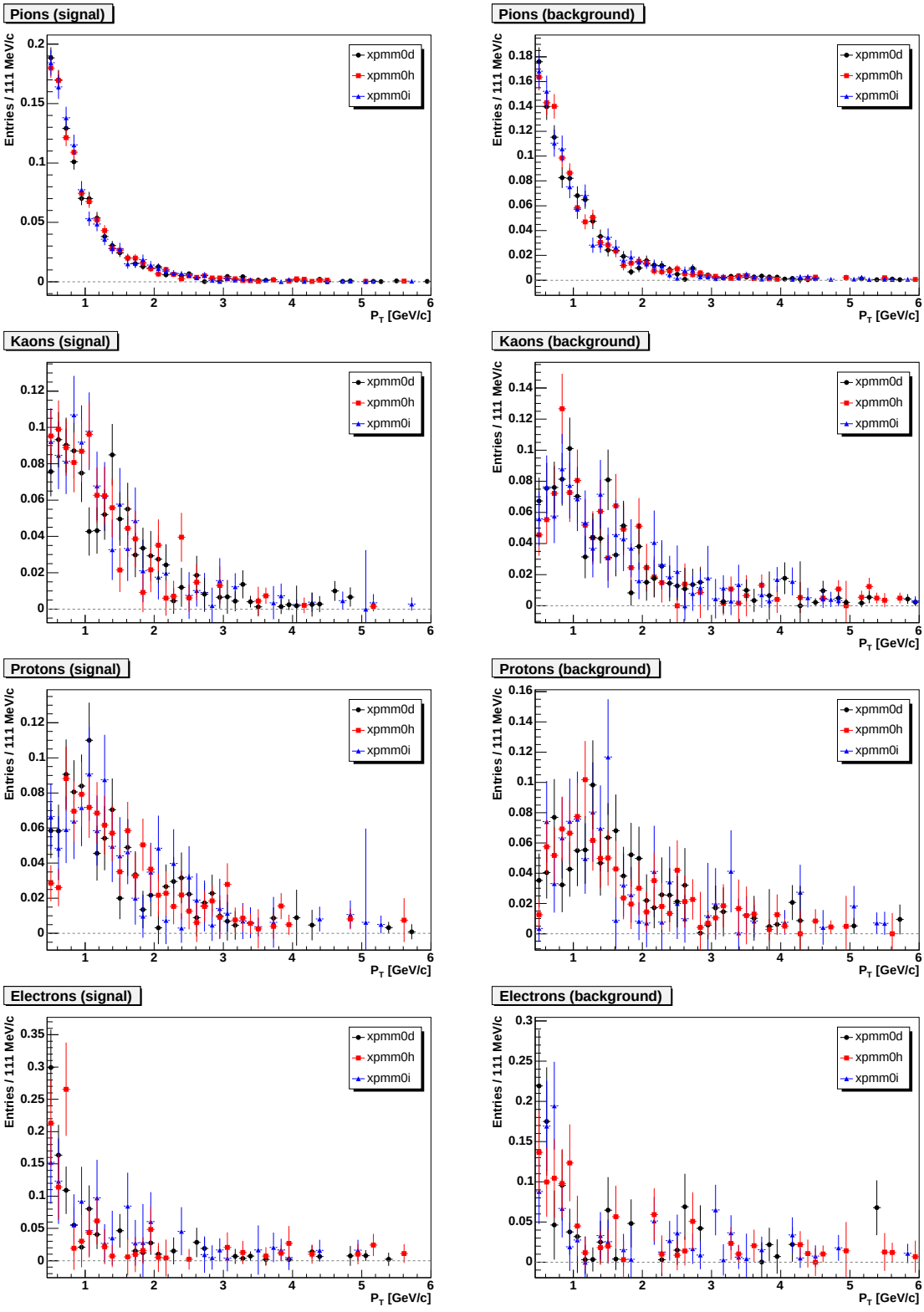

Figure 7.5: $B^+ \to J/\psi K^+$ decay. P_T distributions returned by the Channel-Likelihood fit for pions, kaons, protons, and electrons of signal (left plots) and background (right plots). The distributions obtained in `xpmm0d`, `xpmm0h`, and `xpmm0i` datasets are normalized to one and superimposed.

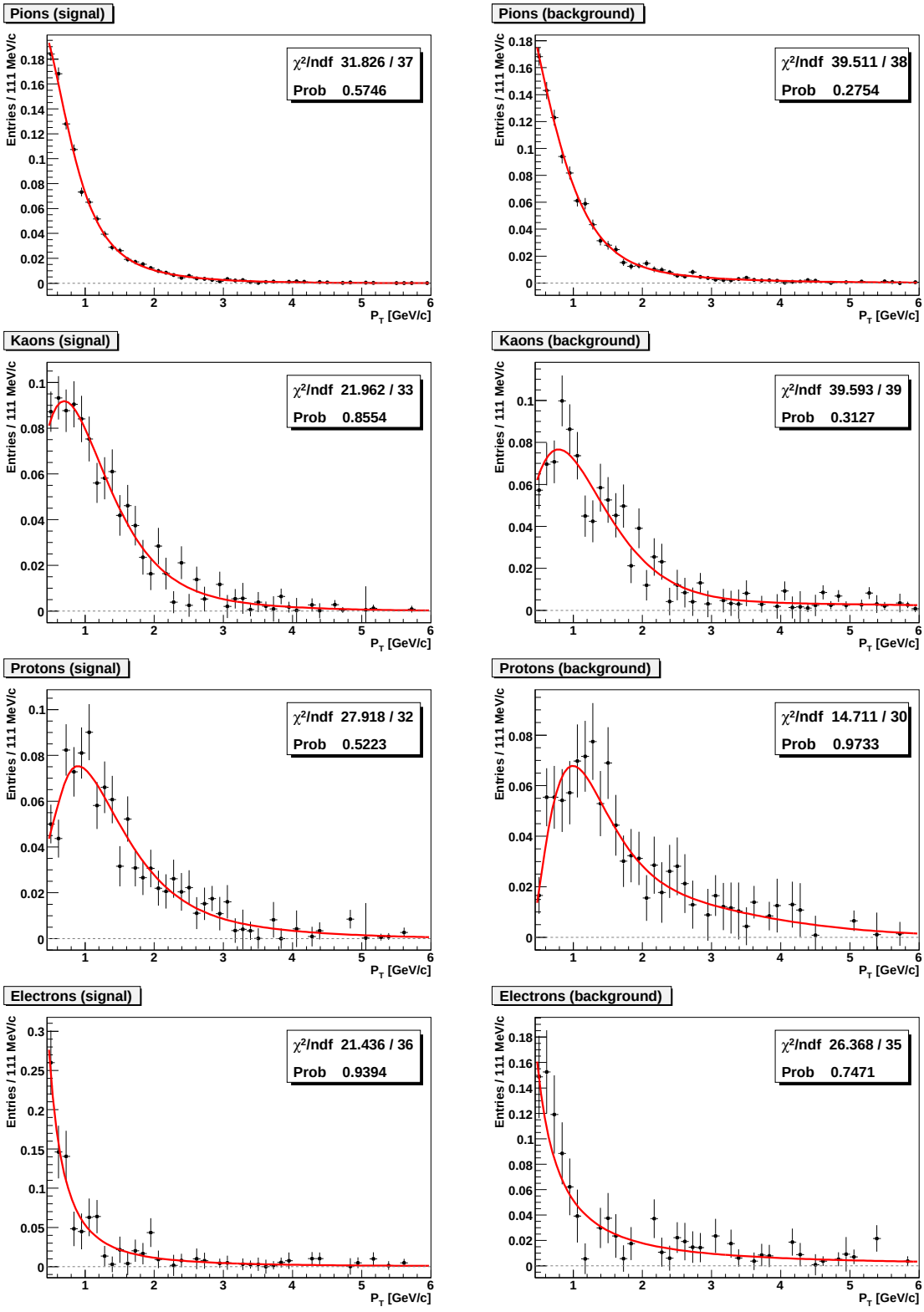

Figure 7.6: $B^+ \to J/\psi\, K^+$ decay. P_T distributions from Channel-Likelihood method for pions, kaons, protons, and electrons of signal (left) and background (right).

			0d	0h	0i	tot
Channel Likelihood	SIGNAL	π	76.08 ± 0.91	78.11 ± 0.87	76.98 ± 1.20	77.37 ± 0.59
		K	13.27 ± 0.77	12.42 ± 0.73	13.53 ± 1.02	13.00 ± 0.50
		p	7.29 ± 0.52	7.54 ± 0.52	7.27 ± 0.74	7.32 ± 0.35
		e	3.35 ± 0.39	1.93 ± 0.31	2.22 ± 0.42	2.31 ± 0.22
	BKG	π	73.59 ± 1.28	74.83 ± 1.23	72.74 ± 1.48	74.05 ± 0.76
		K	16.26 ± 1.13	13.97 ± 1.04	15.91 ± 1.28	15.06 ± 0.65
		p	7.03 ± 0.72	7.83 ± 0.74	7.00 ± 0.85	7.42 ± 0.44
		e	3.12 ± 0.50	3.34 ± 0.51	4.35 ± 0.64	3.47 ± 0.31
Maximum Likelihood	SIGNAL	π	76.57 ± 0.92	78.13 ± 0.91	77.57 ± 1.20	77.33 ± 0.56
		K	12.76 ± 0.75	12.68 ± 0.76	13.68 ± 1.02	13.03 ± 0.47
		p	7.53 ± 0.51	7.32 ± 0.51	7.15 ± 0.65	7.35 ± 0.32
		e	3.14 ± 0.38	1.88 ± 0.31	1.60 ± 0.40	2.29 ± 0.21
	BKG	π	73.56 ± 1.28	75.27 ± 1.21	72.69 ± 1.51	74.05 ± 0.76
		K	16.35 ± 1.10	13.82 ± 1.01	15.53 ± 1.31	15.00 ± 0.64
		p	7.01 ± 0.69	7.86 ± 0.68	7.28 ± 0.83	7.46 ± 0.42
		e	3.08 ± 0.51	3.05 ± 0.49	4.50 ± 0.65	3.49 ± 0.31

Table 7.1: $B^+ \to J/\psi\, K^+$ mode. Comparison of the particle type fractions for signal and background componets calculated with the Channel-Likelihood and the Maximum-Likelihood methods separately for each dataset and for the full sample.

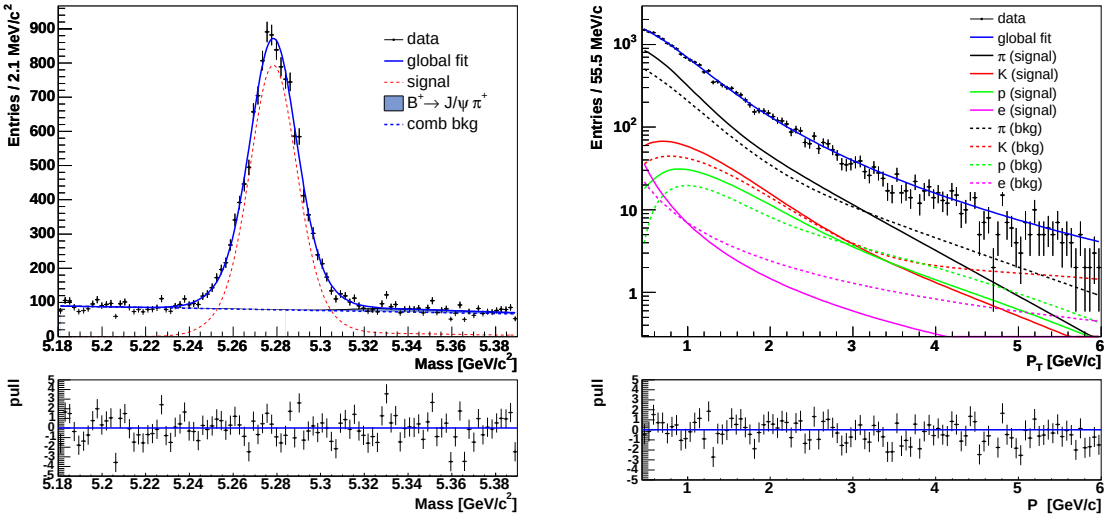

Figure 7.7: $B^+ \to J/\psi\, K^+$ decay. Mass (left), P_T (right), projections of Maximum-Likelihood fit.

The quoted errors are statistical only. We notice that both methods give the same result.

7.4.2 $B^0 \to J/\psi\, K^{*0}$

Like for the $B^+ \to J/\psi\, K^+$ mode, we first compare the P_T spectra of pions, kaons, protons and electrons obtained for signal and background in the three datasets. We run CL with 50 P_T bins in the range 0.45-6 GeV/c. The result is shown in Fig. 7.9, where histograms are normalized to one and the errors are given by the fit covariance matrix.

The result of the CL fit over the whole dataset is reported in Fig. 7.10. Histograms are fitted to the functions (7.5) and (7.6).

Fig. 7.8 shows the mass and P_T projections of the ML fit. The reduced χ^2 of the projections are: $\chi^2/\mathrm{ndf} = 167/100$ and $\chi^2/\mathrm{ndf} = 104/84$.

Tab. 7.2 summarizes the results for the $B^0 \to J/\psi\, K^{*0}$ channel. It reports the results obtained with both the CL and ML methods for the different datasets along with the final result over the whole sample.

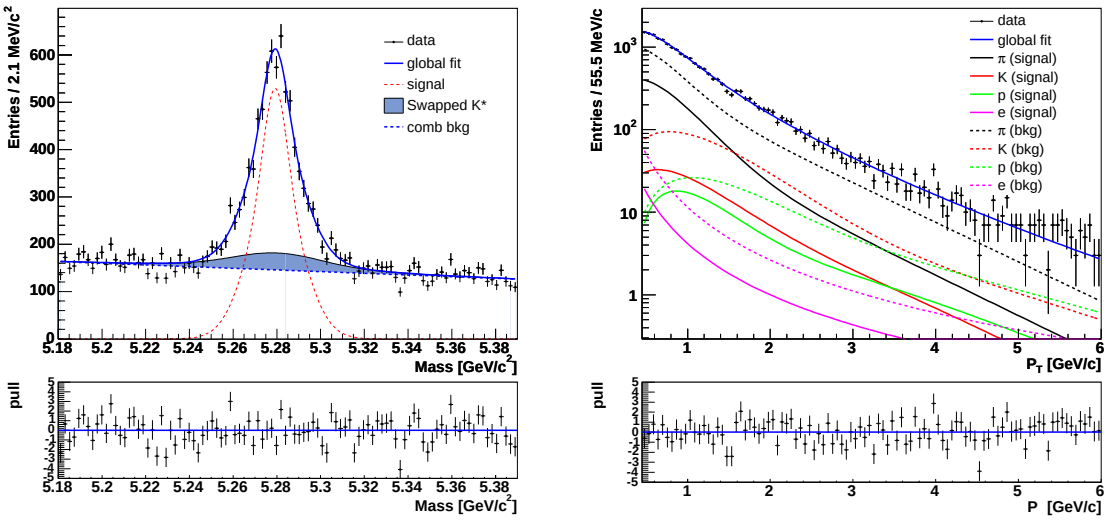

Figure 7.8: $B^0 \to J/\psi\, K^{*0}$ decay. Mass (left) and P_T (right) projections of the Maximum-Likelihood fit.

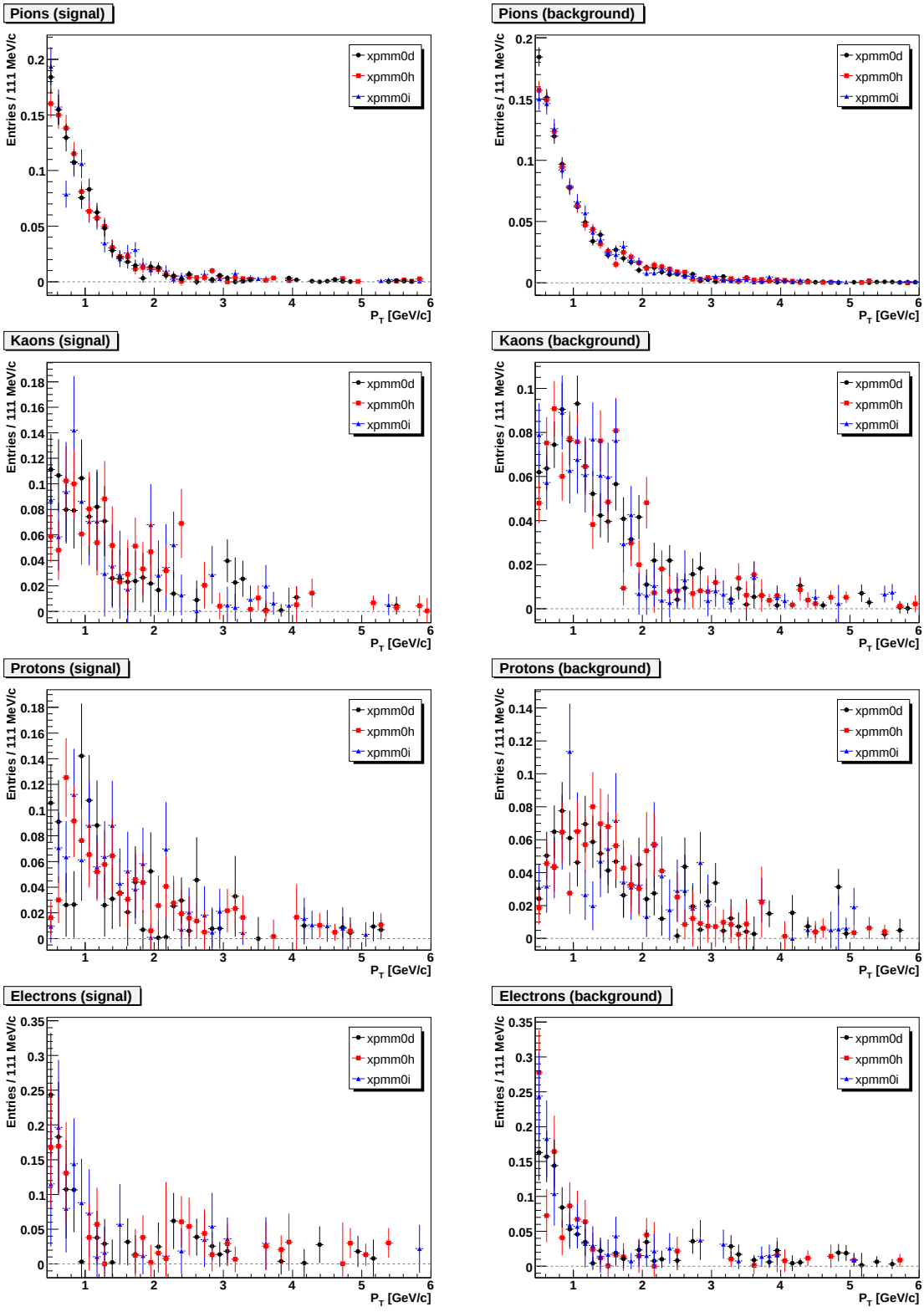

Figure 7.9: $B^0 \to J/\psi K^{*0}$ mode: P_T distributions of pions, kaons, protons, and electrons from the Channel-Likelihood method for both signal (left plots) and background (right plots).

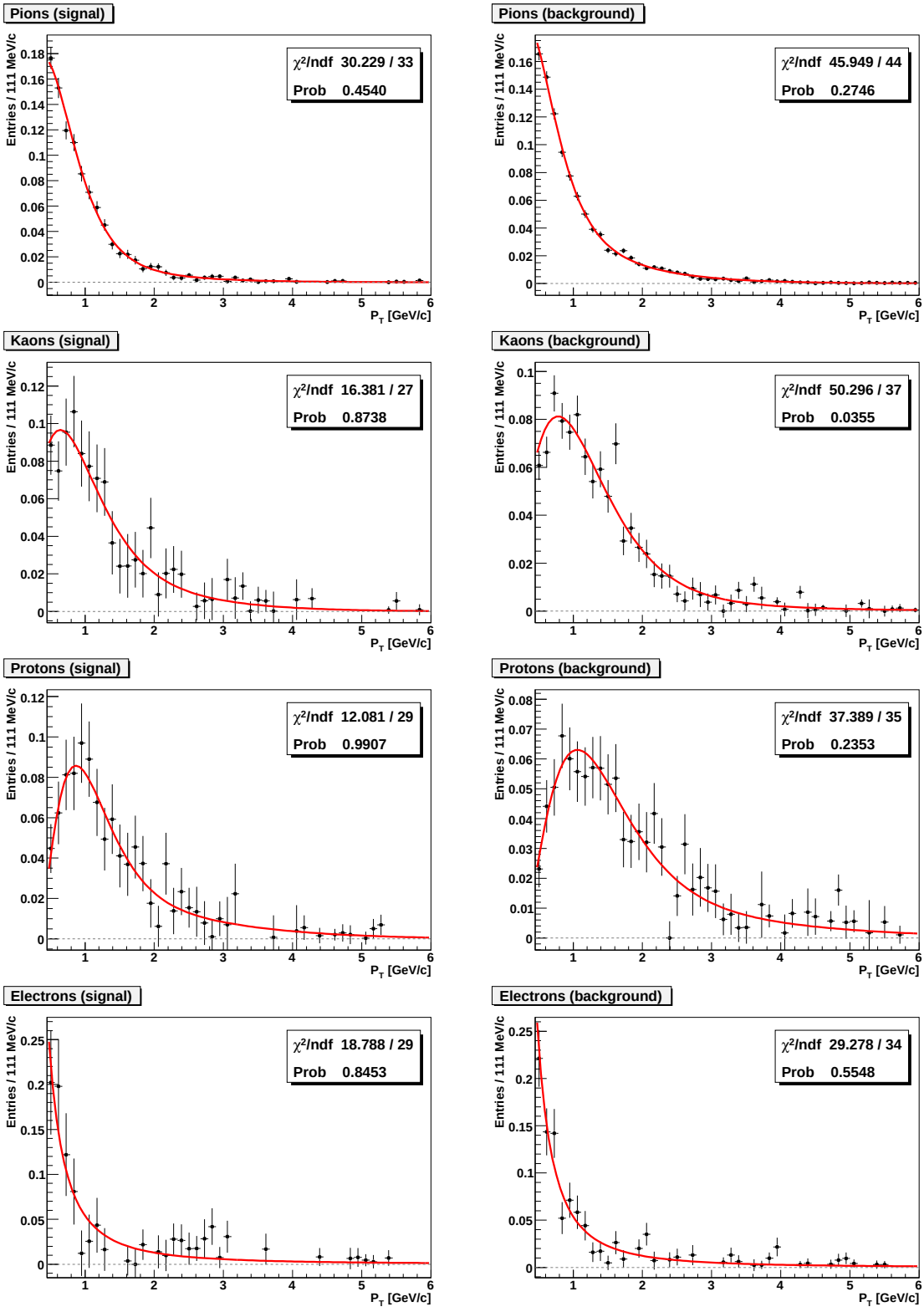

Figure 7.10: $B^0 \to J/\psi\, K^{*0}$ mode: P_T distributions of pions, kaons, protons, and electrons from the Channel-Likelihood method for both signal (left plots) and background (right plots).

			0d	0h	0i	tot
Channel Likelihood	SIGNAL	π	77.64 ± 1.48	77.52 ± 1.44	77.11 ± 1.72	78.25 ± 0.93
		K	12.39 ± 1.24	12.34 ± 1.21	11.45 ± 1.46	11.81 ± 0.80
		p	6.63 ± 0.83	7.35 ± 0.80	8.32 ± 0.99	7.17 ± 0.52
		e	3.35 ± 0.64	2.79 ± 0.64	3.11 ± 0.69	2.78 ± 0.36
	BKG	π	73.93 ± 0.80	75.83 ± 0.88	75.99 ± 1.04	75.19 ± 0.53
		K	16.57 ± 0.70	16.22 ± 0.77	15.51 ± 0.91	16.09 ± 0.47
		p	6.04 ± 0.44	5.41 ± 0.46	5.41 ± 0.54	5.74 ± 0.29
		e	3.45 ± 0.34	2.54 ± 0.36	3.08 ± 0.41	2.98 ± 0.21
Maximum Likelihood	SIGNAL	π	78.28 ± 1.57	79.19 ± 1.57	78.08 ± 1.95	78.54 ± 0.96
		K	12.23 ± 1.30	11.61 ± 1.33	11.35 ± 1.64	11.59 ± 0.80
		p	6.49 ± 0.81	7.07 ± 0.79	8.01 ± 1.01	7.21 ± 0.50
		e	3.00 ± 0.65	2.13 ± 0.55	2.57 ± 0.69	2.65 ± 0.37
	BKG	π	74.55 ± 0.83	75.53 ± 0.92	75.35 ± 1.12	75.20 ± 0.54
		K	16.19 ± 0.71	15.99 ± 0.81	16.38 ± 0.99	16.08 ± 0.47
		p	5.98 ± 0.42	5.78 ± 0.46	5.27 ± 0.54	5.75 ± 0.27
		e	3.27 ± 0.35	2.69 ± 0.35	3.00 ± 0.42	2.96 ± 0.21

Table 7.2: Particle type fraction for signal and background components for $B^0 \to J/\psi\, K^{*0}$ decay.

7.4.3 $B_s \to J/\psi\, \phi$

Also for the $B_s \to J/\psi\, \phi$ mode, we first compare the P_T spectra of pions, kaons, protons and electrons obtained for signal and background from the three datasets. In this case, due to the lower statistics of the data sample, the CL was performed in 25 P_T bins in the usual range 0.45-6 GeV/c. The result is shown in Fig. 7.11, where histograms are normalized to one and the errors are given by the fit covariance matrix.

The result of the CL fit over the whole dataset is reported in Fig. 7.12. Histograms are fitted to functions (7.5) and (7.6). Fig. 7.13 shows the mass and P_T projections of the ML fit.

The reduced χ^2 of the projections are: $\chi^2/\mathrm{ndf} = 98/50$ and $\chi^2/\mathrm{ndf} = 63/33$.

Tab. 7.3 summarizes the results for the $B_s \to J/\psi\, \phi$ channel. It reports the results obtained with both the CL and ML methods for the different datasets along with the final result over the whole sample. Due to the very low statistics, it has not been possible to apply the ML method to the 0i data period alone. The 0i is aniway considered in the ML fit on the whole data sample.

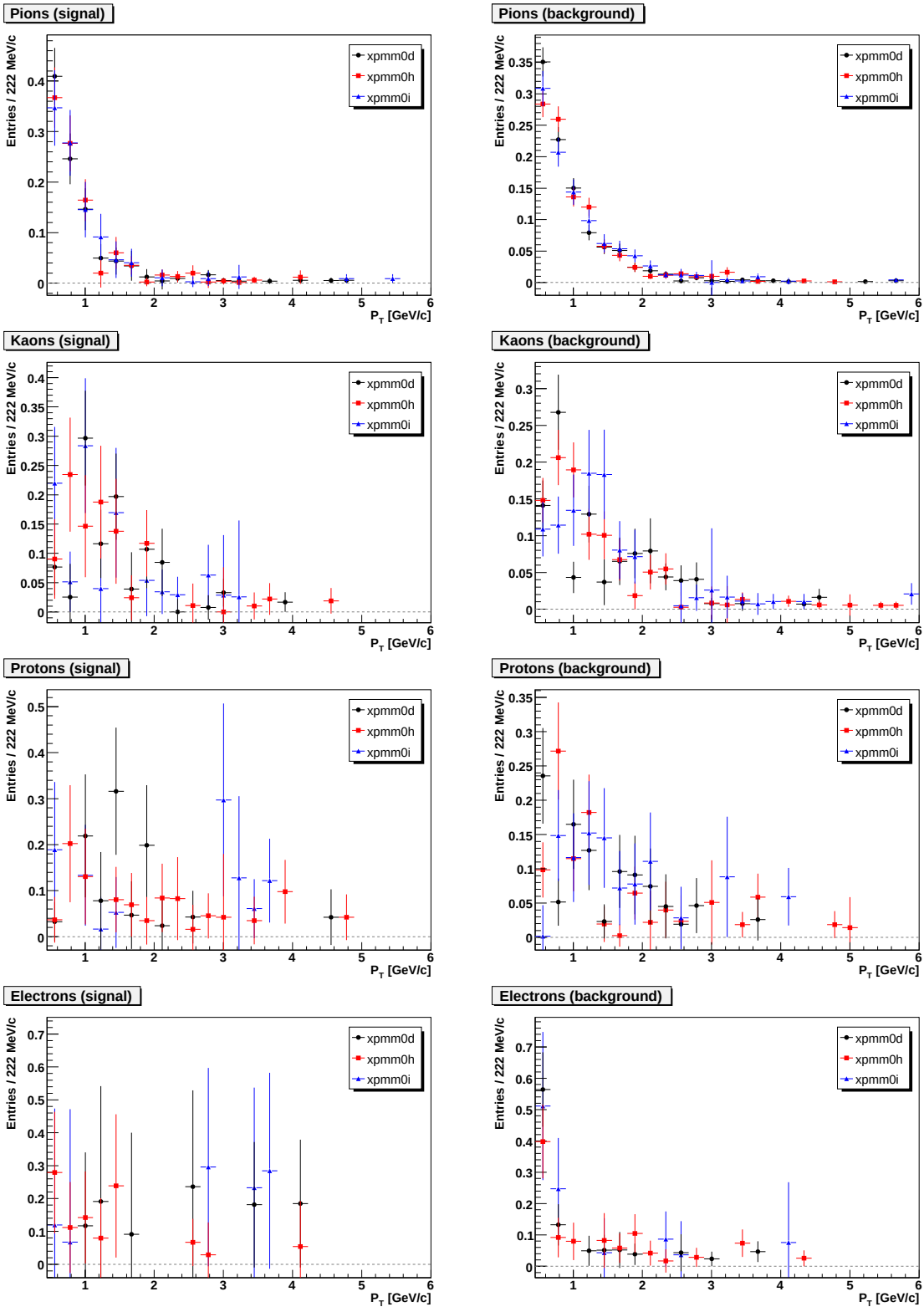

Figure 7.11: $B_s \to J/\psi\,\phi$ decay. P_T distributions from Channel-Likelihood method for pions, kaons, protons, and electrons.

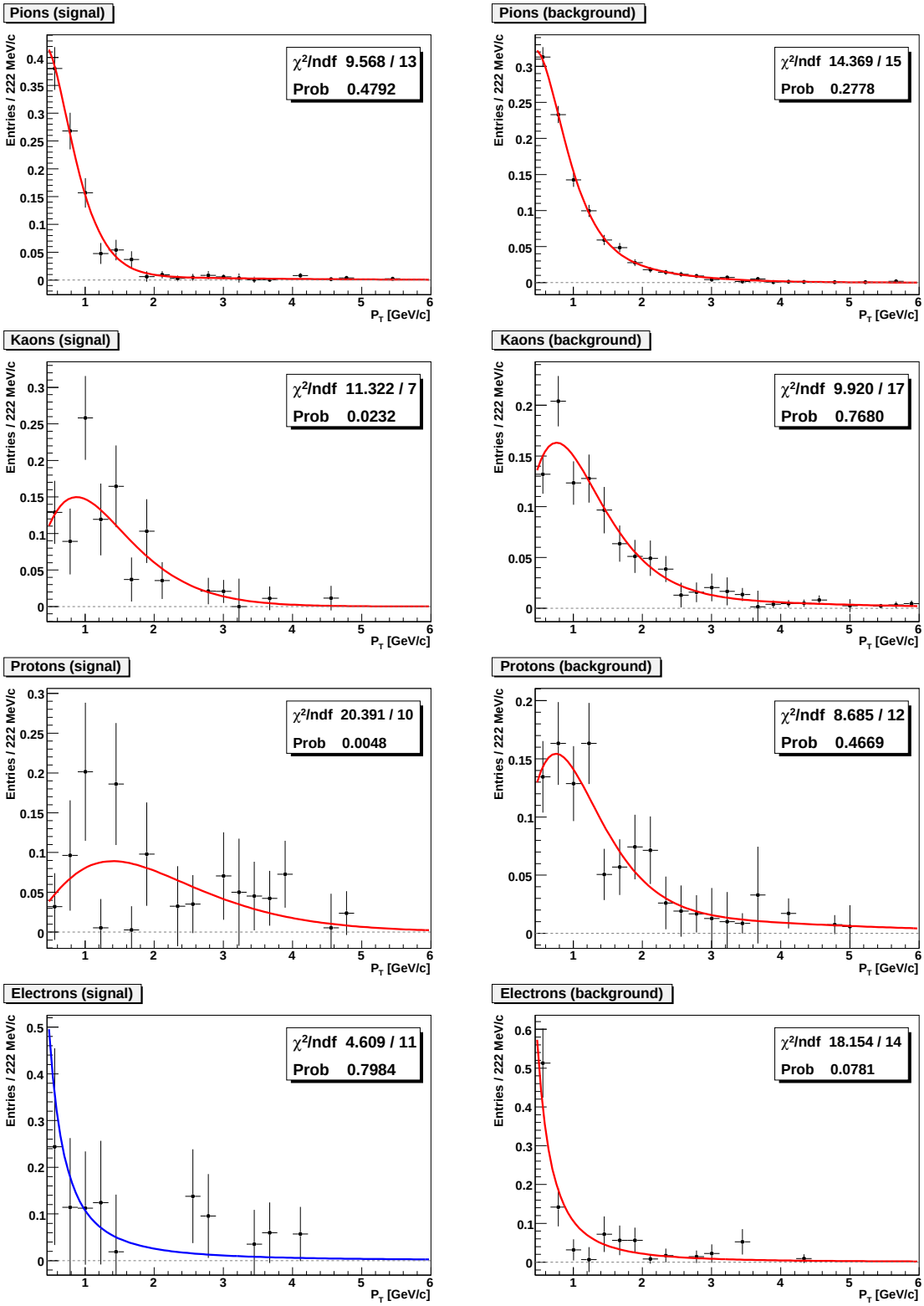

Figure 7.12: $B_s \to J/\psi\,\phi$ decay. P_T distributions from Channel-Likelihood method for pions, kaons, protons, and electrons. In the case of signal electrons, the function fitted for B^0 has been superimposed.

			0d	0h	0i	tot
Channel Likelihood	SIGNAL	π	69.1 ± 3.9	68.8 ± 4.3	68.9 ± 5.4	71.2 ± 2.7
		K	22.2 ± 3.6	17.8 ± 3.6	19.6 ± 4.9	19.8 ± 2.4
		p	6.8 ± 1.9	7.9 ± 2.3	9.5 ± 3.3	6.3 ± 1.3
		e	2.0 ± 1.3	5.5 ± 1.8	2.0 ± 1.5	2.7 ± 1.0
	BKG	π	76.1 ± 1.7	72.2 ± 1.8	77.3 ± 2.7	74.6 ± 1.1
		K	14.5 ± 1.5	18.2 ± 1.6	15.2 ± 2.2	16.4 ± 1.0
		p	5.0 ± 0.8	5.9 ± 0.9	5.3 ± 1.1	5.6 ± 0.6
		e	4.4 ± 0.8	3.7 ± 0.7	2.2 ± 1.7	3.3 ± 0.4
Maximum Likelihood	SIGNAL	π	73.2 ± 5.1	73.2 ± 5.0	–	73.6 ± 3.1
		K	21.6 ± 4.6	16.7 ± 4.4	–	19.4 ± 2.8
		p	4.8 ± 2.3	6.9 ± 2.6	–	5.5 ± 1.5
		e	0.4 ± 1.6	3.2 ± 2.1	–	1.6 ± 1.2
	BKG	π	76.2 ± 1.8	71.1 ± 1.9	–	74.3 ± 1.1
		K	14.1 ± 1.5	19.4 ± 1.7	–	16.7 ± 1.0
		p	5.4 ± 0.9	6.0 ± 0.9	–	5.7 ± 0.5
		e	4.2 ± 0.8	3.5 ± 0.8	–	3.3 ± 0.5

Table 7.3: Particle type fraction for signal and background components for $B_s \to J/\psi\,\phi$ decay. Low statistics does not allow to apply the ML method to the 0i data set.

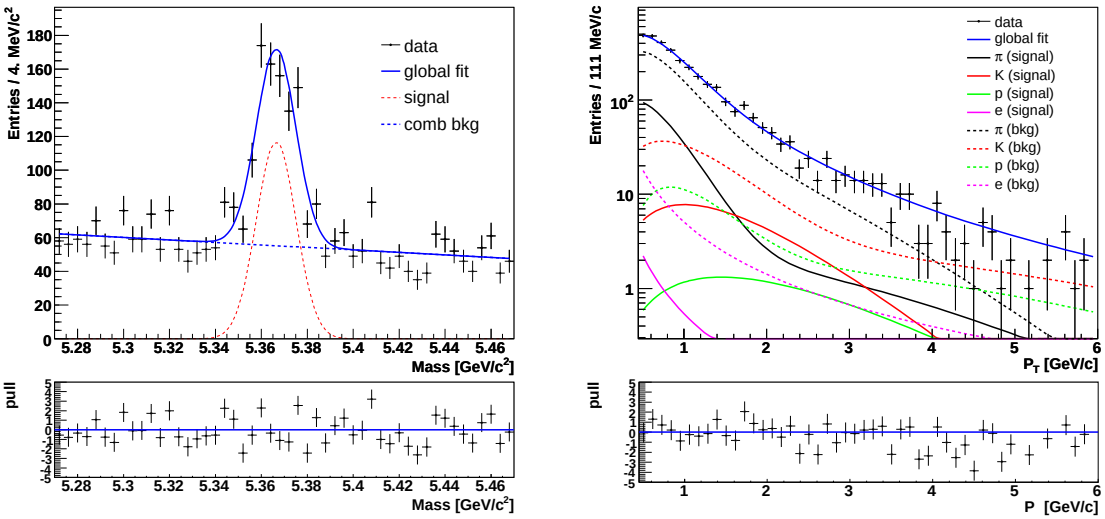

Figure 7.13: $B_s \to J/\psi\,\phi$ decay. Mass (left) and P_T (right) projections of Maximum-Likelihood fit.

7.4.4 $B^+ \to \overline{D}^0 \pi^+$

We divide the P_T range 0.45-6 GeV/c into 50 bins and the CL procedure is performed in each bin. Results are shown in Fig. 7.15: the distributions obtained in `xbhd0d`, `xbhd0h`, and `xbhd0i` datasets are normalized to one and superimposed. Errors are statistically only and have been calculated bin per bin from the fit covariance matrix.

The resulting P_T spectra merging the three datasets, normalized to unity, are shown in Fig. 7.16 with the correspondig fitted function superimposed. The results on the particle composition are listed in the upper half of Tab. 7.4.

Fig. 7.14 shows the mass and P_T projections of the ML fit. The reduced χ^2 of the projections are: $\chi^2/\text{ndf} = 280/100$ and $\chi^2/\text{ndf} = 128/100$.

Tab. 7.4 summarizes the results for the $B^+ \to \overline{D}^0 \pi^+$ channel. It reports the results obtained with both the CL and ML methods for the different datasets along with the final result over the whole sample.

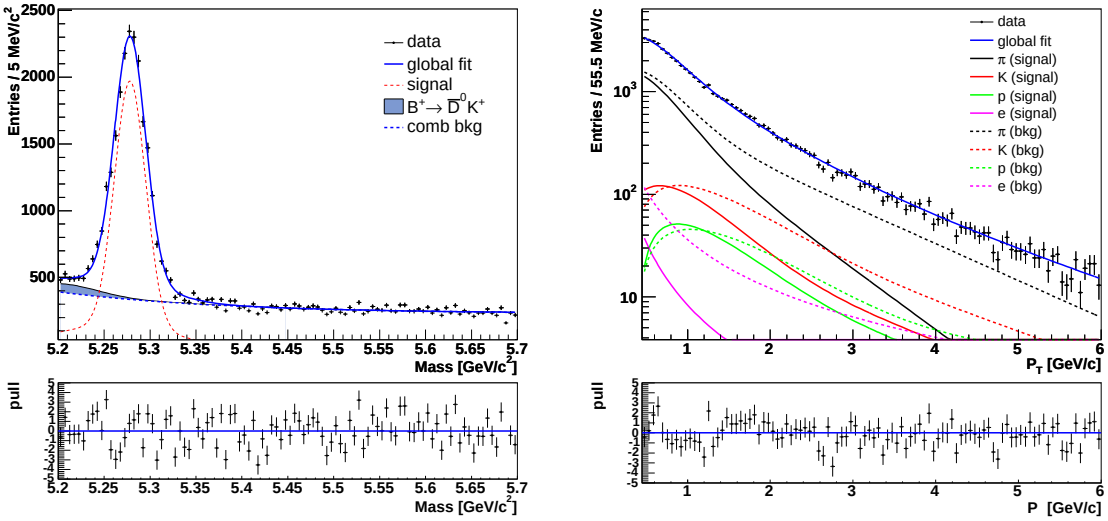

Figure 7.14: $B^+ \to \overline{D}^0 \pi^+$ decay. Mass (left) and P_T (right) projections of Maximum-Likelihood fit.

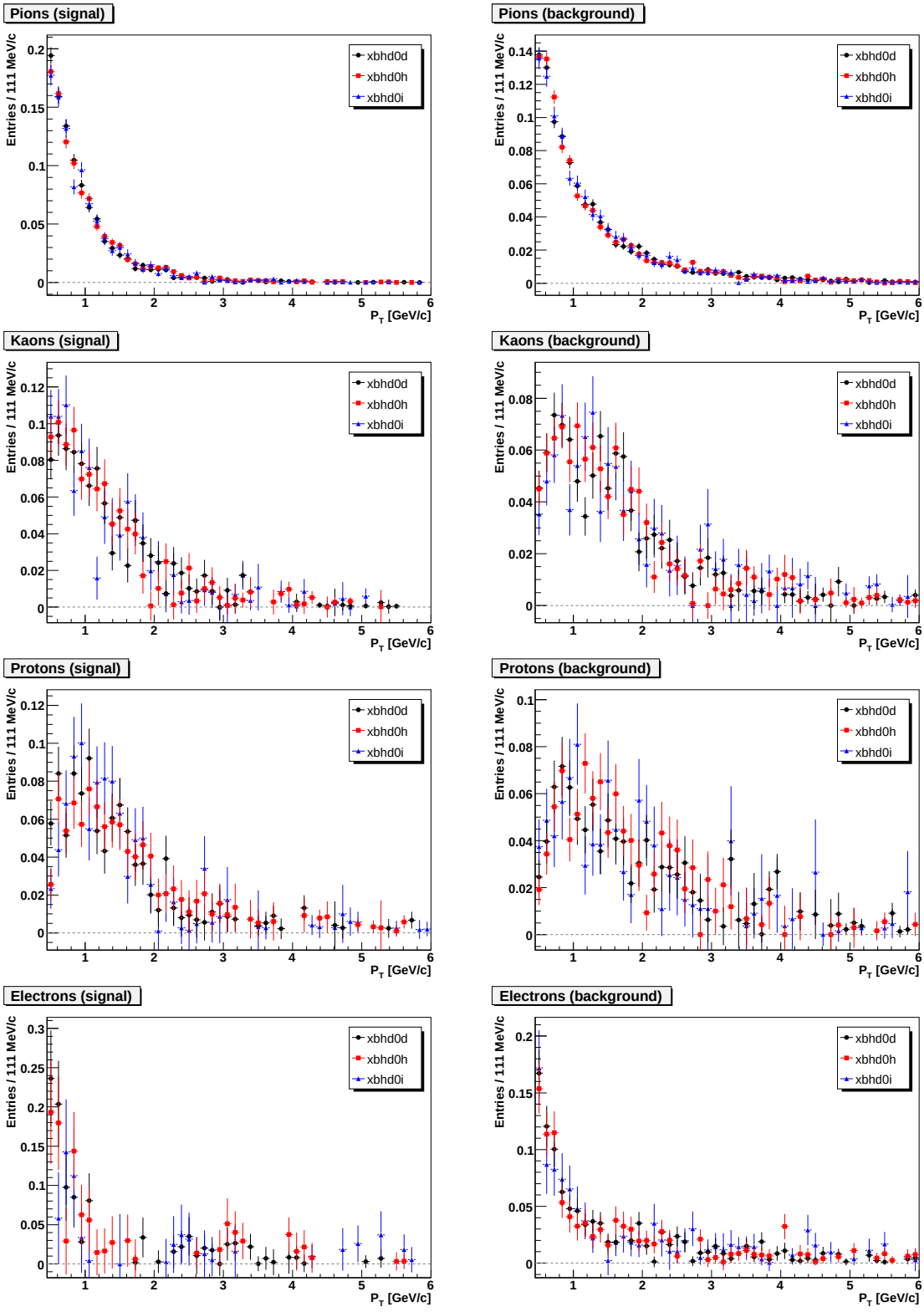

Figure 7.15: $B^+ \to \bar{D}^0 \pi^+$ decay. P_T distributions from Channel Likelihood method for pions, kaons, protons, and electrons.

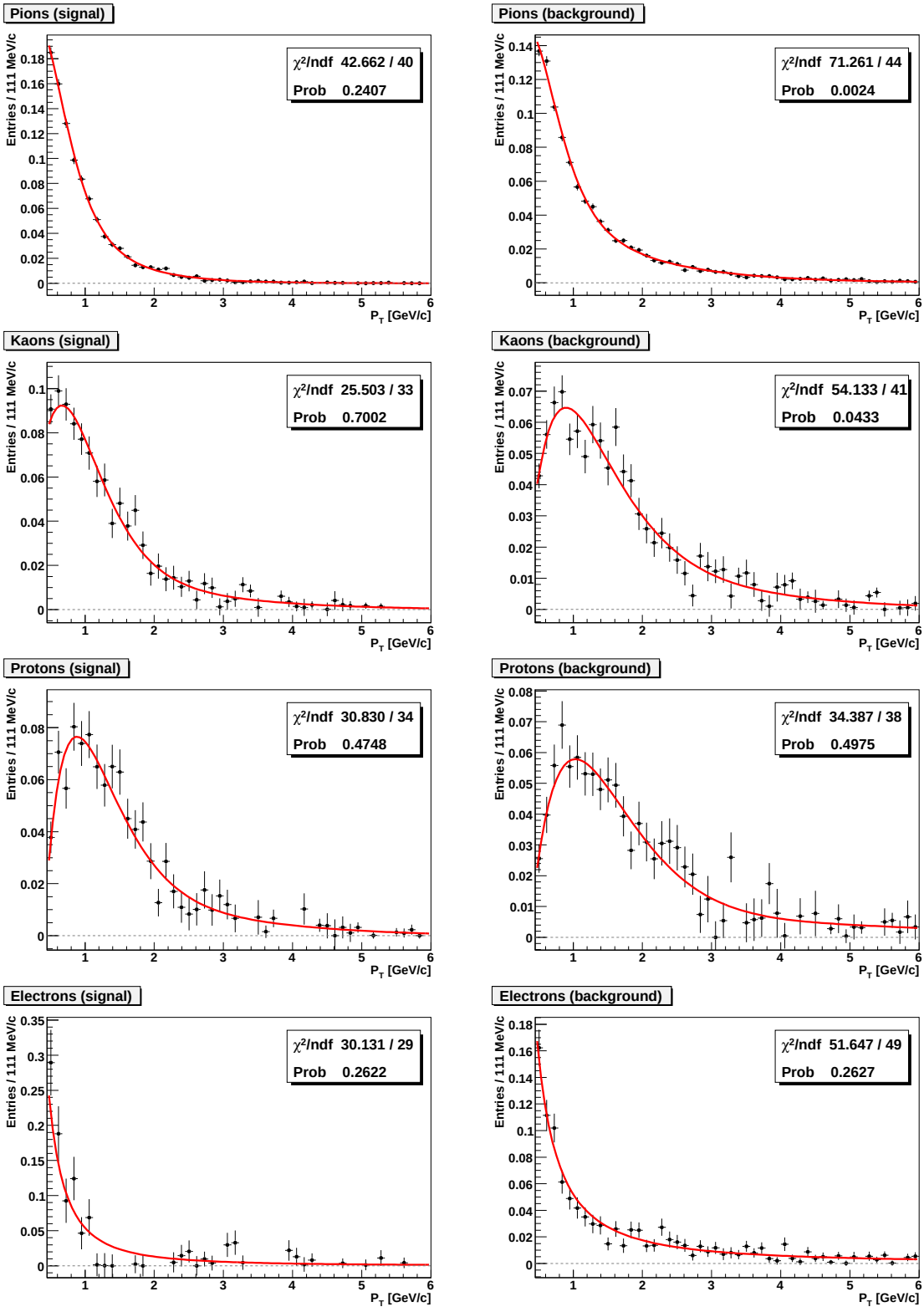

Figure 7.16: $B^+ \to \bar{D}^0 \pi^+$ decay. P_T distributions from Channel Likelihood method for pions, kaons, protons, and electrons.

			0d	0h	0i	tot
Channel Likelihood	SIGNAL	π	77.25 ± 0.72	78.05 ± 0.75	76.04 ± 1.00	77.60 ± 0.46
		K	13.68 ± 0.62	13.31 ± 0.65	14.93 ± 0.87	13.79 ± 0.40
		p	6.93 ± 0.41	7.02 ± 0.44	7.34 ± 0.58	6.99 ± 0.26
		e	2.13 ± 0.29	1.61 ± 0.25	1.68 ± 0.34	1.62 ± 0.17
	BKG	π	76.56 ± 0.60	76.76 ± 0.60	75.87 ± 0.90	76.48 ± 0.39
		K	12.60 ± 0.51	13.32 ± 0.52	13.84 ± 0.79	13.19 ± 0.34
		p	5.45 ± 0.32	5.51 ± 0.33	5.95 ± 0.51	5.51 ± 0.22
		e	5.39 ± 0.29	4.41 ± 0.27	4.33 ± 0.38	4.82 ± 0.18
Maximum Likelihood	SIGNAL	π	78.21 ± 0.76	78.23 ± 0.91	75.88 ± 1.26	77.52 ± 0.48
		K	12.98 ± 0.63	13.69 ± 0.77	15.07 ± 1.07	13.80 ± 0.40
		p	7.23 ± 0.40	7.04 ± 0.43	7.74 ± 0.61	7.06 ± 0.25
		e	1.58 ± 0.23	1.04 ± 0.20	1.31 ± 0.28	1.62 ± 0.17
	BKG	π	76.24 ± 0.59	76.73 ± 0.60	75.94 ± 0.86	76.41 ± 0.38
		K	12.83 ± 0.49	13.26 ± 0.50	13.66 ± 0.74	13.20 ± 0.32
		p	5.33 ± 0.29	5.48 ± 0.29	6.09 ± 0.43	5.52 ± 0.19
		e	5.60 ± 0.30	4.53 ± 0.28	4.31 ± 0.37	4.87 ± 0.18

Table 7.4: Particle type fraction for signal and background components for $B^+ \to \bar{D}^0 \pi^+$ decay.

7.4.5 $B^0 \to D^- \pi^+$

Again, we first compare the P_T spectra of pions, kaons, protons and electrons obtained for signal and background from the three datasets. We run CL with 50 P_T bins in the range 0.45-6 GeV/c. The results are shown in Fig. 7.17, where histograms are normalized to one and the errors are given by the fit covariance matrix.

The result of the CL fit over the whole dataset is reported in Fig. 7.18. Histograms are fitted to the functions (7.5) and (7.6).

Fig. 7.19 shows the mass and P_T projections of the ML fit. The reduced χ^2 of the projections are: $\chi^2/\text{ndf} = 282/100$ and $\chi^2/\text{ndf} = 115/100$.

Tab. 7.5 summarizes the results for the $B^0 \to D^- \pi^+$ channel. It reports the results obtained using both the CL and ML methods for the different datasets along with the final result over the whole sample.

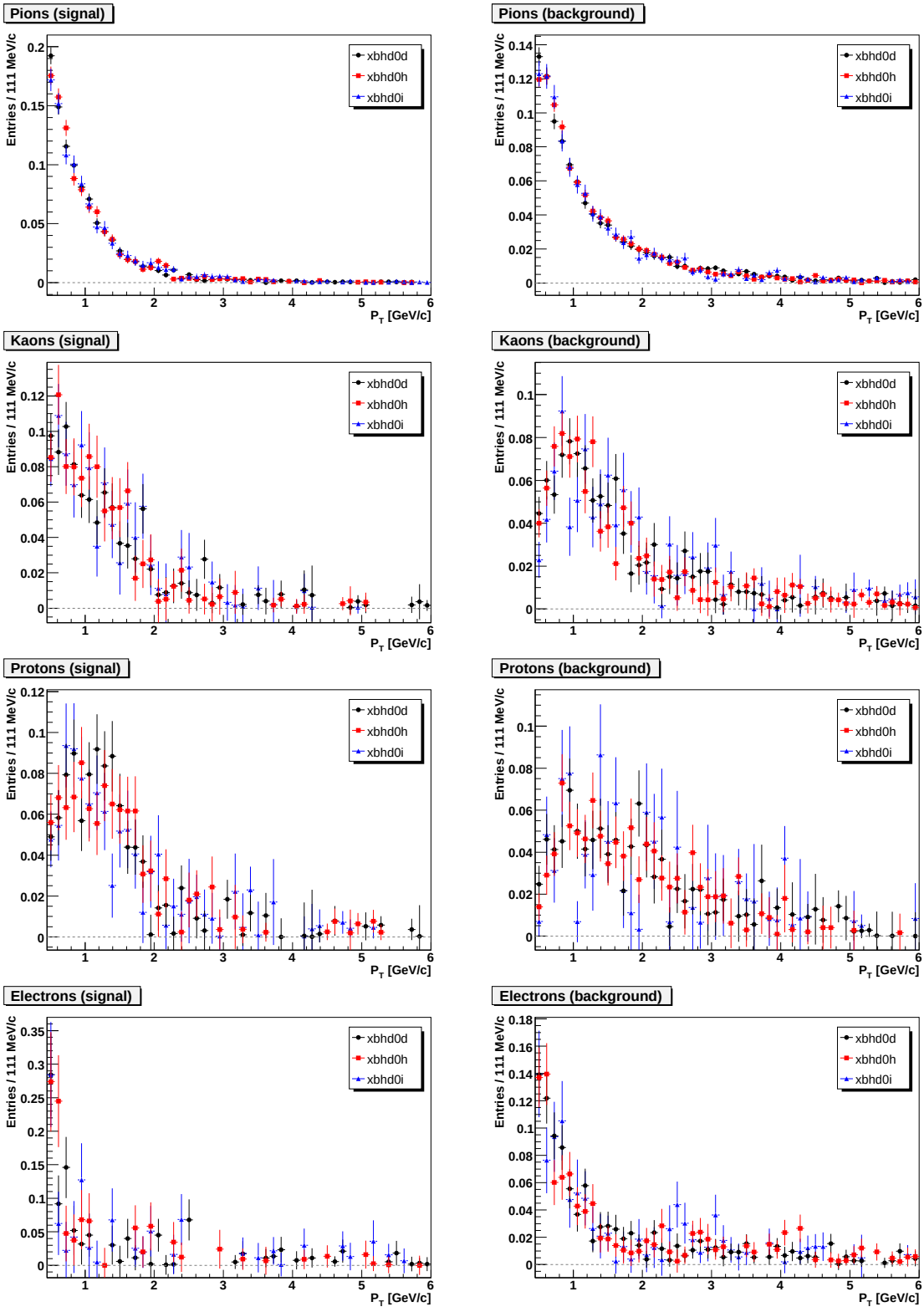

Figure 7.17: $B^0 \to D^- \pi^+$ decay. P_T distributions from Channel Likelihood method for pions, kaons, protons, and electrons.

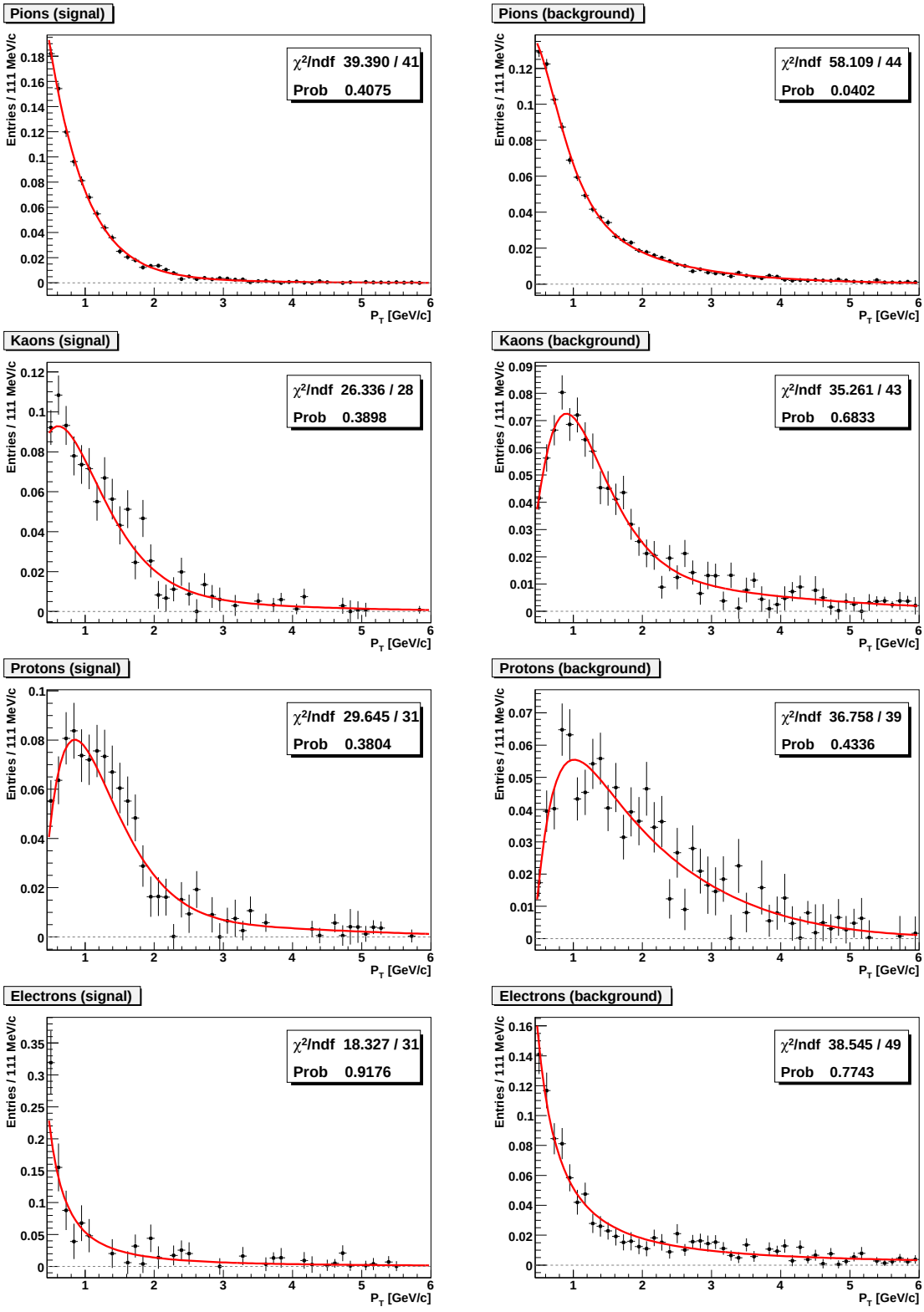

Figure 7.18: $B^0 \to D^- \pi^+$ decay. P_T distributions from Channel Likelihood method for pions, kaons, protons, and electrons.

			0d	0h	0i	tot
Channel Likelihood	SIGNAL	π	79.60 ± 0.78	80.02 ± 0.84	77.80 ± 1.10	79.70 ± 0.54
		K	11.74 ± 0.66	11.30 ± 0.72	12.34 ± 0.94	11.67 ± 0.45
		p	6.28 ± 0.44	6.70 ± 0.47	7.43 ± 0.64	6.63 ± 0.30
		e	2.38 ± 0.32	1.98 ± 0.31	2.44 ± 0.43	1.99 ± 0.21
	BKG	π	76.41 ± 0.72	78.64 ± 0.63	76.25 ± 1.02	77.41 ± 0.42
		K	12.56 ± 0.61	12.11 ± 0.54	13.33 ± 0.87	12.43 ± 0.36
		p	4.97 ± 0.38	5.04 ± 0.34	5.28 ± 0.57	5.21 ± 0.23
		e	6.06 ± 0.35	4.21 ± 0.28	5.13 ± 0.47	4.95 ± 0.19
Maximum Likelihood	SIGNAL	π	79.94 ± 0.76	80.04 ± 0.85	78.20 ± 1.18	79.54 ± 0.51
		K	11.43 ± 0.62	11.68 ± 0.71	12.67 ± 0.98	11.76 ± 0.42
		p	6.52 ± 0.39	6.36 ± 0.43	7.23 ± 0.61	6.68 ± 0.26
		e	2.11 ± 0.33	1.92 ± 0.31	1.90 ± 0.44	2.02 ± 0.20
	BKG	π	76.02 ± 0.66	78.22 ± 0.63	76.41 ± 0.92	77.10 ± 0.41
		K	12.74 ± 0.54	12.40 ± 0.53	12.95 ± 0.78	12.58 ± 0.34
		p	5.06 ± 0.32	5.04 ± 0.31	5.60 ± 0.47	5.14 ± 0.20
		e	6.18 ± 0.35	4.34 ± 0.29	5.03 ± 0.44	5.18 ± 0.20

Table 7.5: Particle type fraction for signal and background components for $B^0 \to D^- \pi^+$ decay.

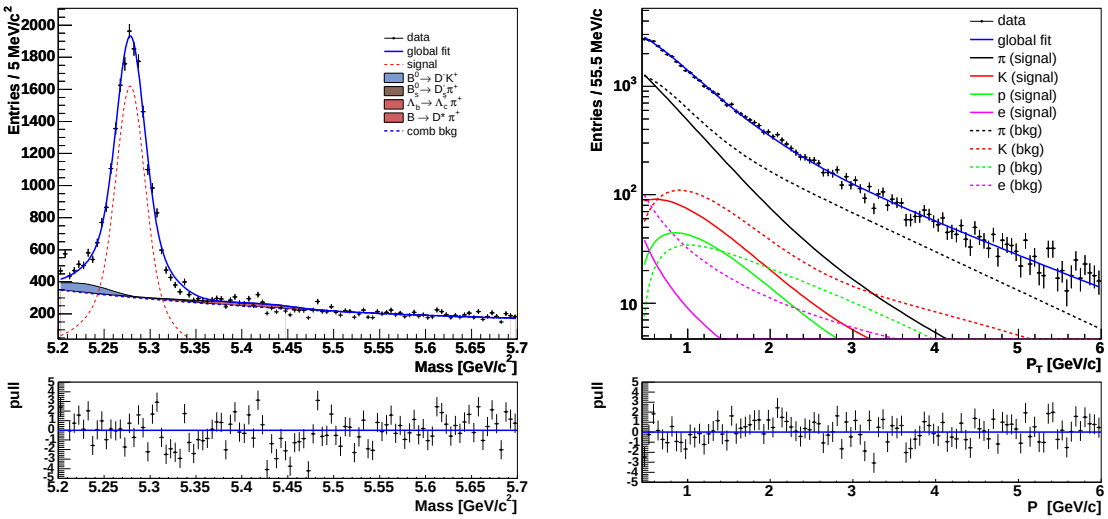

Figure 7.19: $B^0 \to D^- \pi^+$ decay. Mass (left) and P_T (right) projections of Maximum-Likelihood fit.

7.4.6 $B_s \to D_s^- \pi^+$

Finally for the $B_s \to D_s^- \pi^+$ mode, we first compare the P_T spectra of pions, kaons, protons and electrons obtained for signal and background from the three datasets. Also in this case, due to the lower statistics of the data sample, the CL was performed in 25 P_T bins in the usual range 0.45-6 GeV/c. The results are shown in Fig. 7.21, where histograms are normalized to one and the errors are given by the fit covariance matrix.

The result of the CL fit over the whole dataset is reported in Fig. 7.22. Histograms are fitted to the functions (7.5) and (7.6).

Fig. 7.20 shows the mass and P_T projections of the ML fit. The reduced χ^2 of the projections are: $\chi^2/\text{ndf} = 198/69$ and $\chi^2/\text{ndf} = 39/44$.

Tab. 7.6 summarizes the results for the $B_s \to D_s^- \pi^+$ channel. It reports the results obtained using both the CL and ML methods for the different datasets along with the final result over the whole sample.

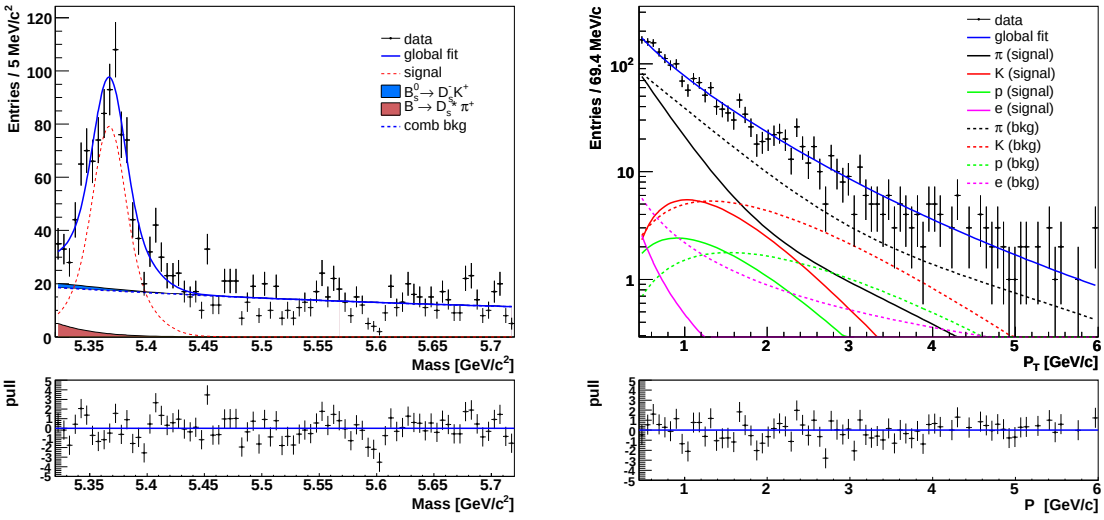

Figure 7.20: $B_s \to D_s^- \pi^+$ decay. Mass (left) and P_T (right) projections of Maximum-Likelihood fit.

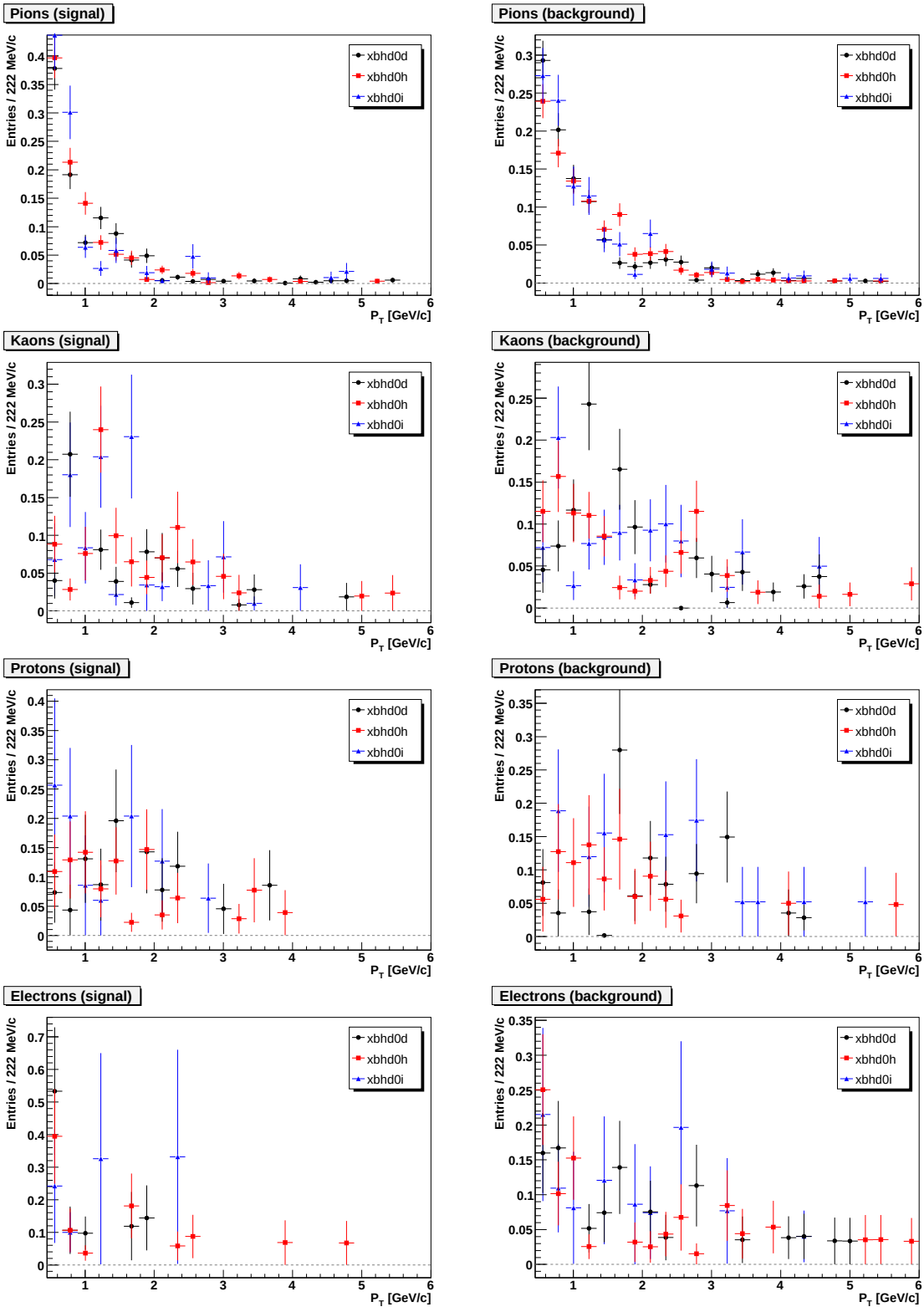

Figure 7.21: $B_s \to D_s^- \pi^+$ decay. P_T distributions from Channel Likelihood method for pions, kaons, protons, and electrons.

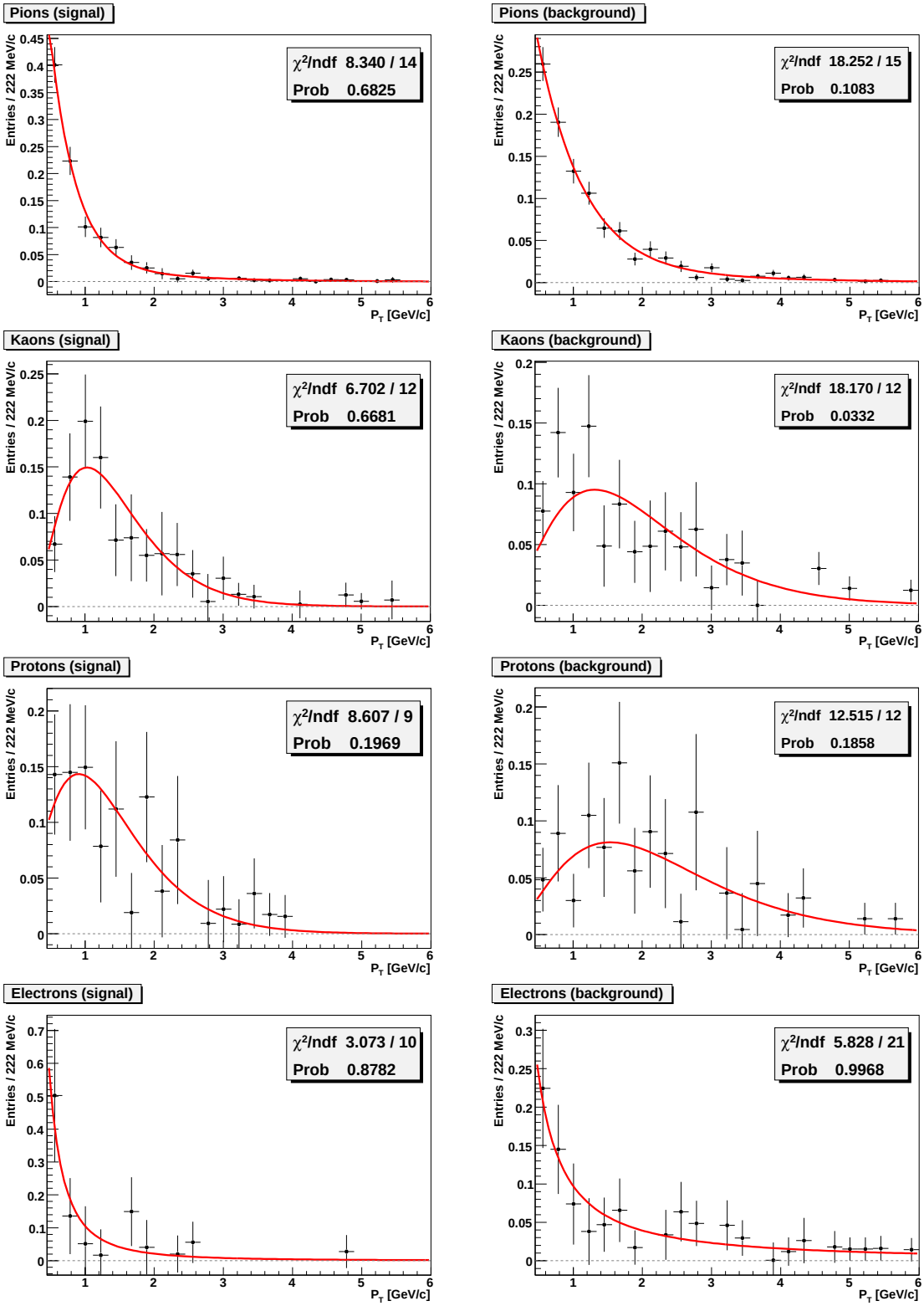

Figure 7.22: $B_s \to D_s^- \pi^+$ decay. P_T distributions from Channel Likelihood method for pions, kaons, protons, and electrons.

			0d	0h	0i	tot
Channel Likelihood	SIGNAL	π	69.7 ± 2.4	74.8 ± 2.0	68.1 ± 3.5	73.5 ± 1.3
		K	18.8 ± 2.0	12.8 ± 1.5	21.2 ± 3.1	16.1 ± 1.1
		p	8.1 ± 1.5	7.9 ± 1.3	8.5 ± 2.2	7.3 ± 0.8
		e	3.3 ± 0.9	4.4 ± 1.0	2.2 ± 1.1	3.0 ± 0.5
	BKG	π	75.7 ± 1.7	75.3 ± 1.7	69.3 ± 2.7	74.8 ± 1.0
		K	11.6 ± 1.2	14.6 ± 1.4	17.5 ± 2.1	13.8 ± 0.8
		p	6.2 ± 1.0	4.3 ± 0.8	8.2 ± 1.7	5.9 ± 0.6
		e	6.5 ± 1.0	5.8 ± 0.9	5.0 ± 1.3	5.5 ± 0.5
Maximum Likelihood	SIGNAL	π	71.4 ± 4.0	78.4 ± 3.6	74.0 ± 6.2	73.7 ± 2.4
		K	21.1 ± 3.6	12.3 ± 3.1	17.4 ± 5.7	16.6 ± 2.1
		p	6.0 ± 2.0	7.6 ± 1.9	8.0 ± 3.1	7.7 ± 1.3
		e	1.6 ± 1.4	1.7 ± 1.5	0.6 ± 2.2	2.0 ± 0.9
	BKG	π	77.3 ± 2.7	75.1 ± 2.8	71.7 ± 4.2	73.8 ± 1.8
		K	10.2 ± 2.2	14.4 ± 2.3	16.2 ± 3.8	14.6 ± 1.6
		p	6.2 ± 1.6	4.5 ± 1.3	7.3 ± 2.3	5.7 ± 0.9
		e	6.4 ± 1.5	6.1 ± 1.6	4.7 ± 1.9	5.9 ± 0.9

Table 7.6: Particle type fraction for signal and background components for $B_s \to D_s^- \pi^+$ decay.

7.5 Systematics

In order to estimate the systematic uncertainties we have to distinguish the two considered cases:

- the systematics associated to the CL fits, where we estimate the particle content in each P_T bin without any assumption on the P_T distribution of the particle species.
- the systematics associated to the particle fractions integrated on the whole P_T spectrum. In this case we perform a ML fit using P_T templates extracted by the CL.

As argued at the beginning of the chapter, we are not going to correct for any detector effects like reconstruction efficiency; therefore we can classify our systematic sources in three categories:

1. the description of the TOF and dE/dx resolution functions (i.e., the particle identification templates used in the fits).
2. the description of the mass distribution of the B candidates associated to the tracks used to distinguish signal tracks respect to background ones.

3. the parameterization of the P_T distribution of each particle type extracted by the CL and fixed in the ML.

While the first two sources affect both the CL and the ML results, the last one is peculiar of the ML and is reflected on the estimation of the total particle fractions only.

7.5.1 The procedure

Due to the large number of parameters needed to describe the templates used both in CL and the ML, it may be quite complicated to disentangle the contribution of each parameter to the systematic uncertainty. In practice, we should vary the parameters of each template in all the possible way taking into account also the effects of possible correlations between parameters affecting the final results.

We then decided to generalize the method described in [83] [84] where a procedure to estimate the systematic associated to the particle identification resolution function is proposed. We consider the multidimensional space defined by all the parameters describing the templates. We then define an iper-sphere of radius $n\sigma$, i.e. the number of standard deviations from the *default* values associated to the parameters, and we randomly varied the parameters in the volume defined by the iper-sphere. In order to statistically sample a significant number of *directions* in the space of systematic parameter shifts, the analysis is repeated for various samples.

Operatively, for each decay mode:

- we generate 2000 pseudo-experiments as described in section 7.3. Each pseudo-experiment is produced using modified templates according to the randomly shifted parameters:
$$P_n = P_n^0 + \Delta_n \tag{7.7}$$
where P_n is the value of the shifted parameter n, P_n^0 is the default value of the parameter n, extracted from data, and Δ_n is the randomly generated shift.

- each toy-sample is fitted using the default templates, i.e. the ones used in the fit on data samples.

- we then extract the residual distributions of the estimators resulting from the 2000 pseudo-experiment: $N_j^{generated} - N_j^{fitted}$ for each species j in each P_T bin for the CL; $f_j^{generated} - f_j^{fitted}$ of each species j integrated in the whole P_T range for the ML.

- Each residual distribution will be characterized by a RMS (σ_{res}) and a mean value (μ). The RMS can be considered as due to two contributions: the systematic uncertainty (σ_{syst}) and the statistical uncertainty due to the finite statistics of generated sample (σ_{stat}). The systematic contribution is then disentangled inverting the relation:
$$\sigma_{res} = \sqrt{\sigma_{syst}^2 + \sigma_{stat}^2} \tag{7.8}$$

where σ_{stat} is evaluated by the residual distributions of the pseudo-experiments introduced in section 7.3, with statistics equivalent to each decay mode. If the mean value μ of the given residual distribution is compatible with zero, σ_{syst} is considered as the final systematics uncertainty σ_{tot}; on the other hand, if $\mu \neq 0$, it means the the corresponding estimator is sensitive to the change of the template parameters in an asymmetric way: we then have to take in to account this *systematic* shift and the final systematic uncertainty will then be:

$$\sigma_{tot} = \sqrt{\sigma_{syst}^2 + \mu^2} \tag{7.9}$$

7.5.2 CL systematics

As already argued, the CL results are affected by the particle identification resolution functions description and by the mass distribution shapes. The toy-samples for systematics evaluation are then generated shifting the corresponding parameters. The procedure previously described is then applied to each P_T bin in order to associate a systematic uncertainty to the content of the bin. Systematic and statistics uncertainties are then added in quadrature in each P_T bin and the resulting histograms are shown in chapter 8 overimposed to Monte Carlo predictions.

7.5.3 ML systematics

In the case of the ML, in addition to the PID and the mass distribution templates, also the P_T parameterization for each particle species must be considered as systematic source. The toy-samples are then generated varying the PID, mass shape and P_T distributions parameters.

The final systematics are summarized in Tab.7.7. We can clearly observe that, due to the low statisctics of the samples, in the case of the B_s modes we obtain big systematic uncertainties on the particle fractions.

Mode	π (%)	K (%)	P (%)	e (%)
$B_u \to J/\psi K$	1.2	0.93	0.55	0.85
$B_d \to J/\psi K^{*0}$	1.3	0.98	0.50	0.93
$B_s \to J/\psi \phi$	2.8	2.2	1.0	2.2
$B_u \to D^0 \pi$	0.87	0.61	0.28	0.74
$B_d \to D^- \pi$	0.89	0.57	0.24	0.78
$B_s \to D_s \pi$	3.7	2.9	1.5	2.4

Table 7.7: ML method systematic uncertaincies for each signal decay mode and for each particle species.

7.6 Final results

We finally report in tab.7.8 the estimated particle type fractions including systematic effects. Statistics and systematic uncertainties of Tab.7.7 are added in quadrature.

Particle fractions estimated in different decay modes of the same B meson are in very good agreement among them.

Meson	Decay	Pions (%)	Kaons (%)	Protons (%)	Electrons (%)
B^+	$\bar{D^0}\pi^+$	77.52 ± 0.99	13.80 ± 0.73	7.06 ± 0.37	1.62 ± 0.76
	$J/\psi K^+$	77.33 ± 1.32	13.03 ± 1.05	7.35 ± 0.64	2.29 ± 0.87
B^0	$D^-\pi^+$	79.54 ± 1.02	11.76 ± 0.71	6.68 ± 0.35	2.02 ± 0.80
	$J/\psi K^*$	78.54 ± 1.62	11.59 ± 1.26	7.21 ± 0.71	2.65 ± 1.00
B_s	$D_s^-\pi^+$	73.7 ± 4.4	16.6 ± 3.6	7.7 ± 2.0	2.0 ± 2.6
	$J/\psi\phi$	73.6 ± 4.2	19.4 ± 3.6	5.5 ± 1.8	1.6 ± 2.5

Table 7.8: Particle type fractions estimated on the considered decay modes; systematic contribution included.

Chapter 8

Data Monte Carlo comparisons

In this chapter we will compare the results obtained on data to the corresponding Monte Carlo predictions about the particle type fractions and related kinematics variables. This represents the first *direct* test of kinematics distributions as generated by Pythia Monte Carlo for each particle species produced in association with the formation of B mesons at CDF.

8.1 Monte Carlo sample

One of the primary motivations of this analysis is to compare the particle fractions produced around B signals in the data with the corresponding predictions of Monte Carlo (MC) generators.

As already discussed in chapter 2, the performances of the Same Side Kaon Tagging (SSKT) algorithms are evaluated using Monte Carlo generators such as Pythia. We then have to relay on the fragmentation models used by the generator. Testing how well the Monte Carlo reproduces the amount of various particle species found around B decays and the corresponding kinematics properties is an important piece of information when deciding whether the MC simulation can be trusted and at which level of accuracy. If needed, those results can be used for MC tuning.

We will now describe the procedure followed to generate a sample of simulated events using the Pythia generator [85]. The MC sample used in this analysis is the same of [57] where the performances of the SSKT algorithm are evaluated.

We start with the generation of a big sample of Pythia/Jetset events that simulates the collisions of $p\bar{p}$ of the Tevatron, the consequent fragmentation processes and the underlying event. The generator includes all the dominant b quark production processes at the Tevatron (chapter 2): flavor creation, flavor excitation and gluon splitting. We run the Pythia generator with the generation parameter msel=1[1], which implies the generation of generic hard scattering QCD processes: $f_i f_j \to f_i f_j$, $f_i \bar{f_i} \to f_k \bar{f_k}$, $f_i f_i \to gg$, $f_i g \to f_i g$, $gg \to f_k \bar{f_k}$ and $gg \to gg$ where $f_{i,j,k}$ are quarks and g gluons. The most of the simulated events will then be characterized by light jets in the final

[1]This parameter determines which hard scattering processes are generated; the hard scattering process in Pythia is defined as the highest energy primary interaction of two partons in the colliding beam particles.

states; however, this process occasionally results in the creation of $b\bar{b}$ pair, via any of the possible mechanisms. Only the events that contain a b quark are collected, while the others are discarded and do not proceed in the the simulation process. Notice that, as shown in [63] and [62], the Pythia generation parameter msel=5, that implies the creation of hard scattering processes with outgoing b and $\bar{b}$ quarks only, does not reproduce data at the same level of accuracy of msel=1.

In order to be able to produce a large Monte Carlo sample for each decay channel in a reasonable amount of time, the generated Pythia sample was stored and used as input to the decay package of unstable particles and to the detector/trigger simulation.

For each decay mode, the original Pythia sample has been re-decayed using the EvtGen [86] package to force the decay of the B meson containing a $b-$quark ($\bar{b}-$quark); at the same time, the decays of the particles containing the $\bar{b}-$quark ($b-$quark) are left unbiassed and free to decay according the most recent branching ratios measurements. In such a way, B mesons and anti-B mesons decays are forced separately in two distinguished samples. A set of twelve Monte Carlo samples, summarized in Tab.8.1, were produced:

$\bar{b}-$quark	$b-$quark
$B_u^+ \to J/\psi K^+$, $J/\psi \to \mu^+\mu^-$	$B_u^- \to J/\psi K^-$, $J/\psi \to \mu^+\mu^-$
$B_d^0 \to J/\psi K^{*0}$, $J/\psi \to \mu^+\mu^-$, $K^{*0} \to K^+\pi^-$	$\bar{B}_d^0 \to J/\psi \bar{K}^{*0}$, $J/\psi \to \mu^+\mu^-$, $\bar{K}^{*0} \to K^-\pi^+$
$B_s^0 \to J/\psi\phi$, $J/\psi \to \mu^+\mu^-$, $\phi \to K^+K^-$	$\bar{B}_s^0 \to J/\psi\phi$, $J/\psi \to \mu^+\mu^-$, $\phi \to K^+K^-$
$B_u^+ \to \bar{D}^0\pi^+$, $\bar{D}^0 \to K^+\pi^-$	$B_u^- \to D^0\pi^-$, $D^0 \to K^-\pi^+$
$B_d^0 \to D^-\pi^+$, $D^- \to K^+\pi^-\pi^-$	$\bar{B}_d^0 \to D^+\pi^-$, $D^+ \to K^-\pi^+\pi^+$
$B_s^0 \to D_s^-\pi^+$, $D_s^- \to \phi\pi^-$, $\phi \to K^+K^-$	$\bar{B}_s^0 \to D_s^+\pi^-$, $D_s^+ \to \phi\pi^+$, $\phi \to K^+K^-$

Table 8.1: Topologies of the 12 Monte Carlo samples.

After these decays are simulated, the events are processed by detector response simulation package based on GEANT [87], [88]. This simulates the low-level response of all detectors systems, allowing for a reliable estimate of trigger, detector and reconstruction effects. We use the standard CDF trigger simulation package TRIGsim to simulate trigger decisions of Level 1 and 2 trigger systems based on the raw data banks[2]. The events are then filtered based on TRIGsim decision. Finally the standard CDF reconstruction is performed on the events to create the final samples. B meson and anti-B meson forced decay samples of the same mode are at this point merged toghether. The complete Monte Carlo samples are then processed and analyzed in the same way as the corresponding data sample.

8.1.1 TOF efficiency correction

Before proceeding to data-MC comparisons, we must consider an additional effect due the TOF detector.

[2]With raw we mean *not yet processed by the standard production software* that converts this information in a format suitable for offline analysis.

The tracks used in the fraction fits are required to have TOF information, otherwise they are discarded. The standard CDF simulation package includes a realistic simulation of the TOF detector response and performances. It was shown in [62] and later in [57] that the TOF efficiency[3] is not constant as a function of the P_T of the tracks. In addition, the TOF efficiency as resulting from Monte Carlo does not reproduce the efficiency found in data. This effect is clearly shown in Fig.8.1, where TOF efficiency of tracks associated to $B^+ \to \overline{D}^0 \pi^+$ data events is overimposed to the corresponding efficiency in $B^+ \to \overline{D}^0 \pi^+$ MC events: in particular, TOF efficiency is found to be higher in MC. Because of this P_T dependence, the P_T distribution of each particle type

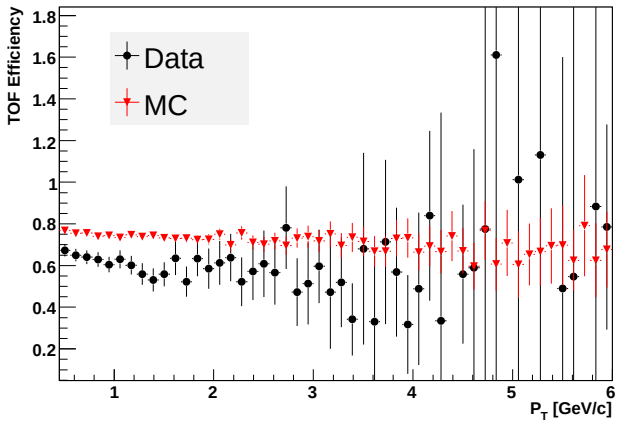

Figure 8.1: TOF efficiency as a function of P_T of the tracks: data (black circles); Monte Carlo (red triangles).

is then modified by the TOF information requirement. If this effect is not properly reproduced by MC, the P_T spectra could be artificially different between data and MC. As TOF performance is highly correlated to the occupancy, those effects can be different in the three data taking period where the accelerator instantaneous luminosity has increased of an order of magnitude. We then decided to correct MC for this effect according the following strategy:

- We produce the distributions of the ratio between the TOF efficiency in data and MC (Eff_{data}/Eff_{MC}) for tracks seen around $B^+ \to \overline{D}^0 \pi^+$ events, one for each of the three data taking periods. The tracks are selected according to the standard cuts of our analysis. The choice of $B^+ \to \overline{D}^0 \pi^+$ is due to the fact that it is the highest statistics sample and no significant differences are expected between each decay mode.
- We then fit, using a second degree polynomial, the three Eff_{data}/Eff_{MC} distributions separately. In Fig.8.2 we overimpose the fit result to the distributions obtained by B^+ and B^0 decay modes of the same data taking period (due to the

[3]The probability that a given track has TOF information.

very low statistics, B_s distribution are not shown). No significant differences are observed and we then decided to use the fit results of $B^+ \to \overline{D}^0 \pi^+$ as correction functions for MC events of all the decay modes.

- As shown in [57], dependencies of other kinematics variables introduced by TOF efficiency differences between data and MC disappear after the P_T correction is applied. Comparisons between data and MC will be performed using the whole statistics available on data, i.e. using the fit results of the merged data taking period samples. Because of this, for each track with a given P_T seen around a given B meson, the TOF efficiency correction weight will then be defined as a linear combination of the weights of the three periods. Called N^l_{0d}, N^l_{0h}, N^l_{0i} the number of tracks found in data for the decay mode l in each period, N^l_{tot} the total number of tracks in the data sample l and w_{0d}, w_{0h}, w_{0i} the efficiency correction weight of each period, we define the weight w^l_{tot} of the MC track from the decay mode l as:

$$w^l_{tot} = \frac{N^l_{0d}}{N^l_{tot}} w^l_{0d} + \frac{N^l_{0h}}{N^l_{tot}} w^l_{0h} + \frac{N^l_{0i}}{N^l_{tot}} w^l_{0i} \tag{8.1}$$

- MC tracks are reweighted according to the linear combination of efficiency correction functions extracted on data defined in eq.(8.1).

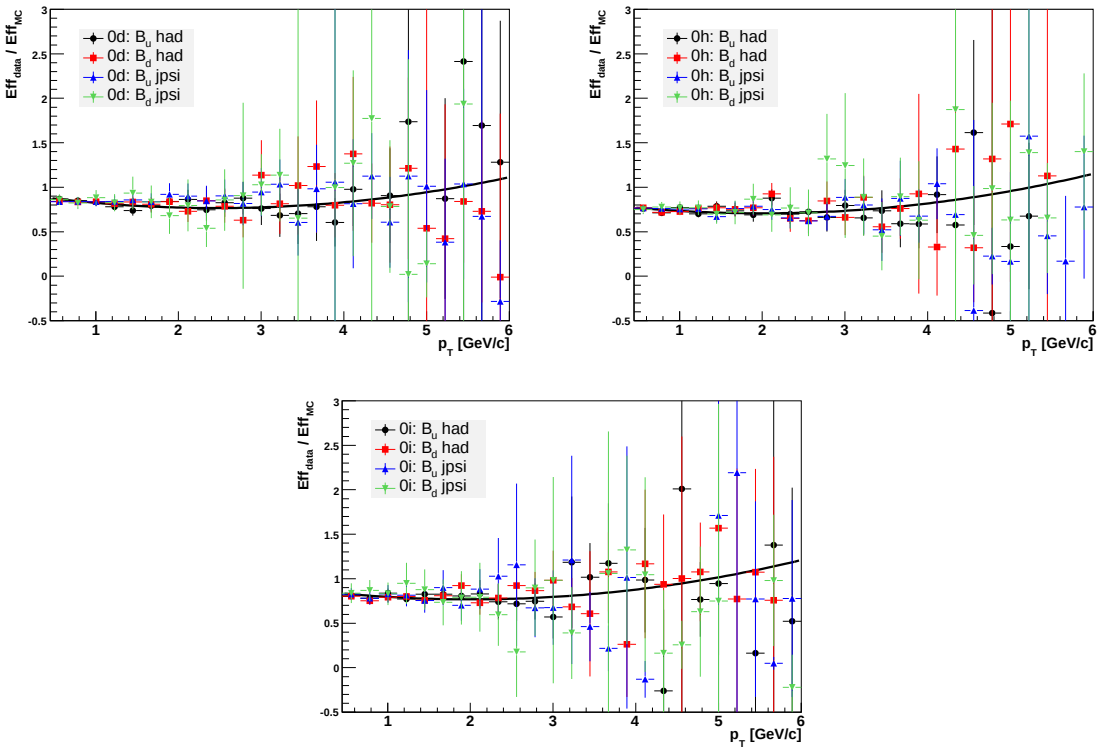

Figure 8.2: TOF efficiency correction for B^+, B^0 and B_s for the three data taking periods.

8.2 Comparison between Data and Monte Carlo

In the following sections we will proceed with the comparison between data and MC results on the particle species. As already mentioned, the same selections are applied both on data and MC events to the B meson candidates and to the tracks produced in association with their formation

Data results are obtained as described in chapter 7 including statics and systematics uncertainties. Monte Carlo results are extracted by the previously described samples by looking at the *truth* information, i.e. looking at the bank that keep records of the true characteristics of each particle as from the generation process, after selection cuts and TOF efficiency correction has been applied. As discussed in chapter 7, TOF and dE/dx information is not able to distinguish between pions and muons in data. As a consequence of this, also in MC all the *true* muons are flagged and considered as pions.

Systematics effects due to the MC reweighting according the TOF efficiency corrections were considered by varying the correction functions and where found to be negligible. Tab.8.2 reports the yield of each B signal sample both in data and MC.

Mode	Yield (Data)	Yield (MC)
$B^+ \to J/\psi K$	18302	369000
$B^0 \to J/\psi K^{*0}$	7564	178000
$B_s \to J/\psi \phi$	1329	28000
$B^+ \to D^0 \pi$	30005	239000
$B^0 \to D^- \pi$	25801	142000
$B_s \to D_s \pi$	1510	34000

Table 8.2: Yields of B meson signals in data and MC.

8.2.1 Particle Content

The comparisons between data and MC of the particle content around B mesons is reported in Tab.8.3. The fraction of each particle species is integrated in the considered P_T spectrum (0.45-6.0 GeV/c).

We can observe discrepancies on the pion fractions of the order of 5σ in the decay modes of the B^+ and B^0 (the highest statistics samples). The effect is not observed in the B_s, where the MC, although high uncertainties, seems to reproduce the pion content. Regarding the Kaon fraction, the MC seems to underestimate the content respect to data in B^+ modes (the effect is anyway around 3σ in the worst case); a similar behavior, but not at the same level, is seen also in B^0 samples. On the other hand, the trend seems to be inverted in the case of the B_s, where the central values of MC predictions on the Kaon content are always higher then the corresponding values found in data, although, due to large uncertainties on data results, more statistics is needed to take a conclusion. Finally, both for proton and electron, the MC seems to systematically underestimate the corresponding content with respect to data.

Meson	Decay	Pions (%)	Kaons (%)	Protons (%)	Electrons (%)
B^+	$\bar{D^0}\pi^+$ (Data)	77.52 ± 0.99	13.80 ± 0.73	7.06 ± 0.37	1.62 ± 0.76
	$\bar{D^0}\pi^+$ (MC)	82.79 ± 0.34	11.19 ± 0.12	5.60 ± 0.09	0.42 ± 0.02
	$J/\psi K^+$ (Data)	77.33 ± 1.32	13.03 ± 1.05	7.35 ± 0.64	2.29 ± 0.87
	$J/\psi K^+$ (MC)	82.99 ± 0.25	11.00 ± 0.09	5.56 ± 0.06	0.45 ± 0.02
B^0	$D^-\pi^+$ (Data)	79.54 ± 1.02	11.76 ± 0.71	6.68 ± 0.35	2.02 ± 0.80
	$D^-\pi^+$ (MC)	85.05 ± 0.43	10.06 ± 0.15	4.49 ± 0.09	0.40 ± 0.03
	$J/\psi K^*$ (Data)	78.54 ± 1.62	11.59 ± 1.26	7.21 ± 0.71	2.65 ± 1.00
	$J/\psi K^*$ (MC)	84.70 ± 0.32	10.42 ± 0.11	4.43 ± 0.07	0.45 ± 0.02
B_s	$D_s^-\pi^+$ (Data)	73.7 ± 4.4	16.6 ± 3.6	7.7 ± 2.0	2.0 ± 2.6
	$D_s^-\pi^+$ (MC)	73.2 ± 0.9	22.2 ± 0.5	4.1 ± 0.2	0.56 ± 0.08
	$J/\psi\phi$ (Data)	73.6 ± 4.2	19.4 ± 3.6	5.5 ± 1.8	1.6 ± 2.5
	$J/\psi\phi$ (MC)	74.3 ± 0.8	21.2 ± 0.4	4.0 ± 0.2	0.55 ± 0.07

Table 8.3: Particle type fractions estimated on the considered decay modes; systematic uncertainties included.

8.2.2 P_T distribution comparison

After having compared the integrated particle contents, we now compare the spectra of each particle type obtained from data to the corresponding Monte Carlo prediction. All the distributions are normalized to their area in order to neglect the discrepancies reported on the integrated fractions and consider only possible differences on the shape of the spectra.

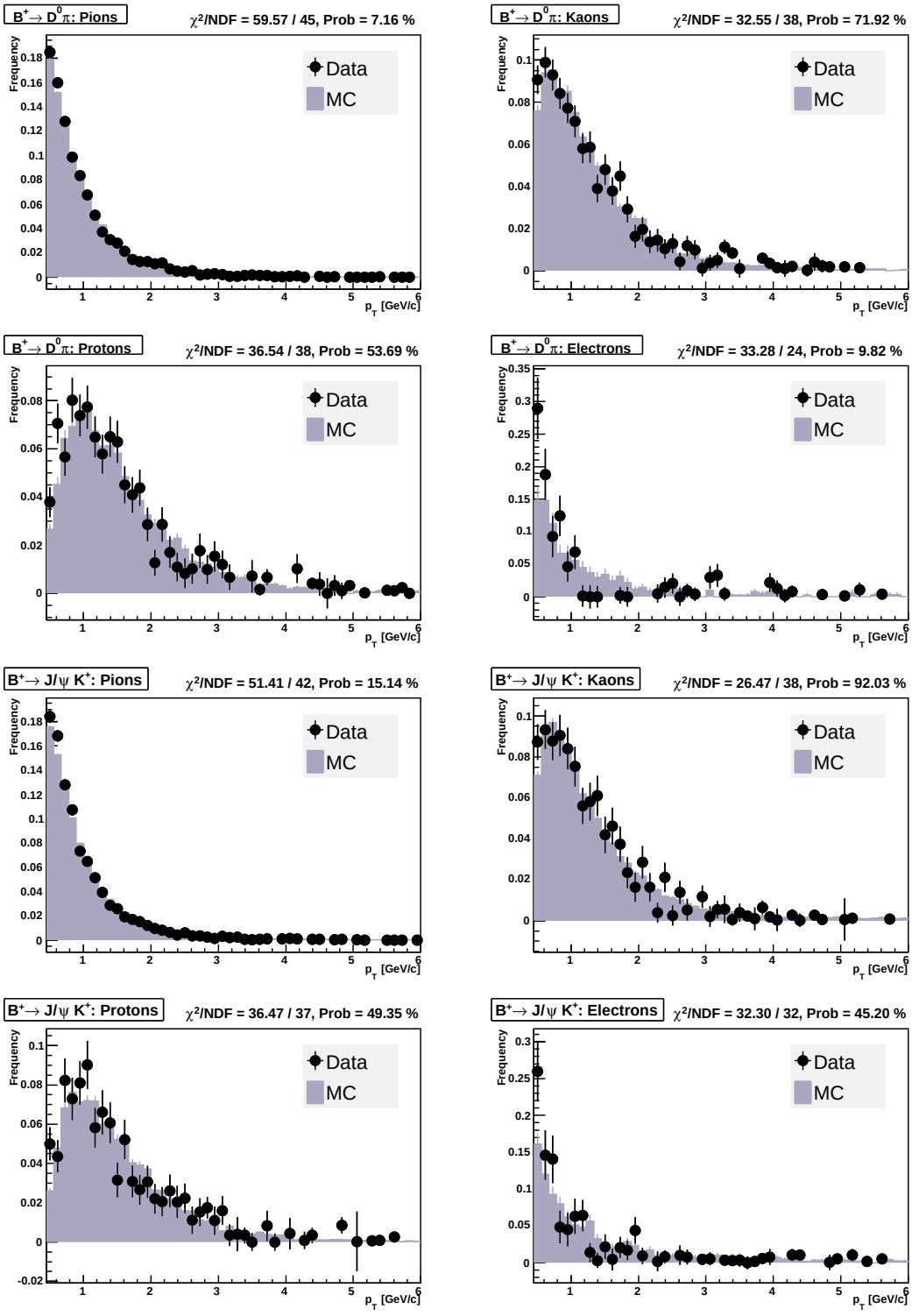

Figure 8.3: $B^+ \to \overline{D}^0 \pi^+$ and $B^+ \to J/\psi\, K^+$, P_T distributions of particle species seen around the B meson direction.

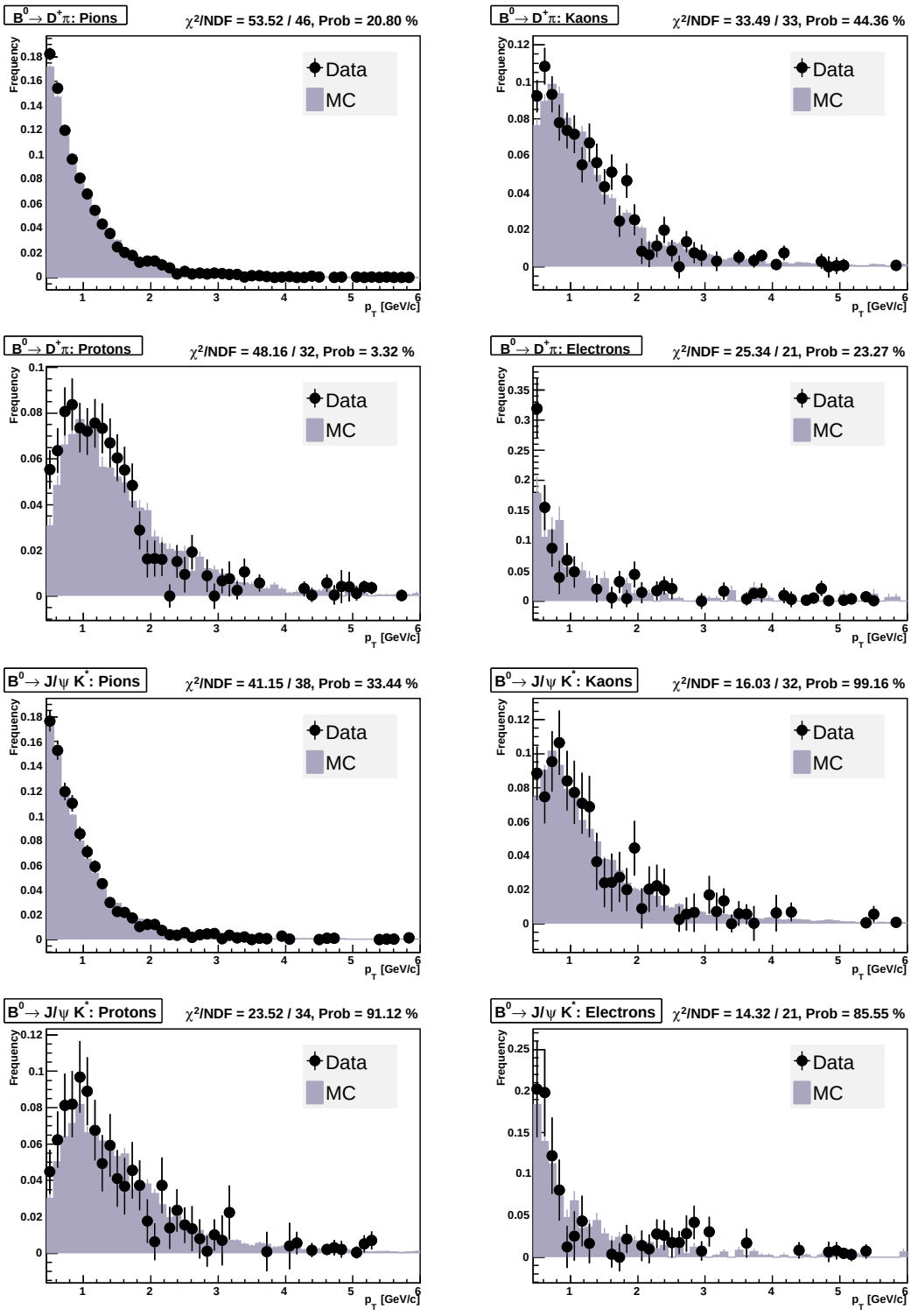

Figure 8.4: $B^0 \to D^- \pi^+$ and $B^0 \to J/\psi\, K^{*0}$, P_T distributions of particle species seen around the B meson direction.

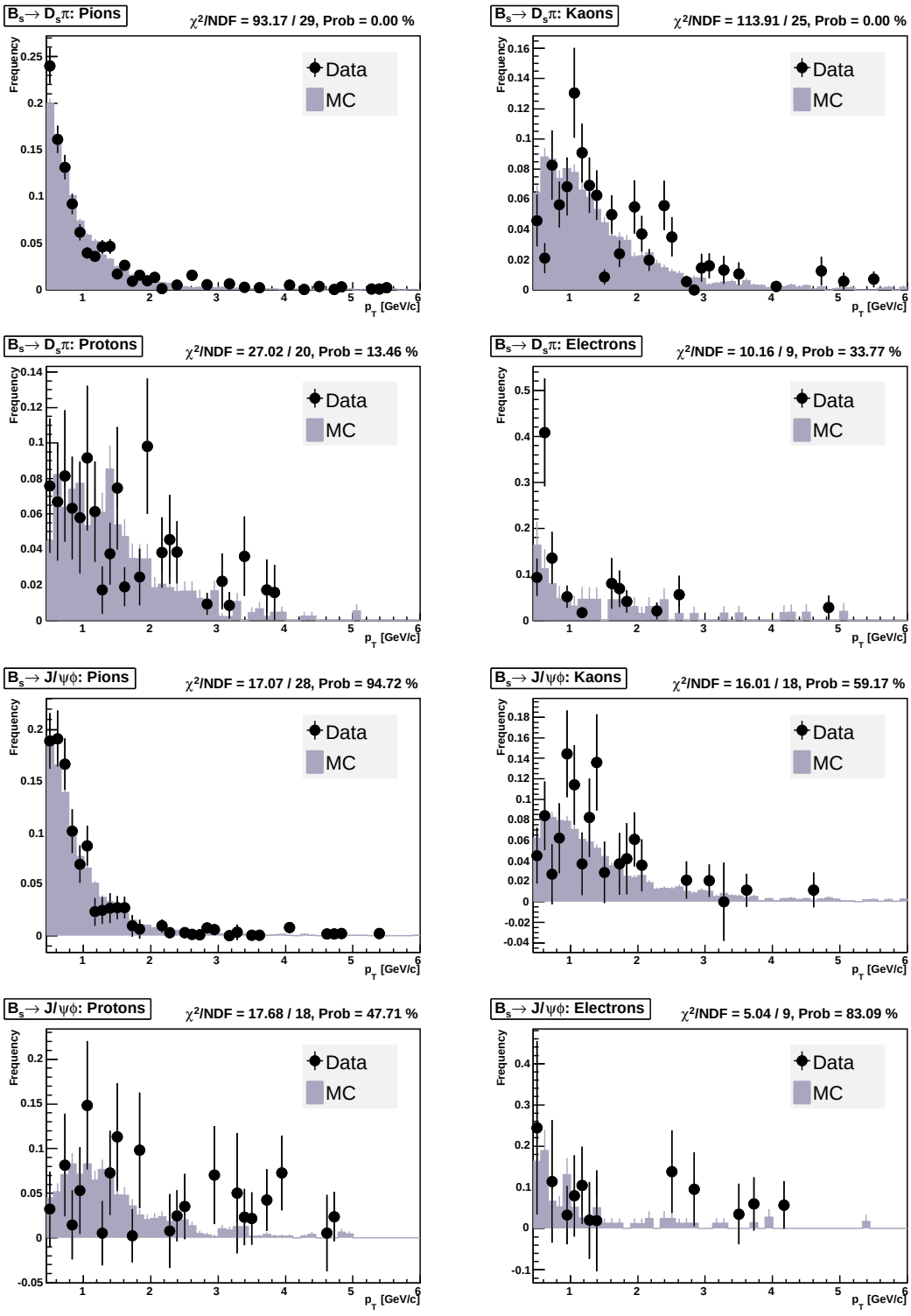

Figure 8.5: $B_s \to D_s^- \pi^+$ and $B_s \to J/\psi\,\phi$, P_T distributions of particle species seen around the B meson direction.

In each bin of data histograms, systematic (evaluated as described in the previous chapter) and statistics uncertainties are added in quadrature. The agreement between data and Monte Carlo spectra is fairly good for all the considered decay modes, even if the B_s modes need more statistics to have a better understanding of the picture. In particular, MC seems to reasonably reproduce what found in chapter 7 where, for a given B meson , the P_T spectrum of each particle species was seen to be different form the others. The shape of those distributions is reproduced by MC within uncertainties.

Conclusions

I started my PhD working on the development and the understanding of a Same Side Kaon Tagging algorithm for B_s mixing. That work provided significant information and triggered a strong effort in the CDF collaboration that made possible the use of SSKT on data analysis and consequently the recent observation of B_s mixing and Δm_s measurement at CDF.

As a consequence of my work on the Same Side Kaon Tagging for B_s mixing, I felt the need for a strategy that would allow to directly compare kinematic properties of different particle species in data and Monte Carlo.

I then developed two statistical methods to measure the particle fractions produced in association with B^+, B^0 and B_s mesons in terms of pions, kaons, protons and electrons. A first method avoids strong biases in Maximum Likelihood fits when the probability distribution of a variable used in the fit is unknown by using series expansions as a description of the unknown distributions. I then found a more interesting generalization, the second method described in chapter 6, that allows to extract at the same time any kinematic variable distribution of each particle species and the corresponding fraction. This method is completely data driven and no assumption is needed about the kinematics properties.

For the first time at hadron colliders, I performed the measurement of the particle species in combination with kinematics properties in fully reconstructed B meson samples. Results are resumed in Tab.8.4 where the corresponding particle content found in Monte Carlo for each decay mode is also reported.

Monte Carlo seems to systematically underestimate the electron content in all the considered decay modes. A similar behavior is observed for the proton content. On the contrary, the pion content around B^+ and B^0 mesons in significantly higher in Monte Carlo than data. The comparison of the P_T distributions is in reasonable agreement within statistics uncertainties.

Perspectives

The method I developed can be used in several cases. I would like to conclude this thesis briefly discussing two future applications on which I am already focusing.

- **Understanding of the tagging algorithms**

  I am currently working to a better understanding of SST and SSKT using the information provided by this method. A detailed data MC comparison is under-

Meson	Decay	Pions (%)	Kaons (%)	Protons (%)	Electrons (%)
B^+	$\bar{D^0}\pi^+$ (Data)	77.52 ± 0.99	13.80 ± 0.73	7.06 ± 0.37	1.62 ± 0.76
	$\bar{D^0}\pi^+$ (MC)	82.79 ± 0.34	11.19 ± 0.12	5.60 ± 0.09	0.42 ± 0.02
	$J/\psi K^+$ (Data)	77.33 ± 1.32	13.03 ± 1.05	7.35 ± 0.64	2.29 ± 0.87
	$J/\psi K^+$ (MC)	82.99 ± 0.25	11.00 ± 0.09	5.56 ± 0.06	0.45 ± 0.02
B^0	$D^-\pi^+$ (Data)	79.54 ± 1.02	11.76 ± 0.71	6.68 ± 0.35	2.02 ± 0.80
	$D^-\pi^+$ (MC)	85.05 ± 0.43	10.06 ± 0.15	4.49 ± 0.09	0.40 ± 0.03
	$J/\psi K^*$ (Data)	78.54 ± 1.62	11.59 ± 1.26	7.21 ± 0.71	2.65 ± 1.00
	$J/\psi K^*$ (MC)	84.70 ± 0.32	10.42 ± 0.11	4.43 ± 0.07	0.45 ± 0.02
B_s	$D_s^-\pi^+$ (Data)	73.7 ± 4.4	16.6 ± 3.6	7.7 ± 2.0	2.0 ± 2.6
	$D_s^-\pi^+$ (MC)	73.2 ± 0.9	22.2 ± 0.5	4.1 ± 0.2	0.56 ± 0.08
	$J/\psi\phi$ (Data)	73.6 ± 4.2	19.4 ± 3.6	5.5 ± 1.8	1.6 ± 2.5
	$J/\psi\phi$ (MC)	74.3 ± 0.8	21.2 ± 0.4	4.0 ± 0.2	0.55 ± 0.07

Table 8.4: Particle type fractions estimated on the considered decay modes; systematic uncertainties included.

way in order to establish the level of accuracy of MC predictions. For example an interesting improvement is the separation of the *right sign* and *wrong sign* component of each particle species, where right sign (wrong sign) means the right (wrong) charge correlation with respect to the B, as discussed in chapter 1. Examples of such distributions are shown in Fig.8.6: Kaons P_T distribution of right and wrong sign around B^+ events (left) and around B^0 events (right). In the latter, to take into account mixing effects, I include in the fit the probability that the B^0 meson has oscillated. Notice the Kaon excess in the case of B^+ where kaons are expected to carry tagging information, while no excess is observed for

B^0 where kaons are not expected to be tagging particles.

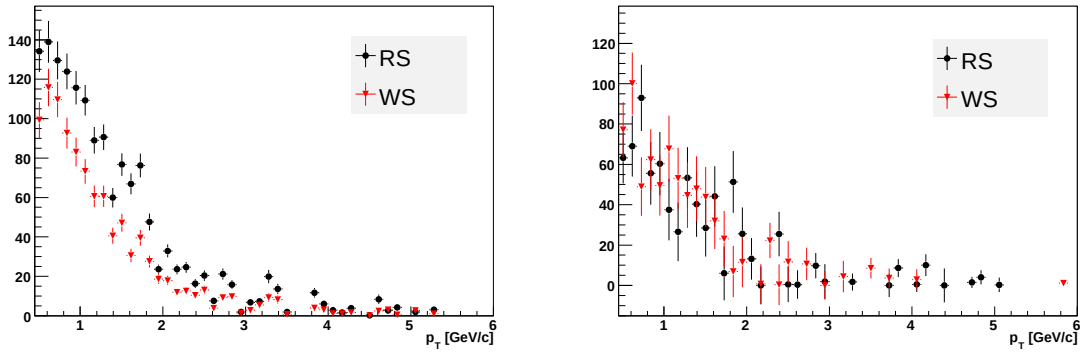

Figure 8.6: Left: P_T distribution of right sign (black) and wrong sign (red) kaons around fully reconstructed $B^+ \to \overline{D}^0 \pi^+$ events. Right: P_T distribution of right sign (black) and wrong sign (red) kaons around fully reconstructed $B^0 \to D^- \pi^+$ events.

These studies are exploiting the use of different kinematic variables of each particle species to develop an optimized algorithm reducing the corresponding systematic uncertainties. Even if B_s mixing has been observed and Δm_s measured, optimized taggers could improve CDF capabilities in time-dependent CP violation analysis of $B_s \to J/\psi\,\phi$ and $B \to h^+h^-$ events [89].

- **Particle produced in association with b-baryons**

  CDF collected the biggest sample of fully reconstructed Λ_b^0 events [90]. The measurement of the particle content around Λ_b^0 baryon and related kinematics variables will be performed for the first time in order to improve our understanding of baryons fragmentation.

Bibliography

[1] The CDF collaboration, Measurement of B^0 Oscillation Using Same-Side Tagging in Fully Reconstructed Decays CDF Note 7187, (2004).

[2] The CDF collaboration, Measurement of B^0 Oscillation and Calibration of Flavor Tagging in Fully Reconstructed Decays CDF Note 7511, (2005).

[3] H. G. Moser and A. Roussarie, *NIM, A384 (1997), 491-505.*

[4] G. Boix, Study of B_s oscillation iwth the ALEPH detector at LEP, ALEPH-THESIS-2001-006, (2001).

[5] G.J.Barker, M.Feindt, U.Kerzel, C.Lecci, G.Bauer, G.Gomez-Ceballos, I.Kravchenko, N.Leonardo, S.Menzemer, Ch.Paus, A.Rakitin, J.Piedra, A.Ruiz, I.Vila, I.Furic, Monte Carlo study of lepton SVT sample, CDF Note 7318, (2004).

[6] G. Bauer, P. Maksimovic *et al.*, Comparison of SST distribution from $lD^{(*)}$ data and Pythiam CDF Note 4555, (1998).

[7] The CDF collaboration, Long-term Sensitivity Projection for B_s Mixing, CDF Note 7671, (2005),

[8] P. Catastini, Same side Koan Tagging at CDF, CKM 2005

[9] P. Catastini, B Fragmentation and Same Side Kaon Tagger, APS April meeting 2005.

[10] M. Rescigno, B mixing at CDF, BEAUTY 2005 - 10th International Conference on B-Physics at Hadron Machines.

[11] G. Gomez-Ceballos, B_s Properties at the Tevatron, Hadron Collider Physics Symposium 2005.

[12] N . Leonardo, B_s Mixing at CDF, HEP2005 - International Europhysics Conference on High Energy Physics.

[13] S. Menzemer, Search for Bs Oscillations at CDF, PANIC 05 - XVII Particles and Nuclei International Conference.

[14] The CDF Collaboration, Observation of $B_s - \bar{B}_s$ Oscillation, [arXiv:hep-ex/0609040].

[15] C. Peterson, D. Shlatter, I. Schmitt and P. M. Zerwas, Scaling violations in inclusive e^+e^- annihilation spectra, Phys. Rev. D **27** (1983) 105.

[16] The SLD Collaboration, Measurement of the b-quark fragmentation function in Z^0 decays, [arXiv:hep-ex/0202031].

[17] J.D. Richman., Heavy Quark Physics and CP Violation. *Elsevier Science B.V.*, (1998)

[18] L.Wolfenstein, *Phys. Rev. Lett.* **51** (1983) 1945.

[19] See review of Particle Data Group, *CKM quark-mixing matrix*, F.J. Gilman, K. Kleinknecht and B. Renk.

[20] J.-M. Gerard and W.-S. Hou, *Phys. Rev.* D **43**, 2909 (1991).

[21] S. Aoki Lattice calculations and hadron physics. *Int. J. Mod. Phys.*, **A** 15S1:657-683 (2000).

[22] M. Battaglia et al., The CKM matrix and the Unitarity Triangle, *hep-ph/0304132* (2003)

[23] The Heavy Flavor Averaging Group (HFAG), Averages of b-hadron Properties as of Summer 2006,
`http://www.slac.stanford.edu/xorg/hfag/triangle/ichep2006/index.html`

[24] http://utfit.roma1.infn.it/, after CDF B_s mixing observation.

[25] B. Aubert *et all.*, (`BaBar` Collaboration), *Phys. Rev. Lett.* **92**, 181801 (2004)

[26] J. Adballah *et all.*, (`DELPHI` Collaboration), *Eur. Phys. J.* C **28**, 115 (2003)

[27] Fermilab Beams Division,
`http://www-ad.fnal.gov/runII/index.html` .

[28] Fermilab Beams Division, Fermilab Linac Upgrade. Conceptual Design, *FERMILAB-LU-Conceptual Design*,
`http://www-lib.fnal.gov/archive/linac/fermilab-lu-conceptualdesign.shtml`.

[29] Fermilab Beams Division, The antiproton source rookie book,
`http://www-bdnew.fnal.gov/pbar/documents/PBAR_Rookie_Book.pdf`.

[30] Fermilab Beams Division, The Recycler ring,
`http://www-recycler.fnal.gov/recycler_main.html`.

[31] F. Abe *et al.*(The CDF II Collaboration), "The CDF II Technical Design Report", *FERMILAB-PUB-96-390-E*, Oct 1996.

[32] S. M. Sze, Physics of Semiconductor Devices, SECOND EDITION, *John Wiley & Sons*

[33] The CDF II Collaboration, Proposal for Enhancement of the CDF II Detector: An Inner Silicon Layer and A Time of Flight Detector, *Fermilab-Proposal-909*, Oct. 1998.
Update to Proposal P-909: Physics performance of CDF II with an Inner Silicon Layer and a Time of Flight detector,
`http://www-cdf.fnal.gov/upgrades/btb-update_jan99.ps`,(1999).

[34] J. Marriner, Secondary vertex fit with mass and pointing constrains (`CTVMFT`), CDF Note 1996, (1993).

[35] W.-M. Yao, and K. Bloom, "Outside-In" silicon Tracking at CDF, CDF Note 5562, (2002).

[36] P.Azzi, G. Busetto, A. Ribon, Histogram tracking in the COT, CDF Note 5562, (2001).

[37] H. Frisch *et. all.*, Conceptual design of a deadtimeless trigger for the CDF trigger upgrade, CDF Note 2038, (1994).

[38] The CDF II Collaboration, CDF Run II trigger table and datasets plan, CDF Note 4718, (2001).

[39] E. Thomson *et. al.*, Online track processor for the CDF Upgrade, *IEEE Transactions on Nuclear Science*, Vol. 49, No. 3,(2002)

[40] A. Bardi, S. Belforte, *et all.*, "SVT: An Online Silicon Vertec Tracker for the CDF upgrade", *Nucl. Instr. Meth.*, Vol. A **409**,658-661, 1998

[41] W. Ashmanskas, A. Bardi, *et all.*, " The CFD Silicon Vertex Tracker: online precision tracking of the CDF Silico Vertex Detector", *Il Nuovo Cimento*, Vol. 112 A, no. 11,1239-1243, 1999.

[42] W. Ashmanskas, A. Bardi, *et all.*, "Silicon Vertex TRacker: A fast precise tracking trigger for CDF", *Nucl. Instr. Meth.*, Vol A **447**,218-222, 2000.

[43] J. A. Walls, " The SVX II Silicon Vertex Detector at CDF", *Nulc. Phys. B*, Vol 78,311-314, 1999.

[44] S. Belforte, M. Dell'Orso, *et all.*, "The SVT Hit Buffer", *IEEE Trans. Nucl. Sci.*, Vol. 43,1810-1813, 1996.

[45] S.R. Amendolia, S. Galeotti, *et all.*, "The AMchip: a full-custom CMOS VLSI Associative Memory for Pattern Recognition", *IEEE Trans. Nucl. Sci.*, Vol. 39,795-797, 1992.

[46] H.C. Andrew, Introduction to mathematical techniques in experimental data evaluation, *Wiley-Interscience*, 1972.

[47] H. Wind, Principal component analysis and its application to track finding, in " Formulae and methods in experimentl data evaluation", vol. III, R. Bock, *Europen Physical Society*, 1984.

[48] W. Ashmanskas *et al.*, Performance of the CDF Online Silicon Vertex Tracker, CDF Note 5854 publeshed also on *Transactions on Nuclear Science*. (2002)

[49] S. Donati et. all., $B^0 \to \pi^+\pi^-$ Trigger Studies with Run Ia Data, CDF Note 3167, (1995)

[50] K. Anikeev *et. all.*, Event Builder and Level-3 for aces,CDF Note 5793,(2001).

[51] S.Klimeno *et. all.*, The CDF Run II luminosity monitor,CDF Note 4330, (1998).

[52] S. Klimeno *et. all.*, CLC production and mechanical assembly, CDF Note 5119, (1999).

[53] D. Acosta *et. all.*, A first look at the CLC luminosity measurements, CDF Note 6052, (2002).

[54] Review of Particle Physics , *The European Physical journal C*, Societ Italiana di Fisica & Springer-Verlag, 2004.

[55] A.Belloni, R.Carosi, S.Donati, I.Fiori, G.Punzi, First look at Two-Track trigger data, CDF Note 5758 Version 1.1, Dec. 2001.

[56] A.Cerri, R. Miqquel, Studying the SVT Efficiency and Resolution with J/ψ Data, CDF Note 5838 Version 1.0, (2002).

[57] The CDF B_s mixing working group, CDF Note 7979.

[58] K. Anikeev, CDF Public Note 7269.

[59] A. Abulencia *et al.* [CDF Collaboration], "Measurement of the ratios of branching fractions $B(B_s^0 \to D_s^-\pi^+)/B(B^0 \to D^-\pi^+)$ and $B(B^+ \to \overline{D}^0\pi^+)/B(B^0 \to D^-\pi^+)$," Phys. Rev. Lett. **96** (2006) 191801 [arXiv:hep-ex/0508014].

[60] The CDF B_s mixing working group, CDF Note 7386.

[61] Petar Maksimovic,*PhD Dissertation, MIT 1997.*

[62] P. Catastini *et al.* Same Side Kaon Tagging Studies, CDF Note 7496, (2005)

[63] F. Bedeschi,E. Ben−Haim, P. Catastini, P. Maksimovic, J. Pursley, A. Savoy−Navarro, CDF Note 7428.

[64] G. Punzi, [arXiv:physics/0401045].

[65] S. Belforte et al., CDF Note 7474

[66] "http://www-cdf.fnal.gov/internal/physics/bottom/b-montecarlo/"

[67] G. Bauer et al., CDF Note 7388

[68] F. Azfar et al., CDF Note 7386

[69] P. Squillacioti et al., CDF Note 7484

[70] Z. Albrecht et al., DELPHI Collaboration, DELPHI 2004-025 CONF 700.

[71] Particle Data Group, Phys. Lett. B 592,1 (2004).

[72] R. Field, CDF Note 6403

[73] P. Catastini, G. Punzi, Proceedings of PHYSTAT05: Statistical Problems in Particle Physics, Astrophysics and Cosmology, Oxford, England, United Kingdom, 12-15 Sep 2005, *[arXiv:physics/0605130]*.

[74] M. Jones, J. Kroll, D. Usynin, CDF Note 7810.

[75] P. E. Condon and P. L. Cowell, *Phys. Rev. D* **9**, *2558 (1974)*.

[76] J. B. Gay *et al.* [Amsterdam-CERN-Nijmegen-Oxford Collaboration], *Phys. Lett. B* **63**, *220 (1976)*.

[77] D. Buskulic *et al.* [ALEPH Collaboration], *Phys. Lett. B* **307**, *209 (1993)*.
P. D. Acton *et al.* [OPAL Collaboration], *Z. Phys. C* **59**, *1 (1993)*.

[78] B. Aubert *et al.* [BABAR Collaboration], *Phys. Rev. D* **69**, *031101 (2004) [arXiv:hep-ex/0310050]*.

[79] G. D'Agostini, *Nucl. Instrum. Meth. A* **362**, *487 (1995)*.

[80] M. Pivk and F. R. Le Diberder, *Nucl. Instrum. Meth. A* **555**, *356 (2005) [arXiv:physics/0402083]*.

[81] J. M. Ortega and W. C. Rheinboldt *"Iterative Solution of Nonlinear Equations in Several Variables", SIAM publications.*

[82] F. James, M. Roos, Minuit: a system for funtcional minimization and analysis of the parameter errors and correlations. *CERN-DD-75-20*, 1975.

[83] P. Squillacioti *et al.* Particle Identification by combining TOF and dEdx information. CDF Note 7488 (2005).

[84] P. Squillacioti *et al.* Update of Combined PID. CDF Note 7866 (2005) and 8478 (2006).

[85] T. Sjostrand, L. Lonnblad, S. Mrenna, Pythia 6.2: Physics and Manual. *[arXiv:hep-ph/0108264]*, 2001.

[86] D. J. Lange, The EvtGen particle decay simulation package. *Nucl. Instrum. Meth. A* **462**, *152 (2001)*

[87] R. Brun, R. Hagelberg, M. Hansroul and J. C. Lassalle, Geant: Simulation program for particle physics experiments. User guide and reference manual. *CERN-DD-78-2-REV*, 1978.

[88] R. Brun, F. Bruyant, M. Maire, A. C. McPherson and P. Zanarini, Geant3. *CERN-DD/EE/84-1*, 1984.

[89] The CDF, D0 and B-TeV collaborations, B Physics at the Tevatron: Run II and beyond, *[arXiv:hep-ph/0201071]*.

[90] The CDF collaboration, Observation of New Heavy Baryons Σ_b and Σ_b^* CDF Note 8523, (2005).